

Effects of nonlinear sound propagation in fisheries research

Audun Pedersen



Dissertation for the degree philosophiae doctor (PhD)
at the University of Bergen

24 October 2006

Preface

This PhD work has been carried out during a three-year period, under the supervision of Associate Professor Magne Vestrheim, Department of Physics and Technology, University of Bergen, and Senior Scientist Dr. Philos. Per Lunde, Department of Industrial Instrumentation, Christian Michelsen Research AS.

The work is part of the project "Minimizing errors due to nonlinear effects in fisheries and research echo sounders and sonar", a joint venture between Christian Michelsen Research AS (CMR), Department of Physics and Technology at the University of Bergen (UoB), Institute of Marine Research (IMR), and Simrad AS. The project is led by Per Lunde, CMR, and funded by the Research Council of Norway under the MARE programme. My workplace during the PhD work has been at CMR, Bergen, Norway.

I wish to thank my supervisors for their guidance. Throughout the work, both have been available for discussions whenever necessary. A weekly meeting has been held between the supervisors and the candidate.

Frank Tichy, Simrad AS (his department now belongs to Kongsberg Maritime AS), and Rolf Korneliussen, IMR, are thanked warmly for useful help and discussions, in particular their indispensable help in providing equipment and access to measurement facilities. Echo sounder equipment has been borrowed from IMR and Simrad. Simrad also granted access to their acoustic measurement facilities in Horten, Norway. The measurements there were carried out with the much-appreciated assistance from Frank Tichy. IMR provided time for echo sounder measurements on the research vessel G. O. Sars. These measurements were made with good support from Rolf Korneliussen. CMR and UoB have also provided important equipment. Several

components needed for the experiments were made at the mechanical workshop of the Department of Physics and Technology, UoB.

Andrew Baker, CMR, and Lucio Calise, Department of Physics and Technology, UoB, are thanked for useful discussions and participation in measurements in seawater. The Marine Biological Station Espeland, which belongs to UoB, provided facilities for some of the seawater measurements. Tomas Sørli, Department of Biology, UoB, is acknowledged in particular for his assistance with practical arrangements at Espeland. Os Yacht Club also granted access to their marina in Os, Norway, where some experiments were made. Frank Ådland, CMR, and Olav Haugland, Os Yacht Club, are thanked for their help with the latter experiments.

Figures on Pages 165–167 have been reproduced with permission from David Blackstock, James Lockwood, Thomas Muir, Jack Shooter, and the Acoustical Society of America. The illustrations on pages 14 and 208 and Figure 6.10 (page 182) are included by courtesy of Simrad AS, MAR-ECO, and IMR, respectively.

I want to thank my fiancée Inger Olin Oppedal and the rest of my family for their patience and support, in particular during the last months of my PhD work.

Preliminary results from the PhD work have been presented at several meetings:

A. Pedersen, P. Lunde, and M. Vestrheim, *Nonlinear effects in fisheries and research echo sounders and sonar*. Presented at the final seminar for the MARE research programme. The Research Council of Norway, Oslo, Norway, 12–13 October, 2005.

A. Pedersen, M. Vestrheim, and P. Lunde, *Ikkelineær lydforplantning ved bruk av ekkolodd i fiskeriforskning (Nonlinear sound propagation in fisheries research applications of echo sounders)*. Presented at the 2005 meeting of the Norwegian Physical Society, Ulvik, Norway, 11–14 August, 2005.

A. Pedersen, M. Vestrheim, and P. Lunde, *Quantification of nonlinear sound propagation effects in fisheries research echo sounders*. In *Proceedings of Underwater Acoustic Measurements: Technologies & Results*, edited by J. Papadakis and L. Bjørnø. Crete, Greece, 28 June–1 July, 2005. Vol. II, pp. 751–756.

A. Pedersen, M. Vestrheim, and P. Lunde, *Consequences of nonlinear sound propagation for target strength measurement – preliminary studies*. Presented at the meeting of the ICES Working Group on Fisheries Acoustic Science and Technology, Rome, Italy, 19–22 April, 2005.

A. Pedersen, M. Vestrheim, and P. Lunde, *Nonlinear sound propagation effects in fisheries research echo sounders – measurements and simulations in fresh water*. In *Proceedings of the 28th Scandinavian Symposium on Physical Acoustics*, edited by U. R. Kristiansen. Ustaoset, Norway, 23–26 January, 2005. ISBN 82-8123-000-2 (abstract).

A. Pedersen, *Nonlinear effects in fisheries and research echo sounders and sonars*. Presented at the 2004 seminar for PhD students under the MARE research programme. The Research Council of Norway, Oslo, Norway, 14–15 October, 2004.

A. Pedersen, P. Lunde, and M. Vestrheim, *Convergence and accuracy of the Bergen Code for investigating nonlinear effects in fisheries echo sounders*. In *Proceedings of the 27th Scandinavian Symposium on Physical Acoustics*, edited by U. R. Kristiansen. Ustaoset, Norway, 25–28 January, 2004. ISBN 82-8123-000-2.

A. Pedersen, *Nonlinear effects in fisheries and research echo sounders and sonars*. Presented at the 2003 seminar for PhD students under the MARE research programme. The Research Council of Norway, Tromsø, Norway, 28 October, 2003.

Table of contents

| | |
|---|-----|
| Preface..... | 3 |
| Table of contents..... | 7 |
| Chapter 1. Introduction..... | 9 |
| 1.1. Motivation..... | 9 |
| 1.2. Overview of the work..... | 11 |
| Chapter 2. Background..... | 14 |
| 2.1. Basic principles of fisheries acoustics..... | 14 |
| 2.1.1. Theory of sound propagation..... | 15 |
| 2.1.2. Transducer properties..... | 17 |
| 2.1.3. Backscattering from a single target..... | 18 |
| 2.1.4. Sonar equation and power budget..... | 20 |
| 2.1.5. Backscatter from a volume..... | 24 |
| 2.1.6. Expressions used in echo sounder measurements..... | 27 |
| 2.1.7. Calibration and accuracy..... | 29 |
| 2.2. Nonlinear sound propagation..... | 31 |
| 2.2.1. Some central developments in nonlinear acoustics..... | 31 |
| 2.2.2. Nonlinear effects and fisheries acoustics..... | 41 |
| 2.2.3. The KZK equation..... | 41 |
| 2.2.4. The Bergen Code..... | 46 |
| Chapter 3. Simulation uncertainty..... | 55 |
| 3.1. Model uncertainty..... | 57 |
| 3.2. Uncertainty contribution due to the numerical algorithm..... | 64 |
| 3.2.1. Indicators for comparison between simulation results..... | 65 |
| 3.2.2. Numerical uncertainty contributors..... | 67 |
| 3.2.3. Test simulations for the influence of grid parameters..... | 74 |
| 3.2.4. Test simulation results, low amplitude..... | 76 |
| 3.2.5. Test simulation results, high amplitudes..... | 80 |
| 3.2.6. Combined numerical uncertainty..... | 87 |
| 3.3. Uncertainty contribution due to physical input parameters..... | 90 |
| 3.3.1. Sensitivity study..... | 91 |
| 3.3.2. Results..... | 92 |
| 3.4. Combined simulation uncertainty..... | 100 |
| Chapter 4. Near field measurements..... | 103 |
| 4.1. Experiment..... | 104 |
| 4.1.1. Experimental arrangement..... | 104 |
| 4.1.2. Signal processing..... | 109 |
| 4.2. Measurement results..... | 114 |
| 4.3. Experimental source conditions for numerical simulations..... | 122 |
| 4.3.1. Source conditions from measurements..... | 122 |
| 4.3.2. Simulation results for linear sound beams..... | 125 |
| Chapter 5. Sound propagation in fresh water..... | 128 |
| 5.1. Measurements in fresh water..... | 129 |

| | |
|---|-----|
| 5.1.1. Measurement facilities and echo sounders | 129 |
| 5.1.2. Hydrophone measurements | 131 |
| 5.1.3. Calibration sphere measurements | 141 |
| 5.2. Simulations for fresh water | 143 |
| 5.2.1. Simulations for comparison with measurements | 143 |
| 5.2.2. Simulations for comparison with other works | 145 |
| 5.3. Results for sound propagation in fresh water | 146 |
| 5.3.1. Hydrophone measurement results | 146 |
| 5.3.2. Nonlinear attenuation in fresh water | 149 |
| 5.3.3. Target strength measurements | 151 |
| 5.3.4. Comparison with earlier works | 155 |
| 5.3.5. Figures | 157 |
| Chapter 6. Sound propagation in seawater | 168 |
| 6.1. Measurements in seawater | 169 |
| 6.1.1. Hydrophone measurements | 169 |
| 6.1.2. Calibration sphere measurements | 178 |
| 6.2. Simulations for seawater | 182 |
| 6.2.1. Simulation parameters | 182 |
| 6.2.2. Absorption frequency dependence | 184 |
| 6.2.3. Bubbles and inhomogeneities | 188 |
| 6.3. Measurement and simulation results for sound propagation in seawater | 190 |
| 6.3.1. Results from hydrophone measurements | 190 |
| 6.3.2. Results from calibration sphere measurements | 194 |
| 6.3.3. Nonlinear attenuation along the sound beam axis | 203 |
| Chapter 7. Volume scattering | 208 |
| 7.1. Compensation of volume backscattering measurements | 208 |
| 7.1.1. Compensated volume backscattering coefficient | 209 |
| 7.1.2. Nonlinear effects in echo sounder calibration | 210 |
| 7.1.3. Compensation factors from simulations | 212 |
| 7.2. Experiment | 218 |
| 7.2.1. Measurement of area backscattering coefficient | 219 |
| 7.2.2. Comparison with simulation results | 222 |
| Chapter 8. Conclusion | 225 |
| 8.1. Summary | 225 |
| 8.2. Suggestions for further work | 230 |
| References | 233 |
| Appendix A: List of symbols | 255 |
| Appendix B: Bergen Code program listing | 265 |
| Appendix C: Hydrophone calibration data | 288 |

Chapter 1. Introduction

1.1. Motivation

Acoustic methods are important tools in fisheries research. For most fish species, the use of echo sounder measurements as a first step in abundance estimation has been experienced to yield at least as accurate results as any other method.^{183,140} Echo sounders are also used for other purposes in marine research, e.g. biomass and size estimation of plankton.

Echo integration based on sound bursts with a single operating frequency is commonly used for fish abundance estimation.¹⁶⁷ The choice of frequency is a trade-off between range and ability to make quantitative measurements on small animals.^{139,223} Modern fisheries research vessels are often capable of using several echo sounder frequencies simultaneously. One potential advantage of multi-frequency methods is improved discrimination between different species compared with single frequency techniques. This can contribute to reducing the uncertainty in fish stock assessments.

During recent development of echo sounders with increased accuracy and dynamic range, one has become aware that significant effects of nonlinear sound propagation can occur with the operating frequencies and output powers used in fisheries research.^{29,30,233,234} Excess sound attenuation due to nonlinear effects (“nonlinear attenuation”) is not accounted for in the presently used echo sounders. Increased knowledge of what importance nonlinear attenuation may have for methods in fisheries acoustics is of interest.

Nonlinear effects depend on several factors such as transmitted frequency, acoustic intensity, sound propagation distance, and properties of the sound source and the water. Tichy *et al.*^{233,234} made measurements along the sound

beam axis of a 200 kHz echo sounder in fresh water and found that the attenuation at the operating frequency due to nonlinear sound propagation can reach several decibels. The experimental results were compared with simulations made by Baker and Lunde.²⁹ Nonlinear attenuation may pose a problem for abundance estimation, and in particular for discrimination between species by means of multiple frequencies. The investigation of Tichy *et al.*^{233,234} uncovered a need for further quantitative investigations of nonlinear attenuation off the sound beam axis, at longer distances from the sound source, and in seawater. The echo sounder frequencies used by IMR at present are 18 kHz, 38 kHz, 70 kHz, 120 kHz, 200 kHz, 364 kHz, and 710 kHz.¹⁴⁴ Nonlinear attenuation seems to be a potential problem for the 120 kHz and higher operating frequencies.¹³

The subject of finite-amplitude sound propagation has been widely studied. The particular implications within fisheries acoustics are however not known well enough to eliminate measurement errors due to nonlinear effects. The goal of the present work is to increase the quantitative knowledge of the nonlinear effects experienced by fisheries research echo sounders using two common operating frequencies. The results may provide a basis for reducing or correcting for measurement errors due to nonlinear attenuation. The accuracy with which such corrections can be made under relevant conditions is investigated. There is also some interest in exploring the possibility of using nonlinear effects, as e.g. the second harmonic frequency component generated through intense sound propagation, to increase the amount of information obtained through echo sounder measurements. Measurement and simulation results for the second harmonic frequency component are reported, but attention is primarily given to the problem of nonlinear attenuation.

1.2. Overview of the work

Nonlinear sound propagation effects in the sound beams of fisheries research echo sounders are investigated experimentally and by numerical simulations. Echo sounders with 120 kHz and 200 kHz operating frequencies are considered. An attempt is made to quantify the excess attenuation due to nonlinear effects in fresh water and seawater. Consequences of such attenuation for fisheries research applications are discussed. Results for the second harmonic frequency component generated through nonlinear distortion are also presented.

Definitions and relations from underwater and fisheries acoustics that are used in the work are summarized in Chapter 2. In addition, a brief account is given of the most relevant features in the history of nonlinear acoustics. The model and numerical algorithm used in the present work are described, and an overview is given of other methods.

One of the questions that the present work seeks an answer to is how accurately the numerical algorithm used here can predict nonlinear attenuation in cases of interest in fisheries acoustics. Test simulations are run to obtain an estimate for the simulation uncertainty. Uncertainty contributions due to the sound propagation model, the numerical algorithm, and uncertainties in the input parameters are investigated in Chapter 3. Source radii, frequencies, amplitudes, and parameters of the water are set so that they correspond to the measurements in the present work. An estimate is made of a combined simulation uncertainty for the paraxial sound field radiated by a uniform circular piston in a stiff baffle.

The sound source descriptions used for simulations are discussed in Chapter 4. Sound pressure measurements are made in the near fields of three echo sounder transducers in order to characterize the sound sources and investigate the applicability of the numerical algorithm. The measurement results are used to make alternative source conditions for numerical simulations. Simulations of

linear sound propagation are made with uniform piston source conditions and those obtained from near field measurements. The results from simulations with different source conditions are compared.

In Chapters 5 and 6, sound pressure measurements in the acoustic fields radiated by 120 kHz and 200 kHz echo sounders are carried out with a hydrophone. In addition, experimental backscatter measurements are made with calibration spheres as reference targets. This is done to establish correspondence between the nonlinear attenuation measured with the hydrophone and possible errors in target strength measurements made with the echo sounders. The calibration spheres are used by IMR in their routine echo sounder calibrations. Moreover, measurements of sound propagation to longer distances than approximately 10 m are made with calibration spheres instead of the hydrophone. The position of the target and the amplitude of the signal transmitted by the echo sounder are varied.

Water tanks offer a well-controlled environment and accurate positioning of the echo sounder transducers, hydrophone, and reference target. Measurements in an indoor fresh water tank are described in Chapter 5. The pressure amplitudes for the fundamental and second harmonic frequency components are investigated. Measurement results are compared with results from simulations using both the uniform piston and near field measurement source conditions. The nonlinear attenuation along the sound beam axis and the increase in the -3 dB beam angle are quantified. Simulations of nonlinear attenuation in fresh water are compared with experimental results reported in the literature.

Chapter 6 describes measurements performed in seawater. Sound pressure and target strength measurements are performed from a floating stage near land. Experimental target strength measurements are also carried out on the research vessel G. O. Sars. The experimental results are compared with results from simulations. The axial nonlinear attenuation is quantified. The volume and area backscattering coefficients for a distribution of small targets are key quantities

in fisheries acoustics. The consequence of nonlinear attenuation for measurements of such coefficients is discussed in Chapter 7. Results from experimental measurements on mackerel schools are reported and compared with simulations.

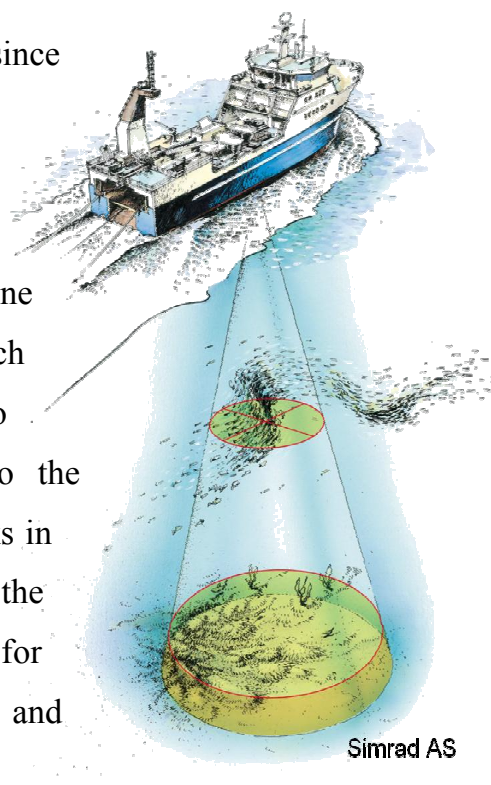
The obtained results are summarized in Chapter 8, and some suggestions are made for further investigations. A list of references follows Chapter 8, organized in alphabetical order after the name of the first author. References without author names are listed first. A list of symbols is included in Appendix A, while the Bergen Code programme used in the present work is listed in Appendix B. Appendix C contains calibration data for the Reson TC 4034 hydrophone that has been used for sound pressure measurements.

Chapter 2. Background

This chapter provides some useful background information for the present work. An overview of relevant definitions and expressions from underwater and fisheries acoustics is given in Section 2.1. Section 2.2 gives a brief account of the most relevant features of the history of nonlinear acoustics. A survey of numerical methods for simulating nonlinear sound propagation is also given, along with a description of the model and numerical algorithm chosen for the present work. As the target audience of this dissertation primarily belongs to the fisheries research society, some more attention is given to nonlinear acoustics than to the history and theoretical basis of fisheries acoustics.

2.1. Basic principles of fisheries acoustics

Echo sounders have been used to detect fish since the first systematic experiments were carried out by R. Balls in the North Sea in 1933.¹⁰¹ Today, acoustic methods are used extensively both in fisheries and in fisheries and marine research. Combined with other information such as trawl sampling data, results from echo counting and echo integration contribute to the knowledge basis for management of fish stocks in rivers, lakes, and the sea.^{167,223} Reviews of the history of fisheries acoustics can be found for example in the books by Simmonds and MacLennan²²³ and Forbes and Nakken.¹⁰¹



Acoustic abundance estimation of marine resources is commonly performed with calibrated echo sounders. Short sound bursts are transmitted vertically into the sea, and backscattered signals from targets in the water column are recorded and processed. In modern echo sounder systems, up to six frequencies are used simultaneously to derive information on sizes, species, and abundance of fish and plankton.¹⁴¹ The volume backscattering coefficient s_v is calculated from the backscattered energy from a volume of small scatterers, and is the acoustic parameter used for abundance estimation. The target strength TS of single scatterer can sometimes provide additional information. Target strength measurements are central in echo sounder calibration. The accuracy of an echo sounder is maintained through regular calibrations by means of copper or tungsten carbide spheres with known acoustic properties.^{86,98}

This section summarizes some definitions and expressions from underwater acoustics that are necessary in the present work, with emphasis on echo sounders for marine research.

2.1.1. Theory of sound propagation

In a homogeneous propagation medium, waves from echo sounder transducers and single scatterers such as isolated fish are regarded as spherically diverging in the far field.²⁵⁰ Consider a spherical sound wave radiated by a source at $r = 0$ (Figure 2.1). The source transmits a harmonic signal on the form of $\exp(j\omega t)$, where t is time and $\omega = 2\pi f$ is angular frequency. The complex sound pressure amplitudes p at two positions (r_0, θ, φ) and (r, θ, φ) along a line through the origin, relate to each other as¹³⁸

$$p(r, \theta, \varphi) = p(r_0, \theta, \varphi) e^{-jk(r-r_0)} \cdot \frac{r_0}{r} 10^{-\frac{\alpha}{20}(r-r_0)}. \quad (2.1)$$

The sound pressure amplitude is assumed sufficiently small to avoid nonlinear effects. r_0 , r , θ , and φ are spherical coordinates with the sound source at their

origin (Figure 2.1). $k = \omega/c_0$ is the wave number, c_0 is the small-signal sound speed, and α is the absorption coefficient measured in decibels per metre.

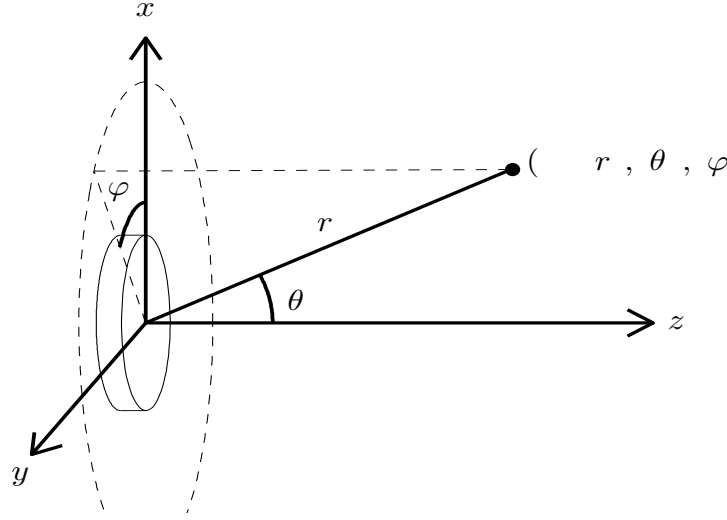


Figure 2.1. Coordinate system for description of sound propagation. The origin is centred at the face of the echo sounder transducer.

$p_{\text{rms}}(r, \theta, \varphi) = |p(r, \theta, \varphi)|/\sqrt{2}$ is the effective sound pressure of the harmonic wave. The sound pressure level (SPL) at a field point (r, θ, φ) (Figure 2.1) is defined as

$$\text{SPL}(r, \theta, \varphi) = 20 \log_{10} \frac{p_{\text{rms}}(r, \theta, \varphi)}{p_{\text{ref}}}, \quad (2.2)$$

where p_{ref} is a reference value normally chosen equal to 1 μPa rms. In the far field, the acoustic intensity can be written¹³⁸

$$I(r, \theta, \varphi) = \frac{p_{\text{rms}}^2(r, \theta, \varphi)}{\rho_0 c_0}, \quad (2.3)$$

and thus the intensity level (IL) is

$$\text{IL} = 10 \log_{10} \frac{I}{I_{\text{ref}}} = \text{SPL} + 10 \log_{10} \frac{p_{\text{ref}}^2}{\rho_0 c_0 I_{\text{ref}}}. \quad (2.4)$$

The reference intensity I_{ref} is customarily equal to 1 Wm^{-2} .¹³⁸ ρ_0 is the ambient density. The transmission loss (TL) due to sound propagation in a spherically diverging field is, from Equations (2.1) and (2.3),²⁵⁰

$$\text{TL} = -10 \log_{10} \frac{I(r, \theta, \varphi)}{I(r_0, \theta, \varphi)} = 20 \log_{10} \frac{r}{r_0} + \alpha(r - r_0). \quad (2.5)$$

2.1.2. Transducer properties

The complex current source (transmit) sensitivity of an acoustic transducer is defined as the ratio of the pressure amplitude produced at the reference point $(r_0, 0, 0)$, to the complex electrical current amplitude i through its terminals upon transmission,²⁵⁰

$$S = \frac{p(r_0, 0, 0)}{i}. \quad (2.6)$$

The reference distance r_0 is normally equal to 1 m. Upon sound reception, an incident plane wave with complex free field pressure amplitude p_{inc} produces an open circuit voltage amplitude U_0 across the transducer terminals. The ratio of U_0 to p_{inc} is the voltage receive sensitivity M ,²⁵⁰

$$M = \frac{U_0}{p_{\text{inc}}}. \quad (2.7)$$

The free-field pressure amplitude of the incident wave is its sound pressure amplitude when it is not affected by the presence of the transducer or other objects. For spherically diverging sound waves, the expression

$$\frac{M}{S} = J_s = \frac{2r_0}{j\rho_0 f} e^{jkr_0} \cdot 10^{\frac{\alpha r_0}{20}} \quad (2.8)$$

relates the receive and transmit sensitivities of a reciprocal transducer.^{165,2} J_s is the spherical reciprocity parameter.

When the radiation pattern of the sound source is known, the sound pressure amplitude at an arbitrary point (r, θ, φ) in the far field can be expressed in terms of the axial amplitude at a reference distance r_0 and the directional factor¹³⁸ $H(\theta, \varphi)$,

$$p(r, \theta, \varphi) = H(\theta, \varphi) \cdot p(r_0, 0, 0) e^{-jk(r-r_0)} \cdot \frac{r_0}{r} 10^{\frac{\alpha}{20}(r-r_0)}. \quad (2.9)$$

The directional factor is normalized to the axial sound pressure amplitude so that $H(0, \varphi) = 1$. In the special case of a uniformly vibrating, circular plane piston with radius a , mounted in an infinitely stiff planar baffle of infinite extent, the far field directional factor is¹³⁸

$$H(\theta, \varphi) = \frac{2J_1(ka \sin \theta)}{ka \sin \theta}. \quad (2.10)$$

J_1 is the first-order Bessel function of the first kind.

The source level (SL) is defined for a projector as the axial far-field sound pressure level at the reference distance r_0 ,²⁵⁰

$$SL = 20 \log_{10} \frac{p_{\text{rms}}(r_0, 0, 0)}{p_{\text{ref}}}. \quad (2.11)$$

If $(r_0, 0, 0)$ is not in the far field, where the signal can be treated as spherically diverging, Equation (2.1) is used for extrapolating the axial sound pressure amplitude from the far field to the reference point.

2.1.3. Backscattering from a single target

Fisheries research echo sounders are used for measuring two key quantities – the target strength TS for a single scatterer, and the volume backscattering coefficient s_v for a volume of scatterers.¹⁶⁸

Backscattering from a single target is illustrated in Figure 2.2. The backscattering cross-section of a target at position (r, θ, φ) is defined as^{141,168}

$$\sigma_{\text{bs}} = \frac{I_{\text{bs}}}{I(r, \theta, \varphi)} \cdot r_0'^2 10^{\frac{\alpha r_0'}{10}}, \quad (2.12)$$

where $I(r, \theta, \varphi)$ is the intensity of the incident sound. I_{bs} is the intensity of the backscattered sound at distance r_0' from the target, in the opposite direction of the incident sound wave. As r_0 in the definition of source sensitivity (Equation (2.6)), the reference distance r_0' is usually one metre.

Target strength is defined as²⁵⁰

$$\text{TS} = 10 \log_{10} \frac{I_{\text{bs}}}{I(r, \theta, \varphi)} = 10 \log_{10} \left(\frac{\sigma_{\text{bs}}}{r_0'^2} 10^{\frac{\alpha r_0'}{10}} \right). \quad (2.13)$$

The target strengths of fish and plankton are important parameters in fisheries research. They vary greatly with species, size, orientation, depth, sound frequency and other parameters.²²³

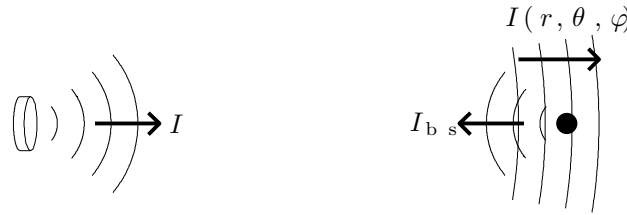


Figure 2.2. Sound transmission and backscattering from a single target.

The definition of backscattering cross-section above refers to a harmonic wave. For signals with finite bandwidth, such as sound bursts, the measured backscattering cross-section depends on the frequency response of the echo sounder and the frequency dependence of the target's scattering properties. The effective backscattering cross-section $\sigma_{\text{bs,eff}}$ is the weighted average of $\sigma_{\text{bs}}(\omega)$ over the bandwidth of the sonar.⁹⁵ A two-way power frequency response $P_{r0}(\omega)$ for the echo sounder system can be used to calculate $\sigma_{\text{bs,eff}}$.²²³

$$\sigma_{\text{bs,eff}} = \int_0^{\infty} \sigma_{\text{bs}}(\omega) P_{r_0}(\omega) d\omega \bigg/ \int_0^{\infty} P_{r_0}(\omega) d\omega. \quad (2.14)$$

The finite bandwidth of the measurement system is accounted for e.g. in the calculation of theoretical target strengths of calibration targets. An echo sounder calibration is thus only valid for measurements made with e.g. the burst duration used during that calibration. Although $\sigma_{\text{bs,eff}}$ is the quantity measured in practice, the harmonic wave backscattering coefficient σ_{bs} is used in the rest of this chapter.

2.1.4. Sonar equation and power budget

The system of an echo sounder that measures the backscattering coefficient of a single target is described by a sonar equation²⁵⁰

$$\text{EL} = \text{SL} - \text{TL} + \text{TS} - \text{TL}, \quad (2.15)$$

where the echo level EL is the free-field sound pressure level of the backscattered sound signal in the water at the position of the echo sounder transducer. The same transmission loss TL appears twice to account for sound attenuation in both propagation directions between the echo sounder transducer and the target.

Substitution of Equations (2.5)–(2.7), (2.11), and (2.13) into Equation (2.15) yields for the axial field,

$$\left| \frac{U_0}{M} \right| = |iS| \left(\frac{r_0}{r} 10^{-\frac{\alpha}{20}(r-r_0)} \right)^2 \sqrt{\frac{\sigma_{\text{bs}}}{r_0'^2} 10^{-\frac{\alpha r_0'}{10}}}, \quad (2.16)$$

where r is the distance between the echo sounder transducer and the target. A form of Equation (2.16) is sought in terms of electrical power transferred through the transducer terminals upon transmission and reception. The transducer intensity gain function $G(\theta, \varphi)$ is¹³⁸

$$G(\theta, \varphi) = \eta D(\theta, \varphi) = \eta \frac{4\pi \cdot |H(\theta, \varphi)|^2}{\int_{4\pi} |H(\theta, \varphi)|^2 d\Omega}, \quad (2.17)$$

where η is the electroacoustic efficiency of the transducer and $D(\theta, \varphi)$ is the directivity function. Ω is solid angle. Unlike the directional factor $H(\theta, \varphi)$, the directivity function refers to intensity, and is not normalized to the axial value. The integral of $D(\theta, \varphi)$ over all solid angles is equal to unity.

The intensity $I_{t,\text{sph}}(r)$ due to an omnidirectional sound source at $r = 0$, is

$$I_{t,\text{sph}}(r) = \frac{P_t \eta}{4\pi r^2} 10^{-\frac{\alpha}{10} r}. \quad (2.18)$$

P_t is the electric power transferred to the sound source, so that $P_t \eta$ becomes the radiated acoustic power. Accounting for transducer directivity by inserting $D(\theta, \varphi)$, the intensity I_t of the transmitted wave at distance r_0 becomes

$$I_t(r_0, \theta, \varphi) = \frac{P_t \eta D(\theta, \varphi)}{4\pi r_0^2} 10^{-\frac{\alpha}{10} r_0} = \frac{P_t G(\theta, \varphi)}{4\pi r_0^2} 10^{-\frac{\alpha}{10} r_0}. \quad (2.19)$$

If the point (r_0, θ, φ) is in the far field,¹³⁸

$$I_t(r_0, \theta, \varphi) = \frac{|p(r_0, \theta, \varphi)|^2}{2\rho_0 c_0}. \quad (2.20)$$

Equations (2.6), (2.9), (2.19), and (2.20) and the relation

$$P_t = \frac{|i|^2 R_T}{2} \quad (2.21)$$

can be combined to

$$\begin{aligned}
|S'(\theta, \varphi)|^2 &= |S \cdot H(\theta, \varphi)|^2 = \left| \frac{p(r_0, \theta, \varphi)}{i} \right|^2 \\
&= \frac{G(\theta, \varphi)}{4\pi r_0^2} 10^{-\frac{\alpha}{10} r_0} \rho_0 c_0 R_T.
\end{aligned} \tag{2.22}$$

R_T is the real part of the transducer's electrical input impedance $Z_T = R_T + jX_T$. $S'(\theta, \varphi)$ is the current source sensitivity generalized from the axial direction to an arbitrary direction (θ, φ) . The spherical reciprocity relation (Equation (2.8)) is assumed to apply to the echo sounder transducer, so that $M \cdot S = J_s \cdot S^2$. Also assuming that the directional factor $H(\theta, \varphi)$ is the same upon signal reception as for transmission, M can be generalized to $M'(\theta, \varphi)$ the same way as S is generalized to S' , and

$$|M' \cdot S'| = |J_s \cdot S'^2| = \frac{2c_0 r_0 G(\theta, \varphi)}{4\pi r_0^2 f} 10^{-\frac{\alpha}{20} r_0} R_T. \tag{2.23}$$

The electrical power P_r transferred through the terminals of the transducer upon signal reception is

$$P_r = \frac{|U|^2}{2|Z_L|^2} R_L = \frac{|U_0|^2 R_L}{2|Z_L|^2} \cdot \left| \frac{U}{U_0} \right|^2. \tag{2.24}$$

U is the complex voltage amplitude across the transducer terminals. The electrical input impedance of the receiving circuit is $Z_L = R_L + jX_L$, and $Z'_T = R'_T + jX'_T$ is the electrical output impedance of the transducer (see Figure 2.3). U is related to the open-circuit voltage amplitude U_0 in Equation (2.7) through Z'_T and Z_L ,

$$\frac{U}{U_0} = 1 - \frac{Z'_T}{Z'_T + Z_L} = \frac{Z_L}{Z'_T + Z_L}. \tag{2.25}$$

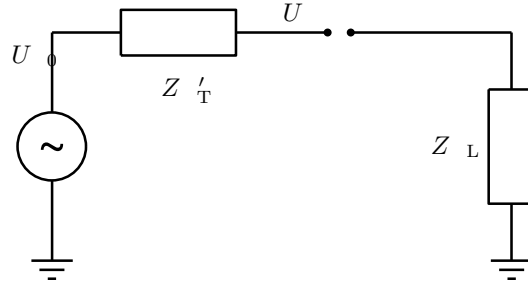


Figure 2.3. Thevenin equivalent circuit for the echo sounder transducer upon signal reception.

Squaring Equation (2.16) and inserting Equations (2.21) and (2.23)–(2.25), one obtains the power budget equation

$$P_r = P_t G(\theta, \varphi) \frac{10^{\frac{\alpha r}{10}}}{4\pi r^2} \sigma_{sp} \frac{10^{\frac{\alpha r}{10}}}{4\pi r^2} \frac{\lambda^2 G(\theta, \varphi)}{4\pi} \cdot F_Z, \quad (2.26)$$

where

$$\sigma_{sp} = 4\pi\sigma_{bs} \quad (2.27)$$

is the spherical scattering cross-section^{141,168} and $\lambda = c_0/f$ is the acoustic wavelength. As the reference distances r_0 and r'_0 are both set equal to 1 m, they have been cancelled against each other. F_Z is a factor due to the relation between the transducer's electrical input and output impedances and the input impedance of the electric receiver circuit,

$$F_Z = \frac{4R_T R_L}{|Z_L|^2} \left| \frac{U}{U_0} \right|^2 = \frac{4R_T R_L}{|Z_L|^2} \left| \frac{Z_L}{Z'_T + Z_L} \right|^2 = \frac{4R_T R_L}{|Z'_T + Z_L|^2}. \quad (2.28)$$

The impedance Z_L of the receiver circuit can be matched to the transducer output impedance Z'_T to maximize the power transfer from the transducer upon signal reception. This is achieved by making Z_L equal to the complex conjugate of Z'_T . F_Z then becomes

$$F_Z = \frac{4R_T R_L}{(2R'_T)^2} = \frac{R_T}{R'_T}. \quad (2.29)$$

Z'_T is not known in practice, but is often assumed equal to the input impedance Z_T . If the transducer's electrical input and output resistances are equal, the impedance matching factor F_Z becomes unity, and Equation (2.26) becomes what is sometimes referred to as the “classic radar equation”.¹

It is not unusual that a high value for the impedance Z_L is chosen instead of the optimal value for power transfer. This is done to maximize the voltage across the receiver terminals. $|U|$ approaches its open-circuit value $|U_0|$ as $|Z_L|$ is increased. F_Z becomes zero in the high impedance limit, as no energy is transferred to the receiver circuit. The formalism of Equation (2.26) with $F_Z = 1$ is still sometimes used, measuring the voltage U across the transducer terminals and e.g. substituting $|U/2|^2 R_T / (2|Z_T|^2)$ for P_r . The measured voltage is in this case approximately twice the value it would have if Z_L were optimised for power transfer. Inaccuracies due to such assumptions are cancelled through the echo sounder calibration.

The choice and implementation of sonar or power budget equations in echo sounders vary. The supplier should be consulted for the details that apply to a specific instrument.

2.1.5. Backscatter from a volume

Counting of detected single echoes is one method for fish abundance estimation. When two or more targets are so close together that their echoes overlap, however, they are not counted correctly by single echo detection algorithms.¹⁶⁷ Such error can be compensated for to a certain point, but regarding the received echo energy as volume backscatter is a better alternative when a certain density of targets is exceeded.¹⁶⁷

The scattering from small targets in the water column can be treated as a continuous signal with varying amplitude.²²³ If all the backscattered energy from a volume V_0 is assumed to be from targets of interest, their density is commonly assumed to be proportional to the volume backscattering coefficient s_v of that volume.⁹⁶ When the distribution of targets is homogeneous, s_v can be written¹⁴¹

$$s_v = \frac{1}{V_0} \sum_i \sigma_{bs,i} \approx \frac{\partial \sigma_{bs}}{\partial V} = \frac{1}{4\pi} \frac{\partial \sigma_{sp}}{\partial V}. \quad (2.30)$$

The $\sigma_{bs,i}$ are the backscattering cross sections of each individual scatterer in the volume. $\partial \sigma_{bs}/\partial V$ is the contribution of the volume element dV to the total backscattering cross section of V_0 .¹⁴¹

Equation (2.26) can be reformulated as an integral over the volume V of contributors to the received backscattered power,¹⁴¹

$$P_r = \int_V P_t G(\theta, \varphi) \frac{10^{-\frac{\alpha r}{10}}}{4\pi r^2} \frac{\partial \sigma_{sp}}{\partial V'} \frac{10^{-\frac{\alpha r}{10}}}{4\pi r^2} \frac{\lambda^2 G(\theta, \varphi)}{4\pi} F_z dV'. \quad (2.31)$$

The volume element dV' can be treated as part of a thin spherical shell of thickness $c_0 \tau/2$, where τ is the time duration of the transmitted signal. When τ is small compared to t , dV' can be approximated by

$$dV' = dr \cdot r^2 d\Omega \approx \frac{1}{2} c_0 \tau \cdot r^2 d\Omega. \quad (2.32)$$

Insertion into Equation (2.31) yields

$$P_r = P_t \frac{10^{-\frac{\alpha r}{10}}}{4\pi r^2} \frac{\partial \sigma_{sp}}{\partial V} \frac{10^{-\frac{\alpha r}{10}}}{4\pi r^2} \frac{\lambda^2}{4\pi} F_z \frac{c_0 \tau}{2} r^2 \int_{4\pi} G^2(\theta, \varphi) d\Omega. \quad (2.33)$$

The equivalent two-way solid beam angle (“equivalent beam angle”) is defined as²⁵⁰

$$\psi = \frac{1}{G_0^2} \int_{4\pi} G^2(\theta, \varphi) d\Omega, \quad (2.34)$$

where $G_0 = G(0,0)$. By inserting (2.34) into (2.33), one obtains for the volume backscattering coefficient,¹⁴¹

$$s_v = \frac{\partial \sigma_{sp} / \partial V}{4\pi} = \frac{P_r 32\pi^2}{G_0^2 \psi P_t \lambda^2 c_0 \tau F_Z} r^2 10^{\frac{2\alpha}{10} r}. \quad (2.35)$$

The distance $r = c_0 t / 2$ if the burst is transmitted at time $t = 0$ and the sound speed c_0 is constant.

The area backscattering coefficient s_a for a layer between the depths z_1 and z_2 is given by¹⁴¹

$$s_a = \int_{z_1}^{z_2} s_v dz. \quad (2.36)$$

The nautical area scattering coefficient (NASC)²²³ is defined as

$$s_A = 4\pi(1852)^2 s_a, \quad (2.37)$$

with unit m^2/nmi^2 (square metre per square nautical mile).

The equivalent beam angle ψ for an echo sounder transducer is normally supplied from the manufacturer in an individual calibration sheet. Its value can in general be affected by such factors as aging and the mounting of the transducer. Methods have been developed to measure the equivalent beam angle on vessel mounted transducers.^{191,208} ψ is sometimes approximated with the expression²⁵⁰

$$\psi \approx \frac{4\theta_{-3 \text{ dB}}^2}{5800} \quad (2.38)$$

for transducers that resemble a circular plane piston with uniform velocity amplitude distribution, where $2\theta_{-3 \text{ dB}}$ is the -3 dB beam width. The logarithmic

quantity

$$\Psi = 10 \log_{10} \frac{\psi}{1 \text{ steradian}} \quad (2.39)$$

is often used for specifying the equivalent beam angle. Since for most transducers only a small fraction of the transmitted energy is projected outside the main lobe, the side lobes have little effect on the value of ψ .²²³

2.1.6. Expressions used in echo sounder measurements

Target strength of single scatterers

Single beam echo sounders cannot measure the direction of incidence of a received echo. This is unimportant for measurements of the volume backscattering coefficient, where the total received echo energy is integrated (Equation (2.35)). The system's ability to measure the target strength of a single scatterer is however limited. A practical power budget equation for such echo sounders is stated with the axial gain $G_0 = G(0,0)$ substituted for the gain function $G(\theta, \varphi)$ in Equation (2.26). Target strength measurements are then only valid for targets on the sound beam axis.¹⁴¹ Assuming that the absorption loss over the distance r_0' is negligible,

$$\begin{aligned} \text{TS}_{\text{unc}} &= 10 \log_{10} \frac{\sigma_{\text{sp}}}{4\pi r_0'} 10^{-\frac{\alpha r_0'}{10}} \approx 10 \log_{10} \frac{\sigma_{\text{sp}}}{4\pi r_0'} \\ &= 10 \log_{10} P_r - 10 \log_{10} \frac{P_t G_0^2 r_0'^2 \lambda^2 F_z}{16\pi^2} + 10 \log_{10} \left(r^4 10^{\frac{2\alpha_r}{10}} \right). \end{aligned} \quad (2.40)$$

Such TS measurement results, which have not been compensated for the transducer's directivity, are referred to as uncompensated target strength TS_{unc} in the present work.

Dual beam and split beam echo sounders sense the angle of incidence of received echoes and compensate for the two-way transducer directivity. Target

strengths of scatterers within a certain off-axis angle can thus be measured more accurately. Split-beam echo sounders are used in the present work, with transducers divided in four quadrants. When single echoes are detected, relative phase measurements between the quadrants indicate the direction to the target. The echo amplitude is compensated with a simple polynomial model, for which the parameters are determined in the echo sounder calibration procedure. Equation (2.41) describes the beam compensation function that is used in the Simrad EK60 echo sounder,¹⁸

$$\text{TS} = \text{TS}_{\text{unc}} + 6.0206 \cdot \left[\left(\frac{\theta_x - \Delta\theta_x}{\theta_{-3 \text{ dB},x}} \right)^2 + \left(\frac{\theta_y - \Delta\theta_y}{\theta_{-3 \text{ dB},y}} \right)^2 - 0.18 \left(\frac{(\theta_x - \Delta\theta_x)(\theta_y - \Delta\theta_y)}{\theta_{-3 \text{ dB},x} \theta_{-3 \text{ dB},y}} \right)^2 \right]. \quad (2.41)$$

θ_x and θ_y are the measured off-axis angles to the target in the along ship and athwart ship directions, respectively. $\Delta\theta_x$, $\Delta\theta_y$, $\theta_{-3 \text{ dB},x}$, and $\theta_{-3 \text{ dB},y}$ are offset angles and half-intensity beam angles, respectively. The offset angles are included to ensure that $\text{TS} = \text{TS}_{\text{unc}}$ on the sound beam axis.

The last term on the right hand side of Equation (2.40) is the only term that contains the distance r to the target. The echo sounder accounts for the sound propagation distance by means of time-varied gain (TVG) in the receiver electronics or in software. The product of the received echo power from a single scatterer sufficiently far from the transducer, and the TVG function

$$f_{\text{TVG40}}(r) = r^4 \cdot 10^{\frac{2\alpha r}{10}}, \quad r = \frac{c_0 t}{2}, \quad (2.42)$$

becomes independent of distance.

Backscatter from a volume

A different TVG function is used for measurements of volume backscattering.

As stated in Equation (2.35), the volume backscattering coefficient can be calculated from the received power P_r as follows,

$$s_v = \frac{\partial \sigma_{sp} / \partial V}{4\pi} = \frac{P_r 32\pi^2}{G_0^2 \psi P_t \lambda^2 c_0 \tau F_z} r^2 10^{\frac{2\alpha}{10} r}.$$

As r appears only to the second order in Equation (2.35), the TVG function f_{TVG20} used for s_v measurements is different from that for target strength measurements,

$$f_{TVG20}(r) = r^2 \cdot 10^{\frac{2\alpha r}{10}}. \quad (2.43)$$

The two functions shown in Equations (2.42) and (2.43) are sometimes called “40 log r ” and “20 log r ” TVG functions, respectively, due to their logarithmic forms. At short distances, a so-called near range correction can be made to the TVG function.^{167,109} Such a correction is not made in the echo sounders studied in the present work.

2.1.7. Calibration and accuracy

The two-way axial transducer gain G_0^2 and the four parameters for the beam compensation function for target strength measurement (Equation (2.41)) are determined through regular echo sounder calibrations.^{98,10} The equivalent two-way beam angle ψ is not measured in the regular echo sounder calibrations, but is usually a transducer calibration result supplied from the manufacturer.

Fisheries research echo sounders are commonly calibrated by means of standard targets. Modern calibration targets are spheres of copper or tungsten carbide, with dimensions that depend on the operating frequency.^{98,100} Their target strengths are calculated from the sphere radius and ratios between material parameters of the sphere and the surrounding medium.^{85,119,95} The accuracy of calculated target strengths has been claimed to be within ± 0.1 dB.^{97,100}

38.1 mm-diameter tungsten carbide spheres with 6% cobalt binder are used for calibration of 120 kHz and 200 kHz echo sounders.^{100,98} The calibration sphere is suspended in the sound beam with monofilament nylon lines to minimize reflections from other objects than the sphere. In particular, trapped air could affect the measurements. To reduce such problems, the sphere is immersed in soap water before it is lowered into the sea. Conductivity and temperature are measured in the water column to provide accurate absorption and sound speed values.

The distance from the echo sounder transducer to the calibration sphere is usually between 10 m and 25 m, depending on surrounding factors such as water depth and currents. While measurements of the echo from the calibration sphere are being recorded, the sphere is moved in the alongship and athwartship directions. Measurements are thus obtained with the calibration sphere in different positions throughout the area approximately within $\theta_{-3 \text{ dB}}$. The distance between the sphere and the echo sounder transducer is kept as constant as possible.

The two-way axial transducer gain and the four parameters of the beam compensation function are calculated from the recorded measurements. In the echo sounders used in the present work, a separate value for the axial gain is obtained for volume backscattering measurements. This is based on the measurements with the calibration sphere near the sound beam axis.¹⁰

Based on a five-year study of EK400 echo sounders, Simmonds²²² concluded that $\pm 6\%$ ($\pm 0.3 \text{ dB}$) accuracy can be achieved for measurements of integrated echo energy with a recently calibrated echo sounder (referred to the 95% confidence level). Better accuracy is expected from more modern echo sounders like the EK60 used in the present work.¹⁷⁸

2.2. Nonlinear sound propagation

2.2.1. Some central developments in nonlinear acoustics

Accounts of the history of nonlinear acoustics can be found many places in the literature.^{52,53,57} A brief summary is given here, focusing on the developments that are seen as the most pertinent to finite-amplitude propagation effects in sound beams. The historical summary is for a large part based on the work of Blackstock.⁵⁷ Reviews of numerical algorithms for nonlinear sound propagation are given by Ginsberg and Hamilton,¹¹⁰ Aanonsen *et al.*,²⁷⁷ and Duck.⁸⁸ The methods that are seen as relevant for the present investigation account for diffraction, absorption, and nonlinear distortion in a finite amplitude sound beam. A simple survey of existing alternatives is presented.

Historical overview of nonlinear acoustics

It is often said that the discipline of nonlinear acoustics was born in 1755 with the work of Leonhard Euler. He formulated the conservation equations of mass and momentum for a fluid and combined them with Boyle's law to arrive at a wave equation for an isothermal gas.⁵⁷ In 1808, Poisson found an exact solution for progressive plane waves of finite amplitude in an isothermal gas. In terms of the particle speed v , it can be written⁵⁷

$$v = g \left[z - (v + b)t \right],$$

where g is an arbitrary function. z is position in a spatial (Eulerian) coordinate system, t is time, and b is the sound speed in an isothermal gas.

According to Poisson's solution, the maximum and minimum pressure of an initially sinusoidal sound wave will coincide after a certain time of propagation. Stokes (1848)²²⁶ made the first sketches that illustrate waveform distortion due to the phase speed variation within a sound wave. He also derived conservation laws for mass and momentum that must hold across a

shock. These were later known as two of the three Rankine-Hugoniot shock relations.²⁰³

Airy¹⁵ studied the frequency contents of an initially sinusoidal wave and found that a second harmonic component is generated through its propagation. He noted that the ratio of pressure amplitudes between the second harmonic and the fundamental frequency component should grow linearly with distance, frequency, and source amplitude. This was later supported by the experimental results of Thuras, Jenkins, and O'Neil,²³² published in 1935.

Until Earnshaw's work in 1860,⁸⁹ sound propagation had been regarded as an isothermal process. This resulted in a discrepancy between theoretical and experimentally measured sound speeds. Following a suggestion from Laplace, Earnshaw derived an expression for sound propagation in an adiabatic gas. Earnshaw also considered an arbitrary pressure-density relation.⁵⁷

In 1931 and 1935, respectively, Fay⁹² and Fubini¹⁰⁸ published explicit expressions for a plane finite-amplitude wave generated by a sinusoidally vibrating source. The two results are not equivalent, but apply to different regions of the sound field. Both can be expressed as Fourier series of fundamental and higher harmonic frequency components.⁵⁷ Fay's solution predicts a sawtooth-like waveform for strong excitations, with increased absorption due to the energy transfer to higher harmonics. The solution is valid in the so-called sawtooth region, where the distance from the sound source $z > 3l_D$. $l_D = c_0/(\beta\varepsilon\omega)$ is the plane wave shock formation distance due to Hugoniot, for an initially sinusoidal wave with angular frequency $\omega = 2\pi f$. β is the nonlinearity coefficient,⁵⁷ and ε is the acoustic Mach number.

The Fubini solution is not valid beyond the point of shock formation.⁵⁵ It applies to a lossless gas, and is consistent with the result found by Airy¹⁵ for the amplitude of the second harmonic frequency component.⁵⁷ By means of weak shock theory, Blackstock⁵⁵ later formulated a more general solution

which agrees with those of Fubini and Fay in their respective regions of validity and also applies to the intermediate region.

Langevin was the first to present measurements of a coefficient of nonlinearity in fluids, based on a Taylor series expansion of the pressure-density relation.^{57,49} His work is reported in an article by Biquard.⁵¹ Langevin also found an expression for the profile of a steady shock wave in a liquid, and observed that decay and thickening of the shocks would eventually restore the wave to sinusoidal form. He predicted that an ideal sawtooth wave would decay inversely with distance, as can also be inferred from Fay's solution.⁵⁷

The generation of sum and difference frequency components in intense sound fields with two primary frequencies was demonstrated by Thuras *et al.* in 1935.²³² Lighthill^{160,161} used the basic equations of fluid dynamics to develop a theory for what he called the aerodynamic generation of sound. Calculations based on his work and measurements of sum and difference frequencies from sound beams intersecting at a right angle in air were presented by Ingard and Pridmore-Brown¹²⁸ in 1956.

Intensity dependent attenuation of finite-amplitude sound waves, as predicted by Fay in 1931,⁹² was reported after several experiments from around 1940.^{102,248,184,169} Several theoretical and experimental works followed the initial investigations. The connection with nonlinear sound propagation was made in 1954 by Fox and Wallace,¹⁰³ who modelled the propagation medium as a nonlinear transmission line.

Burgers' equation⁶³ from 1948 describes the propagation of plane, finite-amplitude waves in thermoviscous fluids. The equation has an exact analytical solution that can be expressed in terms of definite integrals.^{123,76} The Burgers equation has been used by a great number of authors for solving one-dimensional propagation problems.^{54,93,163,190,154} Blackstock generalized the equation to apply to arbitrary absorption and dispersion in 1985.⁵⁶

Keck and Beyer¹³³ presented analytical expressions for the harmonic overtones generated through nonlinear distortion in a plane wave. They compared their results for the second and third harmonic with measurements obtained by Krasil'nikov *et al.*¹⁴⁸ Keck and Beyer also calculated an effective absorption coefficient for a plane sound wave of finite amplitude.¹³³

Westervelt²⁶³ used an equation due to Lighthill to derive a dissipationless second-order wave equation, published in 1957. His result had also been obtained somewhat earlier by Eckart.^{57,90} Westervelt also derived a source function that describes the generation of sound through nonlinear interaction between two primary sound fields.^{263,262} The parametric acoustic array, which he suggested in 1963,²⁶⁴ consists of two collinear sound beams with high amplitude. The primary sound beams can act as an end-fire array of virtual acoustic sources, producing a narrow sound beam with frequency equal to the difference between the primary field frequencies. Several authors conducted further investigations of the parametric acoustic array,^{155,37,40,120,274,175,179} only a small fraction are referenced here. Westervelt also suggested the parametric receiving array. His theory required the primary fields (incident sound field and receiver “pump wave”) to be highly collimated, but the result has been extended to a number of cases that are better suited for practical applications.^{39,41,266,99} Naze Tjøtta, Tjøtta and their co-workers^{186,238,46,83} developed a general theory of the nonlinear interaction between sound waves.

In 1969, Zabolotskaya and Khokhlov²⁷¹ presented a second order wave equation that describes nonlinear sound propagation in a confined, axisymmetric beam in a lossless medium. Asymptotic solutions have been derived for various cases.^{272,216,257,150} An absorption term was added to the Zabolotskaya-Khokhlov equation by Kuznetsov,¹⁵¹ who thus obtained the Khokhlov-Zabolotskaya-Kuznetsov (KZK) equation. An interesting survey of the works of Burgers, Zabolotskaya and Khokhlov, and others, is given by Rudenko *et al.*²¹⁵ Østerbø²⁷⁵ and Naze Tjøtta and Tjøtta²³⁷ have presented alternative derivations of the KZK equation, using inner and outer expansion

methods and a singular perturbation method, respectively. Several asymptotic solutions of the Zabolotskaya-Khokhlov equation were presented during the 1970s.^{216,257,150}

Experimental investigations of finite amplitude sound beams from plane piston-like sources have been carried out by authors such as Gould *et al.*,¹¹² Lockwood *et al.*,¹⁶³ Shooter *et al.*,²²¹ Moffett,¹⁸⁰ and Baker *et al.*²³ The measurements have generally been performed in fresh water, and with higher frequencies and smaller beam widths than in the present work.

In medical ultrasound, where nonlinear harmonic generation is today exploited actively,^{64,88} excess attenuation due to nonlinear effects was pointed out in 1980 by Muir and Carstensen¹⁸¹ and Carstensen *et al.*⁶⁷

Numerical approaches to nonlinear sound propagation

Cook⁷⁸ and Van Buren and Breazeale²⁵¹ used the model suggested by Fox and Wallace¹⁰³ in numerical calculations of the propagation of plane waves of finite amplitude in an absorbing fluid. The effects of nonlinearity and absorption were separated and superposed over incremental propagation steps in space. The effect of nonlinear distortion was calculated in the time domain, and the solution was Fourier transformed in each propagation step to account for thermoviscous absorption in the frequency domain. Pestorius proposed a combined time-frequency numerical algorithm for arbitrary plane finite-amplitude waveforms.²⁰¹ Nonlinear distortion was accounted for in the time domain, and absorption and dispersion in the frequency domain. The Pestorius algorithm was extended by Bass and Raszpet³⁶ and used for calculations of shock wave propagation in the atmosphere. The time domain part of the algorithm is based on weak shock theory and thus assumes thin shocks.

In 1971, Fenlon⁹³ presented an algorithm that solved a set of coupled spectral equations obtained by inserting a Fourier series trial solution in the Burgers equation. The initially infinite set of equations was truncated and solved with a

finite difference method. His pure frequency domain method had the computational advantage that it did not depend on Fourier transformations in each calculation step. Fourier series solutions for plane wave propagation have since been sought on the basis of other governing equations. An overview is given by Aanonsen *et al.*²⁷⁷ Fenlon⁹³ and Trivett and van Buren²⁴⁹ also considered spherically and cylindrically spreading waves using similar methods. Cleveland *et al.*⁷⁴ have used the Burgers equation to describe sound propagation with position-dependent medium parameters by adding an algorithm that determines the ray path.

Bakhvalov *et al.*³¹ integrated the Zabolotskaya-Khokhlov²⁷¹ equation directly by means of finite differences. The sound propagation process is diffusion-like in the parabolic approximation, so that the Zabolotskaya-Khokhlov and KZK¹⁵¹ equations may be integrated step by step in the direction of propagation without concern for backward-propagating wave components.¹¹⁰ The algorithm of Bakhvalov *et al.*³¹ propagates the solution forward in uniform spatial steps, starting from a time continuous boundary condition specified in the source plane. Results were reported for axisymmetric problems with Gaussian and fourth-order polynomial amplitude distributions. The discontinuity in a uniform piston source condition was not handled. The amplitudes of the frequency components were found by analysing the calculated time waveforms. The method of Bakhvalov *et al.* was later extended to account for absorption.³³ Calculations were made for weak focusing³² and for the nonlinear interaction between two collinear sound beams.³⁴

Zhileikin²⁷³ proposed a frequency domain solution of the KZK equation in 1982. He reformulated the problem as an infinite system of equations for the Fourier components of the solution, and solved a truncated system by means of finite differences. The fast Fourier transform was used twice in each step of the calculation to account for nonlinearity in the time domain.

Naze Tjøtta and Tjøtta led the development of a finite difference algorithm that

solves the KZK equation fully in the frequency domain.^{35,276,277} This algorithm and its successors are commonly referred to as the Bergen Code, and have been developed further and applied to a variety of problems. As in the works of Fenlon,⁹³ Zhileikin,²⁷³ and others, a Fourier series trial solution was inserted into the KZK equation.^{276,35} The resulting infinite set of equations was truncated and solved entirely in the frequency domain for the near field of an axisymmetric sound source. Unlike earlier algorithms, the Bergen Code is able to simulate the sound field radiated by a piston source with uniform amplitude distribution. A coordinate transformation that enabled simulation of nonlinear sound propagation in the far field was introduced in 1984.^{278,114} The transform is referred to as the Transformed Beam Equation (TBE). The Bergen Code is discussed further in Section 2.2.4.

The nonlinear progressive equation (NPE) was derived by McDonald and Kuperman^{170,171} for their numerical study of nonlinear sound propagation in inhomogeneous media. The equation was derived from the Euler equations of fluid dynamics and an adiabatic equation of state. It is similar to the KZK equation, but with the roles of time and propagation distance reversed.¹⁷⁰ The KZK equation is more convenient for boundary value problems, where an initial time waveform is prescribed in the plane of the source.^{276,157} The NPE is formulated in a wave-following coordinate system, and the algorithm due to McDonald and Kuperman requires an initial space waveform to be prescribed at an instant in time. The algorithm was originally used to study finite amplitude sound propagation in the ocean.^{171,17,68,69,172} In 1990, Too and Ginsberg²⁴⁴ modified the NPE approach to apply to axisymmetric sound beams in the paraxial approximation. Results from their simulations were compared with the Rayleigh integral and experimental results from the literature.^{23,180,163} The NPE approach and the Bergen Code are reported to yield “comparable accuracy”, although the KZK equation inherently accounts for dissipation and the NPE does not.²⁴⁴ The NPE has been rewritten in spherical coordinates²⁴⁵ to facilitate simulations in the far field of focused and unfocused sound beams. A

thermoviscous absorption term was added by Too and Lee.^{246,247}

In an algorithm described in 1991, Sparrow and Raszpet²²⁴ used a finite difference time stepping approach to solve the second-order fundamental equations of acoustics.¹¹⁵ Their solution was given in two dimensions and applied to the propagation of a spherical spark pulse in a finite axisymmetric geometry. Examples were also given of reflection from hard surfaces. The algorithm is able to describe multiple waves in arbitrary directions, but at a high computational cost.²²⁴

Christopher and Parker⁷¹ proposed an angular spectrum method for modelling nonlinear propagation in an axisymmetric sound beam in 1991. Their numerical solution is propagated forward incrementally from the plane of the sound source using the method of fractional steps. In one substep, a discrete Hankel transform was applied to account for diffraction and attenuation. A frequency domain solution to Burgers' equation was used in a separate substep to account for nonlinear distortion. Christopher and Parker⁷¹ compared their results with some previously reported experiments.^{87,23} A modified version of the code has been used to model sound propagation from an electrohydraulic shock wave lithotripter.⁷² Vecchio and Lewin²⁵² have proposed a similar method for non-axisymmetric sound beams.

Many practical applications involve short sound bursts and pulses with high intensity. Although frequency domain methods can be applied to pulsed ultrasound,^{24,26} they are in general best suited for describing wave propagation that results from a narrow-band excitation signal. The computational cost can be significantly lower for time domain calculations than for simulations in the frequency domain when pulsed sound is simulated.¹⁰⁷ In 1997, Tavakkoli *et al.*^{230,231} presented a pure time domain method based on the work of Christopher and Parker.⁷¹ Arbitrary absorption is accounted for by convolution with a causal finite impulse response filter, while nonlinearity is included in the

form of the Poisson solution. Simulations were compared with experimental results.^{231,206,207}

Khokhlova *et al.*¹³⁵ extended the method of Tavakkoli *et al.*²³¹ to apply to an intense continuous-wave sound beam. They compared the result with a new frequency domain algorithm for solving the KZK equation. The new algorithm is based on operator splitting and optimised for describing shock wave propagation.¹³⁵ Good agreement was reported between both models and experimental data.^{135,219} Nouri-Baranger *et al.*¹⁸⁸ chose a frequency domain approach similar to that of Khokhlova *et al.*¹³⁵ to simulate sound beams from plane, non-axisymmetric transducers.

With the Bergen Code^{276,277} as their starting point, Lee and Hamilton¹⁵⁷ developed an algorithm for solving the KZK equation fully in the time domain. The first results were published in 1995.¹⁵⁷ The so-called Texas Code has been used in numerous works. Averkiou *et al.*¹⁹ investigated self-demodulation of sound bursts in fluids with strong absorption experimentally and theoretically. Averkiou and Hamilton²¹ studied pulsed sound waves from plane and focusing piston sources. Several authors have compared results from the Bergen Code and the Texas code and reported good agreement.^{21,22,158} The Texas Code has been extended from its original axisymmetric geometry to three dimensions,²⁶⁸ and it has been used for calculations involving multiple relaxation phenomena^{157,75} and turbulence.⁵⁸ Bouakaz *et al.*⁵⁹ obtained a three-dimensional algorithm similar to that of Lee and Hamilton, and compared their results with measurements in the sound field of a square transducer⁵⁹ and a clinical scanner.⁶⁰

Hallaj and Cleveland¹¹³ and Huijssen *et al.*¹²⁴ obtained explicit finite difference time domain (FDTD) solutions of an equation due to Westervelt.^{264,115} Huijssen *et al.*¹²⁴ compared their results in the linear, lossless case with analytical solutions to confirm the validity of the model. Simulated nonlinear beam patterns were compared with Texas Code^{157,60} solutions of the KZK equation

and hydrophone measurements. In the regions where the KZK equation is known to be inaccurate, the results of Huijssen *et al.*¹²⁴ was reported to agree better with measurement results. However, as their algorithm operates in the time domain, it is not well suited for simulating continuous waves or long sound bursts. Ginter,¹¹¹ who implemented the equations of mass and momentum conservation and the equation of state directly, also used the explicit FDTD method. Arbitrary frequency power-law attenuation was accounted for in the time domain.^{111,159}

In 1999, Campos-Pozuelo *et al.*⁶⁵ proposed a finite element approach based on second order perturbation theory, yielding results that are said to be consistent with the Westervelt equation⁶⁵. The three-dimensional geometry and surface vibration pattern of the sound source can be arbitrarily chosen. However, approximations are made that are only valid at distances much shorter than the shock formation distance.⁶⁵ Campos-Pozuelo *et al.* compared numerical simulation results with measurements for a stepped-plate transducer.

Kagawa *et al.*¹²⁹ derived approximate equations for the fundamental and second harmonic frequency components based on an equation due to Kuznetsov.¹⁵¹ The equations were solved with the finite element method. FE simulations based on an incrementally linear approach²⁶⁵ were made by Wojcik *et al.*²⁶⁵ Hoffelner *et al.*¹²¹ obtained a finite element solution of the full Kuznetsov's equation,¹⁵¹ avoiding the parabolic approximation and at the same time accounting consistently for diffraction, absorption, and nonlinearity.¹⁵¹ Results from their simulations were compared with the Fubini and Fay solutions and with measurements in the sound field of a high intensity focused ultrasound transducer. Their model has been used in a theoretical investigation of acoustic streaming and radiation force,¹²² and for calculations of nonlinear standing waves.¹⁴⁹

2.2.2. Nonlinear effects and fisheries acoustics

Linear sound propagation has been assumed in fisheries acoustics from the emergence of fisheries research echo sounders in the 1930s until today. During the development of new echo sounders, with increased accuracy and dynamic range, one became aware of waveform distortion due to sound propagation through water.²³³ Experimental^{233,234} and theoretical investigations using the Bergen Code^{29,30} were made in 2000–2002. Their results indicate that significant nonlinear sound propagation effects can occur in the 120 kHz and higher frequency echo sounder sound beams under relevant operating conditions for fisheries research echo sounders.

An investigation was launched in 2003 in cooperation between Christian Michelsen Research AS, the University of Bergen, Institute of Marine Research, and Simrad AS, in order to obtain quantitative results for the nonlinear effects to be expected in fisheries acoustics. The present work is part of this effort.

Tichy, Solli, and Klaveness²³⁴ reported experimental and numerical results for the excess attenuation in the axial field of a 200 kHz echo sounder due to nonlinear effects. They suggested that an adjustment should be introduced to obtain correct target strength measurements, and that the transmitted power should be reduced when possible to minimize the nonlinear effects.²³⁴ Limits on the output powers for fisheries research applications have been recommended by Simrad.¹³ Simmonds and MacLennan²²³ have suggested somewhat different limits to the source level based on the results of Shooter *et al.*²²¹

2.2.3. The KZK equation

The Bergen Code, which is used for numerical simulations in the present work, is based on the Khokhlov-Zabolotskaya-Kuznetsov equation.^{271,151} The KZK equation is a popular model for nonlinear sound propagation in the paraxial

region of a sound beam. As the equation is parabolic, it is well suited for solution by finite differences. Absorption, diffraction and nonlinearity are accounted for to the second order. For the sake of discussions elsewhere in the present work, a derivation that follows the same lines as that of Kuznetsov^{151,115} is sketched below, with emphasis on certain points of interest. The sources referred to above give a more detailed account of the derivation. An overview of the KZK equation and other equations of nonlinear acoustics is found in Hamilton and Morfey.¹¹⁵

The following quantities are defined:

| | |
|---|--|
| position | $\mathbf{x} = (x_1, x_2, x_3),$ |
| particle velocity | $\mathbf{v} = (v_1, v_2, v_3),$ |
| particle speed | $v = \mathbf{v} ,$ |
| characteristic particle speed amplitude | $v_0,$ |
| equilibrium pressure | $P_0,$ |
| sound pressure | $p',$ |
| pressure | $P = P_0 + p',$ |
| equilibrium density | $\rho_0,$ |
| density perturbation | $\rho',$ |
| density | $\rho = \rho_0 + \rho',$ |
| time | $t,$ |
| shear viscosity | $\mu,$ |
| bulk viscosity | $\mu_B,$ |
| heat conductivity | $\kappa,$ |
| frequency | $f,$ |
| angular frequency | $\omega = 2\pi f,$ |
| small-signal sound speed | $c_0 = \sqrt{(\partial P / \partial \rho)_{s,0}},$ |
| entropy at equilibrium | $s_0,$ |
| entropy perturbation | $s',$ |

| | |
|-------------|------------------|
| entropy | $s = s_0 + s'$, |
| temperature | T . |

Pressure, density, and entropy are expressed as sums of their equilibrium values and perturbations. c_0 is the isentropic, small-signal sound speed, as in Chapter 2.

An approximate wave equation valid to the second order in the acoustic Mach number $\varepsilon = v_0/c_0$ and the first order in the Stokes number $\eta = \mu\omega/\rho_0c_0^2$ is sought. ε and η are considered to be of comparable smallness so that their combined order can be characterized by a generic ordering parameter $\tilde{\varepsilon}$.¹¹⁵

The basic equations^{138,115} for the dynamics of a continuous medium are the equation of continuity,

$$\frac{\partial \rho}{\partial t} + \nabla \cdot (\rho \mathbf{v}) = 0, \quad (2.44)$$

the Navier-Stokes momentum equation,

$$\rho \left(\frac{\partial}{\partial t} + \mathbf{v} \cdot \nabla \right) \mathbf{v} = -\nabla P + \mu \nabla^2 \mathbf{v} + \left(\mu_B + \frac{1}{3} \mu \right) \nabla (\nabla \cdot \mathbf{v}), \quad (2.45)$$

the entropy equation,

$$\rho T \left(\frac{\partial}{\partial t} + \mathbf{v} \cdot \nabla \right) s = \kappa \nabla^2 T + \mu_B (\nabla \cdot \mathbf{v})^2 + \frac{1}{2} \mu \left(\frac{\partial v_i}{\partial x_j} + \frac{\partial v_j}{\partial x_i} - \frac{2}{3} \delta_{ij} \frac{\partial v_k}{\partial x_k} \right)^2, \quad (2.46)$$

using Einstein's summation convention, and an equation of state for the medium,

$$P = P(\rho, s). \quad (2.47)$$

For an isentropic fluid, the equation of state can be approximated by a second-order Taylor expansion around equilibrium,¹⁰³

$$P - P_0 \approx A \left(\frac{\rho'}{\rho_0} \right) + \frac{B}{2} \left(\frac{\rho'}{\rho_0} \right)^2. \quad (2.48)$$

The parameter of nonlinearity B/A is thus given by⁴⁹

$$\frac{B}{A} = \frac{\rho_0}{c_0^2} \left(\frac{\partial^2 P}{\partial \rho^2} \right)_{s,0}. \quad (2.49)$$

Also allowing changes in entropy, the $O(\tilde{\varepsilon}^2)$ equation of state becomes¹¹⁵

$$P - P_0 \approx c_0^2 \rho' + \frac{c_0^2}{\rho_0} \frac{B}{2A} \rho'^2 + \left(\frac{\partial p'}{\partial s} \right)_{\rho,0} s'. \quad (2.50)$$

The vector identities $\nabla(\nabla \cdot \mathbf{v}) = \nabla^2 \mathbf{v} + \nabla \times \nabla \times \mathbf{v}$ and $(\mathbf{v} \cdot \nabla) \mathbf{v} = \frac{1}{2} \nabla v^2 - \mathbf{v} \times \nabla \times \mathbf{v}$, where $v^2 = \mathbf{v} \cdot \mathbf{v}$, are inserted into Equation (2.45). Terms that contain $\nabla \times \mathbf{v}$ are mainly associated with vorticity, and decay exponentially with distance from boundaries if the mean motion of the propagation medium is zero. Discarding such terms and those of order higher than ε , $\eta\varepsilon$, and ε^2 , Equations (2.44)–(2.46) combine to¹¹⁵

$$\rho_0 \frac{\partial \mathbf{v}}{\partial t} + \nabla p' = \left(\mu_B + \frac{4}{3} \mu \right) \nabla^2 \mathbf{v} - \frac{1}{2} \rho_0 \nabla^2 v^2 - \rho' \frac{\partial \mathbf{v}}{\partial t}, \quad (2.51)$$

$$\rho_0 T_0 \frac{\partial s'}{\partial t} = \kappa \nabla^2 T'. \quad (2.52)$$

Inserting $O(\tilde{\varepsilon})$ expressions into $O(\tilde{\varepsilon}^2)$ terms are assumed to result in errors of third order. By substitution of the first-order relations¹¹⁵

$$\left(\frac{\partial P}{\partial s} \right)_\rho = \rho^2 \left(\frac{\partial T}{\partial \rho} \right)_s, \quad \left(\frac{\partial T}{\partial \rho} \right)_s^2 = \frac{(c_p - c_v) T c_0^2}{c_v c_p \rho^2}, \quad \nabla^2 p' = \frac{1}{c_0^2} \frac{\partial^2 p'}{\partial t^2}, \quad (2.53)$$

into Equations (2.44), (2.50), (2.51), and (2.52), they can be combined to the second-order nonlinear wave equation²⁷⁸

$$\left(\nabla^2 - \frac{1}{c_0^2} \frac{\partial^2}{\partial t^2}\right) p' + \frac{\delta}{c_0^4} \frac{\partial^3 p'}{\partial t^3} = -\frac{\beta}{\rho_0 c_0^4} \frac{\partial^2 p'^2}{\partial t^2} - \left(\nabla^2 + \frac{1}{c_0^2} \frac{\partial^2}{\partial t^2}\right) \mathcal{L}. \quad (2.54)$$

c_p and c_v are specific heats for constant pressure and volume, respectively. The nonlinearity coefficient $\beta = 1 + B/2A$, and the diffusivity of sound is^{278,115}

$$\delta = \frac{1}{\rho_0} \left(\frac{4}{3} \mu + \mu_B\right) + \frac{\kappa}{\rho_0} \left(\frac{1}{c_v} - \frac{1}{c_p}\right) = \frac{c_0^3 \alpha_2}{2\pi^2}. \quad (2.55)$$

The classical absorption coefficient¹³⁸ for a harmonic wave with frequency f is $\alpha' = \alpha_2 f^2$. The quadratic dependence upon frequency is inherent in the dissipation term in Equation (2.54).⁵⁶

When local nonlinear effects are negligible in comparison with the cumulative nonlinear distortion that builds up through propagation, the term containing the second-order Lagrangian density

$$\mathcal{L} = \frac{1}{2} \rho_0 v^2 - \frac{p'^2}{2\rho_0 c_0^2} \quad (2.56)$$

can be disregarded.²⁷⁷ In general, this is the case for progressive quasi-plane waves at distances greater than one wavelength from the sound source.¹¹⁵ Equation (2.54) then becomes what Hamilton and Morfey¹¹⁵ call the Westervelt equation.²⁶⁴ This is the equation used by Hallaj and Cleveland¹¹³ and Huijssen *et al.*¹²⁴ in their numerical simulations.

A sound beam propagating along the positive x_3 axis is considered in a reference frame that moves at speed c_0 in the same direction. The variations in the sound field with x_3 due to absorption, nonlinearity, and diffraction are all assumed to be of order $\tilde{\epsilon}$.^{271,151} The spatial variations in the x_1 and x_2 directions are assumed to be of the order $\tilde{\epsilon}^{1/2}$ more rapid.^{271,151} The slow scale

$$p' = p'(x'_1, x'_2, x'_3), \quad (x'_1, x'_2, x'_3) = (\tilde{\epsilon}^{1/2} x_1, \tilde{\epsilon}^{1/2} x_2, \tilde{\epsilon} x_3), \quad t' = t - \frac{x_3}{c_0} \quad (2.57)$$

is inserted into Equation (2.54) with $\mathcal{L} = 0$. t' is retarded time. The resulting $O(\tilde{\varepsilon}^3)$ term is omitted. This corresponds to approximating a hyperbolic equation with a parabolic equation.¹¹⁵ Only one-way, paraxial sound propagation is described.²⁶⁵ The so-called parabolic approximation reduces the domain of validity for the model, but yields an equation that is well suited for solution by finite differences.^{31,276} Transforming back from (x'_1, x'_2, x'_3) to (x_1, x_2, x_3) , one obtains the Khokhlov-Zabolotskaya-Kuznetsov (KZK) equation,^{271,151}

$$\left(\frac{\partial^2}{\partial x_3 \partial t'} - \frac{c_0}{2} \nabla_{\perp}^2 - \frac{\delta}{2c_0^3} \frac{\partial^3}{\partial t'^3} \right) p' = \frac{\beta}{2\rho_0 c_0^3} \frac{\partial^2 p'^2}{\partial t'^2}. \quad (2.58)$$

$\nabla_{\perp}^2 = \partial^2/\partial x_1^2 + \partial^2/\partial x_2^2$ is called the transverse Laplacian operator.

2.2.4. The Bergen Code

The development of the Bergen Code was initiated by professors Jaqueline Naze Tjøtta and Sigve Tjøtta at University of Bergen early in the 1980s.^{35,276,277} The entirely frequency domain solution of the KZK equation^{271,151} has become widely used in investigations of time periodic, finite-amplitude wave propagation in sound beams. A version of the Bergen Code has been chosen for the numerical simulations in the present work. The programme is well suited for the geometry of the studied problem. The author is not aware of any indications that other algorithms yield more accurate simulation results for the fundamental and second harmonic frequency components along the sound beam axis.

Development of the programme

The original version of the Bergen Code algorithm assumes an axisymmetric problem, which reduces the geometry to two dimensions. A frequency transform of the dimensionless KZK equation (Equation (2.60) below) is solved in incremental steps in the direction of the symmetry axis. A set of

algebraic equations is obtained by means of implicit finite differences and solved by iteration in each propagation step. Numerical results were first obtained for the near field of uniform and Gaussian circular piston sources.^{35,276,277}

For an axisymmetric problem, the solution is initiated with a source condition specified along a line perpendicular to the symmetry axis. The source condition is given at equidistant points starting on the axis and ending at the chosen width of the numerical grid. In each propagation step, the number of points and the spacing between them are the same as in the previous. The rectangular grid thus produced is not well suited for describing the spherically diverging far field. The grid must be sufficiently wide so that interactions with its boundary do not affect the solution significantly. At the same time, the fine resolution needed to describe the sound source and near field adequately, must be maintained. The great number of grid points that are necessary to meet both demands makes simulations of the far field computationally expensive.

To enable far field simulations without an excessive number of grid points, the KZK equation was recast in a transformed coordinate system by Aanonsen *et al.*²⁷⁸ (Equation (2.63)). The transformation between the coordinate systems corresponds to a mapping between a rectangular grid and one for which the width increases linearly with distance from the source plane (Figure 2.4). The resulting equation is referred to as the Transformed Beam Equation (TBE), and has the same form as the dimensionless KZK equation. A similar coordinate transformation approach has been used by Bakhvalov *et al.*,³¹

Aanonsen *et al.*^{278,114} made simulations of the far field of a circular piston. They compared their results with measurements made by Lockwood *et al.*,¹⁶³ Moffett,¹⁸⁰ and Riley.²¹³ Alternative coordinate transformations have been introduced later to follow the geometry of a focused sound beam.^{118,240,241,269,132} Weakly focused sound beams can be simulated with the Transformed Beam Equation by specifying a phase shaded source condition.^{25,20}

Bergen Code simulations of the sound fields of plane uniform piston sources have been compared with measurements by several authors, such as Baker *et al.*,²³ Kamakura *et al.*,¹³⁰ Nacheff *et al.*,¹⁸² and Averkiou and Hamilton.²⁰ Good agreement is reported, although the parabolic approximation limits the model accuracy close to the sound source and far from the sound beam axis.

The use of implicit finite differences in the first Bergen Code versions^{35,276-278} imposed restrictions on the step length in the direction of propagation. The Richtmyer procedure²¹¹ was taken into the algorithm by Berntsen and Vefring^{44,45} to yield an inherently stable solution without the same restrictions. Moreover, the set of algebraic equations obtained in each propagation step was made to form a tridiagonal system, which can be solved without iteration. The efficiency of the Bergen Code was significantly increased through these changes.

The new algorithm was used by Vefring^{253,255,254} to simulate nonlinear effects in axisymmetric sound beams and nonlinear interactions between collinear sound beams.^{256,239,240} Vefring compared his results for the primary sound waves with linear theory, and those for the sum and difference frequencies with quasilinear theory.²⁵⁴ Reiso^{205,204} made modifications to the Bergen Code for investigating sound propagation in inhomogeneous media.

Although the Bergen Code solves the KZK equation entirely in the frequency domain, the propagation of pulses can be implemented by specifying the Fourier spectrum of the excitation signal in the source condition.^{24,26,187} The signal is represented by a finite number of harmonics of a chosen fundamental frequency. A broadband source condition can drastically increase the computational cost, as one needs to retain a sufficient amount of harmonics of the frequencies contained in the excitation signal.

Kamakura *et al.*¹³¹ developed a new computer programme for solving the Transformed Beam Equation, following the same lines as Aanonsen *et al.*²⁷⁸ They employed the alternating direction implicit (ADI) method to solve the

equation in three dimensions, which made possible the simulation of sound beams radiated by rectangular sound sources. Berg and Naze Tjøtta³⁸ presented another three-dimensional Bergen Code implementation using the ADI method. The improvements that had been introduced by Vefring *et al.*²⁴⁰ to make the axisymmetric version more efficient, were included in their programme. Simulations produced with the implementation due to Berg and Naze Tjøtta³⁸ were compared with measurements by Sahin and Baker²¹⁷ and Baker *et al.*²⁷

The Bergen Code and codes based on it have been used in several recent works such as those of Baker and Lunde,^{29,30} Divall and Humphrey,⁸⁴ Labat *et al.*,¹⁵² Rielly,²¹² Tao *et al.*,²²⁹ and Kourtiche *et al.*¹⁴⁷

Dimensionless KZK equation

The KZK equation (Equation (2.58)) is recast in the dimensionless coordinates $(\xi_1, \xi_2, \sigma) = (x_1/a, x_2/a, x_3/R_0)$. The characteristic lengths a and R_0 are related through the expression $R_0 = ka^2/2$, where $k = \omega/c_0$ is the wave number. Thus, if a is the radius of a uniform circular piston sound source, R_0 is the corresponding Rayleigh distance for a harmonic wave with angular frequency ω . Substituting the dimensionless retarded time $\tau' = \omega t' = \omega(t - x_3/c_0)$ and the normalized sound pressure

$$\bar{p} = p' / \rho_0 c_0 v_0, \quad (2.59)$$

into Equation (2.58), one can write²⁷⁶

$$\left(4 \frac{\partial^2}{\partial \tau' \partial \sigma} - \bar{\nabla}_{\perp}^2 - 4\alpha' R_0 \frac{\partial^3}{\partial \tau'^3} \right) \bar{p} = 2 \frac{R_0}{l_D} \frac{\partial^2}{\partial \tau'^2} \bar{p}. \quad (2.60)$$

v_0 is a particle speed amplitude characteristic of the sound field. In simulations of sound propagation from a uniform piston, v_0 is usually the speed amplitude of the piston. The dimensionless transverse Laplacian operator may be written

$$\bar{\nabla}_{\perp}^2 = \frac{\partial^2}{\partial \xi_1^2} + \frac{\partial^2}{\partial \xi_2^2}, \quad (2.61)$$

and $\alpha' = \delta\omega^2 / 2c_0^3$ and $l_D = (k\beta\varepsilon)^{-1}$ are the absorption coefficient and the plane wave shock formation distance, respectively. One should note that the subscript D has been used in other works to identify the diffraction length (Rayleigh distance). The notation in the present work has been adapted from the works by Naze Tjøtta, Tjøtta, and their co-workers.^{276,277,237} $\varepsilon = v_0/c_0$ is the peak particle speed Mach number. For the special case of an axisymmetric beam, Aanonsen *et al.*²⁷⁸ substituted

$$\bar{\nabla}_{\perp}^2 = \frac{1}{\xi} \frac{\partial}{\partial \xi} \left(\xi \frac{\partial}{\partial \xi} \right), \quad (2.62)$$

where $\xi = |\boldsymbol{\xi}|$, $\boldsymbol{\xi} = \xi_1 \mathbf{e}_1 + \xi_2 \mathbf{e}_2$. Equations (2.61) and (2.62) are equivalent in an axisymmetric geometry. \mathbf{e}_1 and \mathbf{e}_2 are unit vectors in the x_1 and x_2 directions, respectively.

According to Aanonsen *et al.*,²⁷⁷ their result is valid for arbitrary frequency dependent absorption. They propose to add a frequency dependent term to δ to account for relaxation. This should enable the solution to include dispersive effects such as treated by Korpel¹⁴⁶ and Trivett and van Buren²⁴⁹ in their one-dimensional models. However, Aanonsen *et al.*²⁷⁷ only present calculation results for absorption with quadratic frequency dependence.

Transformed Beam Equation

When the axisymmetric version of Equation (2.60) is solved numerically on a rectangular domain in the (ξ, σ) plane,²⁷⁶ the transverse extent of the numerical grid imposes a serious restriction on the tractable propagation distance. As the sound beam diverges spherically in the far field, a wide grid is necessary to avoid reflections from its boundary. The excessive number of calculation points needed to obtain the necessary grid width at the same time as an

adequate resolution is kept near the sound source, restricts the numerical approach of Aanonsen *et al.*^{276,277} for a large part to the near field.

To be able to simulate sound propagation in the far field, Equation (2.60) was transformed into a new set of dimensionless coordinates by Aanonsen *et al.*,²⁷⁸

$$\mathbf{u} = \frac{\xi}{1+\sigma}, \quad \tau_p = \tau' - \frac{\xi^2}{1+\sigma}. \quad (2.63)$$

A rectangular numerical grid in the (u, σ) plane, where $u = |\mathbf{u}|$, corresponds to a physical calculation area for which the width increases with the axial distance σ from the sound source. The transformation is illustrated in Figure 2.4.

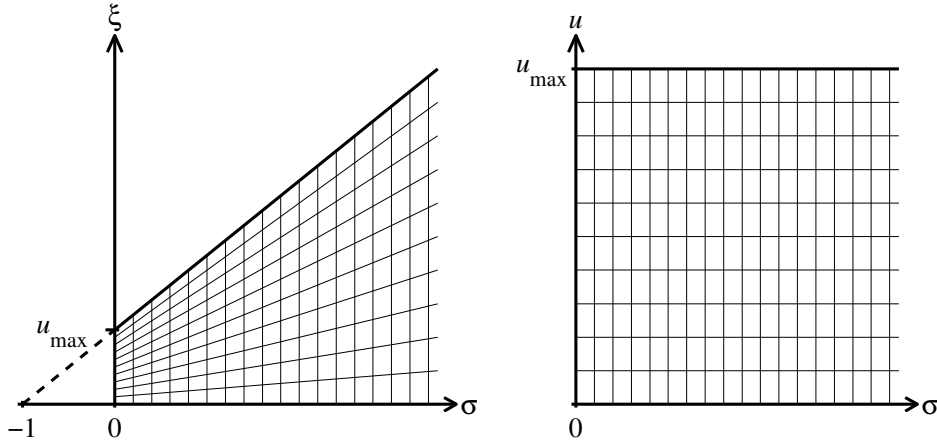


Figure 2.4. Sketches of the two-dimensional calculation region for solving the Transformed Beam Equation for an axisymmetric problem. The same area is shown in the (ξ, σ) dimensionless coordinate system (left) and the (u, σ) transformed coordinate system (right).

A new parabolic equation for

$$T'(\sigma, \mathbf{u}, \tau_p) = (1+\sigma) \bar{p}(\sigma, \xi, \tau'), \quad (2.64)$$

which has the same form as Equation (2.60), can be written in the transformed coordinates,

$$\left(4(1+\sigma)^2 \frac{\partial^2}{\partial \tau_p \partial \sigma} - \nabla_{\mathbf{u}}^2 - 4\alpha' R_0 (1+\sigma)^2 \frac{\partial^3}{\partial \tau_p^3} \right) T' = 2 \frac{R_0}{l_D} (1+\sigma) \frac{\partial^2 T'^2}{\partial \tau_p^2}. \quad (2.65)$$

$\nabla_{\mathbf{u}}^2$ is the transverse Laplacian with respect to \mathbf{u} , defined in the same way as ∇_{\perp}^2 is with respect to \mathbf{x} . Equation (2.65) is referred to as the Transformed Beam Equation (TBE).²⁷⁸

Problem formulation in the frequency domain

By inserting a trial solution^{276,278}

$$T' = \sum_{n=1}^{\infty} (g_n \sin n\tau_p + h_n \cos n\tau_p). \quad (2.66)$$

into Equation (2.65), one obtains a set of coupled partial differential equations for the Fourier coefficients g_n and h_n ,

$$\begin{aligned} \frac{\partial g_n}{\partial \sigma} &= -n^2 \alpha_2 R_0 g_n + \frac{1}{4n(1+\sigma)^2} \nabla_{\mathbf{u}}^2 h_n \\ &+ \frac{nR_0}{2l_D(1+\sigma)} \left[\frac{1}{2} \sum_{m=1}^{n-1} (g_m g_{n-m} - h_m h_{n-m}) - \sum_{m=n+1}^{\infty} (g_{m-n} g_m + h_{m-n} h_m) \right], \\ \frac{\partial h_n}{\partial \sigma} &= -n^2 \alpha_2 R_0 h_n - \frac{1}{4n(1+\sigma)^2} \nabla_{\mathbf{u}}^2 g_n \\ &+ \frac{nR_0}{2l_D(1+\sigma)} \left[\frac{1}{2} \sum_{m=1}^{n-1} (h_m g_{n-m} + g_m h_{n-m}) + \sum_{m=n+1}^{\infty} (h_{m-n} g_m - g_{m-n} h_m) \right], \end{aligned} \quad (2.67)$$

$$n = 1, 2, \dots$$

Insertion of the same trial solution (2.66) into the dimensionless KZK equation (2.60) instead of the TBE yields a set of equations on the same form as Equation (2.67).²⁷⁶ The same approach has been used earlier by Fenlon⁹³ for solving the Burgers equation.

In the following, the first terms on the right-hand sides of Equations (2.67) are referred to as ‘‘absorption terms’’. The second terms are referred to as ‘‘diffraction terms’’, while the third are called ‘‘nonlinearity terms’’.

Boundary conditions

Within the parabolic approximation, the plane wave impedance relation is valid between the axial component v_3 of the particle velocity and the sound pressure²³⁷,

$$p' = \rho_0 c_0 v_3. \quad (2.68)$$

v_3/v_0 consequently satisfies Equation (2.60). The solution of the KZK and TBE equations becomes the same whether the boundary conditions are prescribed in terms of pressure or the axial particle velocity component. Also, as $p' = 0$ when $v_3 = 0$, Equation (2.68) entails that there is no distinction between an infinitely stiff and an infinitely compliant baffle. For an axisymmetric piston source situated in the plane $\sigma = 0$ with particle velocity $v_3 = f_s(\xi) \sin \tau$ on its surface, the source (boundary) condition becomes²⁷⁸

$$\begin{aligned} g_1 &= f_s(u) \cos u^2, & h_1 &= f_s(u) \sin u^2, \\ g_n &= 0, & h_n &= 0, \quad n \geq 2. \end{aligned} \quad (2.69)$$

In the special case of a uniform, circular piston oscillating sinusoidally with peak velocity amplitude v_0 , mounted in an infinitely stiff baffle of infinite extent,

$$f_s(\xi) = \begin{cases} 1, & \xi \leq 1 \\ 0, & \xi > 1 \end{cases}. \quad (2.70)$$

ξ and \mathbf{u} are equal in the source plane (Equation (2.63)). Some alternative amplitude and phase shaded source conditions are discussed in Section 4.3.

When an axisymmetric problem is considered, the axis is a boundary for the numerical grid. The boundary condition at $u = 0$ is $\partial g_n / \partial u = 0$, $\partial h_n / \partial u = 0$ to obtain symmetry in the sound pressure. The artificial boundary at $u = u_{\max}$ is also reflecting. u_{\max} must be set large enough so that the reflections do not cause significant error in the solution of interest.^{278,114}

Numerical solution

The infinite set of equations (2.67) is truncated in order to obtain a numerical solution. The N_h first pairs of equations for g_n and h_n are retained. The solution is calculated in steps in the direction of propagation. The computation starts at the source plane, which is given as an initial condition. In each step, the solution is calculated at N_u equidistant points from $u = 0$ through $u = u_{\max}$ (Figure 2.4). As the solution varies more slowly in the far field than in the near field, the length l_σ of each propagation step can be increased with distance from the source plane. This contributes to reducing the computational cost of the simulations. The step length parameter λ_σ controls the resolution in the axial direction,

$$l_\sigma(\sigma) = \lambda_\sigma(1 + \sigma)^2. \quad (2.71)$$

The Crank-Nicholson method⁸⁰ is used to integrate the absorption and diffraction terms throughout most of the sound field (Richtmyer procedure⁴⁴). The nonlinearity terms are expressed with explicit finite differences.⁴⁵ In order to damp down Gibbs oscillations from discontinuities in the source condition, some initial calculation steps are made with implicit differences instead of the Crank-Nicholson method.²⁵⁴ The effect of this approach is discussed in more detail in Chapter 3.

The Bergen Code version used in the present work has been implemented by Berntsen.^{47,48} The programme includes the modifications described by Berntsen and Vefring in 1986⁴⁴ and 1987.⁴⁵ Slight changes to the representation of the input parameters and the output of calculation results have been made by the author. Moreover, the step length adjustment feature for the initial implicit steps has been disabled as a constant length l_{imp} is used for these steps in the present work. A listing of the used programme has been included in Appendix B to ensure the repeatability of the presented simulations.

Chapter 3. Simulation uncertainty

Simulations performed with the Bergen Code have been compared with measurements and other models in a large number of investigations, as described above. However, the author is not aware of sufficiently detailed and precise accounts of the accuracy with which the programme can be expected to predict finite amplitude sound propagation in cases relevant to the present work. An attempt has therefore been made to identify and quantify as many uncertainty contributions as possible. As far as it has been practical, the obtained uncertainties have been treated in accordance with the Guide to the Expression of Uncertainty in Measurement.³

The Bergen Code offers a direct frequency domain solution of the KZK equation.^{271,151} The KZK equation is generally accepted as a reliable description of the acoustic field in the paraxial region, not too close to the sound source.¹³¹ The sound burst durations used in the present work are 30 periods of the drive frequency or more. A continuous wave approximation is considered adequate for the description of the steady-state region within the burst. The frequency domain representation used in the Bergen Code is suitable for the application.

A Bergen Code implementation for axisymmetric sound beams has been used in the present work. The axial symmetry reduces the numerical problem from three to two physical dimensions, which in turn reduces the computational cost of the algorithm substantially.^{126,268}

The relative combined standard uncertainty $E(p_{\text{sim}}) = u(p_{\text{sim}})/p_{\text{sim}}$ of a numerical simulation result for the effective sound pressure p_{sim} can be expressed as a combination of three uncorrelated contributions,

$$E(p_{\text{sim}}) = \sqrt{E_{\text{model}}^2 + E_{\text{num}}^2 + E_{\text{param}}^2}. \quad (3.1)$$

The model uncertainty E_{model} is the relative standard uncertainty with which the mathematical model is able to describe the intended physical process. The effect of the parabolic approximation inherent in the KZK equation is investigated in the linear case, because in this case simulation results can be compared with analytical solutions not employing the parabolic approximation. Such solutions are not available for finite-amplitude sound propagation. Other uncertainties of the model are identified, but their magnitudes are not determined (Section 3.1).

E_{num} is the relative standard uncertainty introduced by the numerical solution algorithm (Section 3.2). As for the model uncertainty, this uncertainty contribution is investigated directly in the case of linear sound propagation. Analytical solutions for the linearized parabolic equation are used for reference. For finite amplitude sound propagation, the author is not aware of adequate reference solutions. An attempt is therefore made to extrapolate the results for linear propagation to cases of nonlinear sound propagation relevant for the present work.

A sensitivity study is made in order to investigate the uncertainty contribution E_{param} due to uncertainties in the physical input parameters that describe the sound source and the propagation medium. This is treated in Section 3.3.

The identified contributors to each of the uncertainties E_{model} , E_{num} , and E_{param} are summarized in Table 3.1. The meaning of each of the very brief contributor descriptions in the table is explained in Sections 3.1–0. Unless otherwise stated, the uncertainties presented in this work are standard uncertainties, i.e., referred to a 67% confidence level.³

Table 3.1. Overview of contributors to the Bergen Code simulation uncertainty. The abbreviated descriptions of the uncertainty contributors are explained in Sections 3.1–0.

| category | uncertainty contribution | contribution quantified |
|---------------------|---|-------------------------|
| model | - parabolic approximation, E_{par} | yes |
| | - idealized source condition, E_{source} | no |
| | - axisymmetry assumption, E_{symm} | no |
| | - continuous wave approximation, E_{cont} | no |
| | - quadratic absorption law, E_{α} | no |
| | - second order nonlinearity, E_{order} | no |
| | - other uncertainty contributions, $E_{\text{misc},1}$ | no |
| numerical algorithm | - beam pattern convention, E_{geom} | yes |
| | - spectral truncation, E_{harm} | yes |
| | - finite grid width, E_{width} | yes |
| | - numerical rounding, E_{rnd} | no |
| | - finite differences, E_{fd} | no |
| | - numerical grid resolution, E_{grid} | yes |
| | - numerical damping of solution, E_{imp} | yes |
| input parameters | - Gibbs oscillations, E_{imp} | yes |
| | - other contributions, $E_{\text{misc},2}, E_{\text{misc},3}$ | no |
| | source radius, frequency, | |
| | source pressure, sound speed, | |
| | absorption coefficient, density, | yes |
| | nonlinearity coefficient | |

3.1. Model uncertainty

The model relative standard uncertainty E_{model} can be written

$$E_{\text{model}} = \sqrt{E_{\text{par}}^2 + E_{\text{source}}^2 + E_{\text{symm}}^2 + E_{\text{cont}}^2 + E_{\alpha}^2 + E_{\text{order}}^2 + E_{\text{misc},1}^2}, \quad (3.2)$$

where

E_{par} is the relative standard uncertainty contribution due to the parabolic approximation,
 E_{source} is the relative standard uncertainty contribution due to the idealized source condition (circular, uniform plane piston in infinite baffle) used for the simulations,
 E_{symm} is the relative standard uncertainty contribution due to the theoretical assumption of axisymmetry,
 E_{cont} is the relative standard uncertainty contribution due to the assumption of continuous waves,
 E_{α} is the relative standard uncertainty contribution due to the frequency-squared power law absorption inherent in the model
 E_{order} is the relative standard uncertainty contribution due to the KZK equation being of second order, and
 $E_{\text{misc},1}$ is the relative standard model uncertainty contribution due to factors that have not been identified in the present work. This contribution is set equal to zero in the present discussion.

The model uncertainty consists of many contributions that are difficult to estimate. The uniform piston description of the sound source and the parabolic approximation are assumed to dominate when nonlinear effects can be neglected. When finite amplitude sound propagation is simulated, other limitations of the chosen model may well be significant. This is however not easy to investigate, as reference solutions or measurements for nonlinear sound propagation with the required accuracy are not known to the author.

Parabolic approximation

The parabolic approximation inherent in the KZK equation is said to be valid in points that are close to the sound beam axis and at the same time not too close to the sound source.²³⁷ Its precise domain of validity depends on the desired accuracy, and can be investigated in the idealized case of linear sound propagation from a circular, plane piston with uniform velocity distribution

mounted in an infinite baffle. The relative standard uncertainty E_{par} due to the parabolic approximation is assumed similar to the difference between the solutions of the linearized parabolic equation²³⁶ and the ordinary linear solutions¹³⁸ for the same idealized case.

Absorption is disregarded. The exact absolute value of the sound pressure amplitude along the axis of a circular, plane, uniform piston in an infinitely stiff baffle of infinite extent is^{137,138}

$$|p_{\text{tt}}(r, 0)| = 2\rho_0 c_0 v_0 \left| \sin \left\{ \frac{1}{2} kr \left[\sqrt{1 + \left(\frac{a}{r}\right)^2} - 1 \right] \right\} \right|. \quad (3.3)$$

The piston has radius a and oscillates with particle velocity amplitude v_0 and frequency f . The wave number $k = 2\pi f/c_0$, and c_0 is the small-signal sound speed. The coordinates (r, θ) refer to a polar coordinate system with the polar angle $\theta = 0$ along the sound beam axis. r is distance from the sound source. Axisymmetry is assumed, and the azimuth angle φ is omitted. An approximation for the sound pressure amplitude in the point (r, θ) in the far field can be written¹³⁸

$$|p_{\text{tt}}(r, \theta)| = \rho_0 c_0 v_0 \frac{ka^2}{2r} \left| \frac{2J_1(ka \sin \theta)}{ka \sin \theta} \right|, \quad (3.4)$$

where J_1 is the first-order Bessel function of the first kind. The axial lossless solution of the linearized parabolic equation is²³⁶

$$|p_{\text{par}}(r, 0)| = p_0 \sqrt{2 - 2 \cos \frac{ka^2}{2r}}. \quad (3.5)$$

The first term of Naze Tjøtta and Tjøtta's²³⁶ Equation (15) is taken as an approximation for the far field. Without absorption, it becomes

$$|p_{\text{par}}(r, \theta)| = p_0 \frac{ka^2}{2r} \left| \frac{2J_1(ka \tan \theta)}{ka \sin \theta} \right|. \quad (3.6)$$

p_0 is the peak sound pressure amplitude on the surface of the sound source, which within the parabolic approximation satisfies²³⁷ $p_0 = \rho_0 c_0 v_0$.

Equations (3.4)–(3.6) are evaluated for the frequencies, source radii, and sound speeds shown in Tables 3.2 and 3.3. Two cases that correspond to simulations of the 120 kHz and 200 kHz echo sounders used in the present work are considered. Results for the axial sound pressure amplitude and the beam pattern are shown in Figures 3.1 and 3.2, respectively. At distances of more than two metres from the sound source, the agreement between Equations (3.5) and (3.3) is within 0.002 dB. The parabolic approximation changes the calculated number and positions of the axial minima in the near field, causing large discrepancies inside the outermost maximum.

The parabolic equation is commonly said to be invalid near the sound source,^{150,236} where z/a becomes of the same order as $(ka)^{1/3}$. z is the Cartesian coordinate in the direction of the sound beam axis, $z = r \cos \theta$ (Figure 2.1). $a(ka)^{1/3}$ is equal to 0.16 m for the 120 kHz sound source and 0.10 m with the 200 kHz parameters. This condition seems sufficient only if uncertainty less than ± 0.1 dB is not required (Figure 3.1).

In the far field, the parabolic approximation (3.6) agrees well with Equation (3.4) within approximately 4° off the axis (Figure 3.2). The discrepancy between the sound pressure amplitudes is less than 0.1 dB for $\theta < 6^\circ$. The calculated angular position of the first minimum is underestimated with approximately 0.1° , which yields great difference between the calculated sound pressure amplitudes for a given θ when the minimum is approached (Figure 3.2b).

Based on the results shown in Figures 3.1 and 3.2, 0.01 dB is chosen for $20 \log_{10}(1+E_{\text{par}})$ in the far field off axis. For the axial field, $20 \log_{10}(1+E_{\text{par}})$ is 0.001 dB.

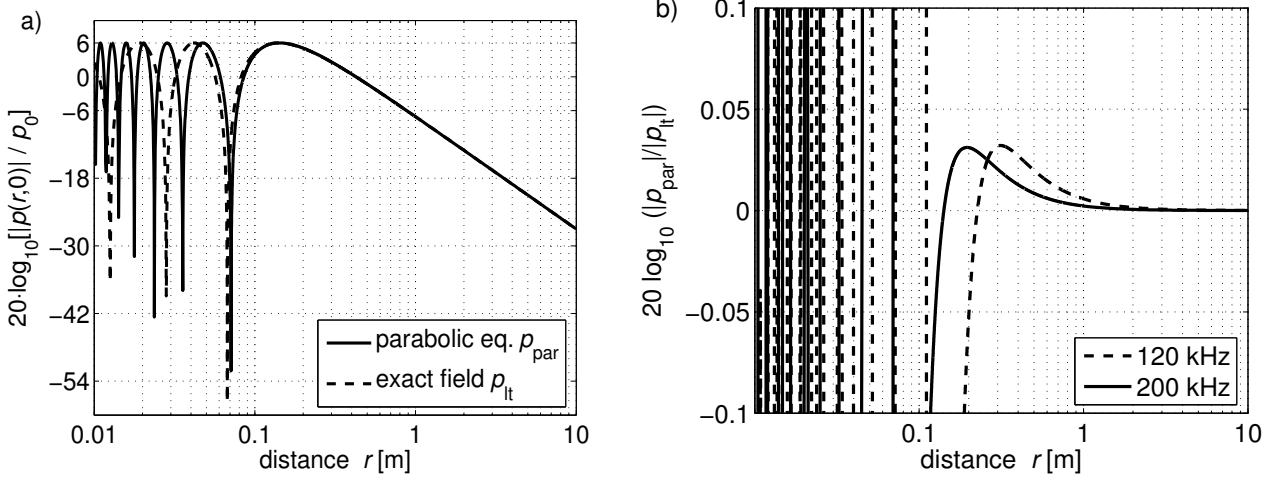


Figure 3.1. a) Axial solution p_{par} of the linearized parabolic equation and exact axial field p_{lt} for a uniform circular piston using parameters for the 200 kHz echo sounder simulations (Tables 3.2 and 3.3).
 b) Ratio between the solutions for the 120 kHz and 200 kHz echo sounder simulations.

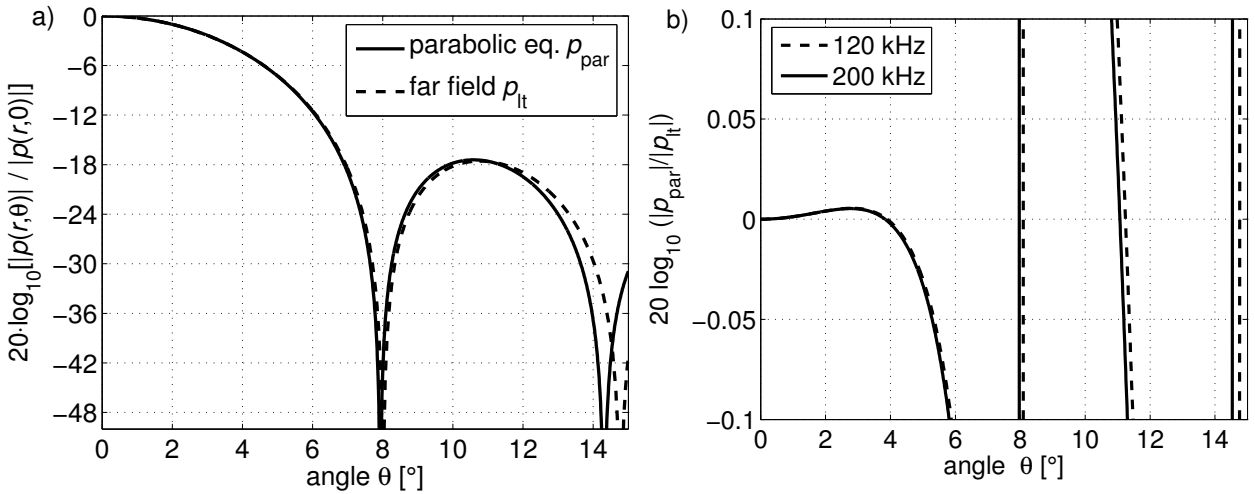


Figure 3.2. a) Far-field solution p_{par} of the linearized parabolic equation and the linear far field approximation p_{lt} using source parameters for the 200 kHz case (Tables 3.2 and 3.3). The distance r from the sound source is 10 m. b) Ratio between p_{par} and p_{lt} for the 120 kHz and 200 kHz echo sounder simulations.

Idealized source condition

In most simulations in the present work, the sound source is described as a baffled, uniform, circular piston that radiates a continuous sinusoidal signal.

The piston radius is selected such that it yields the same -3 dB opening angle as the far field radiation pattern measured in a corresponding experiment. The echo sounder transducers used as sound sources have been designed for lower side lobe levels than in the radiated field of a uniform piston. The discrepancy introduced by the difference between the source description of the model and the vibration pattern of the sound source in the experiments may be expressed in terms of a relative standard uncertainty E_{source} . The importance of this discrepancy is not addressed here, but the subject is revisited in Chapter 4.

Axisymmetry assumption

The effective source radii are calculated from far field directivity measurements where the sound source has been panned around a single axis. This renders the calculation somewhat vulnerable to irregularities in the radiated far field. In a regular echo sounder calibration, -3 dB beam angles (half-beamwidths) are found from a great number of measurements that cover the paraxial region quite uniformly. Both along ship and athwart ship beam angles are calculated. The difference between them ranges from less than 0.01° to 4%, but is typically close to 2% for the calibration measurements that have been made in connection with the present work. The relative uncertainty E_{symm} introduced by the departure from rotational symmetry (also referred to as “axisymmetry” in the present work) has not been quantified here.

Continuous wave approximation

Although the echo sounders use sound bursts of finite duration, the simulations assume continuous waves. The shortest burst duration used in the experiments is 256 μs . A 120 kHz measured sound burst then contains approximately 20 periods with nearly constant amplitude. The reported sound pressure amplitude measurements refer to this part of the signal, and should correspond closely to continuous wave conditions. The uncertainty contribution E_{cont} due to the continuous wave assumption is thus neglected.

Quadratic absorption law

Frequency-squared power law absorption, $\alpha' = \alpha_2 f^2$, where α_2 is a constant absorption coefficient for the propagation medium, is assumed in the theoretical model. This relation is applicable to pure water,^{105,138} but does not describe the absorption in sea water equally well.¹⁰⁶ Also, gas bubbles and other impurities in the water can have great influence on absorption and nonlinearity and thus contribute to the uncertainty contribution E_α . Pure water where the square power law holds is considered in this chapter, and E_α is neglected.

Second order nonlinearity

As the Khokhlov-Zabolotskaya-Kuznetsov^{151,271} equation describes sound propagation to the second order, there are higher order effects that are not accounted for.^{242,243} The error thus made can be expressed in terms of a standard relative uncertainty contribution E_{order} . The purpose of the simulations in the present work is to predict sound pressure amplitudes for the fundamental and second harmonic frequency components. Higher order effects are not expected to influence such results significantly for the frequencies and source levels that are considered. Attempts to quantify their importance have not been made here. E_{order} is neglected in the calculation of the combined simulation uncertainty.

Model uncertainty summary

The full relative uncertainty contribution E_{model} due to the employed mathematical model (KZK equation and idealized source condition) has not been quantified properly.

In particular, the uniform, plane piston description of the sound source, and for seawater the quadratic absorption law, are important uncertainty contributors that have not been accounted for. Within the paraxial region, their contributions to E_{model} are expected to be greater than that of the parabolic approximation. As

these factors are variable and difficult to estimate in a general manner, they are still not included in the uncertainty estimate.

For the purpose of the present discussion, the relative standard model uncertainty $20 \log_{10}(1+E_{\text{model}})$ is set equal to $20 \log_{10}(1+E_{\text{par}})$, i.e., 0.01 dB for the far field off axis ($\theta < 6^\circ$) and 0.001 dB for the axial field.

3.2. Uncertainty contribution due to the numerical algorithm

Finite difference methods are often preferred for solving differential equations due to their formal simplicity, but are generally prone to convergence problems.^{278,220} Although the Richtmyer procedure as implemented in the Bergen Code is considered inherently stable,⁴⁵ care must be taken when simulation results of high accuracy are required. The sensitivity of the solution to grid resolution and other numerical parameters that influence the computational process is investigated here, and the relative standard uncertainty contribution E_{num} due to the numerical algorithm is estimated. E_{num} can be expressed as a combination of several contributions (Table 3.1),

$$E_{\text{num}} = \sqrt{E_{\text{geom}}^2 + E_{\text{np}}^2 + E_{\text{misc},2}^2}, \quad (3.7)$$

where

$$E_{\text{np}}^2 = E_{\text{harm}}^2 + E_{\text{width}}^2 + E_{\text{rnd}}^2 + E_{\text{fd}}^2 + E_{\text{grid}}^2 + E_{\text{imp}}^2 + E_{\text{misc},3}^2. \quad (3.8)$$

E_{geom} is due to a mismatch between how beam patterns are read from the simulation results and the way they are measured in the experiments,

E_{np} is due to the combined uncertainty due to the parameters that govern the numerical solution process,

E_{harm} is due to the limited number of harmonics retained in the

calculations (spectral truncation),

E_{width} is due to the finite extent of the numerical grid in the transverse direction,

E_{rnd} is due to numerical rounding,

E_{fd} is due to the choice of finite differences (order),

E_{grid} is due to the numerical grid resolution,

E_{imp} is due to the number and length of initial implicit steps, which influence the numerical damping and the amount of Gibbs oscillations in the solution, and

$E_{\text{misc},2}$ and $E_{\text{misc},3}$ are due to factors that have not been identified in the present work. They are set to zero in the present discussion.

A series of test simulations is described below. Results for low amplitude sound propagation are compared with analytical solutions. Simulations are also carried out for nonlinear sound propagation, and their sensitivities to the parameters of the calculation are compared with the low amplitude case. Based on this comparison, an estimate is suggested for E_{num} in the finite-amplitude case (Table 3.6). The Bergen Code version discussed in Section 2.2.4, which solves the Transformed Beam Equation by means of the Richtmyer procedure, has been used in this investigation and throughout the present work.

3.2.1. Indicators for comparison between simulation results

In order to make the comparison of a large number of simulation results practical, each is represented by four scalar values for each of the fundamental and the second harmonic frequency component. The indicator values are illustrated in Figure 3.3. $I_{a,1}$ and $I_{a,2}$ are mean values of the simulated effective fundamental sound pressure $p_{1,\text{sim}}$ along the sound beam axis,

$$I_{a,m} = \frac{1}{z_{m,2} - z_{m,1}} \int_{z_{m,1}}^{z_{m,2}} p_{1,\text{sim}}(z, 0) dz, \quad m = 1, 2. \quad (3.9)$$

z and x are Cartesian coordinates in the axial and transverse directions, respectively. Corresponding indicator values for the simulated effective sound pressure amplitude $p_{2,\text{sim}}$ for the second harmonic frequency component are denoted with a prime, $I'_{a,1}$ and $I'_{a,2}$. The first z interval for averaging is chosen to cover the near ranges where the majority of hydrophone and calibration sphere measurements have been made, $[z_{1,1}, z_{1,2}] = [2 \text{ m}, 10 \text{ m}]$. The second indicator value $I_{a,2}$ is intended to cover far distances from the sound source, $[z_{2,1}, z_{2,2}] = [50 \text{ m}, 190 \text{ m}]$ (cf. Figure 3.3a).

Numerical errors are expected to increase with the angular distance off axis. In each calculation step, the axisymmetric Bergen Code version used in the present work calculates the sound pressure amplitude along a line perpendicular to the axis. The indicator values $I_{b,1}$ and $I_{b,2}$ are averages of $p_{1,\text{sim}}$ along such lines, from $x_{m,1} = z_m \tan 4^\circ$ through $x_{m,2} = z_m \tan 6^\circ$ (Figure 3.3b),

$$I_{b,m} = \frac{1}{x_{m,2} - x_{m,1}} \int_{x_{m,1}}^{x_{m,2}} p_{1,\text{sim}}(z_m, x) dx, \quad m = 1, 2. \quad (3.10)$$

As for the axial field, corresponding values $I'_{b,1}$ and $I'_{b,2}$ are defined for the second harmonic frequency component.

To produce beam patterns with constant distances r from the sound source, the simulation algorithm must perform calculations along a series of very closely spaced lines. This involves an unwanted complication of the numerical grid. Averaging along a line is therefore used instead. The consequence of this choice is discussed in the next section. The axial distances z from the source plane are chosen equal to $z_1 = 9.5 \text{ m}$ and $z_2 = 200 \text{ m}$.

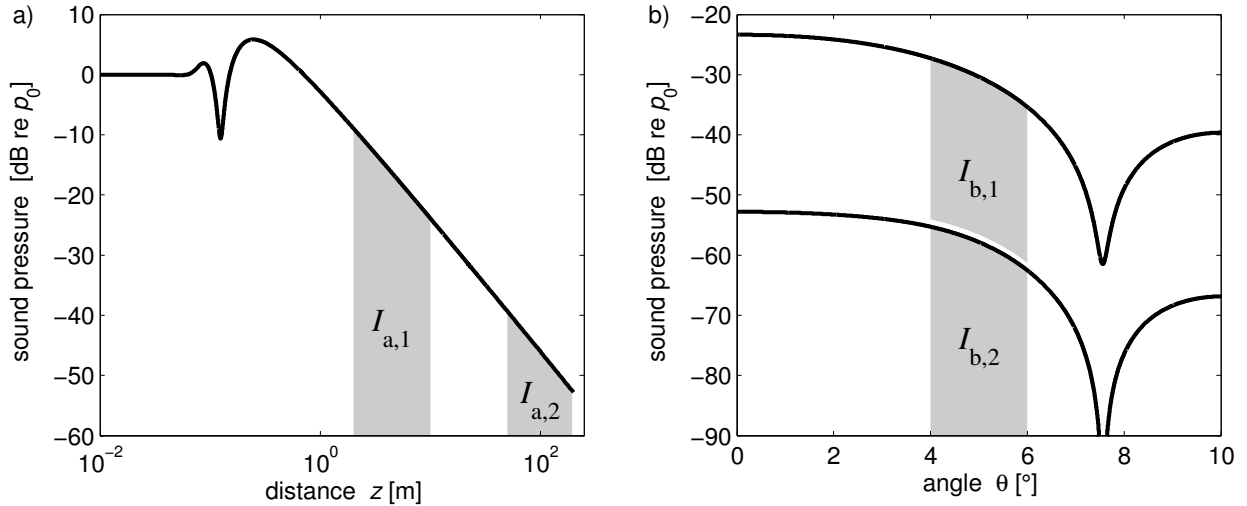


Figure 3.3. Indicators for comparing simulation results. a) Mean values $I_{a,1}$ and $I_{a,2}$ of the sound pressure amplitude along the axis of the sound beam. b) Mean values $I_{b,1}$ and $I_{b,2}$ of the sound pressure amplitude along lines through the axis, in the planes $z = z_1 = 9.5$ m and $z = z_2 = 200$ m, respectively. The

$I_{b,m}$ mean values are taken over the x intervals $x \in [z_m \tan 4^\circ, z_m \tan 6^\circ]$.

3.2.2. Numerical uncertainty contributors

Beam pattern convention

As discussed above, the simulated beam patterns are in the present work taken from the calculated sound pressure along a line perpendicular to the sound beam axis. Directivity measurements are normally specified for constant distance r between the sound source and the hydrophone or acoustic scatterer. Beam patterns for constant r with sufficient angular resolution can be obtained from the Bergen Code either by interpolation between neighbouring calculation steps or by forcing very short propagation steps in a small region leading up to $z = r$. The latter approach would however entail an unwanted change in the numerical grid.

When measured and simulated beam patterns are compared in the present work, an angle dependent contribution Δp_{sim} is added to the difference in sound pressure amplitude. The difference Δr between the distance r from the origin and the axial coordinate z for a field point (Figure 3.4),

$$\Delta r = r - z = z \left(\frac{1}{\cos \theta} - 1 \right), \quad (3.11)$$

is equal to $2.4 \cdot 10^{-3} z$ when $\theta = 4^\circ$. Only considering spherical spreading, the derivative of the sound pressure with respect to r is

$$\frac{\partial p_{\text{sim}}(r, \theta)}{\partial r} \approx -\frac{p_{\text{sim}}(r, \theta)}{r}.$$

For the introduced error Δp_{sim} in the sound pressure, one can write

$$\Delta p_{\text{sim}} \approx \Delta r \cdot \frac{\partial p_{\text{sim}}}{\partial r} = -z \left(\frac{1}{\cos \theta} - 1 \right) \cdot \frac{p_{\text{sim}}}{r} \approx -\left(\frac{1}{\cos \theta} - 1 \right) p_{\text{sim}}. \quad (3.12)$$

The sound pressure level along a line perpendicular to the sound beam axis (constant z) is thus approximately 0.02 dB lower than for constant r when $\theta = 4^\circ$. The error is small compared to other uncertainty contributions (Table 3.12). Simulation results for angles between 0 and 6° are of interest. Instead of introducing an angle dependent correction factor, a relative standard uncertainty contribution E_{geom} is included in the simulation uncertainty budget (Table 3.6) to account for the different beam pattern conventions used in the measurements and the simulations. Its value is chosen such that $20 \log_{10}(1 + E_{\text{geom}}) = 0.02$ dB.

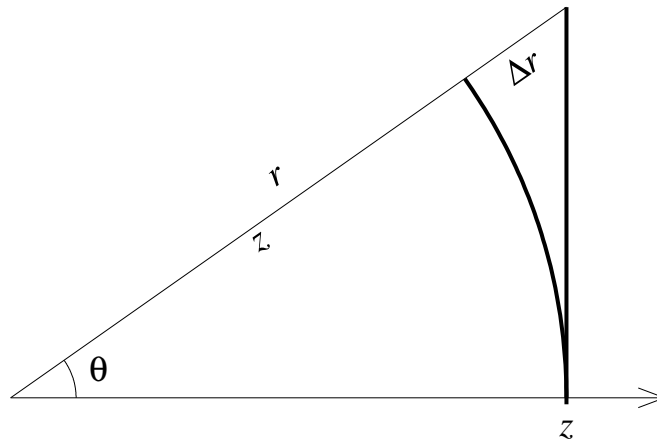


Figure 3.4. Arc (constant r) and line (constant z) for specifying beam patterns.

Spectral truncation

The number N_h of harmonics retained in the calculations and the numerical grid width u_{\max} determine the spectral and spatial limits of the simulation domain (Section 2.2.4). Energy accumulates in the highest-order retained harmonic components, introducing an error that spreads to lower frequency components as the solution is marched forward. A relative standard uncertainty contribution E_{harm} is thus introduced in the simulation result. For simulations with peak source condition amplitude $p_0 = 1$ Pa, N_h is chosen equal to 10 in the present work. The relative change in the calculated fundamental frequency component when the number of harmonics is doubled to 20 is less than $5 \cdot 10^{-5}$.

In all cases where higher source condition amplitudes than 1 Pa are used, N_h is set to 50. The chosen value is a trade-off between truncation error and computational cost. The calculation time for each harmonic component in each step is proportional to N_h^2 . A typical simulation for the present work with $N_h = 50$ requires between two and four hours CPU time on the personal computers that are used (AMD Athlon XP 1900+ and Intel Pentium 4, 2.66 GHz processors). In the test runs where N_h or the numerical grid resolution is varied, the computation times can be several times longer. For simulation series 1 and 2 (Table 3.2), with both source condition amplitudes, a doubling of N_h from 50 to 100 causes a relative change of less than $5 \cdot 10^{-5}$ in the fundamental and second harmonic frequency components. This is insignificant compared with the effects of other parameters.

However, for simulation series 3 and 4 with $p_{0,\text{peak}} = 1000$ kPa, the ratio between results calculated with $N_h = 50$ and $N_h = 100$ reaches 0.15 dB in the second harmonic frequency component. This is considered an unacceptably high value for $20 \log_{10}(1+E_{\text{harm}})$ in comparison with other contributions to the numerical uncertainty (Table 3.5). Increasing N_h to reduce the spectral truncation error is not desirable because of the consequences for the computational cost. Several schemes have been used in earlier works to increase accuracy without having to make calculations for an excessive number

of harmonics. For example, N_h can be varied automatically during the calculation process to ensure a sufficient number of harmonics at the same time as the required time is minimized.²⁵⁴ Analytical methods have been developed to enable reduction of the number of numerically evaluated harmonics without degrading the accuracy of the result.^{24,134,202} Damping schemes that drain excess energy from the highest frequency components also reduce the effect of truncation. A common method is to prevent each harmonic from obtaining greater amplitude than its neighbour of lower order.^{249,35,114}

In the present work, a damping factor similar to the Newtonian friction scheme used by Ystad and Berntsen²⁶⁹ is applied in the frequency domain. The amplitudes of the N_d highest harmonics are multiplied with a quadratic polynomial in each step of the calculation,

$$p''_{N_h-m}(\sigma, u) = p_{N_h-m}(\sigma, u) \cdot \left\{ 1 - \left[\frac{N_d - m}{N_d} \right]^2 \right\}, \quad (3.13)$$

$$m = 0, 1, 2, \dots, (N_d-1).$$

This damping scheme is used in high amplitude simulations for the 200 kHz fundamental frequency throughout this work. It is also used for Series 3 and 4 of test simulations described in this chapter (Table 3.2). The number of damped harmonic components is kept equal to 20, and the total number of retained harmonics $N_h = 50$. Doubling N_h with the damping scheme active yields maximum relative changes of 0.03 dB in the fundamental and second harmonic component amplitudes, which is deemed acceptable. Simulations with $N_h = 100$ with and without the described damping scheme agree at least to within a relative difference of $5 \cdot 10^{-5}$.

Variations with N_h in the indicator values along and off the sound beam axis are shown for simulation series 4 with $p_0 = 1000$ kPa in Figures 3.5a and 3.5b, respectively. Series 4 (Table 3.2) has been chosen because it yields the strongest nonlinear distortion and thus the greatest truncation errors. Results

are shown with and without damping of the $N_d = 20$ highest harmonics. One should note that the result for each indicator is normalized to its value obtained with $N_h = 140$. The different indicators do not tend towards the same value as N_h is increased, nor does Figure 3.5 indicate convergence towards any external reference value. The question of accuracy of the simulations of finite amplitude sound propagation is treated further in Section 3.2.5. Based on the results shown in Figure 3.5, relative standard uncertainty contributions of $20 \log_{10}(1+E_{\text{harm}}) = 0.03$ dB on axis and $20 \log_{10}(1+E_{\text{harm}}) = 0.003$ dB off axis due to the choice of $N_h = 50$ are inserted in Table 3.5 for the simulations of high-amplitude sound propagation.

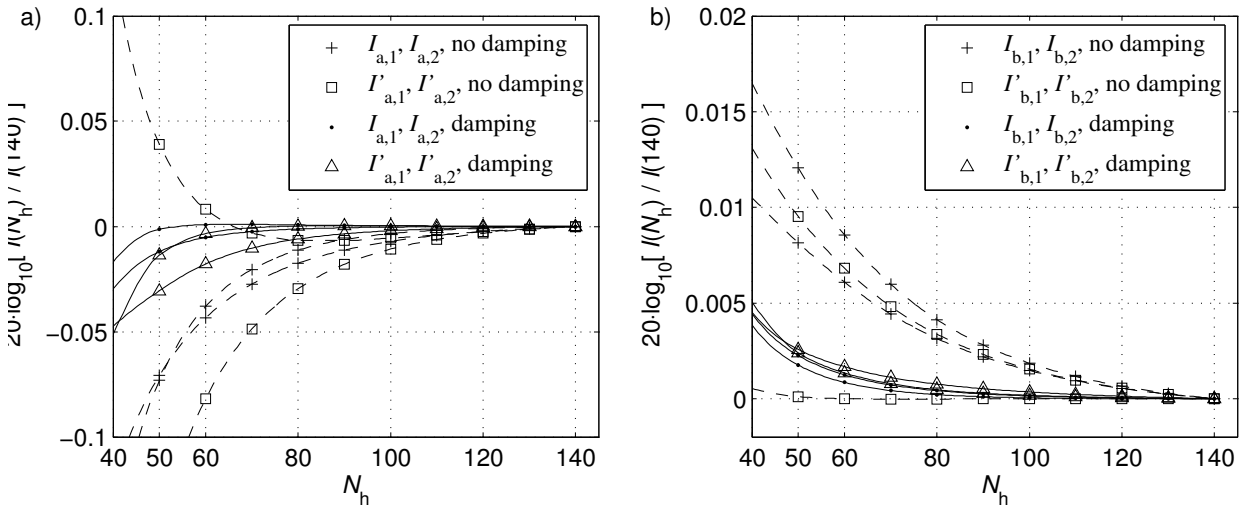


Figure 3.5. Relative values of the indicators $I_{a,1}$, $I_{a,2}$, $I_{b,1}$, and $I_{b,2}$ (fundamental frequency component) and corresponding values for the second harmonic frequency component (indicated with prime), for different N_h . Values are shown for simulations with and without damping of the 20 highest harmonic frequency components. Each indicator is normalized to its value for $N_h = 140$. $f = 210$ kHz, $p_0 = 1000$ kPa (simulation series 4). a) Axial field, b) indicators off axis.

Equation (3.13) describes a fixed scaling of the magnitudes of the N_d highest harmonics in each step of the calculation. Consequently, the damping of the solution depends strongly on the step length l_σ . As l_σ is not constant throughout the calculation region (Equation (2.71)), neither is the damping rate. The step length can easily be compensated for, but this was not considered necessary in the present investigation.

Finite grid width

The zero pressure boundary condition at the outer edge $u = u_{\max}$ of the numerical grid causes reflections that propagate towards the sound beam axis and may eventually interfere with the solution in the paraxial region. Because the numerical grid is rectangular in the transformed coordinates (σ, u) , the width $\xi_{\max}(\sigma)$ in the normalized, spatial (ξ, σ) coordinates increases linearly with σ (Section 2.2.4),

$$\xi_{\max}(\sigma) = u_{\max}(1 + \sigma). \quad (3.14)$$

u_{\max} is chosen such that reflections from the boundary of the numerical grid do not influence the investigated part of the solution, for which θ is less than 6° (Table 3.3). With $u_{\max} = 10$, a doubling does not yield any observed change in the indicators (Equations (3.9) and (3.10)) for the fundamental and second harmonic frequency components. The relative uncertainty contribution E_{width} is therefore neglected.

Other authors have used absorbing boundary layers to reduce reflections.^{269,27,73,91} This is particularly useful in numerical studies of focused ultrasound, but is not deemed necessary in the present work.

Numerical rounding and finite differences

Numerical rounding might cause errors when very high grid resolutions are chosen, though the inherent stability of the algorithm is said to counteract their growth.²⁷⁶ Evidence of such errors are not seen explicitly in the data presented here (Figures 3.7 and 3.8), and the uncertainty contribution E_{rnd} due to such rounding is therefore neglected.

Moreover, the uncertainty contribution E_{fd} due to the Taylor series truncation inherent in the choice of finite-order finite differences^{276,43} is not treated specifically in the present work, but is instead neglected. A comparison of some possible choices for the finite differences can be found in a report by

Numerical grid resolution, damping, and Gibbs oscillations

In each step of the calculation, the truncated set of differential equations (2.67) is solved for N_u equally spaced points from $u = 0$ through $u = u_{\max}$ (Section 2.2.4). For a given u_{\max} (Table 3.3), the grid resolution in the transverse direction is determined by N_u . The numerical grid is illustrated in Figure 3.6.

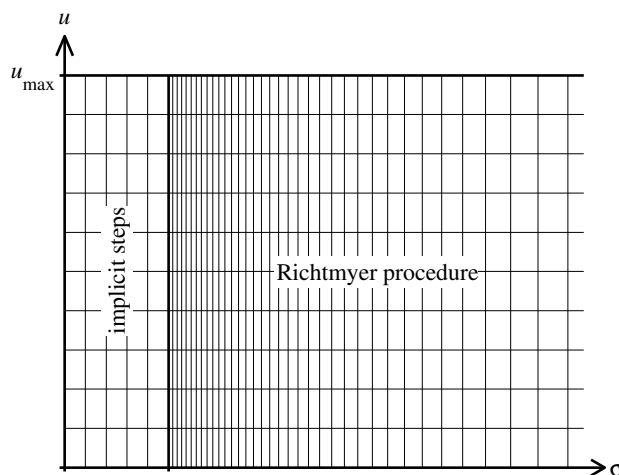


Figure 3.6. Sketch of the numerical grid. N_{imp} initial implicit steps are performed with constant step length l_{imp} . After the implicit steps, the Richtmyer procedure is used. The step length is then determined by Equation (2.71). In each step of the calculation, the solution is calculated in N_u equally spaced points from $u = 0$ through $u = u_{\max}$. Not to scale.

The first few calculation steps are performed with implicit finite differences. The implicit method has a damping effect and is used to suppress Gibbs oscillations due to discontinuities in the source condition.^{45,220} However, the damping also acts upon the sought solution. The number N_{imp} and length l_{imp} of the fully implicit computation steps should be determined such that Gibbs oscillations are eliminated at the same time as the wanted solution is damped as little as possible. The step length parameter λ_σ determines the step length $l_\sigma(\sigma)$ between each calculation step where the Richtmyer procedure is used (Section 2.2.4). $l_\sigma(\sigma)$ increases quadratically with distance from the sound

source (Equation (2.71)). The relative standard simulation uncertainty contributions

$$E_{\text{grid}}^2 = E_1^2 + E_2^2 \quad (3.15)$$

due to the selected values for N_u and λ_σ , respectively, and the uncertainty contribution

$$E_{\text{imp}}^2 = E_3^2 + E_4^2 \quad (3.16)$$

due to the choices for N_{imp} , and l_{imp} are investigated in Sections 3.2.3–3.2.5.

3.2.3. Test simulations for the influence of grid parameters

Sound propagation from a uniform circular piston in an infinitely stiff baffle of infinite extent is considered. Bergen Code simulations are run with different values for the parameters N_u , λ_σ , N_{imp} , and l_{imp} , which control the resolution of the numerical grid and the number and length of initial implicit calculation steps.

The test simulations are organized in four series as shown in Table 3.2. Series 1 and 2 are for frequencies and ka values that bracket those used for the 120 kHz echo sounder in the present work. The parameters for Series 3 and 4 relate the same way to the 200 kHz echo sounder simulations. Simulations for comparison with linear theory are made with $p_0 = 1$ Pa peak pressure amplitude for the source condition. Corresponding finite amplitude simulations are made with somewhat higher amplitudes than in Chapters 5 and 6 (Table 3.2). It is assumed that any amplitude-dependent errors increase or decrease monotonically with p_0 within the range of interest. The medium parameters shown in Table 3.3 correspond approximately to fresh water at room temperature and have been used in the test simulations. Values and ranges of variation for the other parameters (Tables 3.3 and 3.4) were chosen on the basis of initial tests.¹⁹⁶

Table 3.2. Sound source parameters for the test simulations for the numerical uncertainty contribution. The source condition pressure amplitude p_0 refers to the peak sound pressure.

| | | series 1 | series 2 | series 3 | series 4 |
|------------------------------|-------|-----------------|-----------------|-----------------|-----------------|
| fundamental frequency | f | 110 kHz | 130 kHz | 190 kHz | 210 kHz |
| uniform piston source radius | a | 53.7 mm | 52.7 mm | 32.3 mm | 32.6 mm |
| low amplitude on source | p_0 | 1 Pa | 1 Pa | 1 Pa | 1 Pa |
| high amplitude on source | p_0 | 500 kPa | 500 kPa | 1000 kPa | 1000 kPa |
| wave number times radius | ka | 25.0 | 29.0 | 26.0 | 29.0 |

The four parameters N_u , λ_σ , N_{imp} , and l_{imp} are varied systematically to obtain estimates for the relative uncertainty contributions E_{grid} and E_{imp} due to the configuration of the numerical grid (Equations (3.15) and (3.16)). While one of the parameters is being varied, the others are kept at their “unperturbed” values shown in Table 3.4. These unperturbed parameter values are used for the simulations elsewhere in the present work.

Table 3.3. Constant parameters used in the test simulations for E_{num} .

| parameter | | value |
|-------------------------------------|------------------|--|
| sound speed | c_0 | 1485 m/s |
| absorption coefficient | α_2 | $2.5 \cdot 10^{-14}$ Np/(m Hz ²) |
| nonlinearity coefficient | β | 3.51 |
| density | ρ_0 | 998.2 kg/m ³ |
| number of harmonics, low amplitude | N_h | 10 |
| number of harmonics, high amplitude | N_h | 50 |
| damped harmonics, Series 3 and 4 | N_d | 20 |
| numerical grid width | u_{max} | 10 |

Table 3.4. Parameters related to numerical grid resolution and damping of Gibbs oscillations. Unperturbed values and range of variation for each parameter in the test simulations for E_{num} .

| parameter | | unperturbed | minimum | maximum |
|----------------------------------|------------------|---------------------|---------------------|---------------------|
| number of points, transverse | N_u | 16 000 | 4000 | 25 000 |
| step length parameter | λ_σ | $2.0 \cdot 10^{-4}$ | $5.0 \cdot 10^{-6}$ | $4.0 \cdot 10^{-4}$ |
| number of initial implicit steps | N_{imp} | 10 | 5 | 20 |
| length of initial implicit steps | l_{imp} | $5.5 \cdot 10^{-3}$ | $3.0 \cdot 10^{-3}$ | $1.5 \cdot 10^{-2}$ |

3.2.4. Test simulation results, low amplitude

Analytical reference solutions

The effect of nonlinear distortion on the indicator values (Equations (3.9) and (3.10)) is negligible when the peak sound pressure amplitude of the source condition is 1 Pa. Simulation results are compared with analytical solutions of the linearized parabolic equation.²³⁶ These are the same solutions that were used above to investigate the importance of the parabolic approximation, except that absorption is included here. Such comparison yields a direct estimate for the uncertainty contribution $E_{\text{np},0}$ (Equation (3.8)) due to the numerical algorithm in the linear case. Redefining p_{par} from the previous section, taking absorption into account, the analytical solution of the linearized parabolic equation for the sound pressure amplitude can be written²³⁶

$$|p_{\text{par}}(r, 0)| = p_0 \exp \left\{ -\alpha' r \left[1 + \left(\frac{a}{2r} \right)^2 \right] \right\} \sqrt{2 \cosh \frac{\alpha' a^2}{2r} - 2 \cos \frac{ka^2}{2r}} \quad (3.17)$$

for the axial sound field, and

$$|p_{\text{par}}(r, \theta)| = p_0 \frac{ka^2}{2r} \exp \left\{ -\alpha' r \frac{a^2 + r^2 (\cos^2 \theta + 1)}{2r^2 \cos \theta} \right\} \times \left| \frac{J_1((k + j\alpha') a \tan \theta)}{ka \sin \theta} \right| \quad (3.18)$$

for the approximate far field.²³⁶ $\alpha' = \alpha_2 f^2$ is the absorption coefficient in Nepers per metre.

Equation (3.18) is a far field approximation.²³⁶ The thus introduced uncertainty can be investigated through the results shown in Figure 3.7b (treated further below). The ratio between I_b values calculated from Bergen Code simulations and from Equation (3.18) is plotted as a function of the transverse resolution parameter N_u . Ratios between $I_{b,1}$ results ($z = 9.5$ m) are marked with plus signs and dots, while ratios between $I_{b,2}$ results ($z = 200$ m) are marked with triangles and squares. The results for $r = 9.5$ m and $r = 200$ m agree to within 0.003 dB, which is small compared to the ratios themselves. The far field approximation inherent in Equation (3.18) is therefore neglected in the following.

Comparison between numerical and analytical solutions

The differences between the indicator values calculated from simulation results and the analytical expressions (3.17) and (3.18) are shown in Figures 3.7–3.10. The plotted values are

$$\langle \text{deviation from } p_{\text{par}} \rangle = 20 \log_{10} \frac{I(\text{Bergen Code simulations})}{I(\text{analytical, linearized parabolic eq.})}, \quad (3.19)$$

where I is short for $I_{a,1}$, $I_{a,2}$, $I_{b,1}$, or $I_{b,2}$.

The unperturbed parameter values in Table 3.4 yield indicator values between 0.008 dB and 0.013 dB greater than for the analytical solution for the axial field. The discrepancy seems to increase somewhat with distance from the sound source.

The simulated indicator values off axis $I_{b,1}$ and $I_{b,2}$ are between 0.003 dB and 0.016 dB below those of the analytical far field approximation, when the unperturbed parameter values in Table 3.4 are used. The greatest deviations are seen in simulation series 2 and 4, which have the highest ka numbers (Table 3.2). The width of the sound beam decreases with ka , thus increasing the slope of the beam pattern between $\theta = 4^\circ$ and $\theta = 6^\circ$. A slight miscalculation of the width of the main lobe may thus contribute to the observed ka dependence in $I_{b,1}$ and $I_{b,2}$.

Based on the deviations noted above, the standard relative uncertainty contribution E_{np} (Equation (3.8)) due to the numerical algorithm for low amplitude sound propagation (denoted $E_{p,0}$) is estimated such that $20 \log_{10}(1+E_{np,0}) = 0.01$ dB for the axial sound pressure amplitude and 0.02 dB for the simulated sound field within $\theta = 6^\circ$ (Table 3.6). An attempt to extrapolate these results to finite amplitude sound propagation is made in Section 3.2.5.

Sensitivity to individual parameters

To form a basis for estimating the numerical uncertainty in the finite-amplitude sound propagation case, the sensitivity of the solution to each parameter in Table 3.4 is first investigated in the case of the low source condition amplitude (near-linear sound propagation). The results are presented on the form of uncertainty contributions in Table 3.5.

Figure 3.7 indicates that the numerical solution seems to behave asymptotically as the number of grid points in the transverse direction N_u is increased. The greatest ratio between indicator values for $N_u = 8000$ and $N_u = 16000$ is found in the axial field, and is equal to 0.005 dB. This is chosen as the relative standard uncertainty contribution $20 \log_{10}(1+E_1)$ due to the choice of $N_u = 16000$ (Table 3.5).

Figure 3.8 shows the value of Equation (3.19) as a function of the step length parameter λ_σ . Changes in λ_σ over the chosen range (Table 3.4) have negligible effect on the $I_{a,1}$, $I_{b,1}$, and $I_{b,2}$ values, but are more important for $I_{a,2}$ (axial field at great distance from the source). The λ_σ dependence seems more clearly convergence-like than the N_u dependence. For $\lambda_\sigma = 2.0 \cdot 10^{-4}$, $20 \log_{10} I_{a,2}$ is 0.004 dB higher than what it seems to converge towards for small λ_σ . Doubling λ_σ from $2.0 \cdot 10^{-4}$ yields a 0.01 dB increase in $20 \log_{10} I_{a,2}$. This is taken as an upper bound for its contribution to the numerical uncertainty along the sound beam axis ($20 \log_{10}(1+E_2)$ in Table 3.5). It should be noted that the abscissas in

Figures 3.8, 3.12, and 3.16 are logarithmic.

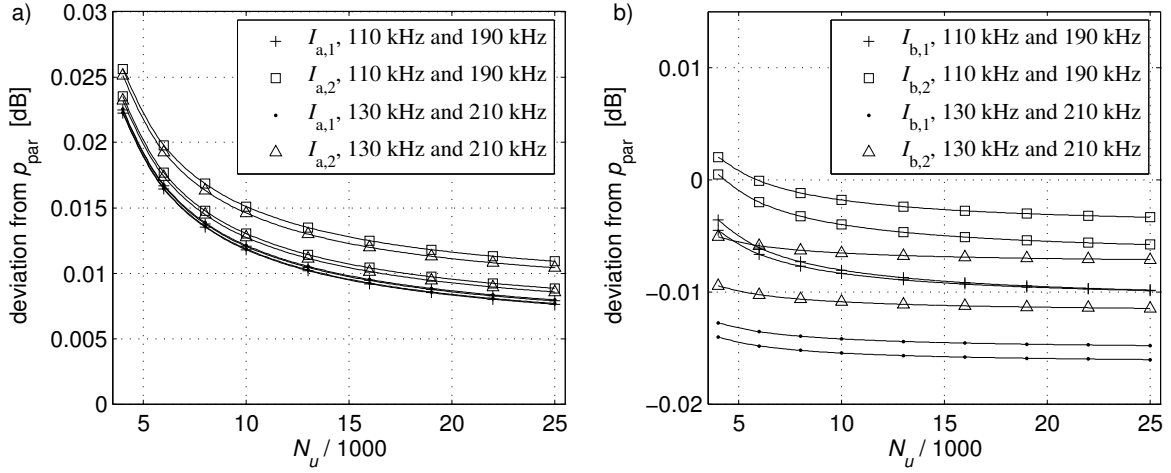


Figure 3.7. Simulation results with $p_0 = 1$ Pa. Deviation in decibels from the analytic solution p_{par} as function of the number N_u of numerical grid points in the transverse direction. a) Axial indicator values. b) Off-axis indicator values.

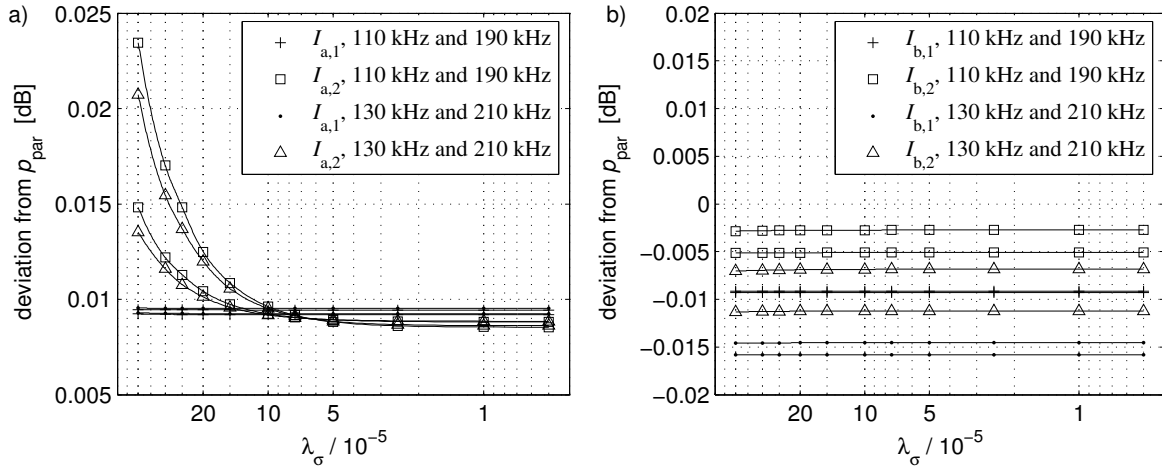


Figure 3.8. Simulation results with $p_0 = 1$ Pa. Deviation in decibels from the analytic solution p_{par} as function of the step length parameter λ_σ . a) Axial indicator values. b) Off-axis indicator values.

The simulated axial field varies rapidly with the number of implicit steps N_{imp} for small values of the parameter (Figure 3.9). This is ascribed to the Gibbs oscillations that the initial implicit steps are intended to reduce. It is therefore assumed that N_{imp} should be above these smallest values. For N_{imp} approximately greater than 9, the magnitude of the axial solution increases linearly with the number of implicit steps. N_{imp} should be chosen in such a way

that the effect of the implicit steps on the solution becomes as small as possible. When $N_{\text{imp}} = 10$, its contribution to the simulation error is assumed similar to the ratio between each axial indicator value and its minimum (Figure 3.9a). This is approximately 0.005 dB ($20 \log_{10}(1+E_3)$ in Table 3.5).

Unlike for the axial field, the off-axis indicator values $I_{b,1}$ and $I_{b,2}$ decrease almost linearly with N_{imp} throughout the investigated interval. This makes the uncertainty contribution difficult to assess. The maximum ratio between the results for $N_{\text{imp}} = 6$, where the minimum in the axial indicator values is found, and the results for $N_{\text{imp}} = 10$, is 0.006 dB. This is chosen as a relative uncertainty estimate ($20 \log_{10}(1+E_3)$) off the sound beam axis.

The implicit step length l_{imp} and the number of steps N_{imp} have similar influence on the numerical solution (Figure 3.10). The uncertainty contribution due to l_{imp} when it is chosen equal to $5.5 \cdot 10^{-3}$ is stipulated on the basis of the observed variations for smaller step lengths, and is set to 0.005 dB for the axial field and 0.01 dB for the indicator values off axis ($20 \log_{10}(1+E_4)$ in Table 3.5).

The estimates of uncertainty contributions due to the individual parameters are not all well founded. They are primarily intended for use in combination with the observed total deviation from the analytical solution. The obtained data form the basis for an uncertainty estimate for the finite amplitude case, as discussed in the next section.

3.2.5. Test simulation results, high amplitudes

The comparison with analytical solutions above yields an estimate of the relative uncertainty contribution $E_{\text{np},0}$ due to the numerical solution process when nonlinear effects are negligible. Although analytical expressions also exist for finite amplitude sound propagation,^{133,54,176,177,150} none that apply to a sound beam and claim the accuracy desired here are known to the author.

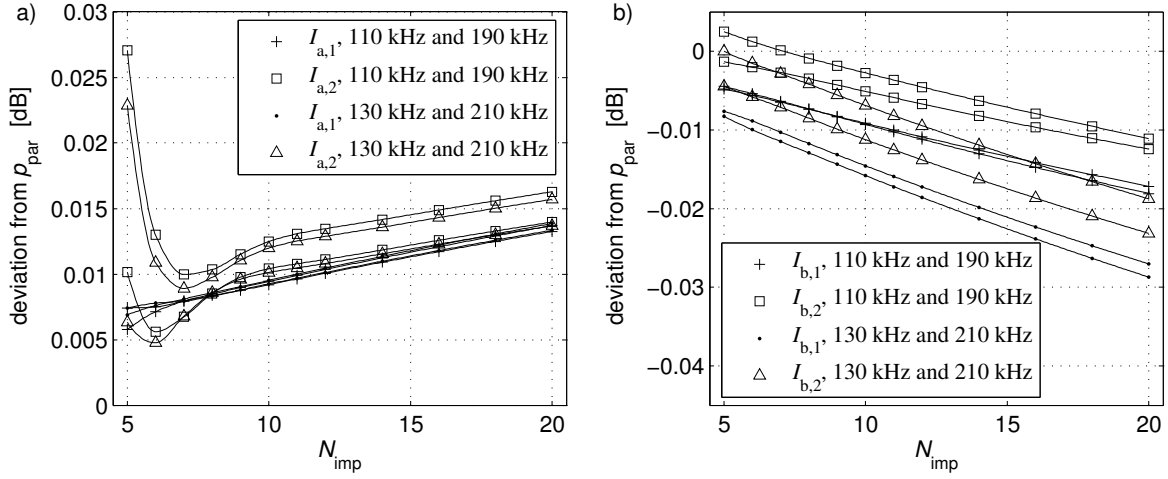


Figure 3.9. Simulation results with $p_0 = 1$ Pa. Deviation from the analytic solution p_{par} as function of the number of initial implicit calculation steps N_{imp} . a) Axial indicator values, b) Off-axis indicator values.

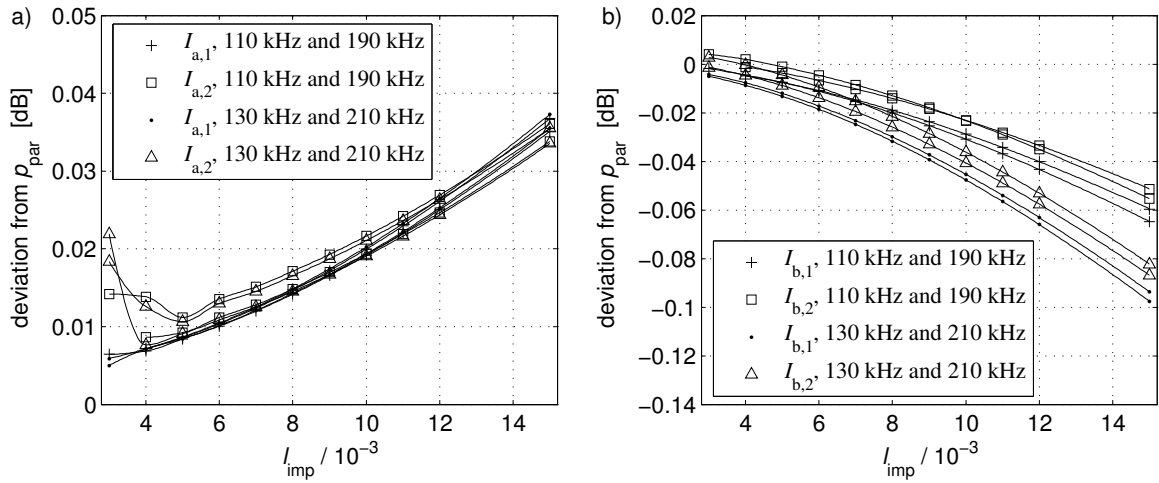


Figure 3.10. Simulation results with $p_0 = 1$ Pa. Deviation from the analytic solution p_{par} as function of the length l_{imp} of the initial implicit calculation steps. a) Axial indicator values, b) Off-axis indicator values.

The solution's sensitivity to the individual parameters is presented in the same way as for the low amplitude case, but without comparison with any reference solution. For each of the four cases in Table 3.2, the indicator values (Equations (3.9) and (3.10)) are plotted relatively to the simulation for which the four parameters in Table 3.4 have their unperturbed values,

$$\langle \text{plotted value} \rangle = 20 \log_{10} \frac{I(\text{one perturbed parameter})}{I(\text{all parameters unperturbed})}. \quad (3.20)$$

The sensitivities to the calculation parameters are compared with the corresponding sensitivities shown above for the low-amplitude case. The numerical uncertainty $E_{np,0}$ obtained for low amplitude is scaled with the ratio between the obtained sensitivities to provide a corresponding uncertainty E_{np} (Equation (3.8)) that applies to the simulated finite amplitude sound propagation.

Sensitivity to individual parameters

The change from low to high source amplitude (Table 3.2) reduces the N_u dependence of the fundamental frequency component somewhat. As shown in Figure 3.11, the I_a indicator values for $N_u = 8000$ are up to 0.004 dB higher than for $N_u = 16000$. For the I_b values, the corresponding ratio is 0.002 dB. These results are taken as uncertainty contributions due to N_u ($20 \log_{10}(1+E_1)$ in Table 3.5), as was also done for the low amplitude case.

Figure 3.12 indicates the λ_σ dependence of the simulation result for the fundamental frequency component. Doubling λ_σ from $1.0 \cdot 10^{-4}$ to its unperturbed value $2.0 \cdot 10^{-4}$ yields a maximum change of 0.01 dB in $20 \log_{10} I_{a,1}$ and 0.02 dB in $20 \log_{10} I_{a,2}$ (Figure 3.12a). Small λ_σ are assumed to yield the most accurate solution. The indicator values seem to converge towards a value approximately 0.01 dB from that of the simulation that corresponds to unperturbed parameter values. The relative uncertainty contribution for the axial field is taken to be $20 \log_{10}(1+E_2) = 0.02$ dB, corresponding to the choice for the low amplitude case. The relative uncertainty value chosen for the indicator values off axis is 0.01 dB (Figure 3.12b). The damping of the N_d highest harmonics has not been employed in the simulations presented in Figure 3.12, as excess damping would obscure the convergence-like behaviour for small λ_σ .

The N_{imp} and l_{imp} dependencies of the indicator values for the fundamental frequency component are shown in Figures 3.13 and 3.14, respectively. The results are similar to those obtained for the low amplitude case, although

especially the solution's sensitivity to l_{imp} is greater. The corresponding uncertainty contributions E_3 and E_4 are estimated the same way as for the low amplitude case. The results are found in Table 3.5.

The indicator values for the second harmonic frequency components are denoted $I'_{a,1}$, $I'_{a,2}$, $I'_{b,1}$, and $I'_{b,2}$. Their dependence on the four varied parameters are indicated in Figures 3.15–3.18. The results for the second harmonic are very similar to those for the fundamental frequency component. Uncertainty contributions due to each of the four parameters N_u , λ_σ , N_{imp} , and l_{imp} are inferred the same way as above and inserted in Table 3.5.

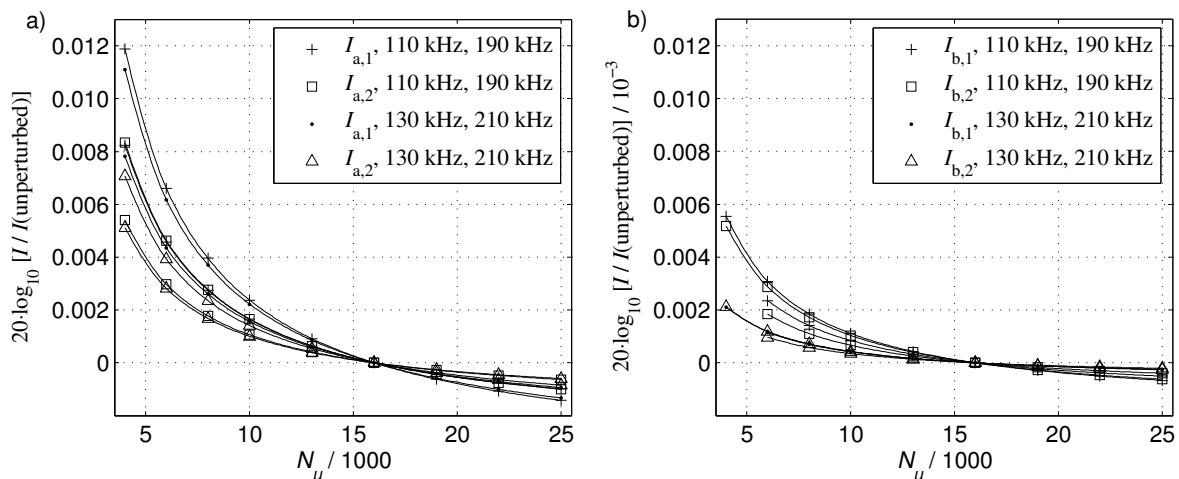


Figure 3.11. Simulation results for the fundamental frequency component with $p_0 = 500$ kPa for the 110 kHz and 130 kHz frequencies, and 1000 kPa for the 190 kHz and 210 kHz frequencies.

Dependence of the indicator values on the transverse grid resolution N_u . a) Axial indicator values, b) off-axis indicator values.

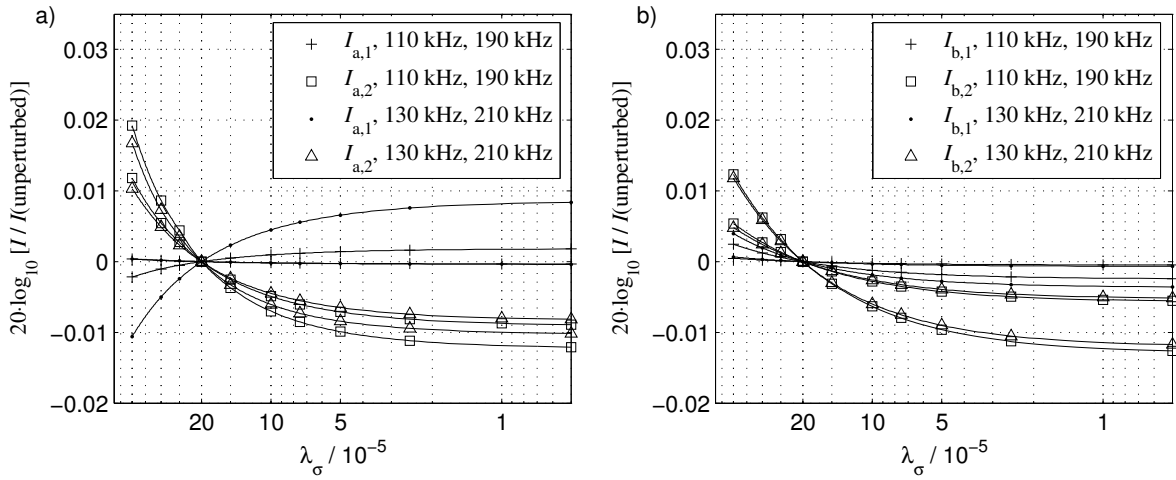


Figure 3.12. Simulation results for the fundamental frequency component with $p_0 = 500$ kPa for the 110 kHz and 130 kHz frequencies, and 1000 kPa for the 190 kHz and 210 kHz frequencies. Dependence of the indicator values on the step length parameter λ_σ . a) Axial indicator values, b) off-axis indicator values.

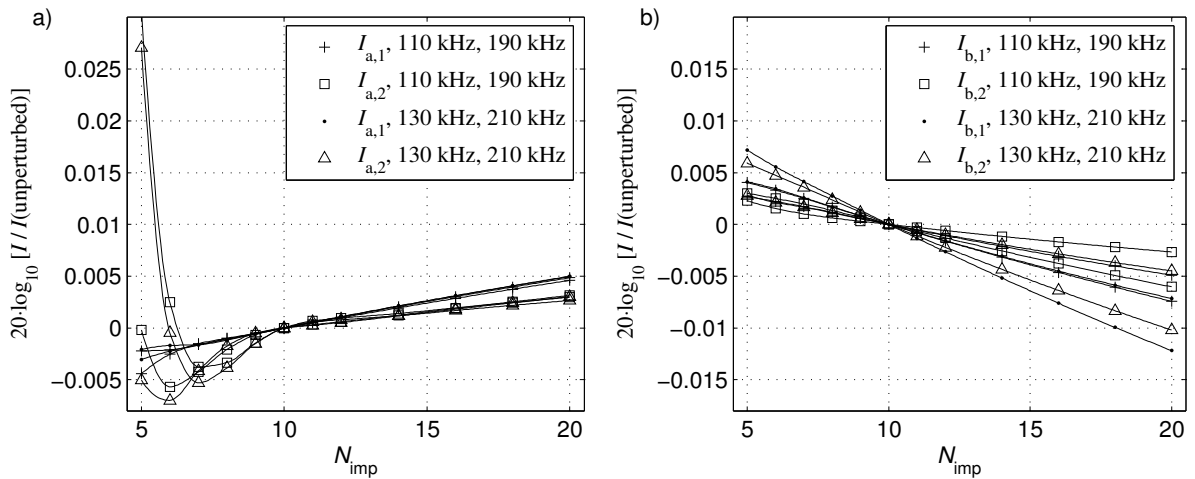


Figure 3.13. Simulation results for the fundamental frequency component with $p_0 = 500$ kPa for the 110 kHz and 130 kHz frequencies, and 1000 kPa for the 190 kHz and 210 kHz frequencies. Dependence of the indicator values on the number N_{imp} of initial implicit calculation steps. a) Axial indicator values, b) off-axis indicator values.

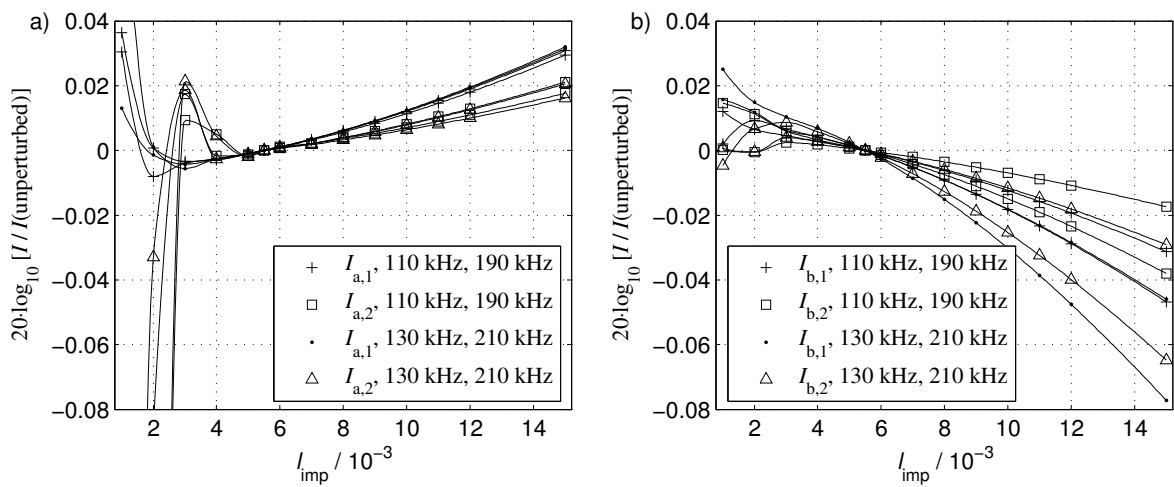


Figure 3.14. Simulation results for the fundamental frequency component with $p_0 = 500$ kPa for the 110 kHz and 130 kHz frequencies, and 1000 kPa for the 190 kHz and 210 kHz frequencies.

Dependence of the indicator values on the length l_{imp} of the initial implicit calculation steps. a) Axial indicator values, b) off-axis indicator values.

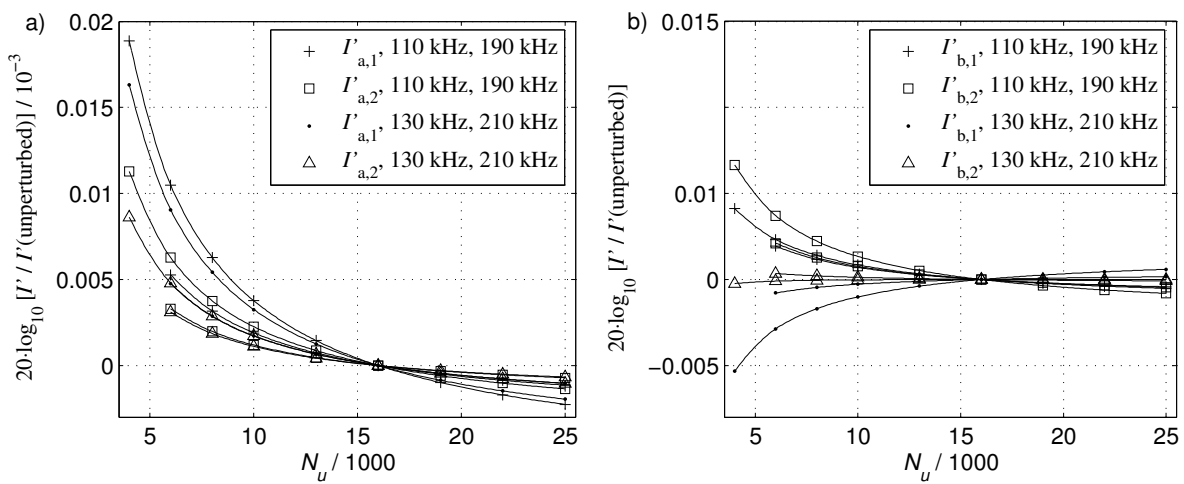


Figure 3.15. Simulation results for the second harmonic frequency component with $p_0 = 500$ kPa for the 110 kHz and 130 kHz frequencies, and 1000 kPa for the 190 kHz and 210 kHz frequencies.

Dependence of the indicator values on the number of numerical grid points in the transverse direction N_u . a) Axial indicator values, b) off-axis indicator values.

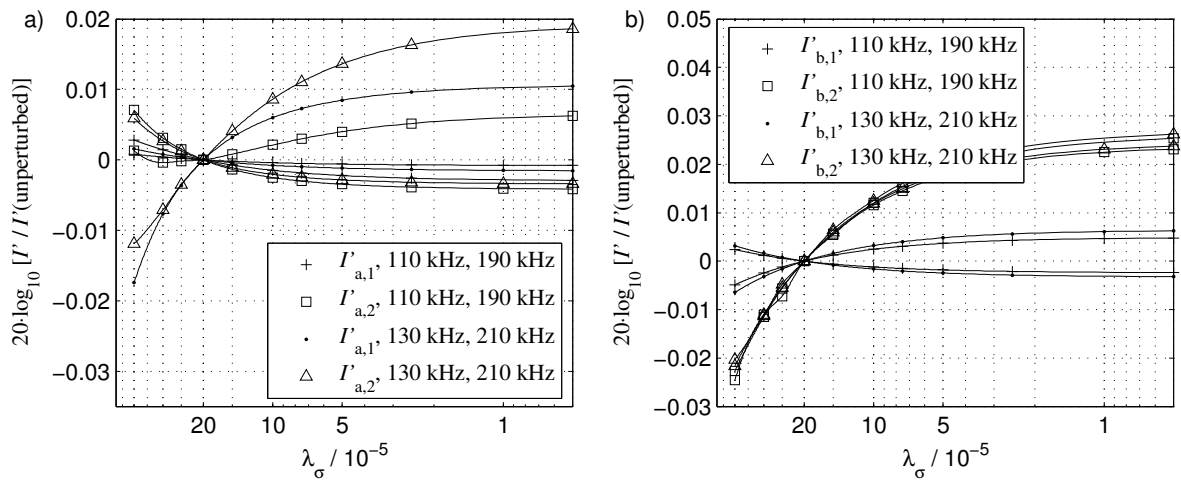


Figure 3.16. Simulation results for the second harmonic frequency component with $p_0 = 500$ kPa for the 110 kHz and 130 kHz frequencies, and 1000 kPa for the 190 kHz and 210 kHz frequencies. Dependence of the indicator values on the step length parameter λ_σ . a) Axial indicator values, b) off-axis indicator values.

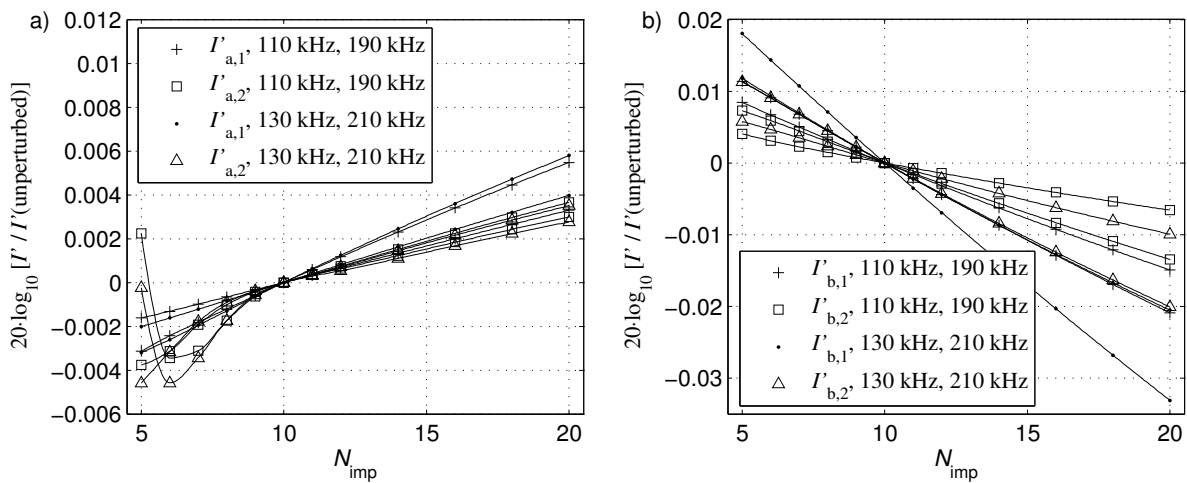


Figure 3.17. Simulation results for the second harmonic frequency component with $p_0 = 500$ kPa for the 110 kHz and 130 kHz frequencies, and 1000 kPa for the 190 kHz and 210 kHz frequencies. Dependence of the indicator values on the number N_{imp} of initial implicit calculation steps. a) Axial indicator values, b) off-axis indicator values.

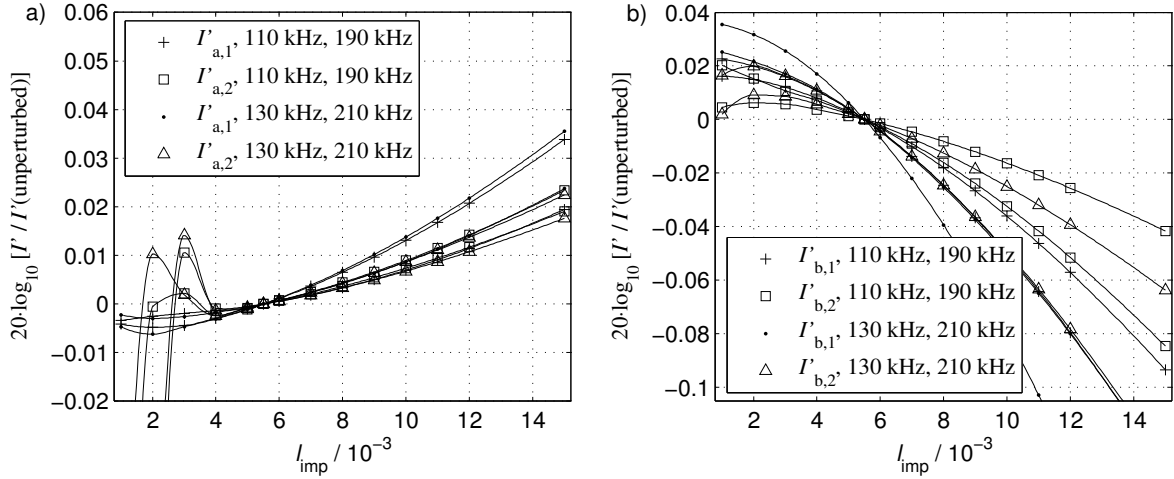


Figure 3.18. Simulation results for the second harmonic frequency component with $p_0 = 500$ kPa for the 110 kHz and 130 kHz frequencies, and 1000 kPa for the 190 kHz and 210 kHz frequencies. Dependence of the indicator values on the length l_{imp} of the initial implicit calculation steps. a) Axial indicator values, b) off-axis indicator values.

3.2.6. Combined numerical uncertainty

An ad-hoc approach is taken to obtain an indication of the numerical uncertainty to expect for simulations of finite amplitude sound propagation. The five relative uncertainty contributions E_{harm} , E_1 , E_2 , E_3 , and E_4 in Table 3.5 are assumed to relate to E_{np} (cf. Equation 3.8) as

$$\begin{aligned}
 E_{\text{np}} &\approx \sqrt{E_{\text{harm}}^2 + E_{\text{grid}}^2 + E_{\text{imp}}^2 + E_{\text{misc},3}^2} \\
 &= \sqrt{E_s^2 + E_{\text{misc},3}^2}
 \end{aligned}
 \tag{3.21}$$

where, from Equations (3.21), (3.15), and (3.16),

$$E_s^2 = E_{\text{harm}}^2 + E_1^2 + E_2^2 + E_3^2 + E_4^2.
 \tag{3.22}$$

The rightmost column in Table 3.5 contains the calculated values for $20 \log_{10}(1+E_s)$ for the low amplitude case and for the simulated fundamental and second harmonic frequency components in the finite-amplitude case.

As discussed above, direct comparison with analytical values in the linear case yields relative standard uncertainties $20 \log_{10}(1+E_{\text{np},0}) = 0.01$ dB and

$20 \log_{10}(1+E_{np,0}) = 0.02$ dB on and off the sound beam axis, respectively (Table 3.6). To obtain a stipulation of the corresponding values E_{np} for high amplitude sound propagation (fundamental and second harmonic component), $E_{pn,0}$ is scaled with the ratios of E_s for the high and low amplitude cases,

$$E_{np}(\text{finite amplitude}) = E_{np,0} \cdot \frac{E_s(\text{finite amplitude})}{E_s(\text{linear case})}. \quad (3.23)$$

The results for $20 \log_{10}(1+E_{np})$ are shown in Table 3.6.

The scaling of the numerical uncertainty is made under the assumption that the chosen values for the five parameters N_h , N_u , λ_σ , N_{imp} , and l_{imp} are the predominant uncertainty contributors.

Table 3.5. Estimated relative uncertainty contributions due to spectral truncation, resolution, and initial damping. Combined uncertainty E_{grid} intended for comparison between low and high amplitude simulation results (Equation 3.21).

| sound pressure indicators | number of harmonics N_h | transverse number of points N_u | axial step length parameter λ_σ | number of implicit steps N_{imp} | length l_{imp} of implicit steps | combined uncertainty contribution |
|--|----------------------------|-----------------------------------|--|------------------------------------|------------------------------------|-----------------------------------|
| | $20 \log_{10}(1+E_{harm})$ | $20 \log_{10}(1+E_1)$ | $20 \log_{10}(1+E_2)$ | $20 \log_{10}(1+E_3)$ | $20 \log_{10}(1+E_4)$ | $20 \log_{10}(1+E_s)$ |
| low amplitude, fundamental frequency component | | | | | | |
| $I_{a,1}, I_{a,2}$ | 0.0004 dB | 0.005 dB | 0.01 dB | 0.005 dB | 0.005 dB | 0.01 dB |
| $I_{b,1}, I_{b,2}$ | 0.0004 dB | 0.005 dB | 0.001 dB | 0.006 dB | 0.01 dB | 0.01 dB |
| high amplitude, fundamental frequency component | | | | | | |
| $I_{a,1}, I_{a,2}$ | 0.03 dB | 0.004 dB | 0.02 dB | 0.007 dB | 0.02 dB | 0.04 dB |
| $I_{b,1}, I_{b,2}$ | 0.003 dB | 0.002 dB | 0.01 dB | 0.006 dB | 0.01 dB | 0.02 dB |
| high amplitude, second harmonic frequency component | | | | | | |
| $I'_{a,1}, I'_{a,2}$ | 0.03 dB | 0.007 dB | 0.02 dB | 0.005 dB | 0.02 dB | 0.04 dB |
| $I'_{b,1}, I'_{b,2}$ | 0.003 dB | 0.005 dB | 0.03 dB | 0.02 dB | 0.04 dB | 0.05 dB |

In addition to the numerical uncertainty E_s , the combined uncertainty E_{num} due to the numerical algorithm (Equation 3.7) encompasses the contribution due to the difference in beam pattern geometries E_{geom} ,

$$E_{\text{num}}^2 = E_{\text{np}}^2 + E_{\text{geom}}^2 . \quad (3.24)$$

Table 3.6 shows the resulting numerical relative uncertainties E_{num} , which are inserted in the total simulation uncertainty budget (Table 3.12). For the highest source condition amplitudes, $20 \log_{10}(1+E_{\text{num}})$ becomes equal to 0.04 dB for all the indicators for the fundamental frequency component. For the second harmonic, the relative numerical uncertainties become 0.04 dB and 0.06 dB on an off the sound beam axis, respectively. In the low-amplitude case ($p_0 = 1$ Pa), $20 \log_{10}(1+E_{\text{num}})$ becomes 0.01 dB for $I_{a,1}$ and $I_{a,2}$, and 0.03 dB for $I_{b,1}$ and $I_{b,2}$.

Table 3.6. Combined numerical relative standard uncertainty E_{num} , calculated by means of Equation (3.7). The relative uncertainties are given in decibels in the table, although they are not defined as logarithmic quantities. The corresponding linear values are used in all calculations.

| | | low | high amplitude | |
|--|-------------------|-------------|----------------|----------|
| | | amplitude | fundamental | second |
| axial pressure amplitude ($I_{a,1}, I_{a,2}$) | | fundamental | component | harmonic |
| beam pattern geometry | E_{geom} | - | - | - |
| uncertainty due to solution process | E_{np} | 0.01 dB | 0.04 dB | 0.04 dB |
| combined numerical uncertainty | E_{num} | 0.01 dB | 0.04 dB | 0.04 dB |
| off-axis pressure amplitude ($I_{b,1}, I_{b,2}$) | | | | |
| beam pattern geometry | E_{geom} | 0.02 dB | 0.02 dB | 0.02 dB |
| uncertainty due to solution process | E_{np} | 0.02 dB | 0.03 dB | 0.06 dB |
| combined numerical uncertainty | E_{num} | 0.03 dB | 0.04 dB | 0.06 dB |

In summary, the numerical uncertainty for the low-amplitude simulations is based on comparison with analytic solutions of the linearized parabolic equation. The sensitivity of the simulation result to parameters that govern the numerical calculation has been compared between the cases of low and high amplitudes. An estimate of the numerical relative uncertainty E_{num} for the high amplitude simulations has been obtained by scaling the uncertainty for the low-amplitude case. The same approach has been used for both the fundamental and the second harmonic frequency component. It has not been confirmed that such

scaling yields a valid result. In particular, the basis for providing an uncertainty estimate for the simulated second harmonic frequency component can be questioned.

3.3. Uncertainty contribution due to physical input parameters

The simulated effective sound pressure p_{sim} is a function of a range of parameters that describe the sound source and the propagation medium (Table 3.1),

$$p_{\text{sim}} = p_{\text{sim}}(r, \theta, q_1, q_2, \dots, q_7). \quad (3.25)$$

The parameters considered are

- source radius, $q_1 = a$,
- operating frequency, $q_2 = f$,
- source condition sound pressure amplitude, $q_3 = p_0$,
- sound speed, $q_4 = c_0$,
- absorption coefficient, $q_5 = \alpha_2$,
- density, $q_6 = \rho_0$, and
- nonlinearity coefficient, $q_7 = \beta$.

The propagation medium is assumed homogeneous so that all the parameters q_m , $m = 1, 2, \dots, 7$, and their uncertainties are constants. All the medium parameters c_0 , α_2 , ρ_0 , and β depend on temperature, salinity, and pressure and are thus correlated. To simplify the calculations the combined uncertainty contribution is here evaluated as if the parameters were not correlated, yielding a worst-case estimate. If the relative standard uncertainty for each parameter q_m is $E(q_m)$, the relative standard simulation uncertainty contribution E_{param} (Equation (3.1)) due to uncorrelated input parameter uncertainties can be written

$$E_{\text{param}} = \sqrt{\sum_{m=1}^7 \left[(s(q_m) \cdot E(q_m))^2 \right]} + E_{\text{misc},4}^2 . \quad (3.26)$$

The relative sensitivity coefficient $s(q_m)$ due to q_m is³

$$s(q_m) = \frac{q_m}{p_{\text{sim}}} \left. \frac{\partial p_{\text{sim}}}{\partial q_m} \right|_{r,\theta}, \quad m = 1, 2, \dots, 7 . \quad (3.27)$$

3.3.1. Sensitivity study

A sensitivity study is performed to determine the relative standard uncertainty contribution E_{param} due to the uncertainties in the 7 parameters listed above. Sampling-based relative sensitivity coefficients are estimated numerically by comparing simulation results for which each physical parameter q_m is perturbed one at a time by $\pm 10\%$ from a centre value (Tables 3.7–3.10). The relative sensitivity coefficients are approximated by

$$s(q_m) \approx \left(\frac{\Delta p_{\text{sim}}}{p_{\text{sim}}} / \frac{\Delta q_m}{q_m} \right)_{q_n, n \neq m}, \quad m, n = 1, 2, \dots, N . \quad (3.28)$$

Two sets of simulations are made for each of the 120 kHz and 200 kHz echo sounders radiating in fresh water. Calculations are made with $p_0 = 1$ Pa peak on-source sound pressure amplitude and with sound pressure amplitudes that correspond approximately to 1000 W electrical output power for the echo sounders used in the present work. The parameters listed in the lower half of Table 3.3 and the “unperturbed” values in Table 3.4 are used for the spectral truncation, numerical grid width and resolution, and damping of Gibbs oscillations.

The physical parameters, i.e., the uniform piston source radius, frequency, source condition amplitude, sound speed,⁵⁰ absorption coefficient,¹³⁸ density,²⁵⁸ and nonlinearity coefficient⁷⁹ are chosen so that they correspond approximately to measurements performed in fresh water at $(20 \pm 2)^\circ\text{C}$ temperature (Chapter 5).

3.3.2. Results

Tables 3.7 and 3.8 show the obtained relative sensitivity coefficients of 120 kHz simulations due to 10% perturbations in the physical parameters (Section 3.3.1). Table 3.7 shows the obtained relative sensitivity coefficients for the axial indicator values $I_{a,1}$, $I'_{a,1}$, $I_{a,2}$, and $I'_{a,2}$ (Equation (3.9)). The prime refers to the second harmonic frequency component. The sensitivity coefficients shown in Table 3.8 are for the off-axis indicator values $I_{b,1}$, $I'_{b,1}$, $I_{b,2}$, and $I'_{b,2}$ (Equation (3.10)). Sensitivity coefficients for the 200 kHz simulations are calculated the same way, and are shown in Tables 3.9 and 3.10 for the indicator values on and off the sound beam axis, respectively.

Low amplitude

The relative sensitivity coefficients for the axial field due to frequency, source condition sound pressure amplitude, and sound speed, are approximately equal to unity when nonlinear effects can be neglected (Tables 3.7 and 3.9). The source radius sensitivity coefficient is twice as large, while the sensitivity to perturbations in the absorption coefficient is an order of magnitude smaller.

Although the source radius is known to influence the beam pattern strongly, the reported sensitivity coefficients for the radiated field off axis are smaller than for the axial field. The I_b indicators are mean values along lines perpendicular to the sound beam axis between $\theta = 4^\circ$ and $\theta = 6^\circ$. As a decrease in source radius yields both widening of the main lobe and loss of axial sound pressure amplitude (Equation (3.6)), much of its effect may be averaged out in the calculation of the indicator value.

Frequency changes have the same relative influence on the width of the beam pattern as changes in the source radius. Its effect on the axial sound pressure amplitude is however an order smaller (Equation (3.6)). The off-axis relative sensitivity coefficient with respect to frequency is close to -1. The sensitivity coefficients due to the sound speed are similar to those for the frequency, but with opposite sign.

The low amplitude solution is not sensitive to density. This is in agreement with the analytical solution of the linearized parabolic equation (Equations (3.5) and (3.6)), where ρ_0 does not appear.

High amplitude

The dependence of the axial fundamental sound pressure amplitude on source radius, frequency, source amplitude, and sound speed, is weakened by nonlinear attenuation.

The pressure amplitude for the source condition p_0 and the nonlinearity coefficient β appear together as a product in the normalized KZK equation (2.60). Its solution is multiplied with $p_0/2^{1/2}$ to obtain the simulated effective sound pressure p_{sim} . The relative sensitivity coefficients $s(p_0)$ due to p_0 and $s(\beta)$ due to β , are thus connected through the relation $s(p_0) = 1 + s(\beta)$. The density ρ_0 appears inverted in the same expression as p_0 and β , yielding a sensitivity coefficient that is equal in magnitude but with opposite sign to that due to β .

The pressure amplitude of the second harmonic frequency component is somewhat more sensitive than that of the fundamental to perturbations in most of the parameters. This yields a greater uncertainty for the simulated second harmonic component than for the fundamental (Table 3.11).

Contribution to the combined simulation uncertainty

Table 3.11 shows an estimate of the relative standard uncertainty E_{param} due to uncertainties in the physical input parameters for simulations of nonlinear sound propagation with 200 kHz fundamental frequency. Comparison of Tables 3.7–3.10 indicates that similar results apply to the 120 kHz case. In order to obtain a conservative uncertainty estimate, the relative sensitivity coefficients with the greatest absolute values in Tables 3.7–3.10 have been chosen for the calculation. The standard uncertainties correspond approximately to fresh water with temperature $(21 \pm 1)^\circ\text{C}$.

The standard uncertainties in the uniform piston source radius a and source condition pressure amplitude p_0 in Table 3.11 are based on the measurements presented in Chapter 5. The uncertainty with which p_0 is determined is clearly the predominant contributor to E_{param} . The uncertainty in the source radius is also important.

Greater variability and hence uncertainties must be expected in the acoustic medium parameters for seawater. The differences in the sensitivity coefficients indicate that the properties of the sound source should still be expected to dominate the estimate for E_{param} .

Table 3.7. Relative sensitivity coefficients calculated from 10% perturbation in parameters of the sound source and propagation medium. 120 kHz, fresh water, axial field.

| parameter q_m | centre value | relative sensitivity coefficient $s(q_m)$ | | | | |
|-----------------------|--------------|---|------------|--------------------|------------|--------|
| | | 2 m < z < 10 m | | 50 m < z < 190 m | | |
| | | $I_{a,1}$ | $I'_{a,1}$ | $I_{a,2}$ | $I'_{a,2}$ | |
| low amplitude | | | | | | |
| source radius | a | 52.8 mm | +2.0 | - | +2.0 | - |
| frequency | f | 121.212 kHz | +0.98 | - | +0.91 | - |
| pressure amp. | p_0 | 1 Pa | +1.0 | - | +1.0 | - |
| sound speed | c_0 | 1485 m/s | -1.0 | - | -1.0 | - |
| absorption coeff. | α_2 | $2.5 \cdot 10^{-14}$ Np/m Hz ² | -0.0018 | - | -0.038 | - |
| density | ρ_0 | 1000 kg/m ³ | 0.0 | - | 0.0 | - |
| nonlinearity coeff. | β | 3.50 | 0.0 | - | 0.0 | - |
| high amplitude | | | | | | |
| source radius | a | 52.8 mm | +1.8 | +2.9 | +1.3 | +1.8 |
| frequency | f | 121.212 kHz | +0.78 | +2.1 | +0.18 | +0.62 |
| pressure amp. | p_0 | 426 kPa | +0.88 | +1.7 | +0.57 | +0.88 |
| sound speed | c_0 | 1485 m/s | -0.48 | -3.1 | +0.62 | -0.52 |
| absorption coeff. | α_2 | $2.5 \cdot 10^{-14}$ Np/m Hz ² | -0.0016 | -0.0055 | -0.024 | -0.084 |
| density | ρ_0 | 1000 kg/m ³ | +0.12 | -0.65 | +0.43 | +0.13 |
| nonlinearity coeff. | β | 3.50 | -0.12 | +0.66 | -0.43 | -0.12 |

Table 3.8. Relative sensitivity coefficients calculated from 10% perturbations in parameters of the sound source and propagation medium. 120 kHz, fresh water, indicator values off axis.

| parameter q_m | centre value | relative sensitivity coefficient $s(q_m)$ | | | | |
|-----------------------|--------------|---|------------|-------------|------------|-------|
| | | $z = 9.8$ m | | $z = 200$ m | | |
| | | $I_{b,1}$ | $I'_{b,1}$ | $I_{b,2}$ | $I'_{b,2}$ | |
| low amplitude | | | | | | |
| source radius | a | 52.8 mm | +0.10 | - | +0.10 | - |
| frequency | f | 121.212 kHz | -0.85 | - | -0.97 | - |
| pressure amp. | p_0 | 1 Pa | +1.0 | - | +1.0 | - |
| sound speed | c_0 | 1485 m/s | +0.92 | - | +0.92 | - |
| absorption coeff. | α_2 | $2.5 \cdot 10^{-14}$ Np/m Hz ² | -0.0036 | - | -0.074 | - |
| density | ρ_0 | 1000 kg/m ³ | 0.0 | - | 0.0 | - |
| nonlinearity coeff. | β | 3.50 | 0.0 | - | 0.0 | - |
| high amplitude | | | | | | |
| source radius | a | 52.8 mm | +0.19 | -1.1 | -0.48 | -0.33 |
| frequency | f | 121.212 kHz | -0.85 | -1.7 | -0.97 | -1.7 |
| pressure amp. | p_0 | 426 kPa | +0.97 | +2.0 | +0.89 | +1.8 |
| sound speed | c_0 | 1485 m/s | +0.95 | +0.081 | +1.1 | -0.17 |
| absorption coeff. | α_2 | $2.5 \cdot 10^{-14}$ Np/m Hz ² | -0.0035 | -0.012 | -0.070 | -0.25 |
| density | ρ_0 | 1000 kg/m ³ | +0.032 | -0.96 | +0.10 | -0.75 |
| nonlinearity coeff. | β | 3.50 | -0.032 | +0.96 | -0.11 | +0.75 |

Table 3.9. Relative sensitivity coefficients calculated from 10% perturbations in parameters of the sound source and propagation medium. 200 kHz, fresh water, axial field.

| parameter q_m | centre value | relative sensitivity coefficient $s(q_m)$ | | | | |
|-----------------------|--------------|---|------------|--------------------|------------|-------|
| | | 2 m < z < 10 m | | 50 m < z < 190 m | | |
| | | $I_{a,1}$ | $I'_{a,1}$ | $I_{a,2}$ | $I'_{a,2}$ | |
| low amplitude | | | | | | |
| source radius | a | 32.5 mm | +2.0 | - | +2.0 | - |
| frequency | f | 200.000 kHz | +0.99 | - | +0.99 | - |
| pressure amp. | p_0 | 1 Pa | +1.0 | - | +1.0 | - |
| sound speed | c_0 | 1485 m/s | -1.0 | - | -1.0 | - |
| absorption coeff. | α_2 | $2.5 \cdot 10^{-14}$ Np/m Hz ² | -0.0050 | - | -0.10 | - |
| density | ρ_0 | 1000 kg/m ³ | 0.0 | - | 0.0 | - |
| nonlinearity coeff. | β | 3.50 | 0.0 | - | 0.0 | - |
| high amplitude | | | | | | |
| source radius | a | 32.5 mm | +1.3 | +1.56 | +0.81 | +0.92 |
| frequency | f | 200.000 kHz | +0.15 | +0.46 | -0.41 | -0.60 |
| pressure amp. | p_0 | 820 kPa | +0.49 | +0.69 | +0.27 | +0.33 |
| sound speed | c_0 | 1485 m/s | +0.93 | +0.25 | +1.7 | +1.8 |
| absorption coeff. | α_2 | $2.5 \cdot 10^{-14}$ Np/m Hz ² | +0.0013 | -0.010 | -0.050 | -0.20 |
| density | ρ_0 | 1000 kg/m ³ | +0.51 | +0.32 | +0.73 | +0.67 |
| nonlinearity coeff. | β | 3.50 | -0.51 | -0.31 | -0.73 | -0.67 |

Table 3.10. Relative sensitivity coefficients calculated from 10% perturbations in parameters of the sound source and propagation medium. 200 kHz, fresh water, indicator values off axis.

| parameter q_m | | centre value | relative sensitivity coefficient $s(q_m)$ | | | |
|-----------------------|------------|---|---|------------|-------------|------------|
| | | | $z = 9.8$ m | | $z = 200$ m | |
| | | | $I_{b,1}$ | $I'_{b,1}$ | $I_{b,2}$ | $I'_{b,2}$ |
| low amplitude | | | | | | |
| source radius | a | 32.5 mm | +0.014 | - | +0.014 | - |
| frequency | f | 200.000 kHz | -0.98 | - | -1.4 | - |
| pressure amp. | p_0 | 1 Pa | +1.0 | - | +1.0 | - |
| sound speed | c_0 | 1485 m/s | +1.0 | - | +1.0 | - |
| absorption coeff. | α_2 | $2.5 \cdot 10^{-14}$ Np/m Hz ² | -0.0098 | - | -0.20 | - |
| density | ρ_0 | 1000 kg/m ³ | 0.0 | - | 0.0 | - |
| nonlinearity coeff. | β | 3.50 | 0.0 | - | 0.0 | - |
| high amplitude | | | | | | |
| source radius | a | 32.5 mm | +0.14 | -0.68 | +0.15 | -0.19 |
| frequency | f | 200.000 kHz | -0.90 | -1.5 | -1.2 | -2.3 |
| pressure amp. | p_0 | 820 kPa | +0.80 | +1.6 | +0.60 | +1.1 |
| sound speed | c_0 | 1485 m/s | +1.3 | +0.45 | +1.7 | +0.96 |
| absorption coeff. | α_2 | $2.5 \cdot 10^{-14}$ Np/m Hz ² | -0.0085 | -0.029 | -0.17 | -0.62 |
| density | ρ_0 | 1000 kg/m ³ | +0.21 | -0.58 | +0.41 | -0.083 |
| nonlinearity coeff. | β | 3.50 | -0.20 | +0.59 | -0.40 | +0.096 |

Table 3.11. Relative simulation uncertainty contribution E_{param} due to the physical input parameters.

| parameter q_m | | value | rel. standard uncertainty $E(q_m)$ | rel. sensitivity coefficient $ s(q_m) $ | rel. standard uncertainty contribution squared |
|---|------------|---|------------------------------------|---|--|
| axial field ($I_{a,1}, I_{a,2}$), fundamental frequency component | | | | | |
| source radius | a | 32.5 mm | 0.003 | 1.5 | $2.0 \cdot 10^{-5}$ |
| frequency | f | 200.000 kHz | 0.0001 | 0.4 | $1.6 \cdot 10^{-9}$ |
| pressure amp. | p_0 | 820 kPa | 0.033 | 0.6 | $3.9 \cdot 10^{-4}$ |
| sound speed | c_0 | 1485 m/s | 0.002 | 1 | $4.0 \cdot 10^{-6}$ |
| absorption coeff. | α_2 | $2.5 \cdot 10^{-14}$ Np/m Hz ² | 0.1 | 0.02 | $4.0 \cdot 10^{-6}$ |
| density | ρ_0 | 1000 kg/m ³ | 0.0002 | 0.5 | $1.0 \cdot 10^{-8}$ |
| nonlinearity coeff. | β | 3.50 | 0.006 | 0.5 | $9.0 \cdot 10^{-6}$ |
| sum of squared uncertainty contributions | | | | | $4.3 \cdot 10^{-4}$ |
| relative standard uncertainty E_{param} due to physical parameters | | | | | 0.021 |
| relative standard uncertainty in decibels | | | | | 0.2 dB |
| axial field ($I_{a,1}, I_{a,2}$), second harmonic frequency component | | | | | |
| source radius | a | 32.5 mm | 0.003 | 2 | $3.6 \cdot 10^{-5}$ |
| frequency | f | 200.000 kHz | 0.0001 | 1 | $1.0 \cdot 10^{-8}$ |
| pressure amp. | p_0 | 820 kPa | 0.033 | 1.5 | $1.1 \cdot 10^{-3}$ |
| sound speed | c_0 | 1485 m/s | 0.002 | 2 | $1.6 \cdot 10^{-5}$ |
| absorption coeff. | α_2 | $2.5 \cdot 10^{-14}$ Np/m Hz ² | 0.1 | 0.5 | $1.0 \cdot 10^{-4}$ |
| density | ρ_0 | 1000 kg/m ³ | 0.0002 | 0.5 | $1.0 \cdot 10^{-8}$ |
| nonlinearity coeff. | β | 3.50 | 0.006 | 0.5 | $9.0 \cdot 10^{-6}$ |
| sum of relative variances | | | | | 0.0050 |
| relative standard uncertainty E_{param} due to physical parameters | | | | | 0.071 |
| relative standard uncertainty in decibels | | | | | 0.6 dB |

| off axis ($I_{b,1}$, $I_{b,2}$), fundamental frequency component | | | | | |
|---|------------|---|--------|------|---------------------|
| source radius | a | 32.5 mm | 0.003 | 0.2 | $3.6 \cdot 10^{-7}$ |
| frequency | f | 200.000 kHz | 0.0001 | 1 | $1.0 \cdot 10^{-8}$ |
| pressure amp. | p_0 | 820 kPa | 0.033 | 1 | $1.1 \cdot 10^{-3}$ |
| sound speed | c_0 | 1485 m/s | 0.002 | 1 | $4.0 \cdot 10^{-6}$ |
| absorption coeff. | α_2 | $2.5 \cdot 10^{-14}$ Np/m Hz ² | 0.1 | 0.06 | $3.6 \cdot 10^{-5}$ |
| density | ρ_0 | 1000 kg/m ³ | 0.0002 | 0.2 | $1.6 \cdot 10^{-9}$ |
| nonlinearity coeff. | β | 3.50 | 0.006 | 0.2 | $1.4 \cdot 10^{-6}$ |
| sum of squared uncertainty contributions | | | | | 0.0011 |
| relative standard uncertainty E_{param} due to physical parameters | | | | | 0.034 |
| relative standard uncertainty in decibels | | | | | 0.3 dB |
| off axis ($I_{b,1}$, $I_{b,2}$), second harmonic frequency component | | | | | |
| source radius | a | 32.5 mm | 0.003 | 0.6 | $3.2 \cdot 10^{-6}$ |
| frequency | f | 200.000 kHz | 0.0001 | 2 | $4.0 \cdot 10^{-8}$ |
| pressure amp. | p_0 | 820 kPa | 0.033 | 1.6 | $2.8 \cdot 10^{-3}$ |
| sound speed | c_0 | 1485 m/s | 0.002 | 1 | $4.0 \cdot 10^{-6}$ |
| absorption coeff. | α_2 | $2.5 \cdot 10^{-14}$ Np/m Hz ² | 0.1 | 0.5 | $2.5 \cdot 10^{-3}$ |
| density | ρ_0 | 1000 kg/m ³ | 0.0002 | 0.6 | $1.4 \cdot 10^{-8}$ |
| nonlinearity coeff. | β | 3.50 | 0.006 | 0.6 | $1.3 \cdot 10^{-5}$ |
| sum of relative variances | | | | | 0.0053 |
| relative standard uncertainty E_{param} due to physical parameters | | | | | 0.073 |
| relative standard uncertainty in decibels | | | | | 0.6 dB |

3.4. Combined simulation uncertainty

The estimated uncertainty contributions for simulations of finite amplitude sound propagation are summarized in Table 3.12. The idealized uniform piston representation of the sound source, which is assumed an important error contributor, has not been accounted for here. The importance of the source condition is investigated to some extent in Chapter 4. The square frequency power law used here for absorption does not apply well to seawater. This is discussed further in Chapter 6.

Adequate reference solutions are not found for finite amplitude sound propagation. The uncertainty estimate has therefore been extrapolated from the linear case by means of sensitivity analyses. As also some error sources are unaccounted for, the uncertainty estimate in Table 3.12 should not be used without careful consideration of the underlying assumptions and which factors have been taken into consideration (cf. Table 3.1).

The relative uncertainty contribution E_{param} related to the physical input parameters dominates the uncertainty estimate.

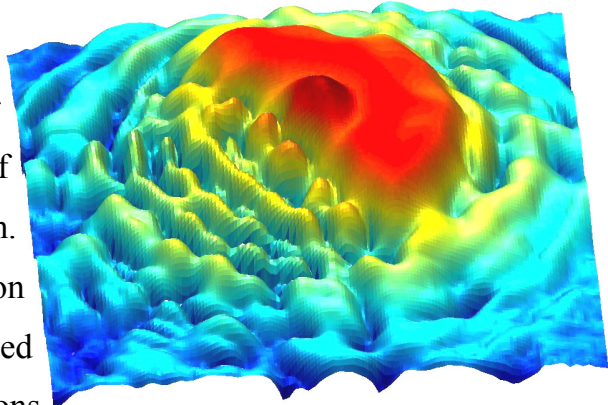
Table 3.12. Estimate of the combined relative standard uncertainty $E(p_{\text{sim}})$ for the simulations of nonlinear sound propagation.

| on axis | | fundamental frequency component | | second harmonic component | |
|--|--------------------|---------------------------------|---------------------|-------------------------------|---------------------|
| | | relative standard uncertainty | relative variance | relative standard uncertainty | relative variance |
| model uncertainty | E_{model} | 0.0001 | $1.3 \cdot 10^{-8}$ | 0.0001 | $1.3 \cdot 10^{-8}$ |
| numerical algorithm | E_{num} | 0.005 | $2.1 \cdot 10^{-5}$ | 0.005 | $2.1 \cdot 10^{-5}$ |
| parameter uncertainties | E_{param} | 0.021 | $4.3 \cdot 10^{-4}$ | 0.071 | $5.0 \cdot 10^{-3}$ |
| sum of relative variances | | | $4.5 \cdot 10^{-4}$ | | $5.0 \cdot 10^{-3}$ |
| relative combined standard uncertainty $E(p_{\text{sim}})$ | | | 0.021 | | 0.071 |
| relative combined standard uncertainty in dB | | | 0.2 dB | | 0.6 dB |

| off axis | | fundamental frequency component | | second harmonic component | |
|--|--------------------|---------------------------------|---------------------|-------------------------------|---------------------|
| | | relative standard uncertainty | relative variance | relative standard uncertainty | relative variance |
| model uncertainty | E_{model} | 0.001 | $1.3 \cdot 10^{-6}$ | 0.001 | $1.4 \cdot 10^{-6}$ |
| numerical algorithm | E_{num} | 0.005 | $2.1 \cdot 10^{-5}$ | 0.007 | $4.8 \cdot 10^{-5}$ |
| parameter uncertainties | E_{param} | 0.034 | $1.1 \cdot 10^{-3}$ | 0.073 | $5.3 \cdot 10^{-3}$ |
| sum of relative variances | | | $1.1 \cdot 10^{-3}$ | | $5.3 \cdot 10^{-3}$ |
| relative combined standard uncertainty $E(p_{\text{sim}})$ | | | 0.034 | | 0.073 |
| relative combined standard uncertainty in dB | | | 0.3 dB | | 0.6 dB |

Chapter 4. Near field measurements

The sound field radiated by a uniformly vibrating, plane, circular piston in an infinitely stiff baffle of infinite extent is a classical problem. The uniform piston source condition used in Chapter 3 is therefore well suited for comparing Bergen Code simulations



with other theoretical results. It is also a convenient starting point for simulations when the details of the sound source's vibration pattern are not well known.

The Bergen Code version used in the present work requires an axisymmetric source condition specified in a plane. It allows shading of the amplitude and phase. The echo sounder transducers used as sound sources in the experiments have been designed to radiate an axisymmetric sound beam with weaker side lobes than for a uniform piston.

To be able to assess the applicability of the circular-piston source condition, a measurement set-up is designed for measuring the relative sound pressure amplitude and phase in a plane parallel to the face of three echo sounder transducers. Measurements are made approximately 2 mm from the face of each transducer. The degree of axisymmetry (rotational symmetry) of the measured near field is investigated. An attempt is made to provide axisymmetric source descriptions for Bergen Code simulations that correspond more closely to the experimental conditions than the uniform piston idealization. The results presented here give some information on the importance of the uncertainty contribution due to the uniform piston idealization.

Similar near field measurements have been described by Saito *et al.*²¹⁸, Ward *et al.*,²⁵⁹ and Humphrey *et al.*¹²⁵ Saito *et al.* used the measurement results to determine the primary velocity amplitude on the face of a focusing sound source. Humphrey *et al.*¹²⁵ compared sound pressure measurements in the near field with optical methods for characterization of sound sources. Ward *et al.*²⁵⁹ obtained a somewhat idealized source condition based on near field measurements, and used it in Bergen Code simulations. The author is not aware of published works where results from near field measurements have been applied directly as source conditions for the Bergen Code.

The experiment is described in Section 4.1, while the measurement results are presented in Section 4.2. In Section 4.3, source conditions for Bergen Code simulations are derived based on the measurement results. Some tests are made for linear sound propagation. The performance of simulations based on the near field measurement source conditions is examined further in Chapter 5.

4.1. Experiment

This section describes how the near field measurements were carried out. The experimental arrangement is described first, followed by an account of the processing of the measurement results.

4.1.1. Experimental arrangement

Near field measurements were made for three Simrad echo sounder transducers (Figure 4.1). Table 4.1 shows the transducer models, serial numbers, operating frequencies, and transmit voltage amplitudes used for the near field measurements. It is also indicated where the transducers are used for measurements of nonlinear sound propagation. The sound propagation measurements are described in Chapter 5 (measurement sets H1, H2, and H3) and Chapter 6 (E1 and E2).

Table 4.1. Echo sounder transducers used in near field measurements.

| transducer model | serial number | operating frequency | rms input voltage amplitude | nonlinearity measurement sets |
|---------------------|------------------|------------------------|--------------------------------|----------------------------------|
| ES120-7C | 230 | 121.212 kHz | 6.1 V | H2, E2 |
| ES200-7C | 120 | 200.000 kHz | 6.4 V | H3, E1 |
| ES200-7CD | 102 | 200.000 kHz | 4.8 V | H1 |

A fresh water tank with dimensions $2.5 \times 2.5 \times 2.5 \text{ m}^3$ was used, with the echo sounder transducer and hydrophone placed sufficiently far from the walls and water surface to keep echoes from interfering with the measurements. The water temperature was $(11 \pm 1)^\circ\text{C}$.

The three transducers are made for split-beam echo sounders. Their active elements are arranged in four quadrants that can be controlled separately. The quadrants were coupled in parallel and driven by an ENI 240L power amplifier (Figure 4.5). An Agilent 33120A function generator was used to generate 80-cycle sine bursts to be transmitted. The burst repetition rate was chosen such that a burst was not transmitted until all detected reverberation from the previous burst had died out.

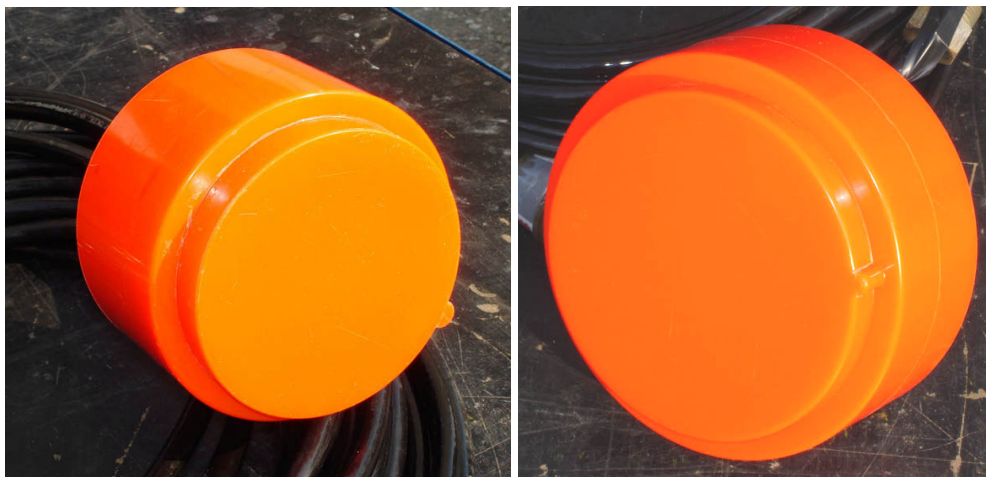


Figure 4.1. ES200-7C (left) and ES120-7C (right) echo sounder transducers. The ES200-7CD transducer looks equal to the ES200-7C.

Each transducer was mounted in a square aluminium plate with 240 mm sides (Figure 4.2). To enable mechanical alignment between the transducer face and

the axes of the two-carriage hydrophone positioning system (Figure 4.6), the transducers were mounted so that they protruded 1.0 mm from the aluminium plate. The intended forward direction when mounted on a vessel is marked on the echo sounder transducer. The transducers were mounted with the forward direction pointing upwards, i.e., in the positive x direction (Figure 4.6). The starboard direction then coincides with the positive y direction.

Test measurements were made to determine whether the presence of the mounting plate had any influence on the radiated far field. As an alternative to the described flush mounting, the transducers were fastened to another plate by screw holes on their back. No difference was measured in the radiation patterns at 1.5 m distance.

A Precision Acoustics PVDF needle hydrophone with 1-mm-diameter active area and integrated preamplifier was mounted as shown in Figures 4.2–4.6. Some trials were carried out to investigate the possibility of standing waves between the sound source and the hydrophone,¹²⁷ but evidence of such problems was not observed. The diameter of the hydrophone needle is much smaller than one wavelength, and its presence is assumed to have negligible influence on the measured sound pressure. Also, it is assumed that the probe is omnidirectional for the frequencies used here, and that the active area of the hydrophone is too small to impose significant spatial averaging on the measurement result.^{28,116}

A Cartesian coordinate system is defined with its origin at the centre of the face of the echo sounder transducer (Figure 2.1). The z axis is parallel with the radiated sound beam. Two linear stages of type PI M521.DG and PI M535.22 with 1 μm specified resolution^{4,5} were used to position the hydrophone in the x and y directions, respectively (Figures 4.2 and 4.6). The positioning system, oscilloscope, and function generator were controlled with a personal computer, which also stored the measured waveforms. The hydrophone was moved in steps of 2.0 mm and 2.5 mm for the 200 kHz and 120 kHz measurements,

respectively. The chosen step lengths were smaller than one-half wavelength, $\lambda/2 = 3.6$ mm for 200 kHz and 6.0 mm for 120 kHz.

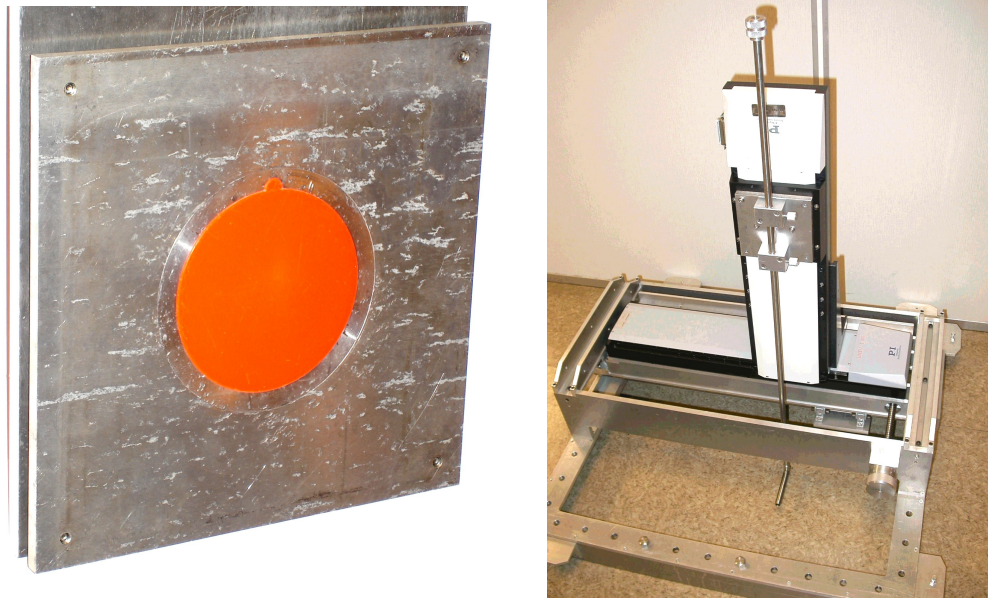


Figure 4.2. Left: Flush mounted ES200-7C echo sounder transducer. Right: Linear translation stages used for two-dimensional positioning of the hydrophone in a plane parallel to the transducer's face. The horizontal hydrophone mounting tube is seen at the bottom of the vertical tube.



Figure 4.3. Needle hydrophone in horizontal mounting tube.

Measurements were made throughout a rectangular area, following a path such as illustrated in Figure 4.6. The size of the covered area should be such that the sound pressure amplitude at its edges is insignificant.¹²⁵ In the present work, the sound pressure amplitudes along the edges were accepted as sufficiently low if they were at least 30 dB below the strongest measured signal.

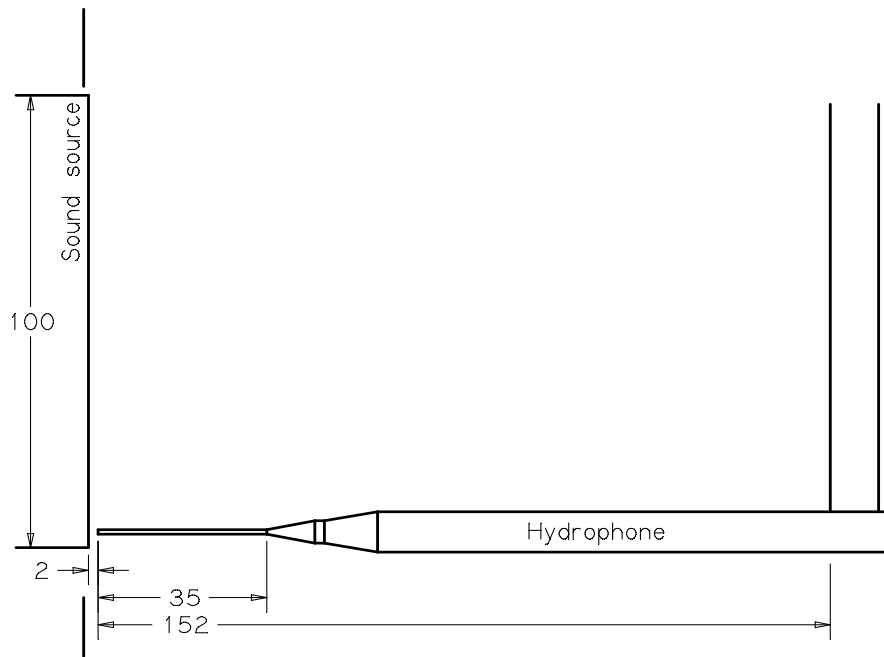


Figure 4.4. Dimensions (in millimetres) of the hydrophone assembly in front of a 200 kHz sound source.

The signal received by the hydrophone was amplified by its integral amplifier and then further with a Reson VP1000 voltage preamplifier, before it was digitized with a LeCroy 9361 digital sampling oscilloscope (Figure 4.5). $50\ \Omega$ terminators were used at the far ends of both the cables connected to preamplifier outputs. The synchronization signal from the function generator was used to trigger the oscilloscope. In order to utilize the 8 bits of resolution optimally, the first few measured bursts for each hydrophone position were used to adjust the oscilloscope's voltage range. The average of 80 sweeps was then transferred to the computer, effectively yielding approximately 11 bits of resolution.⁸ The full waveform was stored together with relative position from the translation stages.

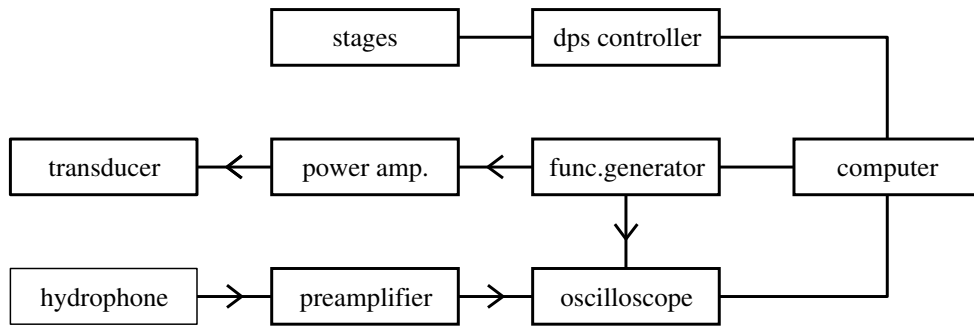


Figure 4.5. Diagram of instruments and signal and control flow.

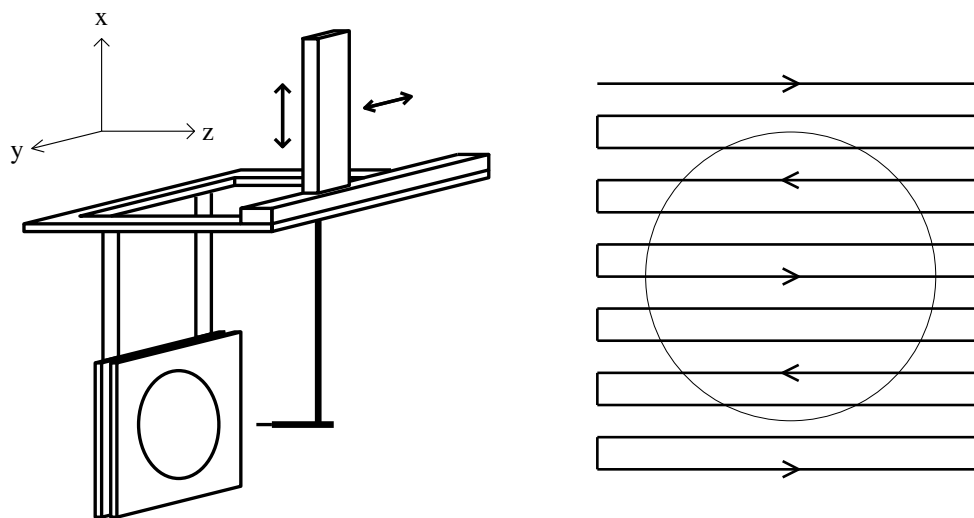


Figure 4.6. Principle sketch of the positioning system (left) and the path followed by the hydrophone across the transducer surface (right). Figure 4.4 shows the distance between the echo sounder transducer and the hydrophone more correctly.

4.1.2. Signal processing

Time window

The first signal arrival at the hydrophone originates from the nearest part of the echo sounder transducer's active area. To obtain a measurement that corresponds to a continuous transmitted wave, it is necessary to wait until all contributions from the surface of the transducer have arrived and reached steady state.

With the hydrophone position (x,y,z) is meant the position of its needle tip. The distance between the hydrophone and the symmetry axis of the echo sounder transducer is

$$r_n = \sqrt{x^2 + y^2} . \quad (4.1)$$

The earliest accepted start time $t_0 = t_0(x,y)$ for steady-state measurements is

$$t_0(x,y) = t_{0,axis} + \frac{1}{c_0} \left[d_{max}(x,y) - \sqrt{a_f^2 + z^2} \right], \quad (4.2)$$

where $t_{0,axis}$ is the time when the signal measured on the z axis has reached steady state. $t_{0,axis}$ is chosen by inspection of the received wave form when $r_n = 0$. $d_{max}(x,y) = \{[a_f + r_n(x,y)]^2 + z^2\}^{1/2}$ is the distance between the hydrophone and the farthest point on the face of the echo sounder transducer, of which the radius is a_f . Due to the spatial resolution of the measurement grid, the maximum error in r_n is approximately 1.8 mm for the ES120-7C transducer and 1.4 mm for the 200 kHz transducers.

The hydrophone mount consists of a horizontal steel tube machined to minimize reflections (Figure 4.3). A vertical tube connects the hydrophone to the translation stages, and is the source of the first significant echo that may interfere with the direct signal from the echo sounder transducer. The time of arrival for this echo is quite insensitive to the hydrophone position. The time window for measurements is ended at its lower bound t_{end} , which, if the sound transmission starts at $t = 0$, is

$$t_{end} = \frac{z + 2l_{mount}}{c_0} . \quad (4.3)$$

$l_{mount} = 152$ mm is the distance from the tip of the hydrophone needle to the vertical tube (Figure 4.4). The distance z between the plane of the transducer face and the hydrophone is approximately 2 mm. With a measured temperature of $(11 \pm 1)^\circ\text{C}$, the sound speed is calculated to $c_0 = (1451 \pm 4)$ m/s,⁵⁰ which

yields $t_{\text{end}} = (210.9 \pm 0.6) \mu\text{s}$ (Table 4.2 and Figure 4.7). Some backscatter from the hydrophone and preamplifier bodies is seen between t_0 and t_{end} , with maximum amplitude 25 dB below the direct signal.

Figure 4.7 shows two acquired waveforms. The section of the received burst that falls between t_0 and t_{end} is coloured red. The first plot (Figure 4.7a) shows a waveform obtained with the hydrophone at the centre of the sound source. The figure is representative of the signals that are stronger than approximately -25 dB relative to the amplitude measured at the centre of the sound source. The waveform shown in Figure 4.7b is obtained with the hydrophone in the corner of the covered rectangle, i.e. with the maximum distance to the sound source. Although the signal seems to have disappeared in noise, the region within the calculated time window is processed the same way as where the signal is clearly visible.

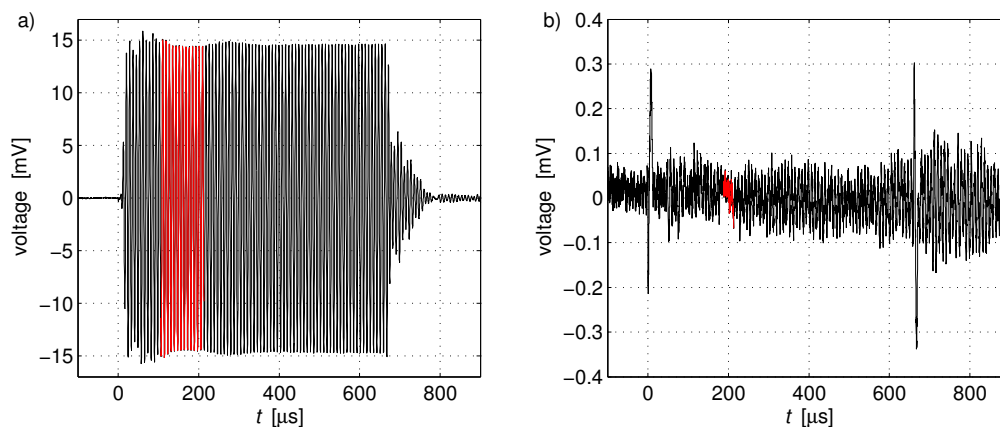


Figure 4.7. Examples of measured wave forms. The part of each measurement that corresponds to steady-state, free field conditions is marked in red. a) Measurement made at the centre of the sound source. b) Measurement made in the corner of the sampled region, at maximum distance from the sound source.

Table 4.2. Time windows for near field measurements with the hydrophone at the centre ($r_n = 0$) and the edge ($r_n = a_f$) of the echo sounder transducer face. The minimum time window length is used where the distance from the symmetry axis is at its maximum.

| transducer | outer radius a_f [mm] | wavelength λ [mm] | periods within time window $(t_{\text{end}} - t_0):f$ | | |
|------------|----------------------------|------------------------------|--|------|---------|
| | | | centre | edge | minimum |
| ES120-7C | 76.0 | 11.94 ± 0.03 | 13 | 6 | 3 |
| ES200-7C | 50.0 | 7.26 ± 0.02 | 26 | 19 | 15 |
| ES200-7CD | 50.0 | 7.26 ± 0.02 | 26 | 19 | 15 |

Fourier transformation

The relative amplitude and phase of each received signal $U(t)$ is extracted from its discrete Fourier transform. Before transformation, the signal is interpolated linearly and resampled so that the sampling rate becomes an integer multiple of the carrier frequency. The greatest integral number of periods between t_0 and t_{end} (Table 4.2) is submitted to discrete Fourier transformation,

$$\hat{U}(f_m) = \hat{U}\left(\frac{m}{N\Delta t}\right) = \frac{1}{N} \sum_{l=0}^{N-1} U(l\Delta t) e^{-j\frac{2\pi lm}{N}}, \quad m = 0, 1, 2, \dots, N-1. \quad (4.4)$$

Δt is the sampling interval. The $\hat{U}(f)$ that corresponds to the carrier frequency is taken from the Fourier spectrum. The same relative results are found with and without multiplying the time signal with the “flattop” window function implemented in Matlab.

Phase compensation

Misalignment between the transducer face and the xy plane of the positioning system could introduce a false asymmetry in the measured phase. The mean values of the phase measured within four rectangles as indicated in Figure 4.8 are calculated. A linear function is added to the phase so that each pair of mean values along the x and y axes, respectively, become equal. The average phase

measurements indicate that the physical alignment between the transducer face and the xy plane is within 0.1° for the 120 kHz transducer and 0.5° for the 200 kHz transducers. Possible deviations between the mechanical and acoustical (phase) symmetry axes of the echo sounder transducers contribute to this angle.

Humphrey *et al.*¹²⁵ point out that the need for phase stability puts stringent requirements on temperature variations during the measurements. The temperature changed less than 0.15° in their case, which did not seem significant. During the measurements presented here, the temperature was not monitored with the same accuracy. Each measurement took approximately 24 hours and the temperature at the end of each measurement was within one degree of the temperature at the start. The measured phase seems axisymmetric. No particular systematic variation is seen with the vertical (x) coordinate, in which direction the hydrophone movement was the slowest (Figure 4.6).

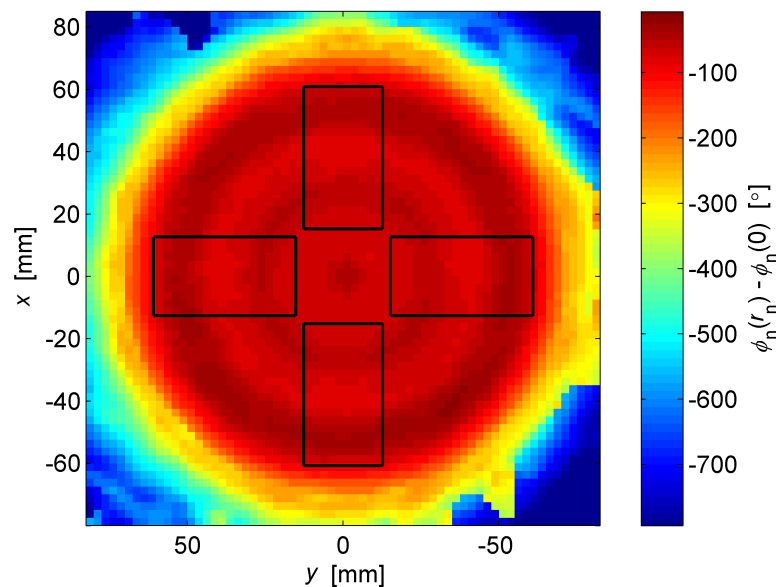


Figure 4.8. Regions for averaging of the measured phase, used to compensate for misalignment between the echo sounder transducer and the hydrophone positioning system.

4.2. Measurement results

The complex pressure amplitude p_n of a measured signal $p_n e^{j\omega t}$ can be expressed through its absolute value and phase,

$$p_n(x, y) = |p_n(x, y)| \cdot e^{j\phi_n(x, y)}. \quad (4.5)$$

Figures 4.9–4.17 show the measured values of $|p_n(x, y)|$ and $\phi_n(x, y)$ relative to those obtained in the point closest to the centre of the sound source. Bilinear interpolation has been used to double the number of data points in each direction for the pseudocolour and surface plots. A phase plot without such smoothing is shown in Figure 4.8. Figures 4.10, 4.13, and 4.16 show all the acquired measurement points (green dots) as function of the distance r_n from the centre of the sound source.

The measurement results obtained along the eight radial paths marked with dashed lines in the pseudo-colour plots (Figures 4.9, 4.12, and 4.15), are indicated with dotted black curves in Figures 4.10, 4.13, and 4.16. The solid black curves represent mean values of the eight traces, and the error bars indicate the standard deviation between them. The agreement between the r_n dependence of amplitude and phase in different directions from the centre provide an indication of the degree of axisymmetry in the measured field. When the amplitude is 20 dB below the value measured at $r_n = 0$, the amplitude and phase standard deviations are as shown in Table 4.3.

Table 4.3. Distance r_n from the centre and standard deviations for the absolute value and phase of $p_n(x, y)$ when the measured sound pressure amplitude is 20 dB below that at the centre of the source.

| transducer | $r_n(-20 \text{ dB})$ | amplitude relative standard deviation | phase standard deviation | figure |
|------------|-----------------------|---------------------------------------|--------------------------|--------|
| ES120-7C | 65 mm | 1.9 dB | 22° | 4.10 |
| ES200-7C | 44 mm | 3.8 dB | 14° | 4.13 |
| ES200-7CD | 47 mm | 1.3 dB | 17° | 4.16 |

The measured amplitude and phase vary slowly with distance from the centre. While the amplitude decreases almost monotonically with r_n in a large part of the covered area, the phase is more constant within the radius of the transducer face. Sharp phase peaks are seen along the edge of the transducers. Outside this area, the phase decreases approximately as $-kr_n$, where k is the wave number. Evidence of some difficulty in extracting the phase from the weakest signals is seen in the outer parts of the measurement areas.

Some systematic departure from axisymmetry is seen in the measurements for the ES120-7C and ES200-7CD transducers, particularly in the phase (Figures 4.9b and 4.15b). The measured phase is slightly greater near the diagonals than near the horizontal and vertical lines through the origin.

The ES200-7CD transducer seems to have a small defect close to the forward edge of its active element (Figures 4.15). A small area with reduced sound pressure amplitude is seen around $(x,y) = (33 \text{ mm}, -7 \text{ mm})$ in Figure 4.15a. The feature can also be seen in the phase (Figure 4.15b).

The measured irregularities are not expected to be of great importance for the far field. Moreover, the departures from axisymmetry are not the same for the two 200 kHz echo sounders. It is concluded that the assumption of an axisymmetric geometry should be adequate for numerical simulations of the radiated sound field.

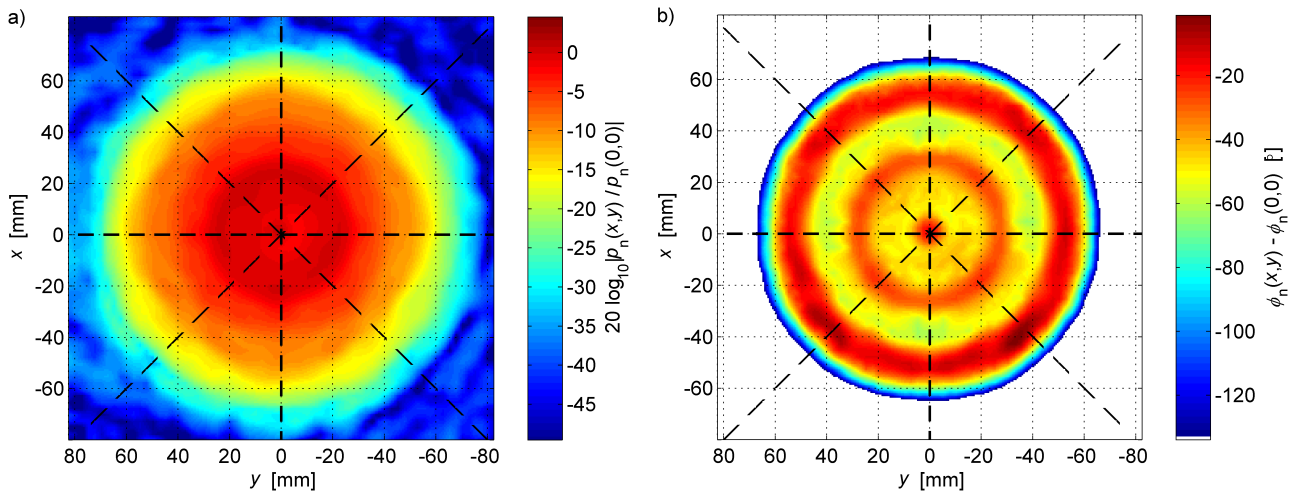


Figure 4.9. a) Relative sound pressure level, and b) relative phase in a plane parallel to the face of the ES120-7C echo sounder transducer. The black dashed lines show the eight paths used for extraction of one-dimensional amplitude and phase data.

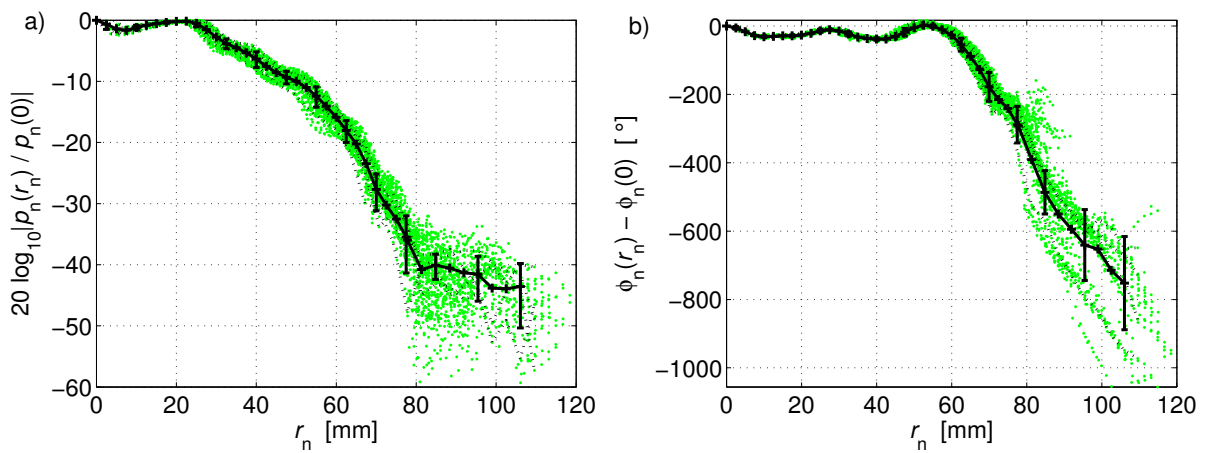


Figure 4.10. One-dimensional amplitude (a) and phase measurements (b) for the ES120-7C transducer. Results from all the measurement points are marked in green. The black curve and error bars show mean value and standard deviations calculated from the values along the eight radial paths marked in Figure 4.9.

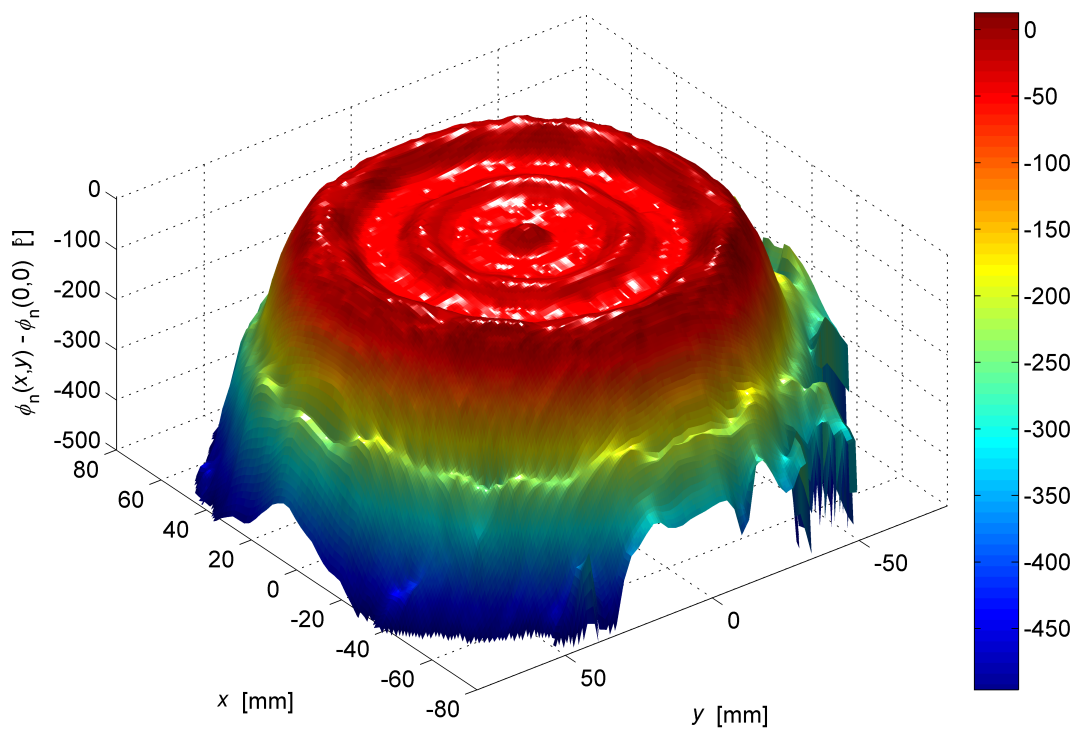
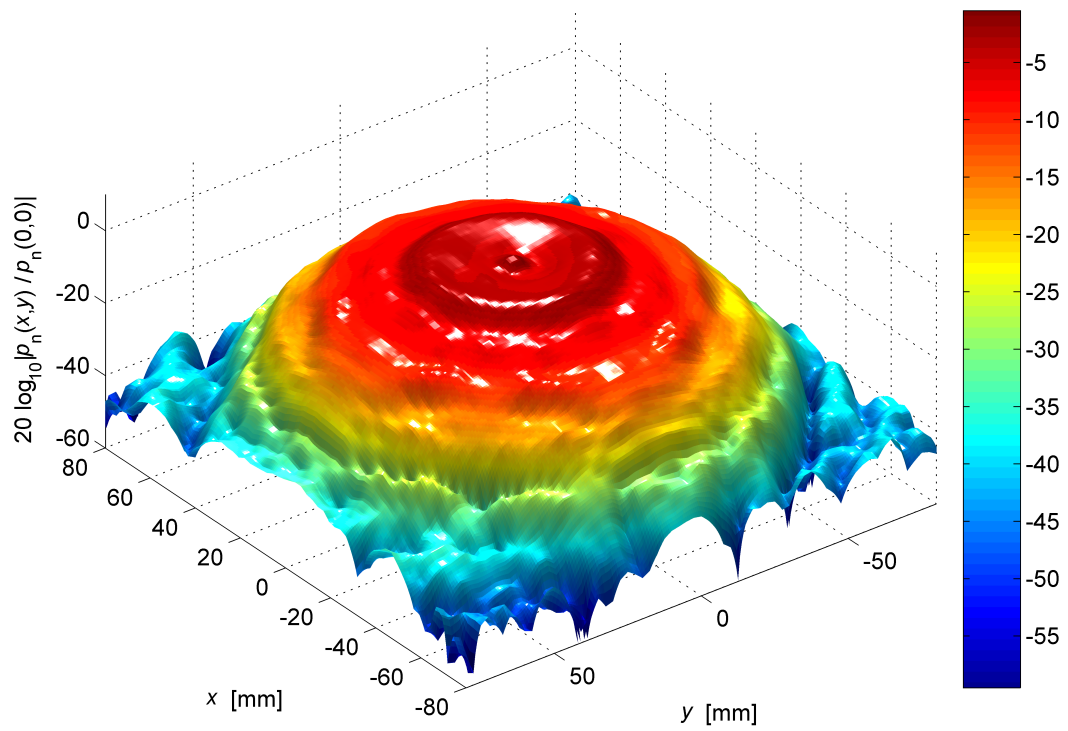


Figure 4.11. Alternative presentation of the amplitude (top) and phase (bottom) measurement results for the ES120-7C transducer, shown in Figure 4.9.

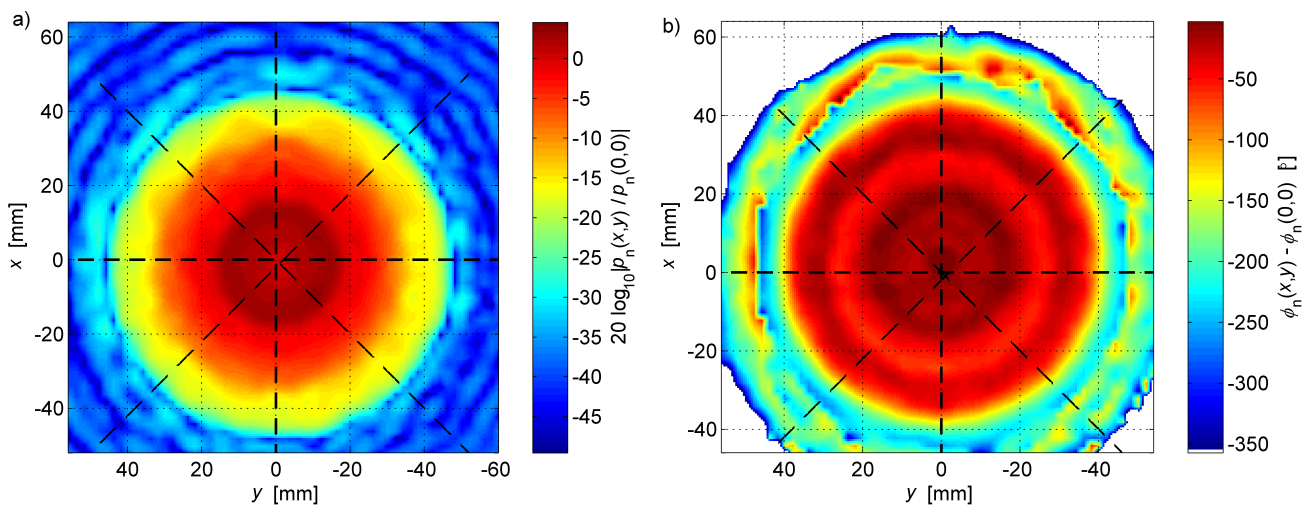


Figure 4.12. a) Relative sound pressure level, and b) relative phase in a plane parallel to the face of the ES200-7C echo sounder transducer. The black dashed lines show the eight paths used for extraction of one-dimensional amplitude and phase data.

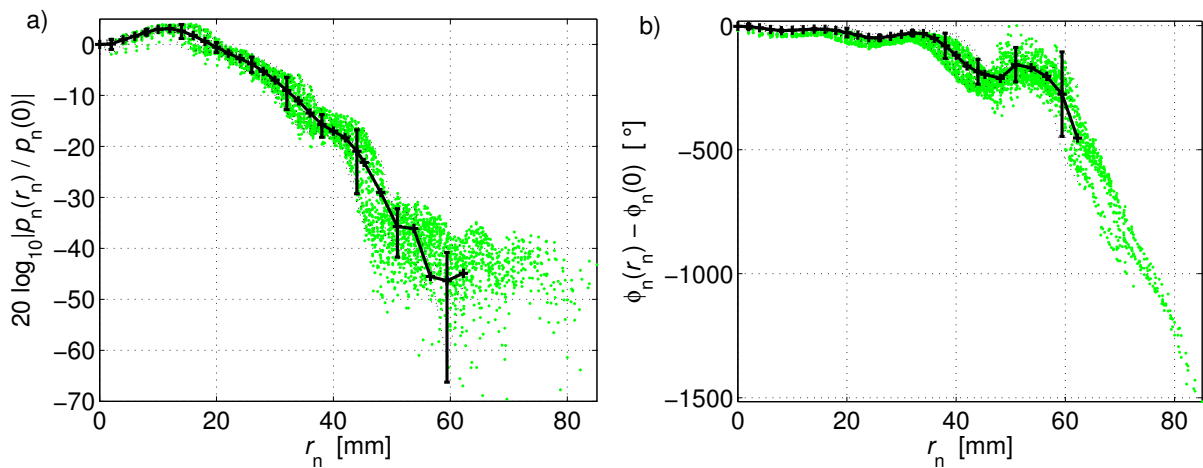


Figure 4.13. One-dimensional amplitude (a) and phase measurements (b) for the ES200-7C transducer. Results from all the measurement points are marked in green. The black curve and error bars show mean value and standard deviations calculated from the values along the eight radial paths marked in Figure 4.12.

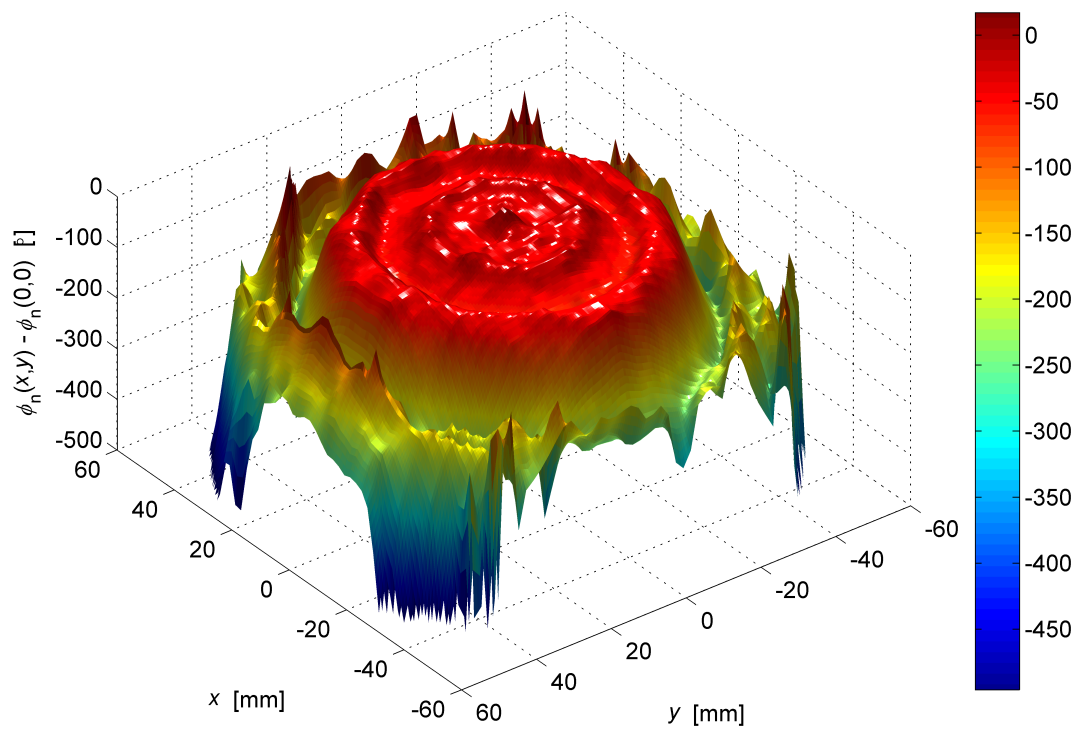
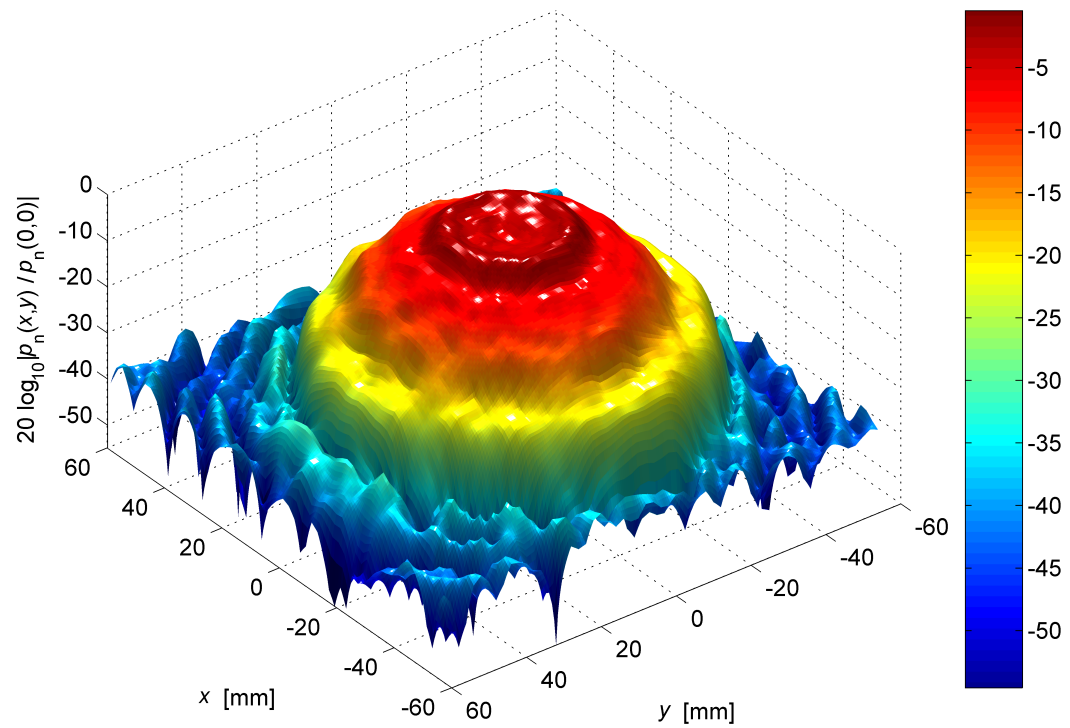


Figure 4.14. Alternative presentation of the amplitude (top) and phase (bottom) measurement results for the ES200-7C transducer, shown in Figure 4.12.

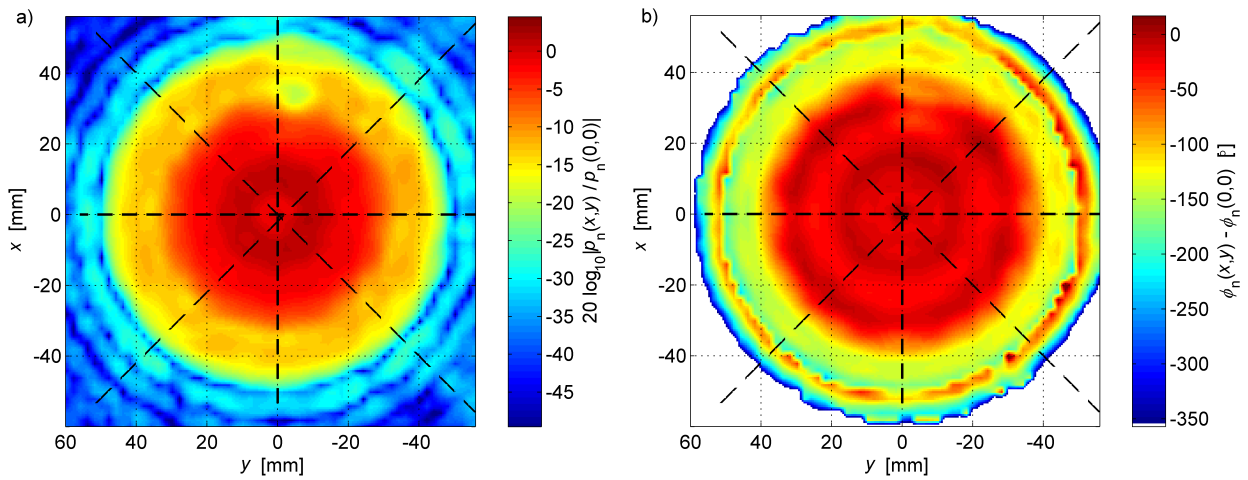


Figure 4.15. a) Relative sound pressure level, and b) relative phase in a plane parallel to the face of the ES200-7CD echo sounder transducer. The black dashed lines show the eight paths used for extraction of one-dimensional amplitude and phase data.

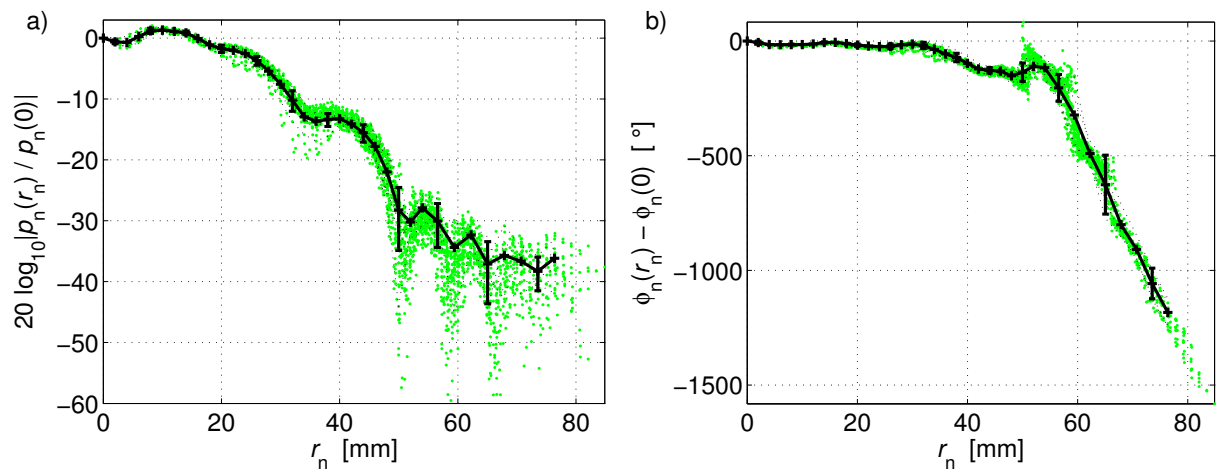


Figure 4.16. One-dimensional amplitude (a) and phase measurements (b) for the ES200-7CD transducer. Results from all the measurement points are marked in green. The black curve and error bars show mean value and standard deviations calculated from the values along the eight radial paths marked in Figure 4.15.

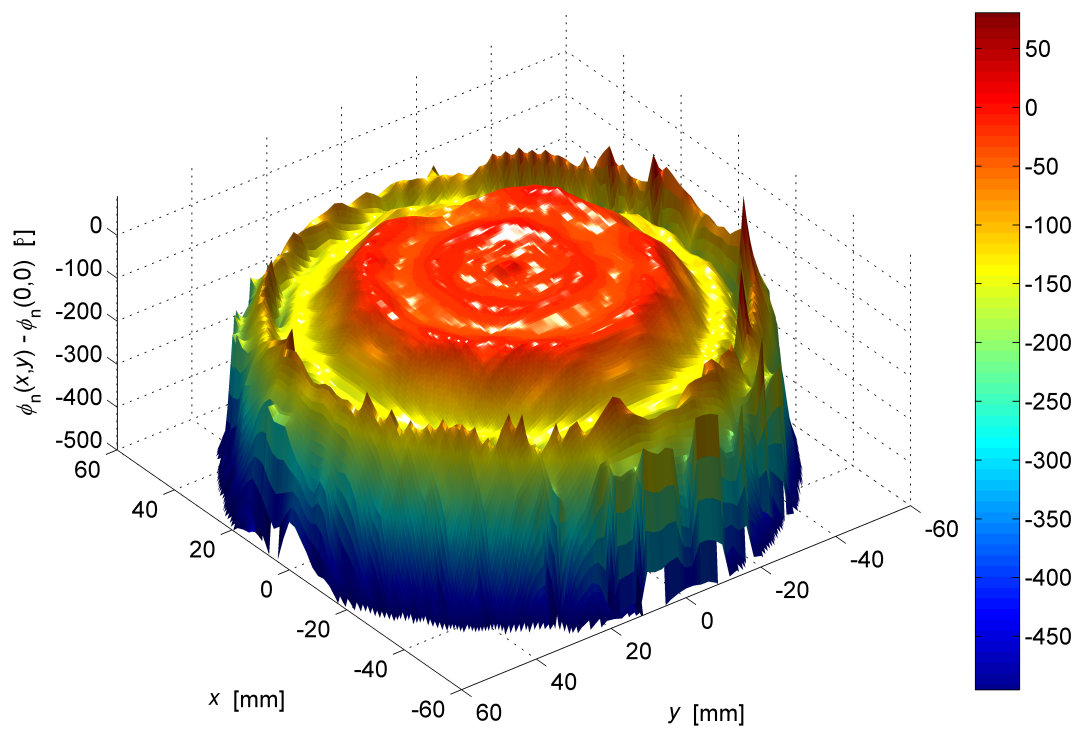
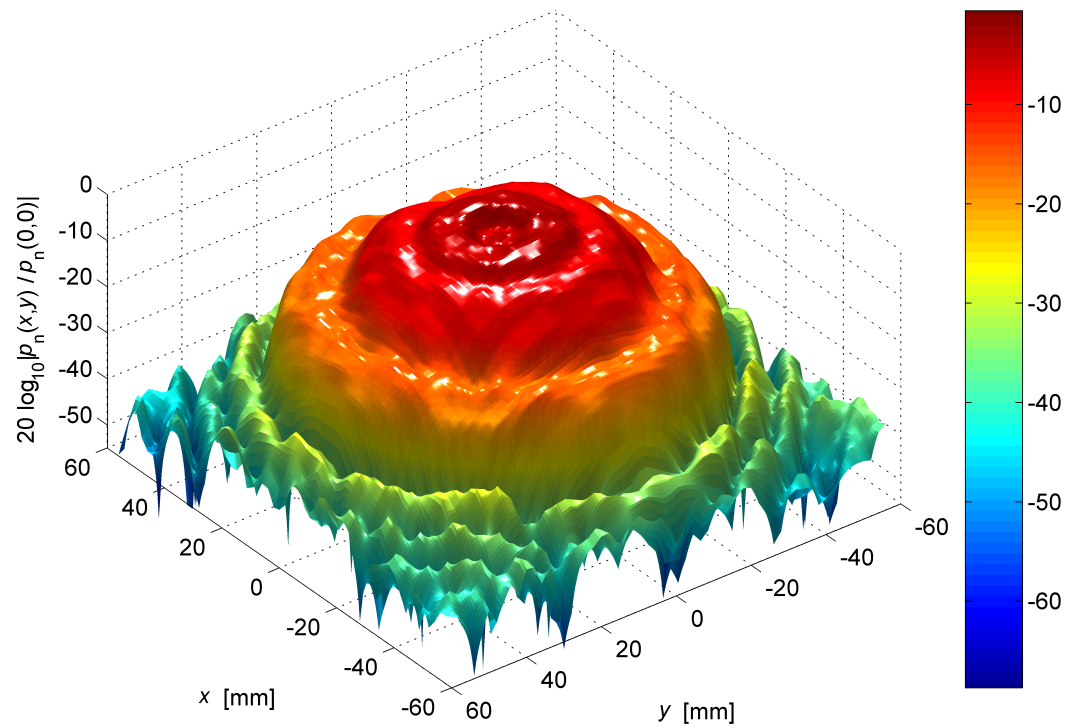


Figure 4.17. Alternative presentation of the amplitude (top) and phase (bottom) measurement results for the ES200-7CD transducer, shown in Figure 4.15.

4.3. Experimental source conditions for numerical simulations

The echo sounder transducers are designed to generate lower side lobes than a uniform circular piston. The possibility of using the results from the near field measurements (Figures 4.10, 4.13, and 4.16) as an alternative to the uniform piston idealization in the simulations is investigated.

4.3.1. Source conditions from measurements

The distance z between the face of the sound source and the plane in which the near field measurements are made is neglected. The measurement results are inserted directly into the source condition for the Bergen Code. Near field measurements made in different planes perpendicular to the sound beam axis may yield different results. It is assumed that measurements made in any such plane would yield essentially the same simulation result for the far field.

A scaling of the measured near field sound pressure amplitude was sought to obtain source conditions that yield the same simulated axial amplitude in the far field as for a uniform circular piston source condition with radius a and peak pressure amplitude p_0 . Within the approximation of the KZK equation^{151,271} (Section 2.2), the pressure and the axial particle velocity component are proportional. The acoustic intensity in the source plane, where the particle velocity is in the axial direction, is thus proportional to the pressure amplitude squared.

As a first estimate, the measured sound pressure amplitude $p_n(r_n)$ is scaled so that the integral of the square of the axisymmetric pressure amplitude over the source plane becomes the same as for the uniform piston source condition. The source condition pressure amplitude p_s then becomes

$$p_s(r_n) = |p_s(r_n)| \cdot e^{j\phi_s(r_n)} = p_n(r_n) \cdot \left[\frac{p_0^2 \cdot \pi a^2}{\int_0^\infty |p_n(r'_n)|^2 2\pi r'_n dr'_n} \right]^{\frac{1}{2}}. \quad (4.6)$$

Equal power transfer through the source plane does not necessarily lead to equal axial sound pressure for different source configurations. The effective uniform piston source radius a is determined from the -3 dB angle measured in the transducer's far field radiation pattern (Section 5.2.1). The integral in Equation (4.6) is evaluated with the trapezoidal rule over the r_n for which measurements have been made (Figures 4.10, 4.13, and 4.16). The sound pressure amplitude is set equal to zero outside the rectangle covered by the near field measurements. The resulting source conditions for the three transducers are shown in Figures 4.18 and 4.19. The corresponding uniform piston source conditions used in Chapters 5 and 6 are indicated in the same figures (4.18a and 4.19a). The radii of the uniform piston source conditions are calculated to yield the same -3 dB beam angles as measured in the far field.

Although the 200 kHz transducers have similar design, the results of the near field measurements are somewhat different (Figure 4.19). The differences may in part be due to amplitude and phase variations with distance from the sound source, as there may be small differences in the distance between each transducer face and the plane in which the measurements were made.

The Bergen Code source condition for an axisymmetric problem is specified in N_u equally spaced points along a radial line in the source plane. The first point is on the symmetry axis, $u = 0$, and the last is at the boundary of the calculation region $u = u_{\max}$. $u = r_n/a$ is a nondimensional transverse coordinate. Values for $p_s(r_n)$ are assigned to the N_u grid points by linear interpolation. In accordance with Equation (2.69), the Fourier coefficients of the source condition become

$$\begin{aligned}
g_1(u) &= |p_s(ua)| \cdot \cos(\phi_s(ua) + u^2), \\
h_1(u) &= |p_s(ua)| \cdot \sin(\phi_s(ua) + u^2), \\
g_n &= 0, h_n = 0, \quad n \geq 2.
\end{aligned} \tag{4.7}$$

The source condition specified in terms of g_1 and h_1 for the ES120-7C transducer is shown in Figure 4.18b.

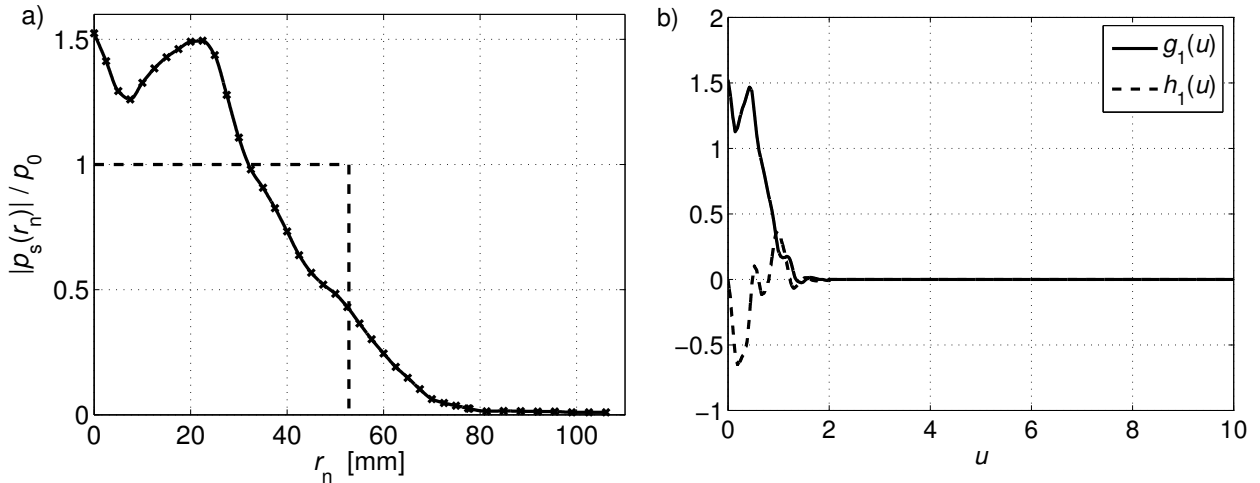


Figure 4.18. a) Scaled sound pressure amplitude for the ES120-7C echo sounder transducer (see Figure 4.10 for the phase $\phi_s = \phi_n$). The corresponding uniform piston source condition is indicated with dashed lines. b) Source condition based on the measurements for the ES120-7C transducer on the form of g_1 and h_1 as input to the Bergen Code.

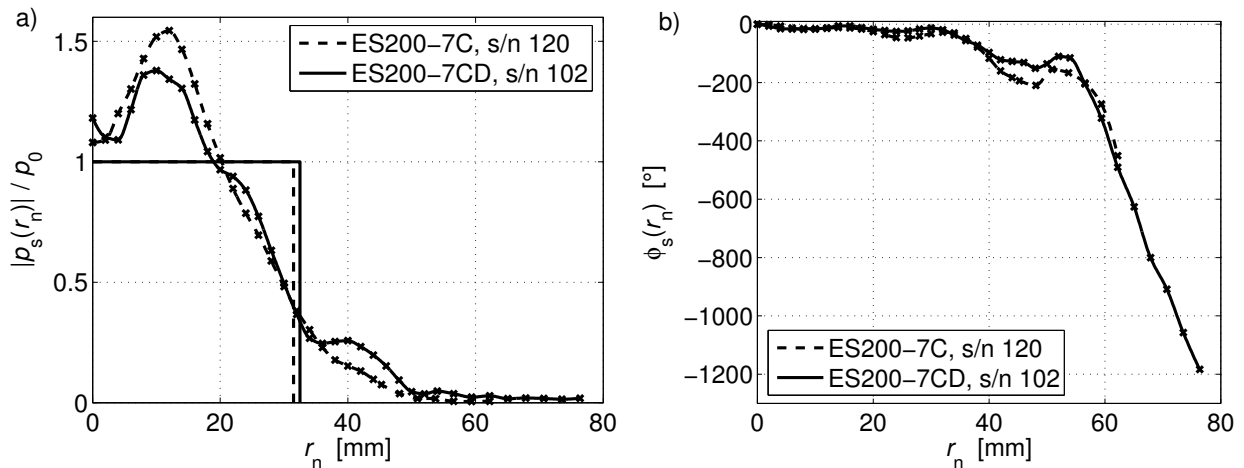


Figure 4.19. Source condition amplitude (a) and phase (b) based on near field measurements for the ES200-7C and ES200-7CD echo sounder transducers (cf. Figures 4.13 and 4.16). The amplitudes are scaled to yield the same integrated pressure squared as each transducer's corresponding uniform piston source condition (shown in Figure a).

4.3.2. Simulation results for linear sound beams

Bergen Code simulations are made for the ES120-7C, ES200-7C, and ES200-7CD echo sounder transducers, respectively. Results for the effective sound pressure p_{lin} are shown in Figures 4.20–4.22. To avoid nonlinear distortion, the simulations have been performed with $p_0 = 1$ Pa peak source condition amplitude. Simulations based on the near field measurements are compared with simulations using the uniform piston source condition.

As good overall agreement is seen in the axial sound pressure levels, no change is made to the scaling of the near field measurements described by Equation (4.6).

The same qualitative differences between simulation results from using different source conditions are seen for all three transducers. The source conditions based on measurements yield smoother axial near fields than the uniform piston source condition, but only small differences are seen in the axial field far from the transducer. The far field main lobe becomes wider with measurement source conditions than with the uniform piston, and the first side lobe is lower. This is not unexpected, as low side lobe levels is among the design specifications for the transducers.²³⁵ The difference in lobe widths is small in terms of the -3 dB beam angle, which is consistent with the effective plane piston source radius a having been determined from the measured -3 dB beam angle.

The differences between the simulation results for the two 200 kHz echo sounders (Figures 4.21 and 4.22) give some indication of the sensitivity of the linear solution to changes in the source condition (Figure 4.19).

Measurements of finite-amplitude sound propagation in fresh water are presented in Chapter 5. Simulations based on both the uniform piston and the near field measurement source conditions obtained here are compared with the measurement results.

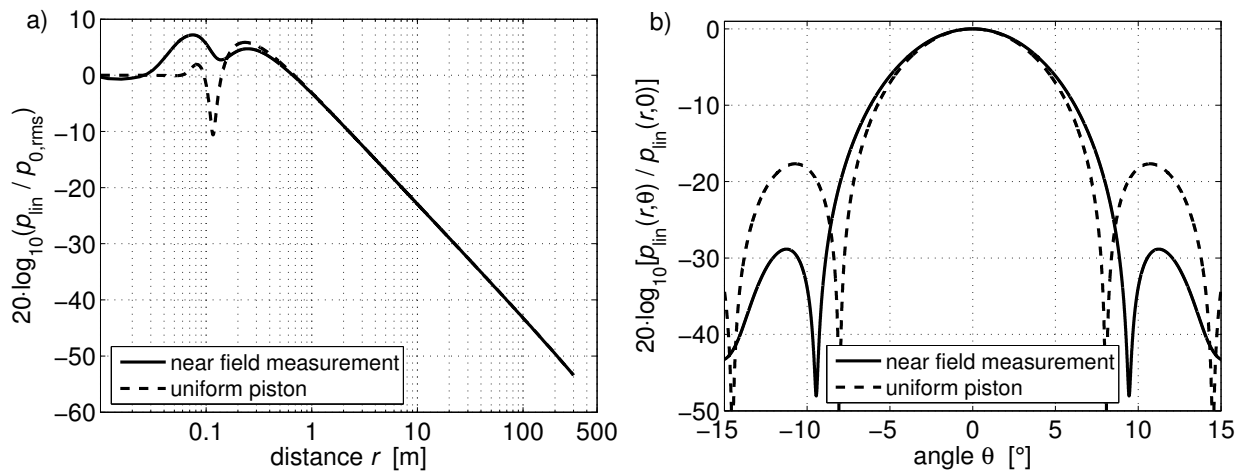


Figure 4.20. Simulated effective sound pressure p_{lin} for low amplitude sound propagation. Comparison between results from the uniform piston source condition and a source condition based on near field measurements for the ES120-7C (s/n 230) transducer. a) Axial pressure amplitude relative to the equivalent plane piston amplitude. b) Far field directivity at distance $r = 300$ m.

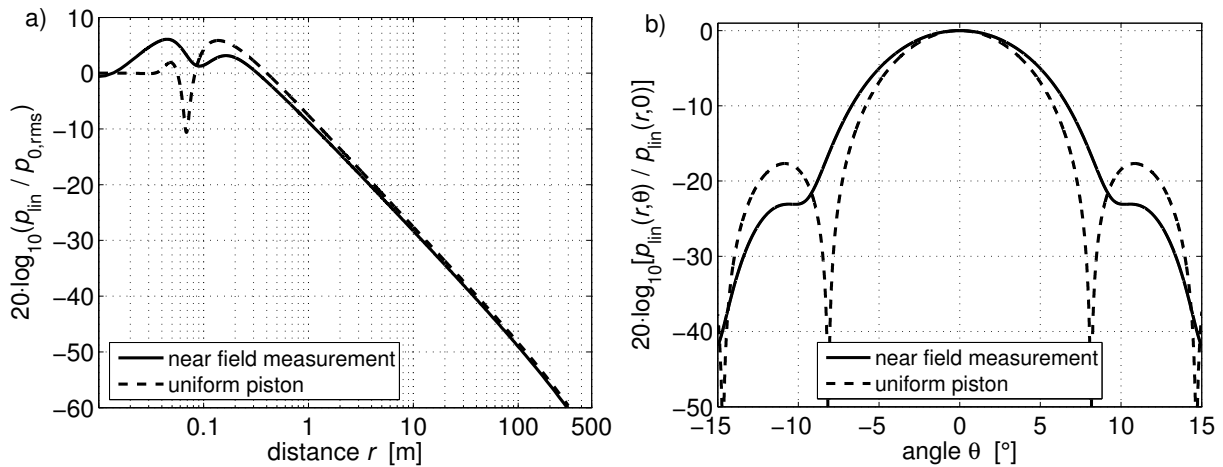


Figure 4.21. Simulated effective sound pressure p_{lin} for low amplitude sound propagation. Comparison between results from the uniform piston source condition and a source condition based on near field measurements for the ES200-7C (s/n 120) transducer. a) Axial pressure amplitude relative to the equivalent plane piston amplitude. b) Far field directivity at distance $r = 300$ m.

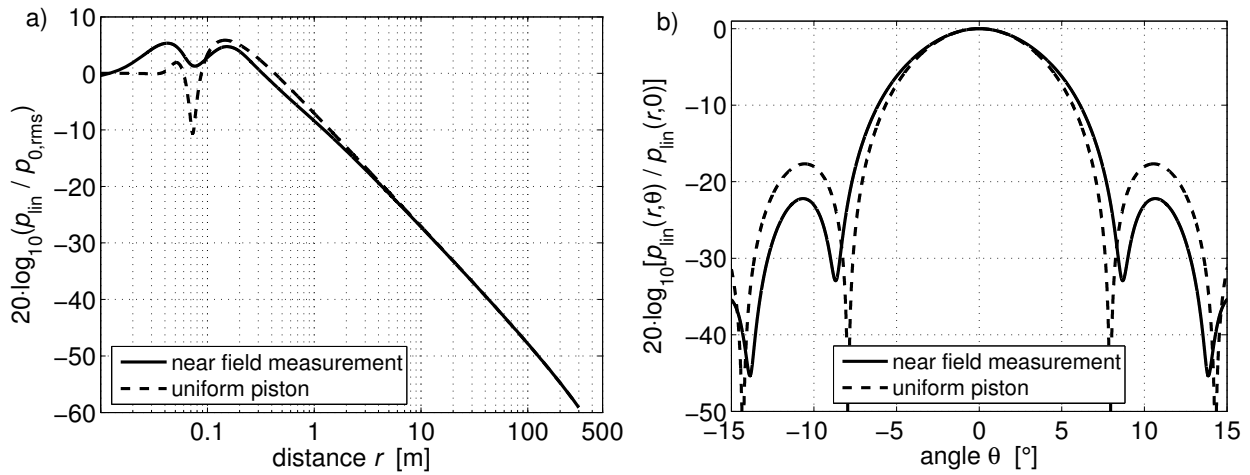


Figure 4.22. Simulated effective sound pressure p_{lin} for low amplitude sound propagation. Comparison between results from the uniform piston source condition and a source condition based on near field measurements for the ES200-7CD (s/n 102) transducer. a) Axial pressure amplitude relative to the equivalent plane piston amplitude. b) Far field directivity at distance $r = 300$ m.

Chapter 5. Sound propagation in fresh water

Fisheries research echo sounders are used in lakes and rivers, in coastal waters, and at sea. A wide variety of water temperatures, salinities, and particle and bubble contents are therefore encountered. Fresh water at room temperature, as normally found in indoor water tanks, is a rare special case. Still, excellent control with the environment and precise positioning systems make sound propagation measurements from indoor facilities invaluable for comparison with theory.

The fresh water tank used by Tichy *et al.*²³⁴ in their measurements of nonlinear attenuation in the axial field of a 200 kHz echo sounder transducer, was made available for further investigations. The results are presented in this chapter. Section 5.1 describes measurements made with a calibrated hydrophone in the sound fields of 120 kHz and 200 kHz echo sounders. The sound pressure amplitudes for the fundamental and second harmonic frequency components are extracted from the measured waveforms. Also, target strength measurements are performed with a 200 kHz echo sounder and a reference target. This is done to obtain an indication to whether errors in target strength measurements can be linked directly to the nonlinear attenuation of the fundamental frequency component.

Numerical simulations of nonlinear sound propagation in fresh water are described in Section 5.2. The simulations for comparison with measurements are carried out with two sets of sound source descriptions. One is the uniform circular piston, with radius and pressure amplitude determined from hydrophone measurements in the far field. The other source condition is based on near field measurements, as described in Section 4.3. Simulation results are

also compared qualitatively with some measurement results for long range sound propagation in fresh water, described in the literature.^{221,163}

The results from measurements and simulations are presented in Section 5.3. The simulations with the two types of source conditions are compared with each other and with the hydrophone measurements for the fundamental and second harmonic frequency components. Simulation results are used to isolate the nonlinear attenuation of the fundamental frequency component. The experimental target strength measurements are compared with the same simulations.

5.1. Measurements in fresh water

5.1.1. Measurement facilities and echo sounders

Sound fields of Simrad EK60 echo sounders with 120 kHz and 200 kHz operating frequencies (Figure 5.1) were investigated experimentally in a $15 \times 6 \times 6 \text{ m}^3$ (length \times width \times depth) fresh water tank in the laboratory of Simrad AS in Horten, Norway. The water kept $(20 \pm 2)^\circ\text{C}$ temperature and was stirred and filtered daily to reduce temperature gradients and particle contents. A digital positioning system enabled rotation of the echo sounder transducers around the x and z axes (Figure 5.4), with relative accuracy of at least 0.1° . The transducers were mounted one at a time at the centre of a short end of the tank, at approximately 2.5 m depth.

Tables 5.1 and 5.2 give an overview of the measurements discussed in this chapter. The results are divided into measurement sets H1, H2, and H3, corresponding to experiments made at different times. The H1 and H3 measurements were made with 200-kHz echo sounders, while the H2 measurements are for the 120 kHz drive frequency. Three different instrument set-ups have been used. The hydrophone measurements with and without a preamplifier at the hydrophone terminals are described in the following section,

while the backscatter measurements using calibration spheres are discussed in Section 5.1.3.



Figure 5.1. ES200-7C transducer (left) and ES120-7C transducer (right).

The EK60 echo sounder was controlled from a standard personal computer. The echo sounder consists of the computer, one or more transceiver units and one transducer for each transceiver. Burst duration, burst interval, and electrical output power are selected in the echo sounder control software. The burst duration was set to 256 μs . The time interval between bursts was 0.30 s for the H1 and H2 measurement sets and 0.40 s for the H3 measurements (Tables 5.1 and 5.2). The 0.30 s interval was sufficient to ensure that no reverberation from the previous burst was noticed when a new was transmitted. For simplicity, the output power settings are referred to by their nominal values W in this work, although there is some discrepancy between the nominal value and the actual transferred electrical power. The effective voltage amplitude U_t across the transducer terminals was measured for each of the used power settings (Table 5.5).

100 W, 600 W and 1000 W nominal power settings were used with the 120 kHz echo sounder. The power settings chosen for the 200 kHz echo sounder were 150 W, 1050 W, and 1500 W in the first (H1) measurement set, and 50 W, 150 W, and 1000 W in the second (H3). The normal maximum power setting for both echo sounders when used for fisheries research is 1000 W.

Table 5.1. Axial measurements of nonlinear distortion in fresh water.

| measure- ment set | time | frequency | EK60 power setting | axial fields | instrument set-up |
|----------------------|-----------|-----------|-----------------------|-----------------|----------------------|
| H1a | Aug. 2004 | 200 kHz | 150 W | 1 | hydrophone |
| H1b | Aug. 2004 | 200 kHz | 1050 W | 1 | hydrophone |
| H1c | Aug. 2004 | 200 kHz | 1500 W | 1 | hydrophone |
| H1d | Aug. 2004 | 200 kHz | 45 W | 1 | sphere |
| H1e | Aug. 2004 | 200 kHz | 150 W | 1 | sphere |
| H1f | Aug. 2004 | 200 kHz | 1500 W | 2 | sphere |
| H2a | Dec. 2004 | 120 kHz | 100 W | 1 | hydrophone |
| H2b | Dec. 2004 | 120 kHz | 600 W | 1 | hydrophone |
| H2c | Dec. 2004 | 120 kHz | 1000 W | 1 | hydrophone |
| H3a | Mar. 2006 | 200 kHz | 50 W | 1 | hyd. preamp. |
| H3b | Mar. 2006 | 200 kHz | 150 W | 1 | hyd. preamp. |
| H3c | Mar. 2006 | 200 kHz | 1000 W | 1 | hyd. preamp. |

Table 5.2. Directivity measurements in fresh water.

| measure- ment sets | frequency | no. of distances | distances r [m] | instrument set-up |
|-----------------------|-----------|---------------------|----------------------|----------------------|
| H1abc | 200 kHz | 2 | 5.60, 9.18 | hydrophone |
| H1ef | 200 kHz | 2 | 9.12, 9.22 | sphere |
| H2 | 120 kHz | 1 | 9.50 | hydrophone |
| H3 | 200 kHz | 1 | 8.65 | hyd. preamp. |

5.1.2. Hydrophone measurements

Hydrophone and positioning

A Reson TC 4034 hydrophone was used for measurements of axial sound pressure and radiation patterns of the echo sounder transducers. Results from hydrophone directivity measurements for 100 kHz, 200 kHz, and 300 kHz incident sound waves were supplied with the hydrophone.⁹ An additional

directivity measurement at 400 kHz was made by National Physical Laboratory, UK (NPL).¹¹ The hydrophone is nearly omnidirectional at frequencies of 200 kHz and below.⁹ For the 400 kHz frequency, its sensitivity changes with 0.25 dB per degree within 10° of the axial direction of incidence.¹¹

The hydrophone's sensitivity has been calibrated by NPL using three-transducer spherical reciprocity at frequencies from 100 kHz through 500 kHz. Spot measurements were made at 121.212 kHz, 200.000 kHz, and their integer multiples.¹² These hydrophone sensitivities of special interest to the present work are listed in Table 5.3. The sensitivity calibration has been made for sound waves impinging from a direction normal to the hydrophone's symmetry axis. A reference mark has been made on its side to specify the direction toward the sound source.¹² $\pm 3^\circ$ uncertainty is specified for the orientation of the hydrophone.¹²

The orientation used by NPL for the hydrophone sensitivity calibration is referred to as 0° in their "xy plane" directivity plot.¹¹ For the corresponding, "horizontal" directivity plots provided by Reson,⁹ however, the serial number printed on the side of the hydrophone is used as a reference mark. Reson's 0° orientation is therefore 14° counter clockwise from that used by NPL when the hydrophone is viewed from its rear (cable) end.

The "xz plane" directivity plot from NPL¹¹ and the "vertical" directivity plots provided by Reson⁹ refer to the orientation for which the sound source lies on the hydrophone's symmetry axis as 0°. This is the hydrophone orientation used for the measurements reported in the present work. The direction of incidence during the measurements is thus 90° off the direction for which the hydrophone calibration was performed.¹² The standard uncertainties listed in Table 5.3 are root-mean-square combinations of the reported ± 0.5 dB calibration uncertainty (referred to the 95% confidence level),¹² the contribution of the $\pm 3^\circ$ orientation uncertainty during calibration,¹² and the difference between the hydrophone's

orientation during calibration and during the measurements presented below. The two latter uncertainty contributions have been estimated by linear interpolation of linear-scale relative uncertainties read from the directivity plots for 100, 200, 300, and 400 kHz operating frequencies.^{9,11} Calibration certificates for the hydrophone can be found in Appendix C.

Table 5.3. Open-circuit sensitivity levels from the Reson TC4034 hydrophone calibration certificate.¹² Estimated relative standard uncertainties when the tip of the transducer is pointed towards the sound source.

| frequency [kHz] | sensitivity level [dB re 1 V/ μ Pa] | rel. standard uncertainty [dB] |
|--------------------|--|-----------------------------------|
| 121.212 | -218.4 | 0.3 |
| 200.000 | -217.8 | 0.4 |
| 242.424 | -219.1 | 0.7 |
| 363.636 | -216.0 | 0.8 |
| 400.000 | -222.3 | 0.7 |

The hydrophone was mounted at the end of a custom-made horizontal steel tube, machined to minimize reflections (Figures 5.2 and 5.3). The length of the horizontal tube was 2 metres (Figure 5.3) in order for the hydrophone to reach the shortest distances to the echo sounder transducer. A counterweight was attached on the rear end of the tube to reduce strain in the vertical tube that connected it with the positioning system (Figure 5.3). A three-axis digital positioning system enabled movement of the hydrophone with relative uncertainty of approximately 1 mm in the x , y , and z directions. The hydrophone assembly vibrated somewhat after each move to a new position. Detectable phase oscillations were allowed to die out before any sound pressure measurements were recorded. The waiting time after each repositioning was typically 2 minutes.

Measurements of the axial field were made for distances up to 10 m between the echo sounder transducer and the hydrophone. For directivity measurements,

the hydrophone was kept at a constant position to make the angle between the incident sound wave and the hydrophone axis as small and constant as possible. The echo sounder was rotated around the x axis (cf. the coordinate axes in Figure 5.4), which corresponds to the alongship direction for a hull-mounted transducer. Negative angles put the hydrophone in the forward direction relative to the echo sounder transducer.



Figure 5.2. Side view of the Reson TC4034 hydrophone mounted in a steel tube.

Signal reception

The H1abc and H2 measurement sets (Tables 5.1 and 5.2) were performed with the hydrophone connected by its 10 m integral cable to an Agilent 54621A digital sampling oscilloscope (Figure 5.3). For the H3 measurements, a Philips PM5171 preamplifier was used at the end of the hydrophone cable. A 15 metre RG58 coaxial cable connected the preamplifier to the oscilloscope, with a $50\ \Omega$ terminator across the oscilloscope terminals. The preamplifier gain was set to 0 dB. Calibration measurements on the preamplifier with cable and terminator were made with an Agilent 33120A function generator as signal source, yielding the gain factor 0.54 ± 0.02 for the relevant signal amplitudes at 200 kHz and 400 kHz frequencies.

The electrical load on the hydrophone can be treated as a parallel combination of a resistance $R_L = 1\ \text{M}\Omega$ and a capacitance C_L . $C_L = 14\ \text{pF}$ when the hydrophone is connected directly to the oscilloscope, and $50\ \text{pF}$ when the Philips PM5171 preamplifier is used. The resulting impedance Z_L is²¹⁴

$$Z_L = \frac{R_L - j\omega C_L R_L^2}{1 + \omega^2 C_L^2 R_L^2}. \quad (5.1)$$

The ratio between the end-of-cable loaded hydrophone sensitivity M_L and the corresponding open circuit sensitivity M reported in the hydrophone calibration data is²¹⁴

$$\frac{|M_L|}{|M|} = \sqrt{\frac{\text{Re}(Z_L)^2 + \text{Im}(Z_L)^2}{[\text{Re}(Z_L) + \text{Re}(Z_H)]^2 + [\text{Im}(Z_L) + \text{Im}(Z_H)]^2}} \quad (5.2)$$

Z_L is the load impedance, and Z_H is the hydrophone output impedance. Assuming that the hydrophone's input and output impedances are equal, calibration data supplied from the manufacturer suggest that the worst-case absolute value of the ratio M_L/M should be approximately 0.99 for the fundamental and second harmonic frequencies. As the results seem somewhat inconclusive, loading corrections are not made to the presented results. The electrical loading of the hydrophone is instead included as a contributor to the measurement uncertainty (Table 5.4).

Data acquisition and processing

The digital sampling oscilloscope was used for recording the signals received from the hydrophone. 2000-point waveforms were transferred to a computer for storage (Figure 5.3). The acquired waveforms were multiplied with the “flat-top” time window implemented in Matlab, and 16 000-point discrete Fourier transforms (Equation (4.4)) were obtained by zero padding. To obtain the measured root-mean-square sound pressure amplitude for each frequency component, the corresponding rms voltage magnitude was divided by the corresponding hydrophone sensitivity (Table 5.3). For the H3 measurements, where a preamplifier was used, the result was also divided by the preamplifier gain factor.

The Agilent 54621A oscilloscope has 8 bit analogue to digital converters (ADCs) and was operated with 200 MS/s sample rate. A built-in smoothing feature averaged the samples that corresponded to each of the 2000 points in the waveform transferred to the computer. 12 bit and 10 bit effective

resolutions were thus obtained for the 120 kHz and 200 kHz measurements, respectively, depending on the chosen time scale setting.⁸ The oscilloscope voltage range was adjusted so that the peak-to-peak amplitude of the signal spanned approximately 90%. For an ideal b -bit ADC, the signal to noise ratio for a sinusoidal signal is then (in decibels)²²⁵

$$\begin{aligned} \text{SNR}_{\text{ADC}} &= 10b \cdot \log_{10} 4 + 10 \cdot \log_{10} \left(\frac{3}{2} \cdot 0.90^2 \right) \\ &= 6.02b + 0.846 \end{aligned} \quad (5.3)$$

The peak-to-peak amplitude of the measured ambient noise was 0.5 mV immediately before signal transmission from the echo sounder. This is 46 dB below the lowest-amplitude echo sounder signal measured along the sound beam axis. The ratio between the lowest signal power spectra and the measured noise power spectrum is 80 dB or greater for the fundamental frequencies.

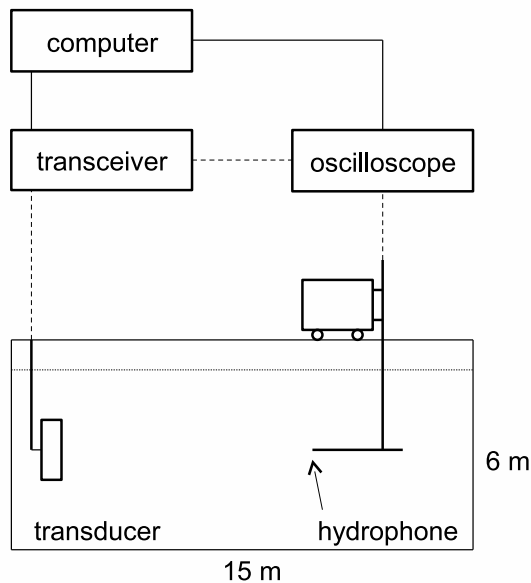


Figure 5.3. Experimental set-up for hydrophone measurements (H1abc and H2).

The set-up for the H3 measurement series is equal except that a preamplifier is used between the hydrophone and the digital sampling oscilloscope.

Combined uncertainty

The combined standard uncertainties indicated in Table 5.5 are based on the hydrophone calibration uncertainty (cf. Table 5.3), noise, positioning

uncertainty, and slight voltage amplitude fluctuations that are observed in the transmit signal across the transducer terminals. An uncertainty budget is shown in Table 5.4.⁸¹ The sound pressure level for the second harmonic frequency component is taken to be 20 dB lower than the fundamental in the uncertainty estimates for ambient noise and quantization. This yields a conservative relative uncertainty estimate for the central part of the main lobe, where the second harmonic level is higher for most of the source levels used.

The uncertainties are somewhat different for the directivity measurements. In this case, the measured sound pressures depend more strongly on the hydrophone's position in the sound beam. The importance of ambient noise also increases with distance from the axis due to the lower signal amplitudes.

The H3 measurements are made with the oscilloscope set to average over 16 bursts. This may yield more stable results when the amplitude of the transmitted signal fluctuates. On the other hand, if the hydrophone is not completely still during the measurements, the phases of received signals change between each burst. This can cause deformation of the average signal. Oscillations in the measured phase was observed in a small period after each time the hydrophone had been moved to a new position. The measurements were delayed until such oscillations had died out.

Table 5.4. Uncertainty budget for the axial sound pressure measurements.

Fundamental frequency components

| source | rel. standard uncertainty contribution | contribution to relative variance |
|--|---|--|
| angular alignment of hydrophone | 0.02 | $4 \cdot 10^{-4}$ |
| hydrophone positioning on axis | 0.012 | $1.4 \cdot 10^{-4}$ |
| hydrophone sensitivity | 0.047 | $2.2 \cdot 10^{-3}$ |
| electrical loading of hydrophone | 0.01 | $1.0 \cdot 10^{-4}$ |
| ambient noise | $5 \cdot 10^{-5}$ | $2.5 \cdot 10^{-9}$ |
| quantization | 0.001 | $1 \cdot 10^{-6}$ |
| digital postprocessing | 0.001 | $1 \cdot 10^{-6}$ |
| sum of relative variances: | | $2.8 \cdot 10^{-3}$ |
| relative combined standard uncertainty: | | 0.053 |
| relative combined standard uncertainty (dB): | | 0.5 dB |
| relative expanded uncertainty (95% confidence level, dB): | | 0.9 dB |

Second harmonic frequency component

| source | rel. standard uncertainty contribution | contribution to relative variance |
|--|---|--|
| angular alignment of hydrophone | 0.035 | $1.23 \cdot 10^{-3}$ |
| hydrophone positioning on axis | 0.012 | $1.4 \cdot 10^{-4}$ |
| hydrophone sensitivity | 0.084 | $7.0 \cdot 10^{-3}$ |
| electrical loading of hydrophone | 0.01 | $1.0 \cdot 10^{-4}$ |
| ambient noise | $5 \cdot 10^{-4}$ | $2.5 \cdot 10^{-7}$ |
| quantization | 0.01 | $1 \cdot 10^{-4}$ |
| digital postprocessing | 0.001 | $1 \cdot 10^{-6}$ |
| sum of relative variances: | | $8.6 \cdot 10^{-3}$ |
| relative combined standard uncertainty: | | 0.093 |
| relative combined standard uncertainty (dB): | | 0.8 dB |
| relative expanded uncertainty (95% confidence level, dB): | | 1.5 dB |

Measured parameters

The water temperature is assumed uniform, and was measured to $(21 \pm 1)^\circ\text{C}$ for the H1 and H2 measurement sets and $(19 \pm 1)^\circ\text{C}$ for the H3 measurements.

The effective transmit voltage amplitude U_t was measured across the terminals of each transducer quadrant. The amplitudes reported in Table 5.5 are mean values for the transducer. The standard uncertainty estimates for the voltages are due to small differences between the four quadrants and on fluctuations between bursts, caused by the echo sounder hardware. The fluctuations seem to depend on power setting, burst duration, and burst interval.

Sound propagation is assumed nearly linear for the lowest power settings (Table 5.5). By finding the best fit between the absolute value of Equation (2.1),

$$|p(r, \theta, \varphi)| = |p(r_0, \theta, \varphi)| \cdot \frac{r_0}{r} 10^{-\frac{\alpha}{20}(r-r_0)}, \quad (5.4)$$

and the measured axial sound pressure amplitudes between $r = 3$ m and $r = 10$ m, one can obtain the spherical-wave extrapolated value of the sound pressure amplitude $p_{\text{rms}}(r_0, 0, 0)$ at $r_0 = 1$ m. The polar coordinates r , θ , and φ relate to the Cartesian coordinate system as illustrated in Figure 2.1. r is distance to the sound source, θ is angle off the sound beam axis, and φ is azimuth angle. The transmit voltage response (TVR) is defined as

$$\text{TVR} = 20 \cdot \log_{10} \frac{S_V}{1 \mu\text{Pa/V}} = 20 \cdot \log_{10} \left[\frac{p_{\text{rms}}(r_0, 0, 0)}{U_t} \frac{1}{1 \mu\text{Pa/V}} \right], \quad (5.5)$$

where S_V is the voltage source sensitivity of the transducer.

For the higher power settings, where nonlinear distortion cannot be neglected, $p_{\text{rms}}(r_0, 0, 0)$ is not calculated from measurements. Equivalent source levels are obtained by scaling the low-power source level with the ratios of input

voltages. The calculated values for $p_{\text{rms}}(r_0,0,0)$, TVR, and SL are shown in Table 5.5.

The difference between the obtained results for TVR in the H3a and H3b measurements indicates that the 150 W power setting is somewhat high for assuming linear sound propagation. The source sensitivity obtained from the H1a measurement set is therefore probably a slight underestimate (Table 5.5). The cause of the difference between the TVR values obtained from H1a and H3b is that different transducers were used in the H1 and H3 measurement sets.

Table 5.5. Measured parameters with estimated standard uncertainties for the sound propagation measurements in fresh water. Effective (rms) voltage amplitude U_t across the transducer upon signal transmission, axial sound pressure amplitude p extrapolated to $r = r_0 = 1$ m, transmit voltage response, and source level.

| measure- ment set | frequ- ency | EK60 power setting | effective transducer input voltage | extrapolated eff. sound pressure @ 1 m | calculated transmit voltage response (TVR) | linear equivalent source level |
|----------------------|----------------|--------------------------|--|---|--|--------------------------------------|
| | f | W | U_t | $p_{\text{rms}}(r_0,0,0)$ | [dB re 1 $\mu\text{Pa}/\text{V}$ @ 1 m] | [dB re 1 μPa @ 1 m] |
| | [kHz] | [W] | [V] | [kPa] | | |
| H1a,e | 200 | 150 | 44 ± 2 | 92 ± 4 | 186.4 ± 0.5 | 219.3 ± 0.3 |
| H1b | 200 | 1050 | 119 ± 2 | | | 227.9 ± 0.5 |
| H1c,f | 200 | 1500 | 143 ± 2 | | | 229.5 ± 0.5 |
| H2a | 120 | 100 | 38 ± 2 | 65 ± 2 | 184.7 ± 0.5 | 216.3 ± 0.3 |
| H2b | 120 | 600 | 96 ± 2 | | | 224.3 ± 0.5 |
| H2c | 120 | 1000 | 125 ± 2 | | | 226.6 ± 0.5 |
| H3a | 200 | 50 | 26 ± 1 | 49 ± 2 | 185.1 ± 0.5 | 213.8 ± 0.3 |
| H3b | 200 | 150 | 47 ± 2 | (85 ± 4) | (184.7 ± 0.5) | 218.5 ± 0.6 |
| H3c | 200 | 1000 | 127 ± 1 | | | 227.2 ± 0.5 |

5.1.3. Calibration sphere measurements

In the analysis of hydrophone measurement results, stable sections of the measured sound bursts are Fourier decomposed, as described above. The magnitude of each harmonic component is compared with continuous-wave simulation results in Section 5.3.1. Nonlinear attenuation is defined in terms of the magnitude of the fundamental frequency component (Equation (5.10)). An echo sounder system, on the other hand, operates with sound bursts of finite duration, and backscattered acoustic energy is evaluated over a finite bandwidth (Section 2.1).

To investigate whether the continuous-wave approach of simulations and hydrophone measurements is adequate for predicting the nonlinear attenuation experienced by the echo sounder, an additional series of measurements was performed in the fresh water tank. The target strength of a 38.1-mm-diameter tungsten carbide sphere with 6% cobalt binder was measured with different power settings and with the sphere at different positions in the radiated sound field.

Prior to the nonlinearity measurements, the standard EK60 calibration routine (Section 2.1.7) was carried out with the ES200-7CD transducer (Table 4.1). The calibration sphere was suspended with two 0.4 mm monofilament nylon lines approximately 5 m from the echo sounder transducer (Figure 5.4). As for the hydrophone measurements, the 256 μ s burst duration was selected, for which the echo sounder reported a receiver bandwidth of 10.64 kHz. The receiver bandwidth is set automatically depending on the duration of the transmitted burst. The 300 W power setting used for the calibration was somewhat too high to avoid nonlinear effects, but as the purpose here is only to calibrate the split-beam direction measurement to the target, the waveform distortion should not affect the result significantly.

With sound speed⁵⁰ $c_0 = 1485 \text{ ms}^{-1}$ and burst duration 1024 μ s, the theoretical target strength for a WC38.1 calibration sphere is¹⁰⁰ $(-39.3 \pm 0.1) \text{ dB}$. Although

it has been calculated for somewhat different burst duration, and hence bandwidth, than what was used in the experiment, the value is sufficient for the present investigation.

Axial target strength measurements were made with the echo sounder set to 45 W, 150 W, and 1500 W nominal transmit powers (Table 5.1). 45 W is approximately the lowest output power setting available with the EK60 echo sounder. The reference target was centred on the sound beam axis, and its suspension lines were fixed to the digital positioning system. This allowed precision movement in the axial direction (Figure 5.4). The split beam functionality of the echo sounder was used to measure whether the calibration sphere was on the sound beam axis each time it has been moved. Adjustments were made when necessary to keep the sphere within $\theta = 0.1^\circ$.

Directivity measurements were made by panning the transducer around the x axis in steps of 1.0° . The transducer was mounted so that negative angles placed the sphere in the transducer's intended forward direction when mounted on a vessel. 150 W and 1500 W power settings were used for the directivity measurements (Table 5.2).

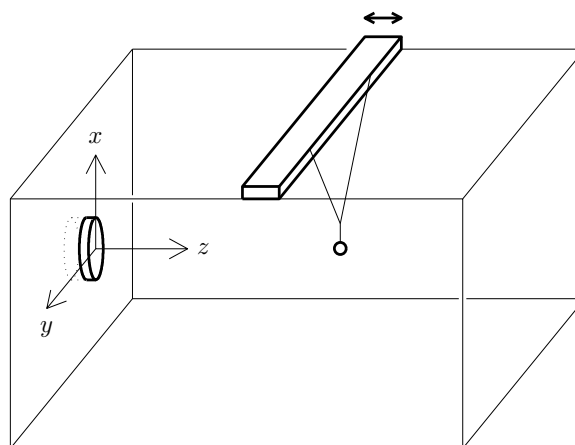


Figure 5.4. Positioning of the calibration sphere.

5.2. Simulations for fresh water

5.2.1. Simulations for comparison with measurements

Finite-amplitude sound propagation is simulated with the Bergen Code version discussed in Section 2.2.4, which solves the Transformed Beam Equation by means of the Richtmyer procedure. Throughout Chapters 5, 6, and 7, the “unperturbed” values of the simulation parameters in Table 3.4 are used in the calculations. The 20 highest harmonics are damped according to Equation (3.13) when high amplitude sound with the 200 kHz operating frequency is simulated. The parameters N_h and u_{\max} are selected as in Table 3.3.

Medium parameters for pure water were calculated from formulae taken from Kinsler *et al.*¹³⁸ for the sound speed, Cotaras and Morfey⁷⁹ for the nonlinearity coefficient, Wagner and Pruß²⁵⁸ for the density, and Francois and Garrison¹⁰⁵ for the absorption coefficient (Table 5.6).

The polar coordinates (r, θ) are defined as illustrated in Figure (2.1). As the geometry for the simulations is axisymmetric, the azimuth angle φ is omitted. The origin is at the centre of the surface of the sound source, and the axis $\theta = 0$ coincides with the sound beam axis. From Equation (2.10) it follows that the half-intensity angle of a plane piston source with radius a in an infinitely stiff baffle of infinite extent satisfies

$$ka \sin \theta_{-3 \text{ dB}} \approx 1.6137. \quad (5.6)$$

This value is slightly different from that for the half-intensity beam angle, for which $ka \sin \theta = 1.6163$. Using Equation (5.6) and the hydrophone directivity measurements taken with the lowest power settings (Table 5.1), equivalent plane piston source radii are obtained for the three echo sounder transducers (Tables 4.1 and 5.7). The effective source radius for the ES200-7C transducer becomes different depending on whether it is calculated from the 50 W or the 150 W measurements (Table 5.7, H3). The result from the 50 W measurement

is used for the simulations. The difference is attributed to flattening of the main lobe due to nonlinear attenuation near the sound beam axis. The effective source radius for the ES200-7CD transducer, for which 150 W is the lowest power setting (measurement set H1), may thus be slightly underestimated.

When linear sound propagation is to be simulated, a proper velocity amplitude v_0 for the plane piston source condition is the one that yields the best fit between the measured axial sound pressure amplitude and the expression^{137,138} (Equation (3.3))

$$|p_{tt}(r, 0)| = 2\rho_0 c_0 v_0 \left| \sin \left\{ \frac{1}{2} kr \left[\sqrt{1 + \left(\frac{a}{r} \right)^2} - 1 \right] \right\} \right|. \quad (5.7)$$

Equation (5.7) gives the exact linear sound pressure amplitude along the axis of a uniform plane circular piston with radius a in an infinitely stiff baffle of infinite extent. Within the approximation of the KZK equation,²³⁷ the plane-wave impedance relation holds between the sound pressure and the axial component of the particle velocity. The pressure amplitude p_0 at the face of the piston is thus given by

$$p_0 = \rho_0 c_0 v_0. \quad (5.8)$$

When the lowest power settings are used (measurement sets H1a, H2a, and H3a, see Table 5.7), nonlinear attenuation is assumed to be weak or negligible. The p_0 values for simulations in these cases are determined from the measured axial fields and Equations (5.7) and (5.8). For the higher power settings, source condition amplitudes are found by scaling the p_0 for the lowest used output power with the ratios between transmit voltage amplitudes U_t (Table 5.7). The source condition pressure amplitudes in Table 5.7 are written in terms of the effective sound pressure $p_{0,\text{rms}} = p_0 / \sqrt{2}$.

Table 5.6. Parameters for the propagation medium

| measu- rement set | frequency f [Hz] | temp- erature T [°C] | sound speed c_0 [m/s] | nonlinearity coefficient β | density ρ_0 [kg m ⁻³] | absorption coefficient α_2 [Np m ⁻¹ Hz ⁻²] |
|-------------------------|--------------------------|---------------------------------|----------------------------------|--|--|---|
| H1 | 200 000 | 21±1 | 1485±3 | 3.52±0.02 | 998.0±0.2 | (25±1)·10 ⁻¹⁵ |
| H2 | 121 212 | 21±1 | 1485±3 | 3.52±0.02 | 998.0±0.2 | (25±1)·10 ⁻¹⁵ |
| H3 | 200 000 | 19±1 | 1479±3 | 3.49±0.02 | 998.4±0.2 | (25±1)·10 ⁻¹⁵ |

Table 5.7. Source radii and rms pressure amplitudes for the simulations of nonlinear sound propagation in fresh water.

| measure- ment set | frequency f [Hz] | power setting W [W] | effective transducer input voltage U_t [V] | equivalent plane piston source radius a [mm] | rms plane piston pressure amplitude $p_{0,rms}$ [MPa] |
|----------------------|--------------------------|--------------------------------|--|--|---|
| H1a,e | 200 000 | 150 | 44 ± 2 | 32.5 ± 0.1 | 0.208 ± 0.009 |
| H1b | 200 000 | 1050 | 119 ± 2 | - | 0.56 ± 0.03 |
| H1c,f | 200 000 | 1500 | 143 ± 2 | - | 0.67 ± 0.03 |
| H2a | 121 212 | 100 | 38 ± 2 | 52.8 ± 0.1 | 0.091 ± 0.003 |
| H2b | 121 212 | 600 | 96 ± 2 | - | 0.23 ± 0.01 |
| H2c | 121 212 | 1000 | 125 ± 2 | - | 0.30 ± 0.02 |
| H3a | 200 000 | 50 | 26 ± 1 | 31.5 ± 0.1 | 0.118 ± 0.005 |
| H3b | 200 000 | 150 | 47 ± 2 | (30.6 ± 0.1) | 0.21 ± 0.01 |
| H3c | 200 000 | 1000 | 127 ± 1 | - | 0.58 ± 0.02 |

5.2.2. Simulations for comparison with other works

A separate set of simulations is run for comparison with the measurements of Lockwood *et al.*¹⁶³ and Shooter *et al.*,¹⁶³ who made measurements of finite amplitude sound radiated by circular, piston-like sound sources in fresh water. Two sets of source and medium parameters were taken from each of their papers^{163,221} (“Shooter 1”, “Shooter 2”, “Lockwood 1”, and “Lockwood 2”).

Table 5.8 shows the sound speeds⁵⁰, nonlinearity coefficients⁷⁹, absorption coefficients¹⁰⁵, densities²⁵⁸, frequencies, source radius, source condition amplitudes, and axial distances from the sound source, that were used as input to the test simulations.

Table 5.8. Simulation parameters for comparison with Lockwood *et al.*¹⁶³ and Shooter *et al.*²²¹

| parameter | Shooter 1 | Shooter 2 | Lockwood 1 | Lockwood 2 |
|--|----------------------|----------------------|--------------------|--------------------|
| temperature T [°C] | 17.8 | 24.6 | 12.2 | 12.2 |
| sound speed c_0 [m/s] | 1476 | 1495 | 1456 | 1456 |
| nonlinearity coeff. β | 3.5 | 3.6 | 3.3 | 3.3 |
| absorption coeff. α_2 [Np/m/Hz ²] | $2.7 \cdot 10^{-14}$ | $2.2 \cdot 10^{-14}$ | $3 \cdot 10^{-14}$ | $3 \cdot 10^{-14}$ |
| density ρ_0 [kg/m ³] | 999 | 997 | 1000 | 1000 |
| frequency f [kHz] | 454 | 454 | 454 | 450 |
| equiv. source radius a [mm] | 37.8 | 37.8 | 37.8 | 37.8 |
| source cond. amplitude p_0 [kPa] | 1–405 | 1–405 | 20.5 | 163 |
| axial distance from source z [m] | ≤ 33 | 101.5 | 107 | 37.5 |

5.3. Results for sound propagation in fresh water

5.3.1. Hydrophone measurement results

200 kHz operating frequency

Measurements were made in the sound beams radiated by 200 kHz echo sounders with 50 W, 150 W, 1000 W, 1050 W, and 1500 W power settings (Tables 5.1 and 5.2). The measured and simulated effective sound pressure amplitudes $p_{1,\text{rms}}(r, \theta)$ for the fundamental frequency component, and $p_{2,\text{rms}}(r, \theta)$ for the second harmonic, are given as functions of the distance r from the sound source and polar angle θ off the sound beam axis (Figure 2.1).

Measured and simulated axial fields are shown in Figure 5.5 for the H1

measurement set, Figure 5.7 for the H3 measurements, and Figure 5.9 for the H2 measurement set. To facilitate comparison between the results, $p_{1,\text{rms}}(r,0)$ has been multiplied with the distance r from the sound source. For linear sound propagation in the far field, $p_{1,\text{rms}}(r,0) \cdot r$ is nearly independent of distance, only decreasing slightly due to thermoviscous absorption. Simulation results using both uniform piston source conditions and source conditions based on near field measurements (Section 4.3) are plotted together with the measurement results. The measured and simulated sound pressure amplitudes $p_{2,\text{rms}}(r,0)$ for the second harmonic frequency component are shown relative to the respective fundamental components $p_{1,\text{rms}}(r,0)$.

For the 200 kHz operating frequency (Figures 5.5 and 5.7), agreement within 0.5 dB is seen in the far field between measurements and simulations for both the fundamental frequency component and the second harmonic relative to the fundamental. The H3 measurements are an exception, as in this case the source condition based on near field measurements yields a greater underestimate of the fundamental frequency component. The simulations based on the uniform piston source condition are within 0.5 dB of the measurements also here (Figure 5.7). When the source levels are high, the second harmonic amplitude approaches one-half of that of the fundamental. This is consistent with the frequency contents of a sawtooth wave.

Far field radiation patterns were measured at $r = 5.60$ m and $r = 9.18$ m distances from the sound source in the H1 measurement set and at $r = 8.65$ m in the H3 measurement set (Figures 5.6 and 5.8, respectively). Sound pressure levels are shown for both the fundamental and the second harmonic frequency component in each plot. The simulations based on near field measurements seem to yield somewhat better agreement with the measurement results off axis than the uniform piston simulations.

As nonlinear attenuation depends strongly on sound pressure amplitude, it alters the radiation pattern. The central part of the main lobe is attenuated the

most, since the sound pressure amplitude there is the highest. Flattening of the main lobe is seen in particular when the power setting is increased to 1000 W (Figures 5.8 c), 1050 W (Figures 5.6 c and d), and 1500 W (Figures 5.6 e and f). In the H1 directivity measurements at $r = 9.18$ m (Figures 5.6 b, d, and f), the measured -3 dB beam angle increases from 3.5° for the 150 W power setting to 4.7° for 1500 W (Table 5.9). The main lobe for the second harmonic frequency component also flattens when the source level is high.

120 kHz operating frequency

Figures 5.9 and 5.10 show the results from hydrophone measurements and simulations of the sound beam radiated by the 120 kHz echo sounder. 100 W, 600 W, and 1000 W power settings were used. Along the sound beam axis, agreement to within 0.5 dB is seen between simulations and measurements for the fundamental frequency component (Figures 5.9 a, c, and e). However, the measured nonlinear attenuation and second harmonic generation is clearly greater than what the simulation results indicate.

While the discrepancy for the fundamental frequency component increases with the power setting, the differences between the measured and simulated second harmonic sound pressure levels seem more similar in Figures 5.9 b, d, and f. At $r = 9.6$ m, the simulated second harmonic sound pressure level for the 100 W power setting is approximately 2.5 dB lower than the measured value. The corresponding discrepancy for the 1000 W power setting is 2.0 dB.

The measured axial sound pressure level for the second harmonic component approaches -6 dB relative to the fundamental when the 1000 W power setting is used. This relative increase seems more rapid than expected when compared to the 200 kHz measurement results. This, combined with the discrepancy between the measurement results shown in Figures 5.5 f and 5.7 f, might give reason to doubt the accuracy of some of the measurement results.

Directivity measurements were made at 9.50 m distance from the 120 kHz echo

sounder transducer (Figure 5.10). The source condition based on near field measurements seems to yield somewhat better agreement between measurement and simulation results than the uniform piston source condition, in particular for the fundamental frequency component. The flattening of the main lobe in the 120 kHz case is not as pronounced as for the 200 kHz operating frequency. A 9% increase in the -3 dB angle is seen from the 100 W to the 1000 W power settings (Table 5.9).

5.3.2. Nonlinear attenuation in fresh water

Choice of source condition

The presented measurement and simulation results do not indicate clearly which type of source condition yields the best agreement between simulations and experiments. The source conditions based on near field measurements give the best qualitative description of the radiation pattern off axis, where the measured sound field departs markedly from that of a uniform piston. Simulations based on the uniform piston source condition, on the other hand, might seem to yield the most generic results. In addition, the problem of acoustic radiation from a plane, circular, uniformly vibrating piston in an infinitely stiff, plane baffle of infinite extent has been treated extensively in the literature. For these reasons the uniform piston source conditions are chosen for the simulations of nonlinear attenuation, although this choice is not optimal. The agreement between measurements and uniform piston-based simulations is in general good near the sound beam axis and becomes gradually worse with the off-axis angle.

Calculated nonlinear attenuation

There is some nonlinear distortion even in the sound fields radiated with the lowest power settings used in the present work. Hence, the nonlinear attenuation cannot be quantified by mere comparison between the high and low power measurements. Simulation results with and without accounting for

nonlinear effects are compared as an alternative. Bergen Code simulations are made with 1 Pa peak source condition amplitude and otherwise the same parameters that have been used to obtain the results shown in Figures 5.5–5.10 (Section 5.2.1). The simulated effective sound pressures for the fundamental component using the 1 Pa source conditions are called $p_{\text{lin}}(r, \theta)$.

The fundamental effective sound pressures $p_{1,\text{sim}}(r, \theta)$ are simulation results for the source condition amplitudes $p_{0,\text{rms}}$ in Table (5.7). The simulation results are normalized to their respective rms source condition amplitudes,

$$\bar{p}_{1,\text{sim}}(r, \theta) = \frac{p_{1,\text{sim}}(r, \theta)}{p_{0,\text{rms}}}, \quad \bar{p}_{\text{lin}}(r, \theta) = \frac{p_{\text{lin}}(r, \theta)}{1 \text{ Pa}/\sqrt{2}}. \quad (5.9)$$

The normalized axial sound pressure amplitudes are compared in Figure 5.11. The values plotted are the negative of what might be called the simulated nonlinear attenuation NA_{sim} ,

$$\text{NA}_{\text{sim}}(r, \theta) = -20 \log_{10} \frac{\bar{p}_{1,\text{sim}}(r, \theta)}{\bar{p}_{\text{lin}}(r, \theta)}. \quad (5.10)$$

For the 1000 W power setting, simulated nonlinear attenuation of 3.4 dB and 0.8 dB is obtained for the 200 kHz and 120 kHz drive frequencies, respectively, at $r = 10$ m. The H3 and H2 measurements indicate approximately 0.2 dB and 0.5 dB higher nonlinear attenuation, respectively (Figures 5.7 and 5.9). It should be noted that the relative standard measurement uncertainty has been estimated to 0.3 dB (Table 5.4). Further attenuation is predicted at longer distances. Measurements for confirmation have however not been made beyond 10 m in the present work.

Table 5.9 lists some values for the axial nonlinear attenuation based on the simulation results. -3 dB beam angles from the hydrophone measurements are also shown. In the column marked “ $r \approx 9$ m”, the axial nonlinear attenuation is for $r = 9.0$ m, and the -3 dB angles are measured at distances $r = 9.18$ m (H1), $r = 9.50$ m (H2), and $r = 8.65$ m (H3). The values reported in Figure 5.11 and

Table 5.9 should be interpreted in the context of the degree of agreement reported between measurements and simulations.

Table 5.9. Simulated axial nonlinear attenuation (Equation (5.10)) and measured -3 dB angles for some power settings and distances from the sound source.

| | $r = 5.6 \text{ m}$ | | $r \approx 9 \text{ m}$ | | $r = 50 \text{ m}$ | $r = 100 \text{ m}$ | $r = 300 \text{ m}$ |
|----------------|---------------------|--------------------------|-------------------------|--------------------------|--------------------|---------------------|---------------------|
| | NA_{sim} | $\theta_{-3 \text{ dB}}$ | NA_{sim} | $\theta_{-3 \text{ dB}}$ | NA_{sim} | NA_{sim} | NA_{sim} |
| 200 kHz | | | | | | | |
| 50 W (H3) | 0.1 dB | - | 0.1 dB | 3.4° | 0.3 dB | 0.3 dB | 0.4 dB |
| 150 W (H3) | 0.4 dB | - | 0.5 dB | 3.5° | 0.9 dB | 1.1 dB | 1.3 dB |
| 150 W (H1) | 0.4 dB | 3.6° | 0.5 dB | 3.5° | 1.0 dB | 1.2 dB | 1.4 dB |
| 1000 W (H3) | 2.7 dB | - | 3.3 dB | 4.3° | 5.0 dB | 5.5 dB | 5.9 dB |
| 1050 W (H1) | 2.8 dB | 4.3° | 3.3 dB | 4.5° | 5.0 dB | 5.5 dB | 6.0 dB |
| 1500 W (H1) | 3.6 dB | 4.6° | 4.2 dB | 4.7° | 6.1 dB | 6.6 dB | 7.1 dB |
| 120 kHz | | | | | | | |
| 100 W (H2) | 0.1 dB | - | 0.1 dB | 3.4° | 0.2 dB | 0.2 dB | 0.3 dB |
| 600 W (H2) | 0.3 dB | - | 0.5 dB | 3.6° | 1.0 dB | 1.2 dB | 1.6 dB |
| 1000 W (H2) | 0.6 dB | - | 0.8 dB | 3.7° | 1.7 dB | 2.1 dB | 2.6 dB |

5.3.3. Target strength measurements

A 200 kHz EK60 echo sounder with the ES200-7CD (s/n 102) transducer was used with different output power settings to measure the target strength of a 38.1 mm tungsten carbide calibration sphere. Nonlinear effects contribute to the difference between the target strength TS_{meas} measured by the echo sounder and the actual target strength of the target. The hypothesis that the measurement error due to nonlinear effects is approximately equal to the nonlinear attenuation (NA) of the fundamental frequency component (Equation (5.10)),

$$TS_{\text{meas}} - TS_{\text{lin}} \approx NA, \quad (5.11)$$

is tested by comparing measurement and simulation results. TS_{lin} is the target strength that would be measured by the echo sounder in the absence of nonlinear effects.

Numerical simulation

A numerical result for the measured, or apparent, target strength TS_{meas} reported by the echo sounder, is sought. The normalized sound pressure amplitudes $\bar{p}_{\text{lin}}(r, \theta)$ and $\bar{p}_{1,\text{sim}}(r, \theta)$ are defined as in Section 5.3.2 (Equation (5.9)). Simulations for the ES200-7CD transducer (used in the H1 measurement set) are used.

Consider a reference target at the position (r, θ) . The simulated incident acoustic energy at the position of the sphere is proportional to $\bar{p}_{1,\text{sim}}^2(r, \theta)$. Contributions to the intensity from other frequency components than the fundamental are ignored. Since the intensity level of the backscattered wave is approximately 39 dB lower than that of the incident sound field, this wave is assumed to propagate linearly back to the transducer. A similar assumption was made by Li and Zagzebski¹⁵⁸ in an investigation related to medical imaging. The “40 log r ” time varying gain factor (Equation (2.42)) is used by the echo sounder to compensate for two-way spherical spreading and absorption. By applying the square root of $f_{\text{TVG40}}(r)$, one accounts for the attenuation of the back-propagating signal only. A correction for the transducer directivity upon reception remains. The absolute value of the directional factor $H(\theta, \varphi)$ (Section 2.1) can be approximated by

$$|H(\theta, \varphi)| = |H(\theta)| \approx \frac{\bar{p}_{\text{lin}}(r, \theta)}{\bar{p}_{\text{lin}}(r, 0)}. \quad (5.12)$$

A simulation result for TS_{meas} is thus

$$TS_{\text{meas}}(\text{simulated}) = 10 \log_{10} \left[\bar{p}_{\text{sim},1}^2(r, \theta) \cdot r^2 10^{\frac{\alpha r}{10}} \cdot \frac{\bar{p}_{\text{lin}}^2(r, \theta)}{\bar{p}_{\text{lin}}^2(r, 0)} \cdot C \right]. \quad (5.13)$$

The constant factor C accounts for the constants in the calculation of the target strength (Equation (2.40)). Its value is adjusted to fit the measurement results below.

The simulated value for TS_{lin} is obtained by substituting $\bar{p}_{lin}(r, \theta)$ for $\bar{p}_{1,sim}(r, \theta)$ in Equation (5.13),

$$TS_{lin}(\text{simulated}) = 10 \log_{10} \left[\bar{p}_{lin}^2(r, \theta) \cdot r^2 10^{\frac{ar}{10}} \cdot \frac{\bar{p}_{lin}^2(r, \theta)}{\bar{p}_{lin}^2(r, 0)} \cdot C \right]. \quad (5.14)$$

It is seen that Equations (5.13) and (5.14) combine to

$$TS_{meas}(\text{simulated}) - TS_{lin}(\text{simulated}) = NA_{sim}. \quad (5.15)$$

Equations (5.13) and (5.14) are thus consistent with Equation (5.11).

Measurement and simulation results

Simulated values of TS_{lin} and TS_{meas} with $10 \cdot \log_{10} C = -32.3$ are shown with full-drawn curves in Figure 5.12. The upper curve in Figure 5.12a shows the simulated axial value for TS_{lin} . The result is compared with measured target strengths made with the 45 W power setting. Each plotted measurement point indicates the mean value of approximately 50 target strength measurements. The error bars indicate the standard deviation. The average values and standard deviations have been evaluated in the linear domain. The lower full-drawn curve and points shows the simulated (TS_{meas}) and measured values for the 1500 W power setting, respectively.

When the 45 W power setting is used, the measured target strength is approximately the same with the sphere at all distances. The measurement results for the 1500 W power setting are 3 dB–4 dB lower, depending on the distance. It should be noted that the target strength measurements are not expected to be accurate at short ranges because of the limited domain of validity for the time varying gain function^{109,166} (Section 2.1). Differences

between target strength values measured with different power settings for the same target position, however, should not be sensitive to near range effects.

Figure 5.12b shows results from target strength measurements and simulations with the calibration sphere at different angles θ off axis, at distance $r = 9.12$ m from the transducer. The values shown with plus signs are average results from approximately 50 target strength measurements. The beam compensation function has not been applied (cf. Section 2.1). The full-drawn curves show simulation results for TS_{meas} . Two pairs of measurement and simulation results are shown in the figure. The upper curve corresponds to the 150 W power setting, while the lower corresponds to the 1500 W power setting.

The agreement of the simulations used in Figure 5.12 with hydrophone measurements is indicated in Figure 5.5.

The results suggest that the difference in measured target strength obtained with different power settings is mainly due to nonlinear sound propagation, i.e., Equation (5.11) applies approximately. Evidence that the finite bandwidth of the echo sounder system has significant influence on the experienced nonlinear attenuation, is not seen. Depending on how the echo sounder has been calibrated, however, the NA_{sim} values shown in Table 5.9 do not necessarily correspond directly to absolute TS measurement errors due to nonlinear attenuation (cf. Chapter 7).

Although the general sound pressure level in the radiated field is decreased by nonlinear attenuation, it can also be said to increase the width of the main lobe. The sampling volume for volume backscattering measurements (Section 2.1) is thus effectively enlarged. The excess attenuation integrated over the sound beam will be discussed in Chapter 7.

5.3.4. Comparison with earlier works

Tichy *et al.*²³⁴ made measurements of the fundamental frequency component in the axial field of a 200 kHz EK60 echo sounder with power settings 100 W, 1000 W, and 2000 W. They compared their experimental results with Bergen Code simulations.²⁹ The results for the 1000 W power setting in Figure 5.11 seem generally 0.3 dB lower (i.e., the attenuation seems stronger) than in the data presented by Tichy *et al.* Their definition of “nonlinear loss” is however not clearly stated, and it might be different from that used in the present work. Tichy *et al.* refer to the 1000 W power setting as 550 W acoustic output power.²³⁴ Simmonds and MacLennan²²³ point out that the waveforms presented by Tichy *et al.*²³⁴ seem uncharacteristic of finite-amplitude sound propagation. This is presumably due to the frequency dependence of the hydrophone sensitivity, which distorts the measured waveform. This distortion should not be of any importance to measurements of nonlinear attenuation at the fundamental frequency.

Shooter *et al.*²²¹ made measurements of nonlinear attenuation along the axis of a 454 kHz sound beam in fresh water. Bergen Code simulations with approximate parameters taken from their article (“Shooter 1” and “Shooter 2” in Table 5.8) seem to agree within 0.5 dB with their measurement results except for the two shortest ranges (Figure 5.13). At the 0.76 yd and 1.8 yd distances, agreement within 0.3 dB is seen for the difference between nonlinear sound propagation and linear theory, but the overall simulated sound pressure levels are approximately 1 dB higher in the simulations than what was measured by Shooter *et al.*²²¹

In Figures 5.14 and 5.15 Bergen Code simulations are compared with experimental results from Lockwood *et al.*¹⁶³ (their Figures 1 and 2, corresponding respectively to the “Lockwood 1” and “Lockwood 2” parameter sets in Table 5.8). A similar comparison was made by Hamilton *et al.*¹¹⁴ with another set of measurements reported by Lockwood.¹⁶² As also reported by Hamilton *et al.*, good qualitative agreement is seen between the simulated and

measured width of the main lobe and between the positions of the side lobes. The side lobe levels seem somewhat underestimated by the simulations. A narrow peak (“finger”⁴²) in the level of the second harmonic component is seen between the main lobe and the first side lobe in Figure 5.15. This feature was first reported by Lockwood *et al.*¹⁶³ and later described theoretically by Berntsen *et al.*⁴² Hamilton *et al.*¹¹⁴ reported some discrepancies between the measured and calculated sound pressure amplitude on the axis of the sound beam. This underlines the importance of combining experimental and theoretical results when attempting to predict nonlinear sound propagation accurately.

5.3.5. Figures

200 kHz, H1 measurements

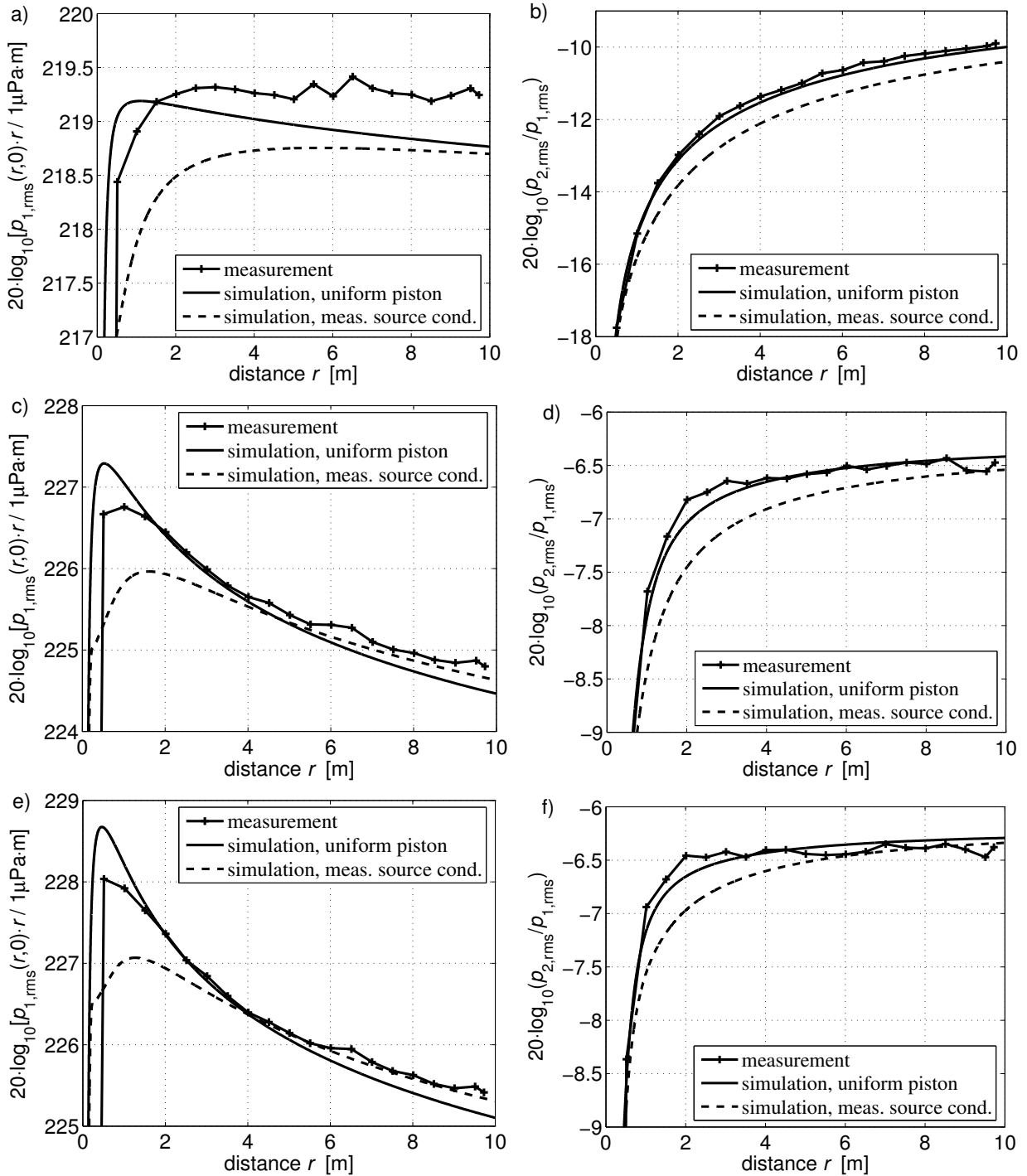


Figure 5.5. Measured (+) and simulated (—, - -) axial fields for the H1 measurement set (cf. Table 5.1). The sound pressure amplitude of the fundamental frequency component (left) has been multiplied with distance from the sound source. The plots on the right-hand side show the amplitude of the fundamental frequency component relative to that of the fundamental. a), b): 150 W, c), d): 1050 W, e), f): 1500 W.

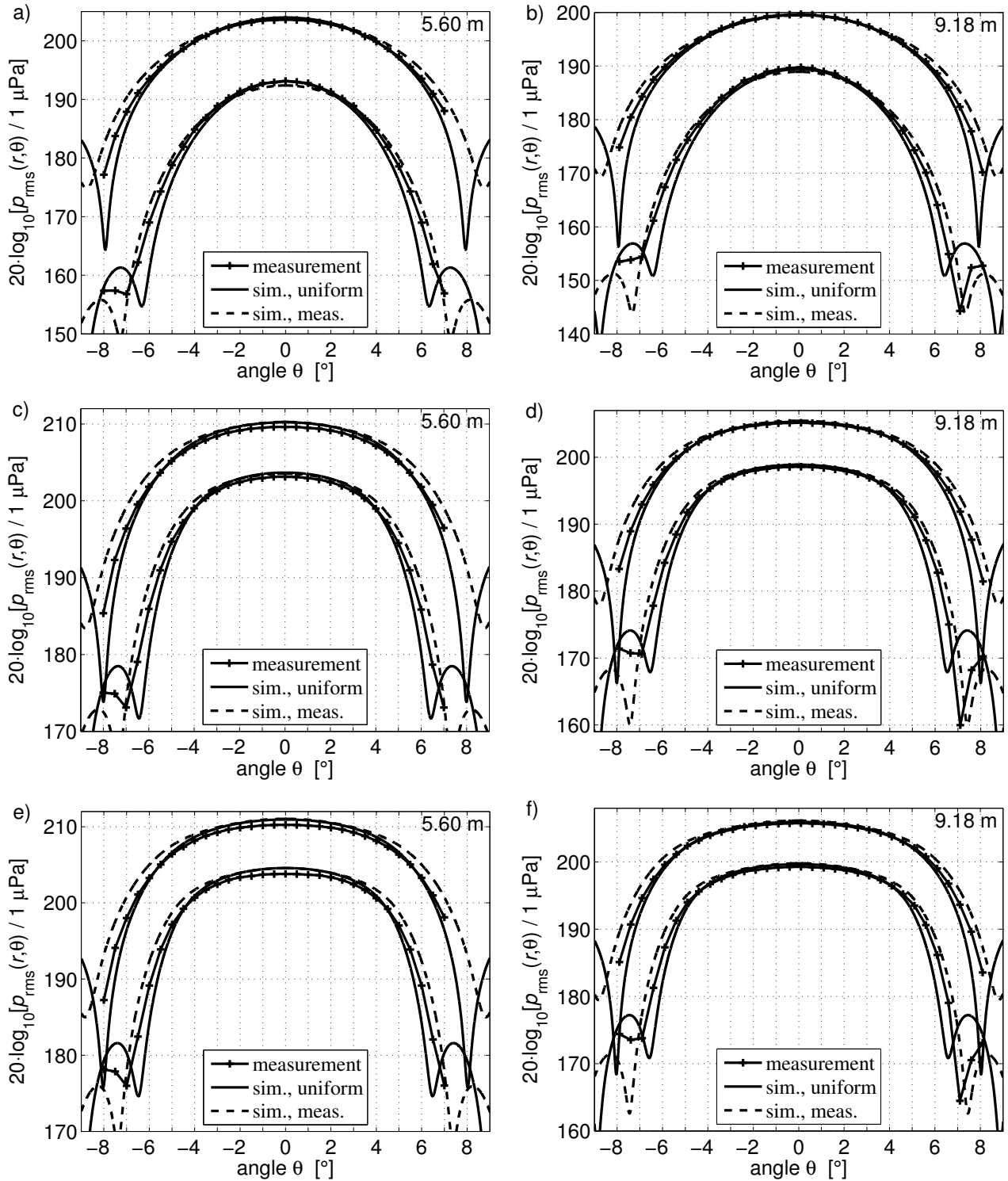


Figure 5.6. Measured (+) and simulated (—, - -) directivity for the H1 measurement set (cf. Table 5.1). Results for both the fundamental and second harmonic frequency components are shown in each plot, the fundamental having the highest amplitude near the axis. The leftmost plots are taken 5.60 m from the sound source, while those on the right hand side are for 9.18 m distance. Figures a) and b) show results for the 150 W power setting, c) and d) the 1050 W power setting, and e) and f) the 1500 W power setting.

200 kHz, H3 measurements

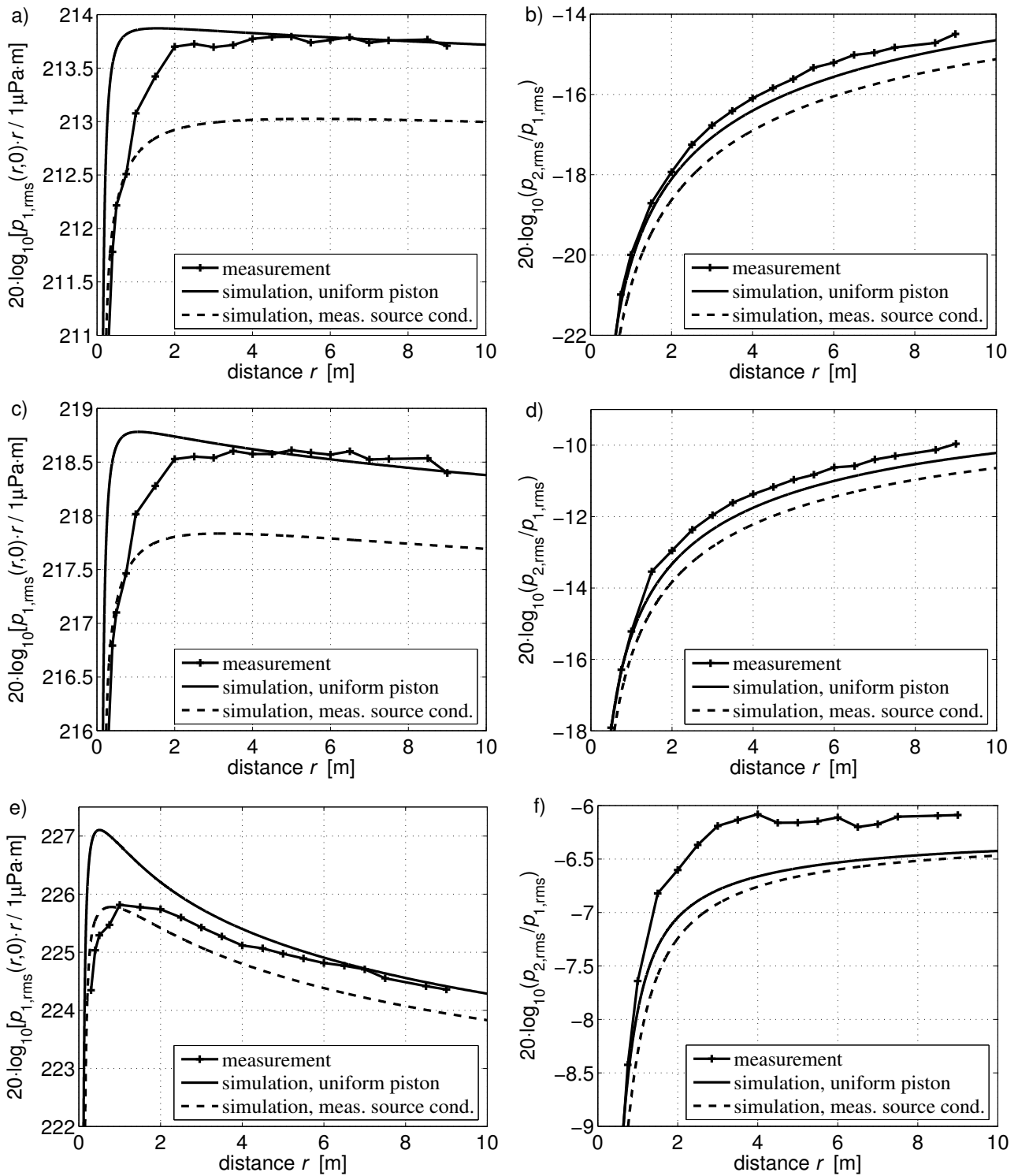


Figure 5.7. Measured (+) and simulated (—, - -) axial fields for the H3 measurement set (cf. Table 5.1). The sound pressure amplitude of the fundamental frequency component (left) has been multiplied with distance from the sound source. The plots on the right-hand side show the amplitude of the fundamental frequency component relative to that of the fundamental. a), b): 50 W, c), d): 150 W, e), f): 1000 W.

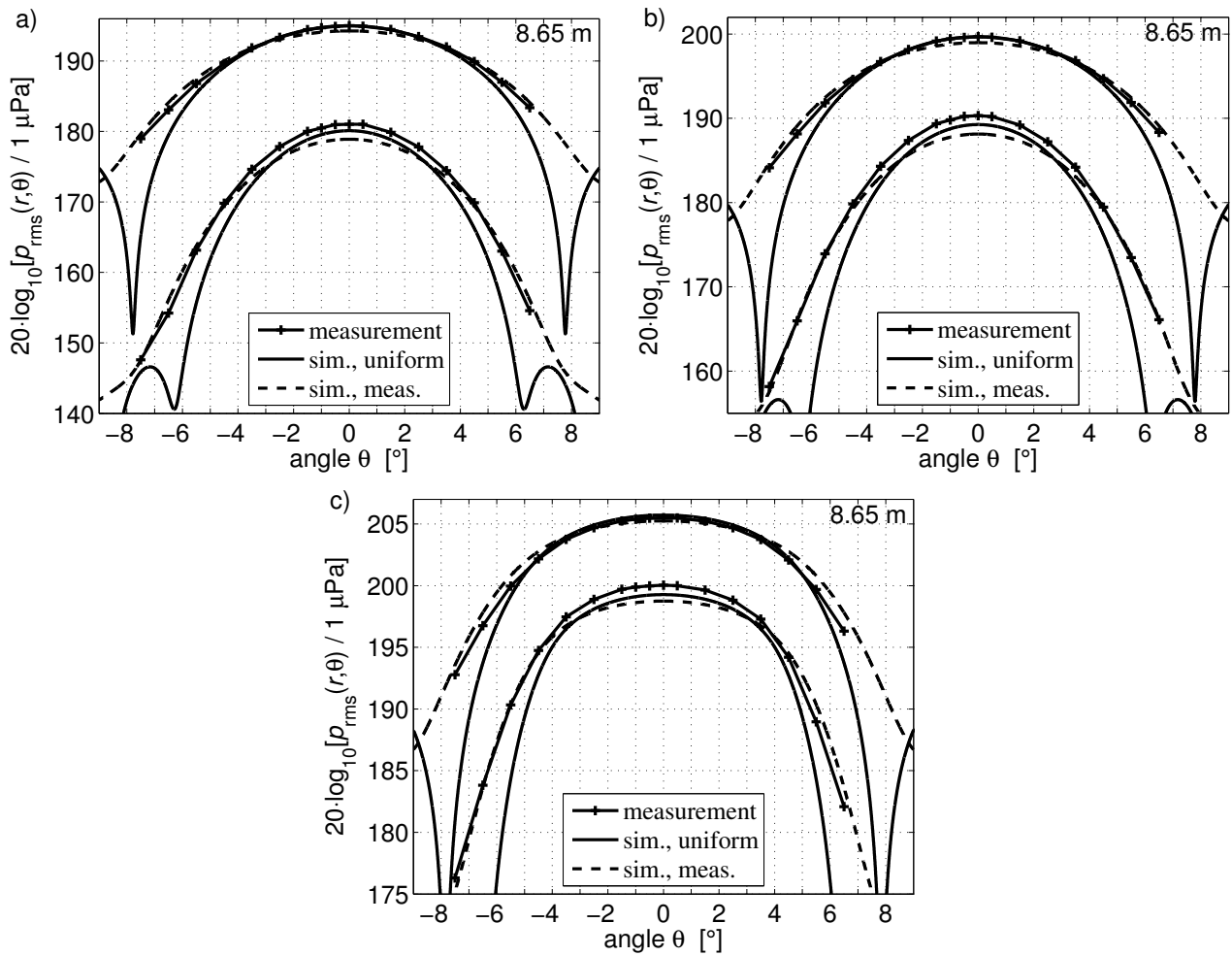


Figure 5.8. Measured (+) and simulated (—, - -) directivity for the H3 measurement set, for the 50 W (a), 150 W (b), and 1000 W (c) power settings. The pressure amplitudes of both the fundamental and second harmonic frequency components are shown in each plot, the fundamental being the highest. The distance from the sound source is 8.65 m.

120 kHz, H2 measurements

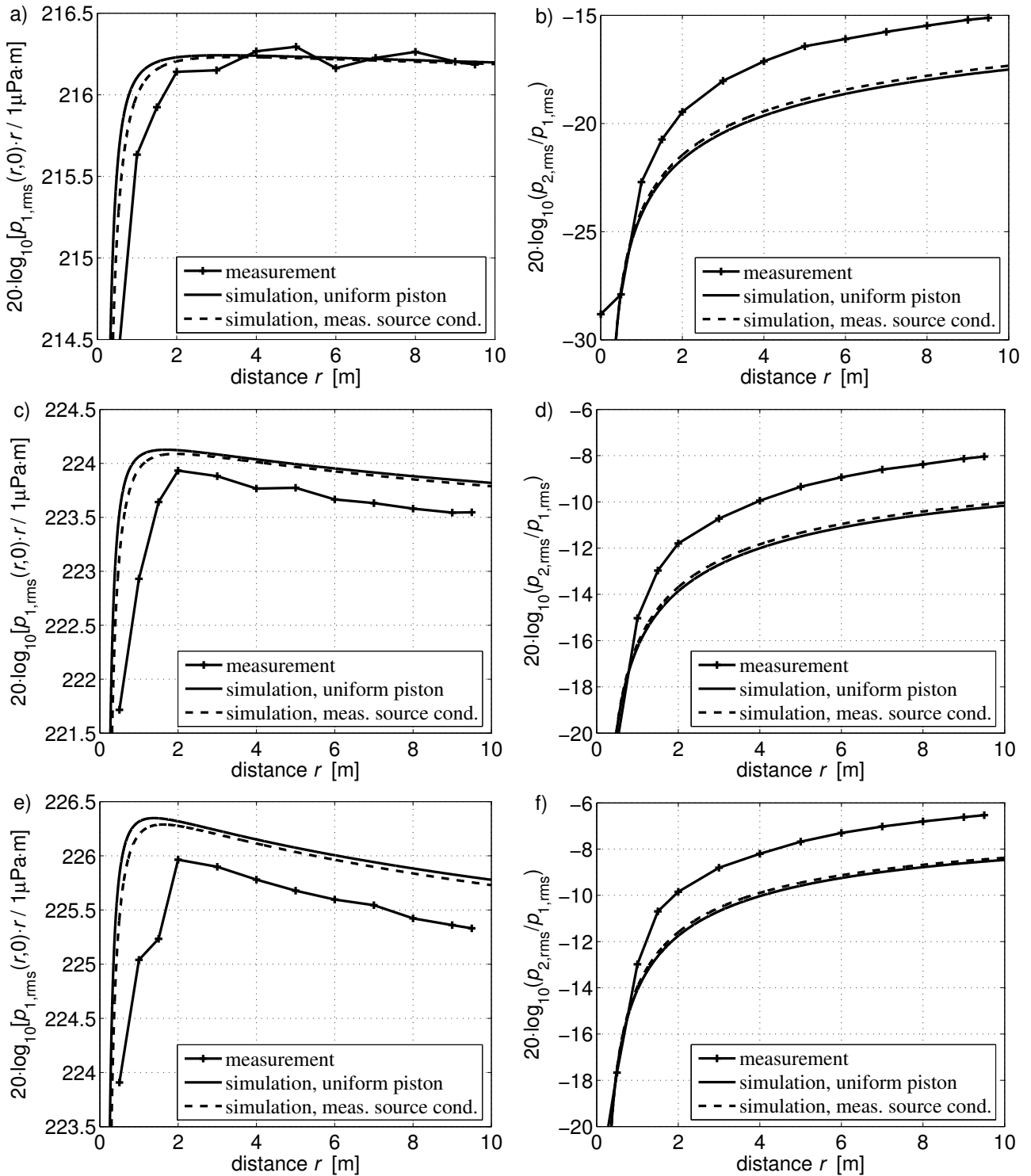


Figure 5.9. Measured (+) and simulated (—, - -) axial fields for the H2 measurement set (ES120-7C transducer, cf. Table 5.1). The sound pressure amplitude of the fundamental frequency component (left) has been multiplied with distance from the sound source. The plots on the right-hand side show the amplitude of the fundamental frequency component relative to that of the fundamental. a), b): 100 W, c), d): 600 W, e), f): 1000 W.

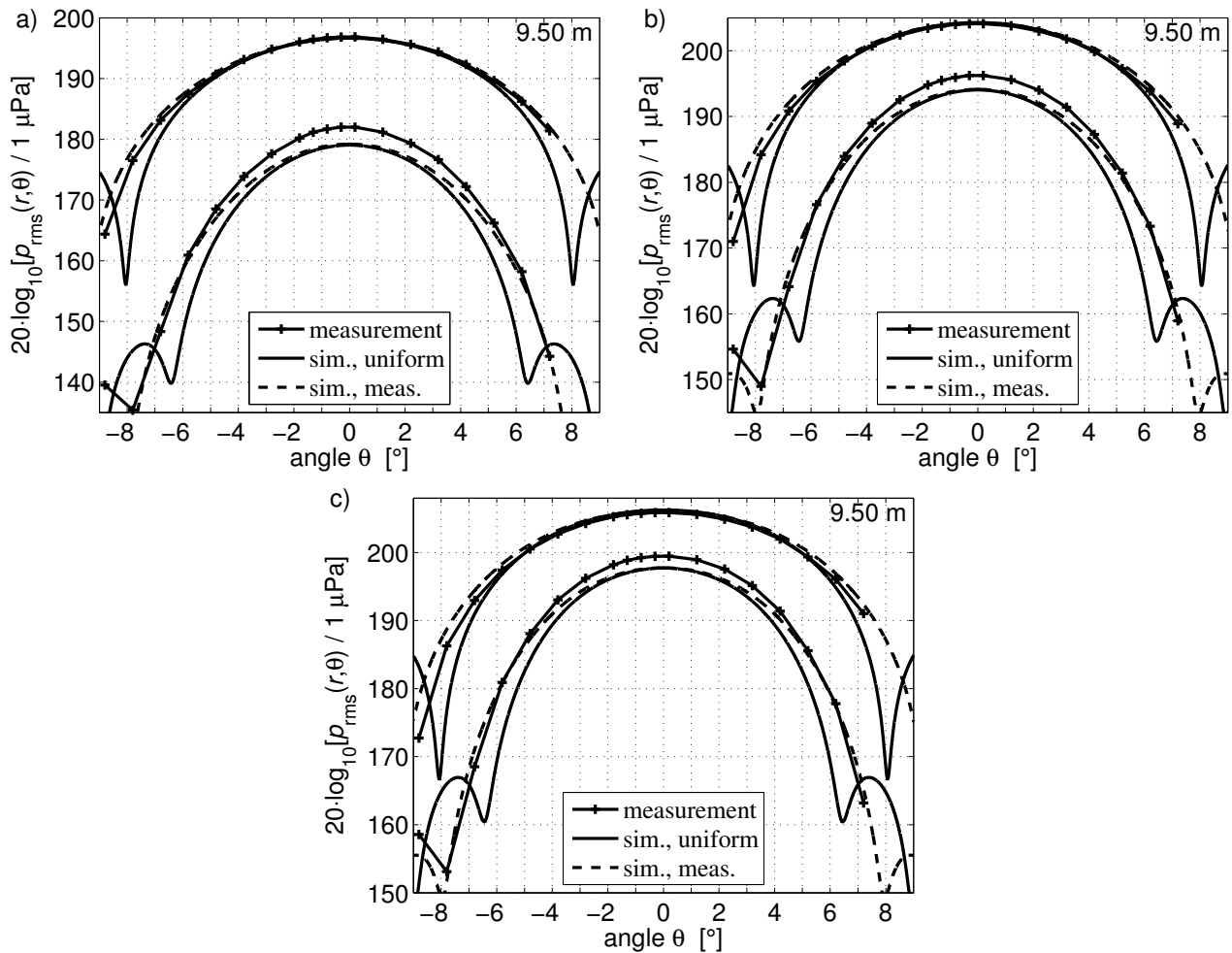


Figure 5.10. Measured (+) and simulated (—, - -) directivity for the H2 measurement set, with power settings 100 W (a), 600 W (b), and 1000 W (c). The pressure amplitudes of both the fundamental and second harmonic frequency components are shown in each plot, the fundamental being the highest. The distance from the sound source is 9.50 m.

Nonlinear attenuation

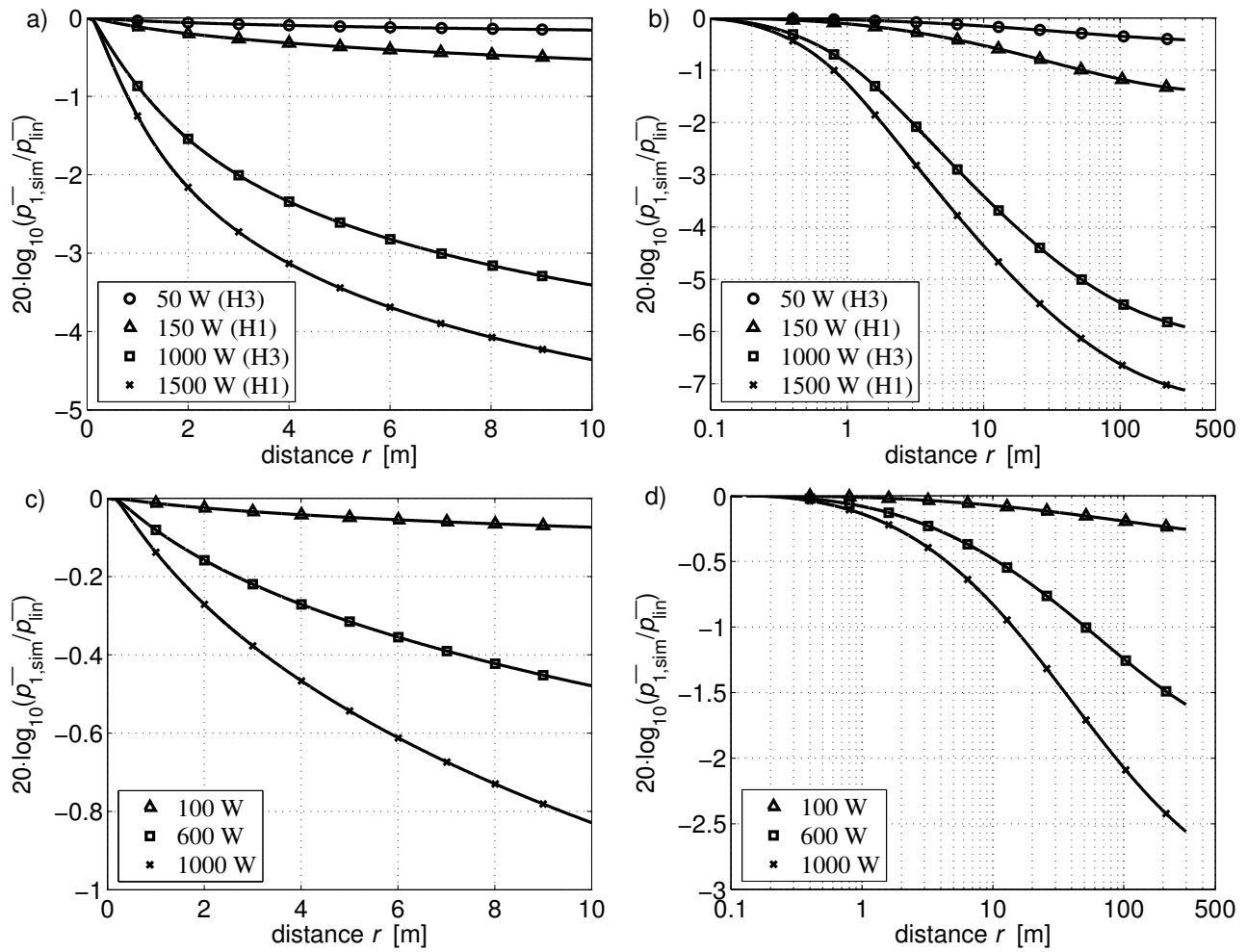


Figure 5.11. Ratio between the simulated axial sound pressure level for the fundamental frequency component and a corresponding simulation result without accounting for nonlinear distortion. a) Results for 200 kHz fundamental frequency, covering the power settings used in the present work. b) Same as on the left, but including longer distances. Corresponding results from the 120 kHz simulations are shown in Figures c) and d).

Calibration sphere measurements

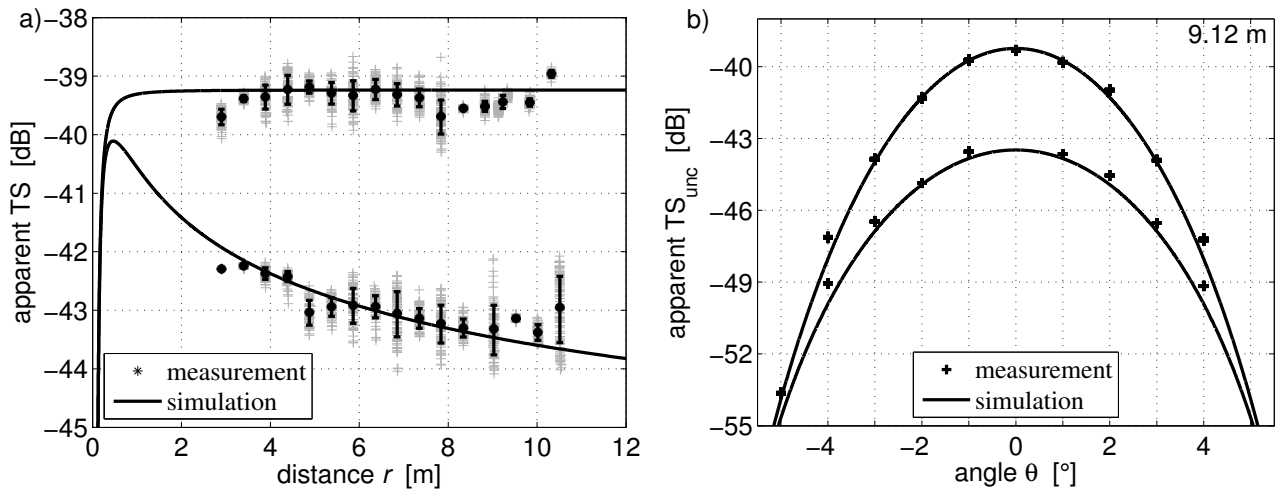


Figure 5.12. Measured target strength and simulations for a 200 kHz echo sounder. a) Target strength along axis, power settings 45 W (upper curve and data points) and 1500 W (lower). b) Directivity in the along ship direction at 9.12 m distance. 150 W (upper curve and data points) and 1500 W (lower) power settings.

Comparison with Lockwood et al. and Shooter et al.

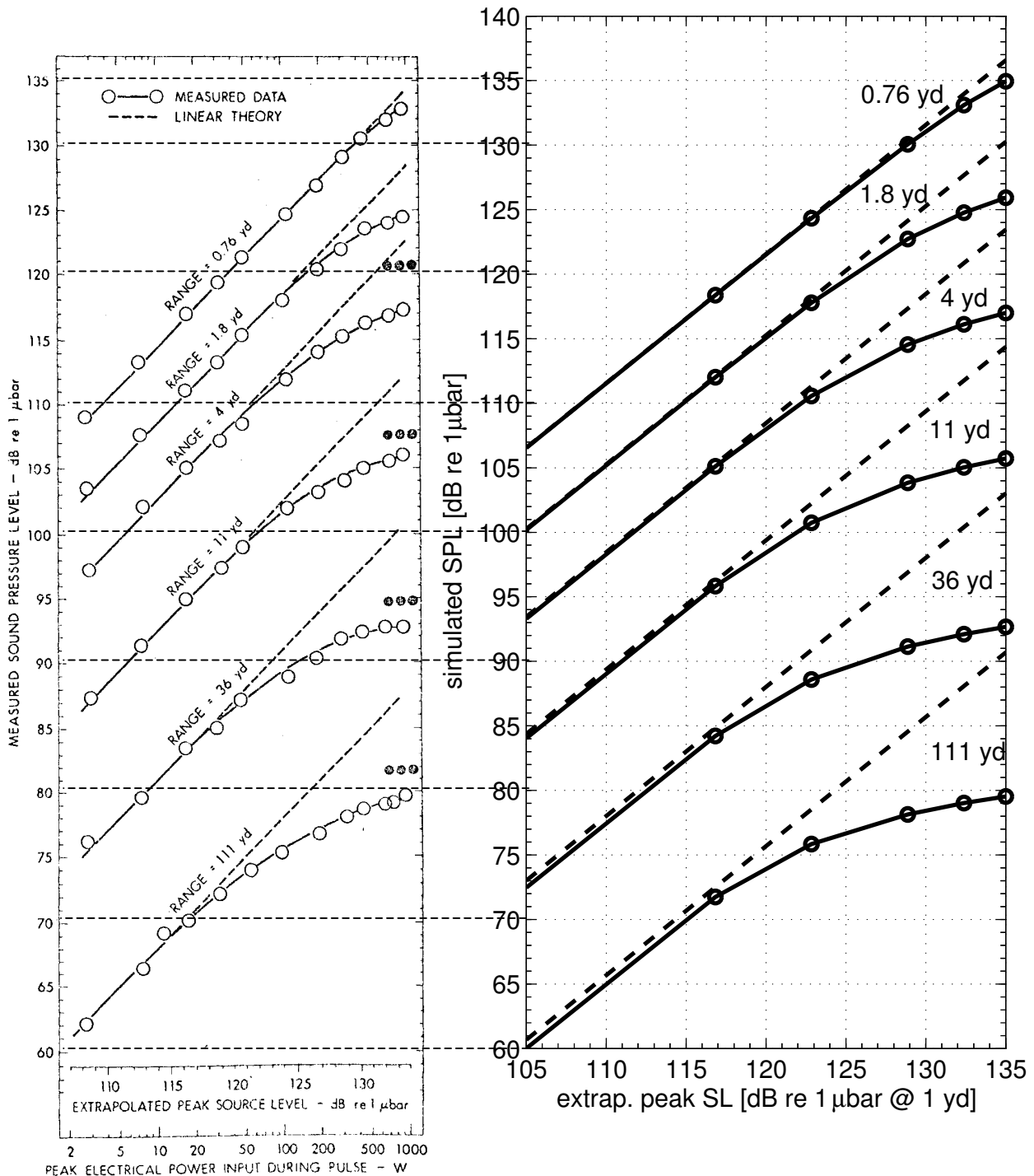


Figure 5.13. Comparison between measurement results obtained by Shooter *et al.*²²¹ (their Figure 6) (left) and corresponding simulations made with the Bergen Code program used in the present work (right). The leftmost plot is reprinted with permission from Shooter, Muir, and Blackstock, *J. Acoust. Soc. Am.* 55(1), 54-62 (1974). Copyright 1974, Acoustical Society of America.

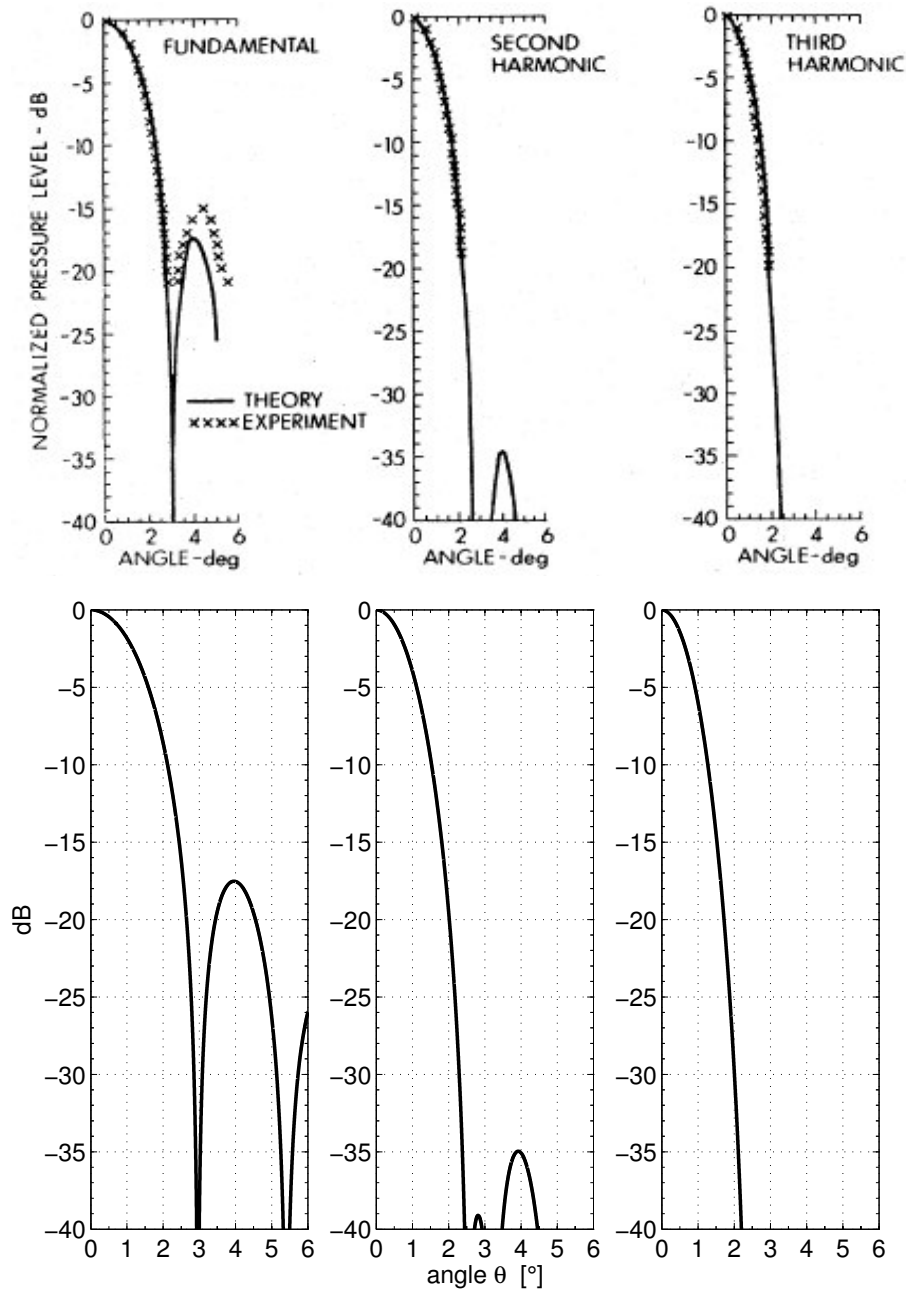


Figure 5.14. Comparison between Figure 1 in the paper by Lockwood *et al.*¹⁶³ (top) and simulation results using the set of parameters labelled "Lockwood 1" in Table 5.8 (bottom graph).

The upper graph is reprinted with permission from Lockwood, Muir, and Blackstock, *J. Acoust. Soc. Am.* 53(4), 1148-1153 (1973). Copyright 1973, Acoustical Society of America.

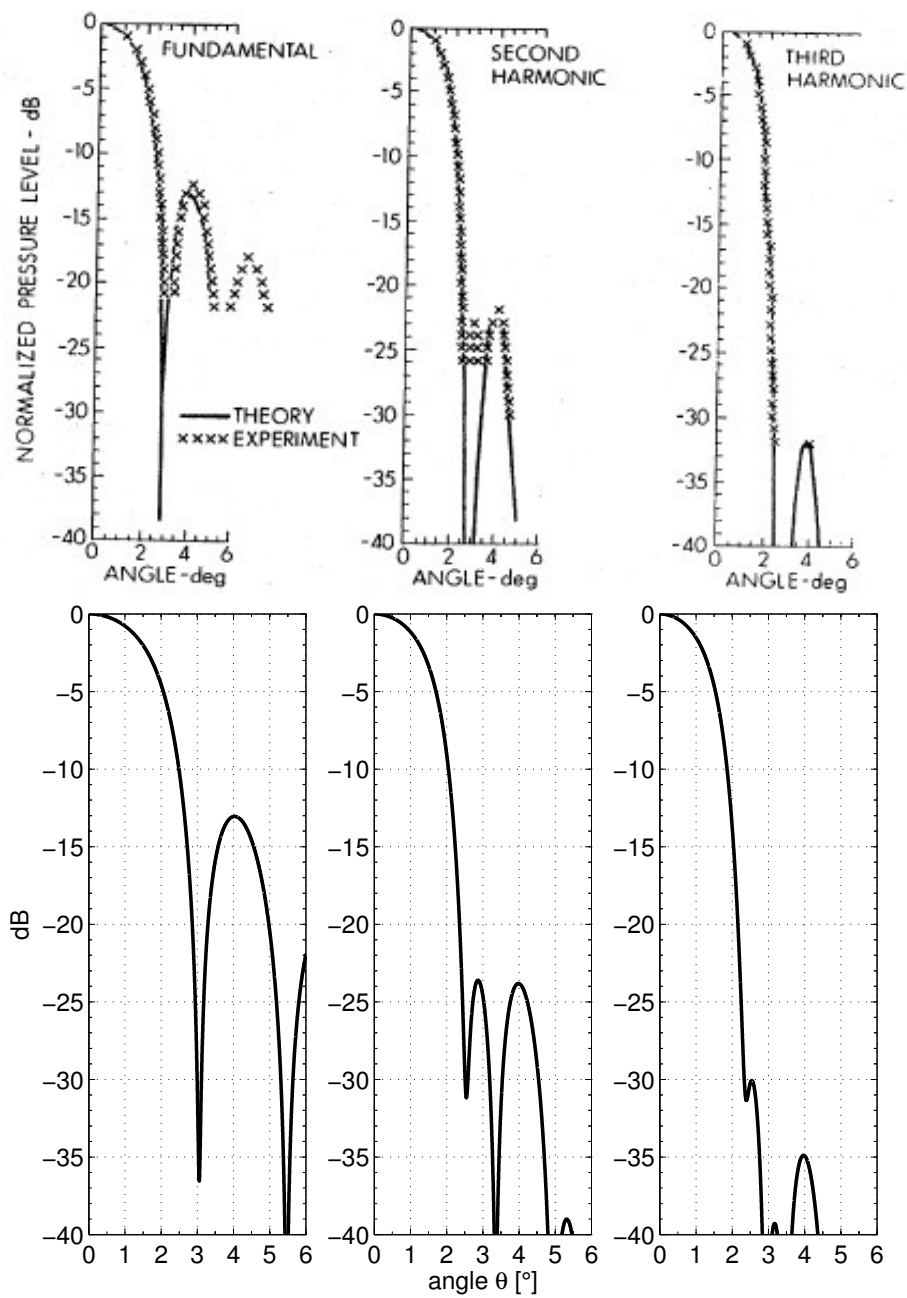


Figure 5.15. Comparison between Figure 2 in the paper by Lockwood *et al.*¹⁶³ (top) and simulation results using the set of parameters labelled "Lockwood 2" in Table 5.8 (bottom). The upper graph is reprinted with permission from Lockwood, Muir, and Blackstock, *J. Acoust. Soc. Am.* 53(4), 1148-1153 (1973). Copyright 1973, Acoustical Society of America.

Chapter 6. Sound propagation in seawater

The acoustical properties that influence nonlinear effects are somewhat different in seawater and fresh water. The sound speed, nonlinearity coefficient, density, and absorption coefficient all depend on salinity. Acoustic methods for fisheries research are widely used in the sea. Empirical results for water with a range of relevant salinities and temperatures are needed to establish a basis for



quantifying the nonlinear attenuation in seawater. Also of interest is measurements of nonlinear sound propagation over longer distances than could be obtained in the available indoor water tanks.

Three series of sound propagation measurements are made in coastal waters near Bergen, Norway (Section 6.1). A hydrophone is used for measuring the amplitudes of the fundamental and second harmonic frequency components at distances up to approximately 10 m. Target strength measurements with calibration spheres as targets are also performed, in order to investigate the nonlinear attenuation at distances up to 50 m. Numerical simulations were made for comparison with each set of experimental data, with input parameters based on CTD measurements. The simulations are described in Section 6.2.

The experimental and numerical results are presented and compared in Section 6.3. The agreement between measured and simulated sound pressure levels for the fundamental and second harmonic frequency components is assessed. Simulation results are used to predict the difference between

“apparent” target strength measured by the echo sounder with different power settings. These predictions are compared with the measurements of calibration sphere target strength. Values for the nonlinear attenuation along the sound beam axis are calculated from the simulation results, and its consequence for target strength measurements is discussed.

6.1. Measurements in seawater

Table 6.1 gives an overview of the measurements that have been made in seawater for the present work. The E1, E2, G1, and G3 measurement sets are treated in the present chapter, while the details of the G2 measurements are discussed in Chapter 7.

6.1.1. Hydrophone measurements

The E1 and E2b measurement sets are hydrophone measurements made at the Marine Biological Station Espejord near Bergen, Norway. A floating stage moored close to the shore provides access to approximately 14 m deep, relatively calm water (Figures 6.1 and 6.2). The salinity is somewhat lower than in the open sea (Figure 6.7). This is often also the case on locations that are suitable for calibrating fisheries research echo sounders.

Conductivity and temperature profiles were obtained once each day of measurements with a SAIV SD204 CTD probe. Results are shown in Figure 6.7, with calculated values for salinity,⁹⁴ sound speed,⁷⁰ density,⁹⁴ absorption at the fundamental frequency,¹⁰⁶ and the nonlinearity coefficient.⁷⁹ On the day of the E1a measurements (Table 6.1), approximately 12 m visibility was measured by lowering a white Secchi disc until it was invisible from above the sea surface.

Table 6.1. Overview of nonlinear sound propagation measurements in seawater. The number of axial field and beam pattern measurements performed in each measurement set, and the types of measurements, are indicated.

| measurement set | date | frequency | axial field | beam pattern | measurement method |
|-----------------|----------|-----------|-------------|--------------|--------------------|
| E1a | 15.03.05 | 200 kHz | 1 | - | hydrophone |
| E1b | 16.03.05 | 200 kHz | 1 | 1 | hydrophone |
| E2a | 08.03.05 | 120 kHz | - | 1 | cal. sphere |
| E2b | 09.03.05 | 120 kHz | 1 | 1 | hydrophone |
| G1a | 19.10.04 | 200 kHz | 1 | 1 | cal. sphere |
| G1b | 20.10.04 | 120 kHz | - | 1 | cal. sphere |
| G2a | 04.11.04 | both | - | - | s_a (Chapter 7) |
| G2b | 05.11.04 | both | - | - | s_a (Chapter 7) |
| G3a | 18.01.06 | 200 kHz | 1 | 5 | cal. sphere |
| G3b | 19.01.06 | 120 kHz | 1 | 2 | cal. sphere |



Figure 6.1. Floating stage used as a measurement platform at the Marine Biological Station Espegrend.



Figure 6.2. Floating stage used as a measurement platform at the Marine Biological Station Espegrend.

A sketch of the measurement set-up is shown in Figure 6.3. Simrad EK60 echo sounders with the ES120-7C (s/n 230) and ES200-7C (s/n 120) transducers (Table 4.1) were used as sound sources. The transducers were mounted with their back to an aluminium plate, pointing downward (Figure 6.4). A thin fresh water layer at the surface was avoided by lowering the transducers to 1 m depth. Measured effective voltage amplitudes U_t across the transducer terminals upon transmission are shown in Tables 6.2 and 6.3 for different echo sounder power settings. The tables also show source levels, transmit voltage responses, and source condition pressure amplitudes used for simulations. These are calculated from the axial sound pressure amplitudes measured with low echo sounder power settings, the same way as described in Sections 3.2 and 5.2.

The Reson TC4034 hydrophone described in Section 5.1 was mounted in the steel tube shown in Figure 5.2. A suspension ring was placed 0.40 m behind the acoustic centre of the hydrophone, and a mass was attached to the rear end of the tube to keep the hydrophone vertical (Figure 6.5). Backscatter from the suspension ring did not reach the hydrophone in time to interfere with the measured direct signal from the echo sounder transducer. Three monofilament nylon lines were tied to the suspension ring, and the hydrophone was

positioned by means of electrical winches of a type that is commonly used for echo sounder calibration on fisheries research vessels (Figure 6.6).

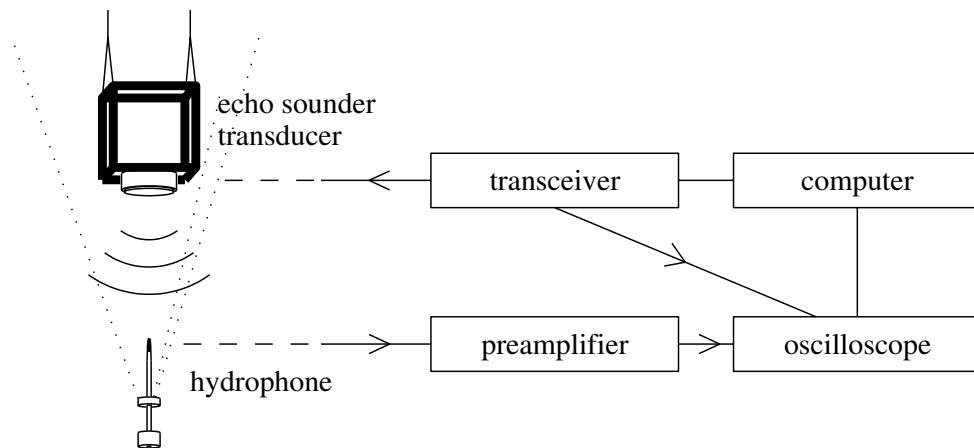


Figure 6.3. Experimental set-up for hydrophone measurements (E1, E2).

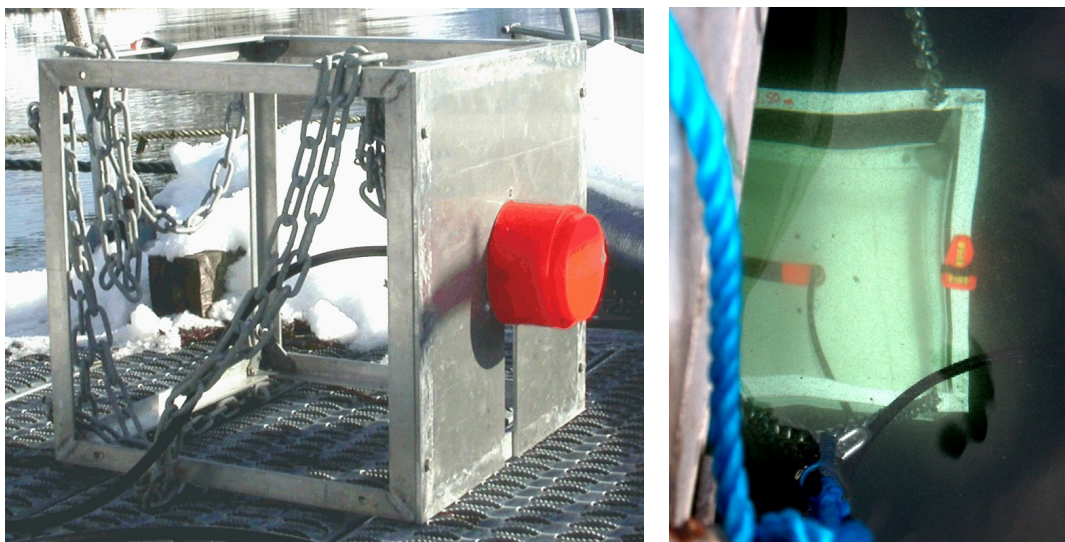


Figure 6.4. Left: ES200-7C echo sounder transducer mounted for measurements at Espjrend. Right: Transducer lowered to 1 m depth.

The orientation of the hydrophone assembly was not determined precisely (Figures 6.3 and 6.5). Care was taken to minimize the pull in the hydrophone cable. The three winches were positioned approximately at the corners of an equilateral triangle with the echo sounder transducer at its centre, in order to minimize the difference in tension between the suspension lines. The standard uncertainty in the angle between the hydrophone axis and the direction of the

incident sound wave was estimated to 5°. The directivity of the hydrophone is then assumed to contribute with 1.3 dB to the uncertainty in its sensitivity for the second harmonic frequency components.¹¹ At the fundamental frequencies, the uncertainty contribution is estimated to 0.3 dB⁹ (Table 6.4).

Table 6.2. Parameters for the sound transmission from the 200 kHz echo sounder. Transmit effective voltage across the transducer terminals, measured axial effective sound pressure at $r = 1$ m for the lowest power setting, calculated source condition amplitudes $p_{0,rms}$, transmit voltage response, and linear equivalent source levels.

| EK60 power setting [W] | effective voltage U_t [V] | sound pressure $p_{rms}(1\text{ m})$ [kPa] | source condition sound pressure $p_{0,rms}$ [MPa] | TVR [dB re 1 μPa/V] | SL [dB re 1 μPa @ 1 m] |
|---|---|--|---|---|--|
| 100 | 39.6 ± 0.2 | 72 ± 4 | 0.17±0.01 | 185.2 ± 0.5 | 217.1 ± 0.5 |
| 200 | 57.0 ± 0.1 | - | 0.25±0.01 | - | 220.3 ± 0.5 |
| 400 | 81.5 ± 0.4 | - | 0.35±0.02 | - | 223.4 ± 0.5 |
| 500 | 91.4 ± 0.2 | - | 0.39±0.02 | - | 224.4 ± 0.5 |
| 600 | 100.3 ± 0.2 | - | 0.43±0.03 | - | 225.2 ± 0.5 |
| 800 | 116.0 ± 0.2 | - | 0.50±0.03 | - | 226.5 ± 0.5 |
| 1000 | 129.8 ± 0.3 | - | 0.56±0.03 | - | 227.5 ± 0.5 |

The echo sounder did not see the hydrophone, but interpreted the suspension ring (Figure 6.5) as a single target. Range and direction information from the echo sounder was used to determine the hydrophone's position, subtracting the 0.40 m distance between the suspension ring and the acoustic centre of the hydrophone from the measured depth. The average sound speed between 1 m and 11 m depths was entered in the echo sounder software and thus used for the distance measurement. At 5 m distance, the above-mentioned 5° uncertainty in the hydrophone orientation represents a 0.4° uncertainty for the hydrophone's position in the sound beam. The uncertainty in the distance measurement is assumed approximately equal to 1%. With the hydrophone at small angles off the sound beam axis, its positioning uncertainty combined with the echo

sounder transducer directivity are estimated to yield a standard uncertainty contribution of 0.3 dB (Table 6.4).

Table 6.3. Parameters for the sound transmission from the 120 kHz echo sounder. Transmit effective voltage across the transducer terminals, measured axial effective sound pressure at $r = 1$ m for the lowest power setting, calculated source condition amplitudes $p_{0,rms}$, transmit voltage response, and linear equivalent source levels.

| EK60 power setting [W] | effective voltage U_t [V] | sound pressure $p_{rms}(1\text{ m})$ [kPa] | source condition sound pressure $p_{0,rms}$ [MPa] | TVR [dB re 1 μPa/V] | SL [dB re 1 μPa @ 1 m] |
|---|---|--|---|---|--|
| 100 | 39.7 ± 0.5 | 62 ± 5 | 0.085 ± 0.007 | 183.9 ± 0.8 | 215.8 ± 0.7 |
| 200 | 57.2 ± 0.6 | - | 0.12 ± 0.01 | - | 219.0 ± 0.8 |
| 400 | 81.9 ± 0.9 | - | 0.18 ± 0.02 | - | 222.1 ± 0.8 |
| 500 | 92.4 ± 0.9 | - | 0.20 ± 0.02 | - | 223.2 ± 0.8 |
| 600 | 101 ± 1 | - | 0.22 ± 0.02 | - | 224.0 ± 0.8 |
| 800 | 117 ± 1 | - | 0.25 ± 0.02 | - | 225.2 ± 0.8 |
| 1000 | 131 ± 1 | - | 0.28 ± 0.02 | - | 226.2 ± 0.8 |

The hydrophone was calibrated at temperature¹¹ (19.0 ± 0.4)°C (Appendix C), while the temperature during the seawater measurements was between 3.6°C and 4.6°C (Figure 6.7a). Measurements that have been made with a hydrophone of the same model suggest that the temperature difference should yield a change of 0.3 dB or less in the hydrophone sensitivity.¹⁴ This constitutes an additional uncertainty contribution that was insignificant for the fresh water measurements described in the previous chapter. Combined with the standard uncertainty in the hydrophone calibration (Table 5.3), the relative standard uncertainty for the axial hydrophone sensitivity becomes 0.5 dB for the fundamental frequency components and 0.8 dB for the second harmonics (Table 6.4).

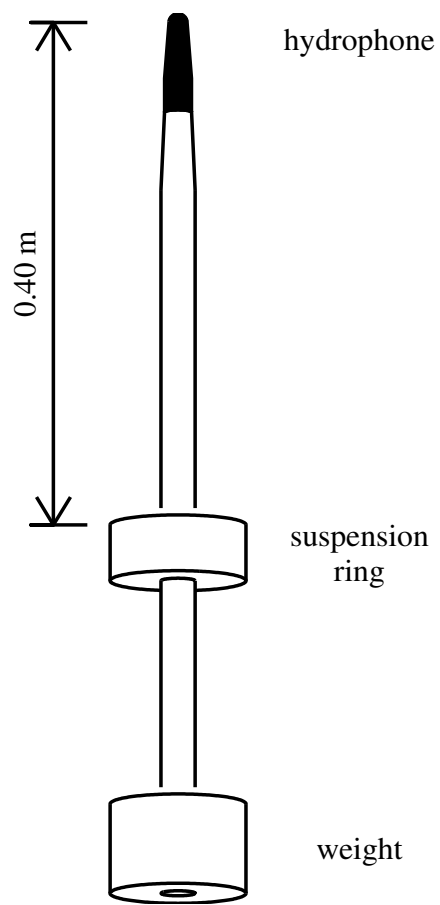


Figure 6.5. Hydrophone assembly.

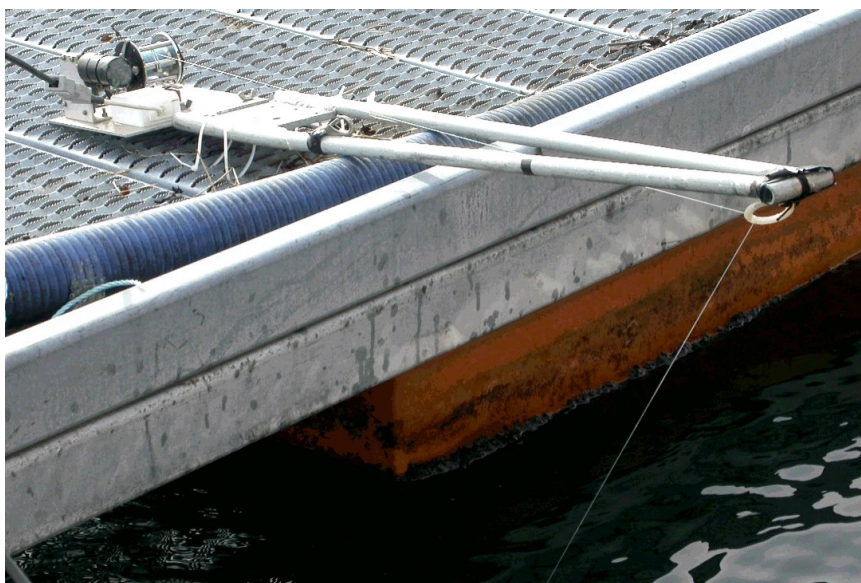


Figure 6.6. Winch for positioning of hydrophone and calibration sphere.

A Reson VP1000 voltage preamplifier was used at the output terminals of the hydrophone's integral 10 m cable. The load of its 100 M Ω , 2.5 pF input reduces the hydrophone sensitivity with approximately 0.01 dB.²¹⁴ The preamplifier is set to 0 dB gain, and acts as a buffer between the hydrophone and a 15 m long RG-58 coaxial cable to a Tektronix TDS-220 digital sampling oscilloscope. Calibration measurements on the preamplifier with the coaxial cable indicate that the voltage across the hydrophone terminals is 1.98 ± 0.02 times the voltage at the oscilloscope. The oscilloscope is coupled in parallel with a 50 Ω terminating resistance. The uncertainty in the amplification factor corresponds to a 0.09 dB relative standard uncertainty (Table 6.4).

The oscilloscope was used for digitising the received signal and transferring the acquired waveforms to a personal computer that was also used to control the echo sounder (Figure 6.3). According to Equation (5.3), the signal-to-noise ratio SNR_{ADC} due to ideal 8-bit quantization is 49 dB for a signal that spans 90% of the selected voltage range. For each hydrophone position and power setting, 10 individual waveforms were collected immediately after each other. The sound pressure amplitudes for the fundamental and second harmonic frequency components were extracted from stable regions of each acquired waveform. The signals were multiplied with a flat-top window and zero padded the same way as for the fresh water measurements (Section 5.1), to obtain 16 000-point discrete Fourier transforms (Equation (4.4)). The calibration factors shown in Table 5.3 were used to obtain sound pressure amplitudes.

To minimize noise and movements, the experiment was interrupted each time a boat was seen near the measurement site. The observed ambient noise was 0.1 dB below the weakest measured echo sounder signal. The uncertainty contributions for the hydrophone measurements are summarized in Table 6.4. The combined relative standard uncertainty of the measurements is estimated to ± 0.7 dB for the fundamental and ± 1.7 dB for the second harmonic frequency component.

Table 6.4. Uncertainty budget for the hydrophone measurements in seawater.

Fundamental frequency component

| source | contrib. rel. standard uncertainty | contribution to relative variance |
|--|---|--|
| hydrophone directivity and angle | 0.3 dB | $1.2 \cdot 10^{-3}$ |
| hydrophone position uncertainty | 0.3 dB | $1.2 \cdot 10^{-3}$ |
| hydrophone sensitivity | 0.5 dB | $3.5 \cdot 10^{-3}$ |
| electrical loading of hydrophone | 0.01 dB | $1.3 \cdot 10^{-6}$ |
| preamplifier gain | 0.09 dB | $1.1 \cdot 10^{-4}$ |
| ambient noise | 0.1 dB | $1.3 \cdot 10^{-4}$ |
| quantization and postprocessing | 0.03 dB | $1.3 \cdot 10^{-5}$ |
| sum of relative variances: | | $6.2 \cdot 10^{-3}$ |
| relative combined standard uncertainty: | | 0.079 |
| relative combined standard uncertainty (dB): | | 0.7 dB |
| relative expanded uncertainty (95% confidence level, dB): | | 1.3 dB |

Second harmonic frequency component

| source | contrib. rel. standard uncertainty | contribution to relative variance |
|--|---|--|
| hydrophone directivity and angle | 1.3 dB | $2.6 \cdot 10^{-2}$ |
| hydrophone position uncertainty | 0.3 dB | $1.2 \cdot 10^{-3}$ |
| hydrophone sensitivity | 0.8 dB | $9.3 \cdot 10^{-3}$ |
| electrical loading of hydrophone | 0.01 dB | $1.3 \cdot 10^{-6}$ |
| preamplifier gain | 0.09 dB | $1.1 \cdot 10^{-4}$ |
| ambient noise | 0.8 dB | $9.3 \cdot 10^{-3}$ |
| quantization and postprocessing | 0.3 dB | $1.2 \cdot 10^{-3}$ |
| sum of relative variances: | | 0.047 |
| relative combined standard uncertainty: | | 0.22 |
| relative combined standard uncertainty (dB): | | 1.7 dB |
| relative expanded uncertainty (95% confidence level, dB): | | 3.1 dB |

6.1.2. Calibration sphere measurements

Echo sounder measurements with a calibration sphere as a target were made at Espeland and from the research vessel G. O. Sars (Figure 6.10). 38.1-mm-diameter spheres made of tungsten carbide with 6% cobalt binder were used in both cases. The calibration sphere was hung under the echo sounder transducer with three monofilament nylon lines and positioned by means of electric winches. Split-beam echo sounders are used throughout the present work. Single echo detection data were used to determine the position of the calibration sphere relative to the transducer.

The E2a measurements (Table 6.1) were performed under the same conditions as the hydrophone measurements described above. CTD data taken the same day as the E2a measurements are shown in Figure 6.7.

The G1 and G3 measurements were made from the research vessel G. O. Sars (Figure 6.10) while anchored in a small, sheltered bay at Uggdalseid, south of Bergen, Norway. Results from CTD measurements are shown in Figures 6.8 and 6.9. The echo sounder transducers were 9 m below the water surface. Average sound speed and temperature values between 9 m and 34 m depths were inserted in the ER60 echo sounder software as a basis for distance and angle calculations.

The echo sounders were calibrated immediately prior to all the reported measurements. This was done to make the measured angular positions of the target relative to the sound beam axis as accurate as possible.

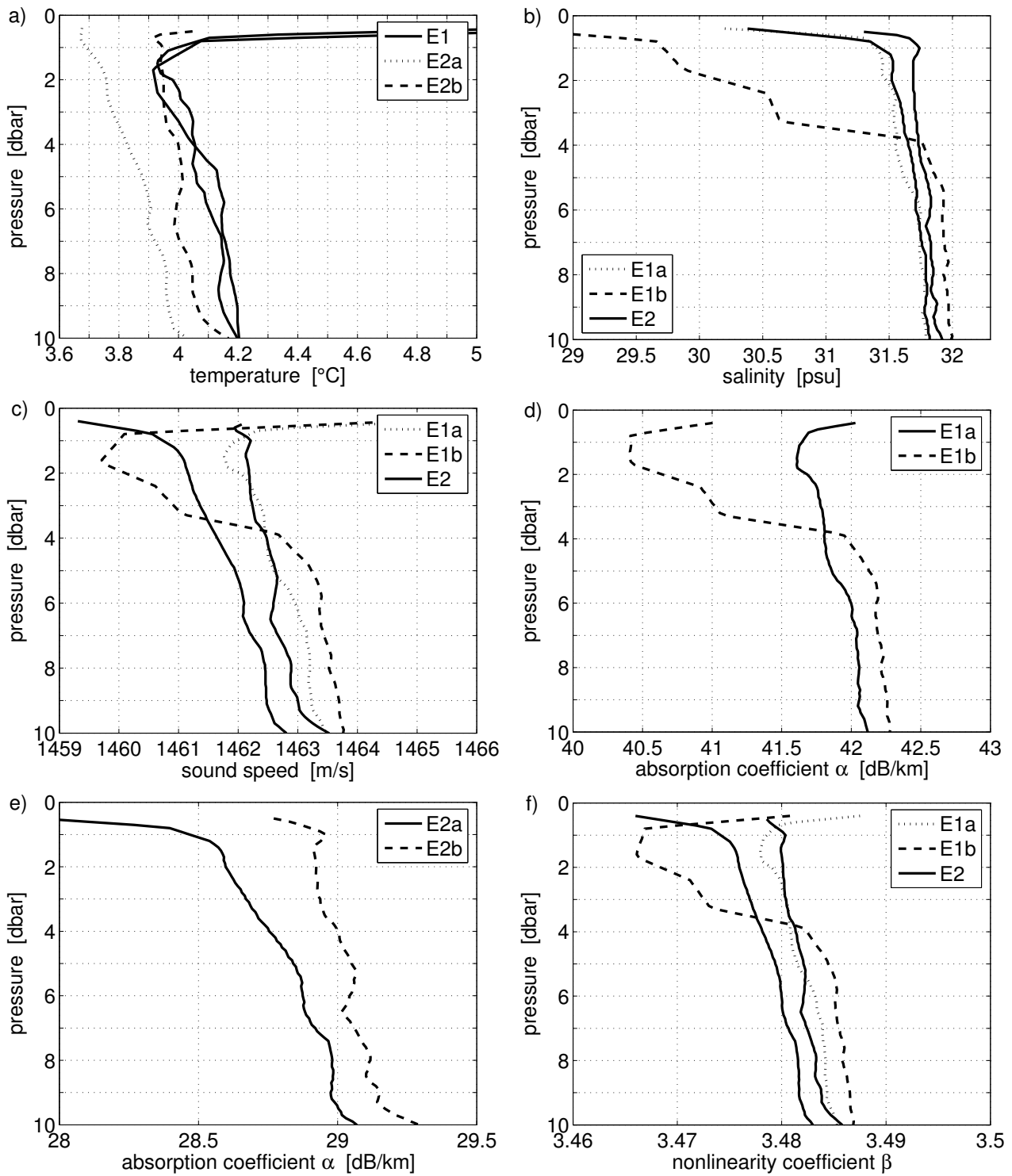


Figure 6.7. CTD data for the measurements made at the Marine Biological Station Espeland. a) Temperature, b) salinity,⁹⁴ c) sound speed,⁷⁰ d) absorption coefficient, 200 kHz,¹⁰⁶ e) absorption coefficient, 120 kHz, f) nonlinearity coefficient.⁷⁹

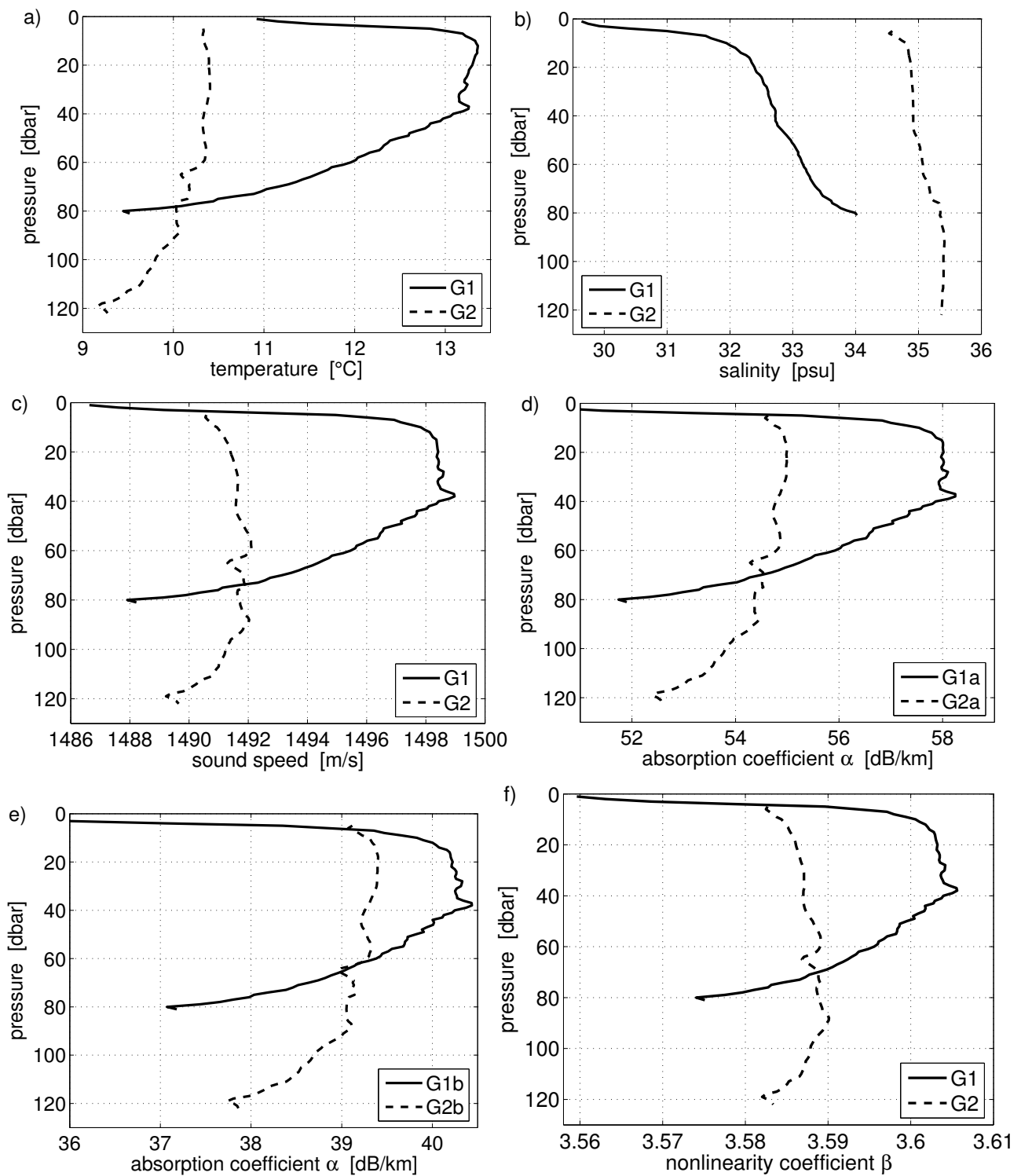


Figure 6.8. CTD data for the measurements made on RV G. O. Sars in 2004. a) Temperature, b) salinity,⁹⁴ c) sound speed,⁷⁰ d) absorption coefficient, 200 kHz,¹⁰⁶ e) absorption coefficient, 120 kHz, f) nonlinearity coefficient.⁷⁹

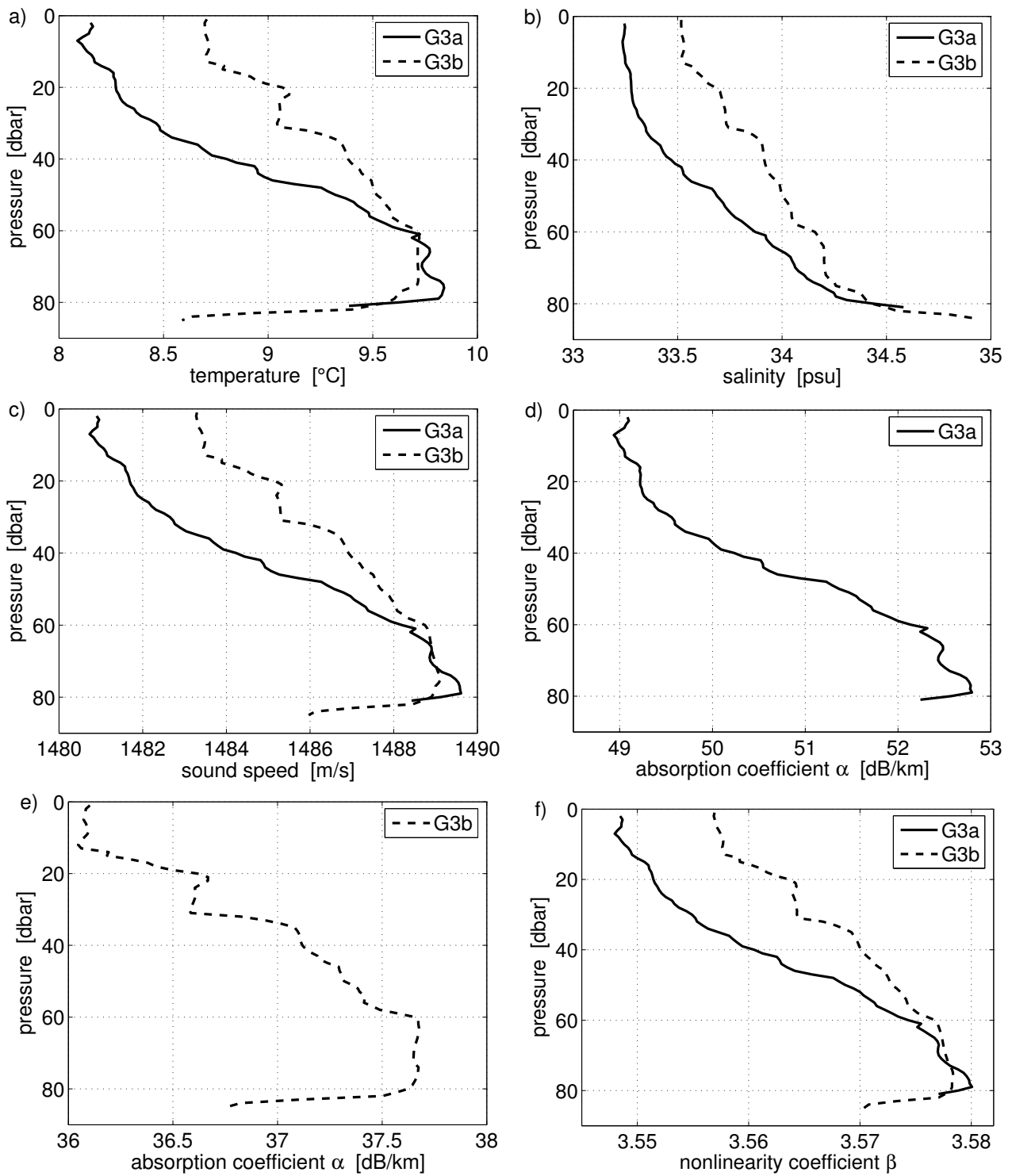


Figure 6.9. CTD data for the measurements made on RV G. O. Sars in Uggdalseid in 2006. a) Temperature, b) salinity,⁹⁴ c) sound speed,⁷⁰ d) absorption coefficient, 200 kHz,¹⁰⁶ e) absorption coefficient, 120 kHz, f) nonlinearity coefficient.⁷⁹



Figure 6.10. RV G. O. Sars. Photo: Hege Iren Svendsen / IMR

6.2. Simulations for seawater

6.2.1. Simulation parameters

Bergen Code simulations are carried out for comparison with the measurements made in seawater. The parameters for the propagation medium are taken from the CTD data obtained in connection with each acoustic measurement series (Figures 6.7–6.9).

Table 6.5 shows the operating frequencies and the medium parameters that are used for the simulations for seawater. The sound speed is based on Chen and Millero,⁷⁰ while the absorption coefficient is calculated from the formula presented by Francois and Garrison.¹⁰⁶ The nonlinearity coefficient and density are based on Cotaras and Morfey⁷⁹ and Fofonoff and Millard,⁹⁴ respectively. The parameter values are averaged over depth ranges as summarized in Table 6.6, depending on the depths over which the main part of the corresponding measurements have been made.

Table 6.5. Medium parameters used in simulations of nonlinear sound propagation in seawater.

| corresp. measur- ement set | frequency | sound speed | absorption at fundamental frequency | absorption coefficient | nonlinearity coefficient | density |
|-------------------------------------|-------------|----------------|---|---------------------------------------|-----------------------------|--------------------------------|
| | f [Hz] | c_0 [m/s] | α [dB/km] | α_2 [Np/m/Hz ²] | β | ρ [kg/m ³] |
| E1 | 200 000 | 1462 | 41.5 | $1.19 \cdot 10^{-13}$ | 3.48 | 1025.0 |
| E2 | 121 212 | 1462 | 28.7 | $2.25 \cdot 10^{-13}$ | 3.48 | 1025.1 |
| G1a | 200 000 | 1496 | 57.5 | $1.65 \cdot 10^{-13}$ | 3.60 | 1024.6 |
| G1b | 121 212 | 1496 | 40.0 | $3.13 \cdot 10^{-13}$ | 3.60 | 1024.6 |
| G2 | 200 000 | 1491 | 54.4 | $1.57 \cdot 10^{-13}$ | 3.59 | 1027.0 |
| G2 | 121 212 | 1491 | 39.0 | $3.06 \cdot 10^{-13}$ | 3.59 | 1027.0 |
| G3a | 200 000 | 1484 | 50.1 | $1.44 \cdot 10^{-13}$ | 3.56 | 1026.0 |
| G3b | 121 212 | 1486 | 36.9 | $2.89 \cdot 10^{-13}$ | 3.57 | 1026.2 |

Table 6.6. Depth intervals used for the average seawater parameters used in simulations.

| corresponding measurement set | interval for averaging | |
|-------------------------------------|------------------------|------------------|
| | minimum depth | maximum depth |
| E1, E2 | 1 m | 11 m |
| G1, G3 | 9 m | 60 m |
| G2 | 9 m | 120 m |

The simulations are initialised with source conditions that correspond to a baffled, uniform circular piston. The same Simrad ES200-7C and ES120-7C echo sounder transducers were used at Espegrend (E1 and E2) as in measurement sets H2 and H3 in fresh water (Tables 4.1 and 5.7). The effective source radii in Table 5.7 are therefore used for the corresponding simulations.

The echo sounder transducers used for the G1, G2, and G3 measurements are permanently mounted on the hull of RV G. O. Sars. Hydrophone measurements

of the -3 dB beam angle have not been conducted for these transducers in the present work, but they are of the same type as those used at Espegrend. Based on the results from Table 5.7, 32.0 mm and 52.8 mm piston radii are chosen for the simulations for 200 kHz and 120 kHz operating frequencies, respectively.

The approach described in Section 5.2.1 was followed to obtain the source condition effective sound pressures $p_{0,rms}$ (Tables 6.2 and 6.3) from the axial fields measured with the hydrophone at Espegrend (measurement sets E1, E2b).

The parameters that govern spectral truncation, damping of high harmonics, numerical grid width and resolution, and damping of Gibbs oscillations due to the source condition, are chosen equal to those used for fresh water in Section 5.2. Their values are listed in Tables 3.3 and 3.4 (“unperturbed” values).

6.2.2. Absorption frequency dependence

The KZK equation^{271,151} assumes square frequency power law attenuation.^{56,228} The constant absorption coefficient α_2 is defined such that the absorption at frequency f , measured in Nepers per metre, is $\alpha' = \alpha_2 f^2$. This applies well to pure water, but the frequency dependence of absorption in seawater is more complex.^{105,106}

Although the square power law is an inherent assumption in the KZK equation, several authors^{117,277,249,261} suggest that arbitrary absorption and dispersion may be introduced by substitution of a complex absorption coefficient $\alpha'(f)$ into the set of equations (2.67). Szabo²²⁸ has suggested alternative operators for the absorption term to account for a general power law with arbitrary real exponent, $\alpha' = \alpha'_0 |\omega|^\gamma$. Li and Zagzebski¹⁵⁸ substituted the absorption term in the KZK equation with a temporal convolution between the incident pulse and a filter function.

Here, simulations to correspond to the measurements are carried out with square power-law attenuation. The absorption coefficient α_2 is chosen such that the Francois-Garrison¹⁰⁶ absorption is obtained for the fundamental frequency component. The absorption coefficients for the harmonics generated through nonlinear distortion thus become higher than under the experimental conditions.^{105,106}

In addition, alternative simulations with modified absorption are run for the E1, E2, and G2 measurement sets. The absorption coefficient for the second harmonic frequency component is decreased to match the results of Francois and Garrison¹⁰⁶ (Table 6.7). The absorption coefficients for the higher harmonic components are kept as before.

Results of both simulation alternatives are shown for the axial field in Figures 6.11 and 6.12, in terms of the effective sound pressures $p_{1,\text{sim}}$ for the fundamental and $p_{2,\text{sim}}$ for the second harmonic frequency component. A small change is found in the fundamental frequency component. 10 m from the sound source the modified absorption coefficient yields 0.1 dB and 0.03 dB reductions in the simulated 200 kHz and 120 kHz sound pressure levels, respectively. The corresponding ratios for $r = 300$ m are 0.7 dB and 0.6 dB.

The modified absorption is more important for the second harmonic component. At $r = 10$ m, the simulations with the reduced absorption coefficient yield 0.9 dB and 0.8 dB higher second harmonic sound pressure levels, respectively, than for the square power law absorption. The simulations with modified absorption are used for comparison with the hydrophone measurements (Figures 6.13 and 6.14), as they yield improved agreement for the second harmonic frequency component.

The target strength measurements do not contain information about the second harmonic. As the reduced absorption coefficient for the second harmonic component entails a violation of the conditions for the derivation of the model

equation,^{56,228} the simulations with $\alpha_2 f^2$ absorption are used to obtain the results shown in Figures 6.15–6.18, 6.21, and 6.22.

Table 6.7. Absorption coefficients for the fundamental and second harmonic components,¹⁰⁶ used in simulations with modified absorption for the second harmonic frequency component.

| corr. measure- ment set | frequency f [kHz] | absorption fundamental α [dB/km] | absorption second harmonic α [dB/km] |
|--|---|---|---|
| E1 | 200.000 | 41.5 | 91.2 |
| E2 | 121.212 | 28.7 | 49.7 |
| G1a | 200.000 | 57.5 | 97.6 |
| G1b | 121.212 | 40.0 | 65.4 |
| G2 | 200.000 | 54.4 | 95.9 |
| G2 | 121.212 | 39.0 | 62.0 |
| G3a | 200.000 | 50.1 | 92.7 |
| G3b | 121.212 | 36.9 | 59.0 |

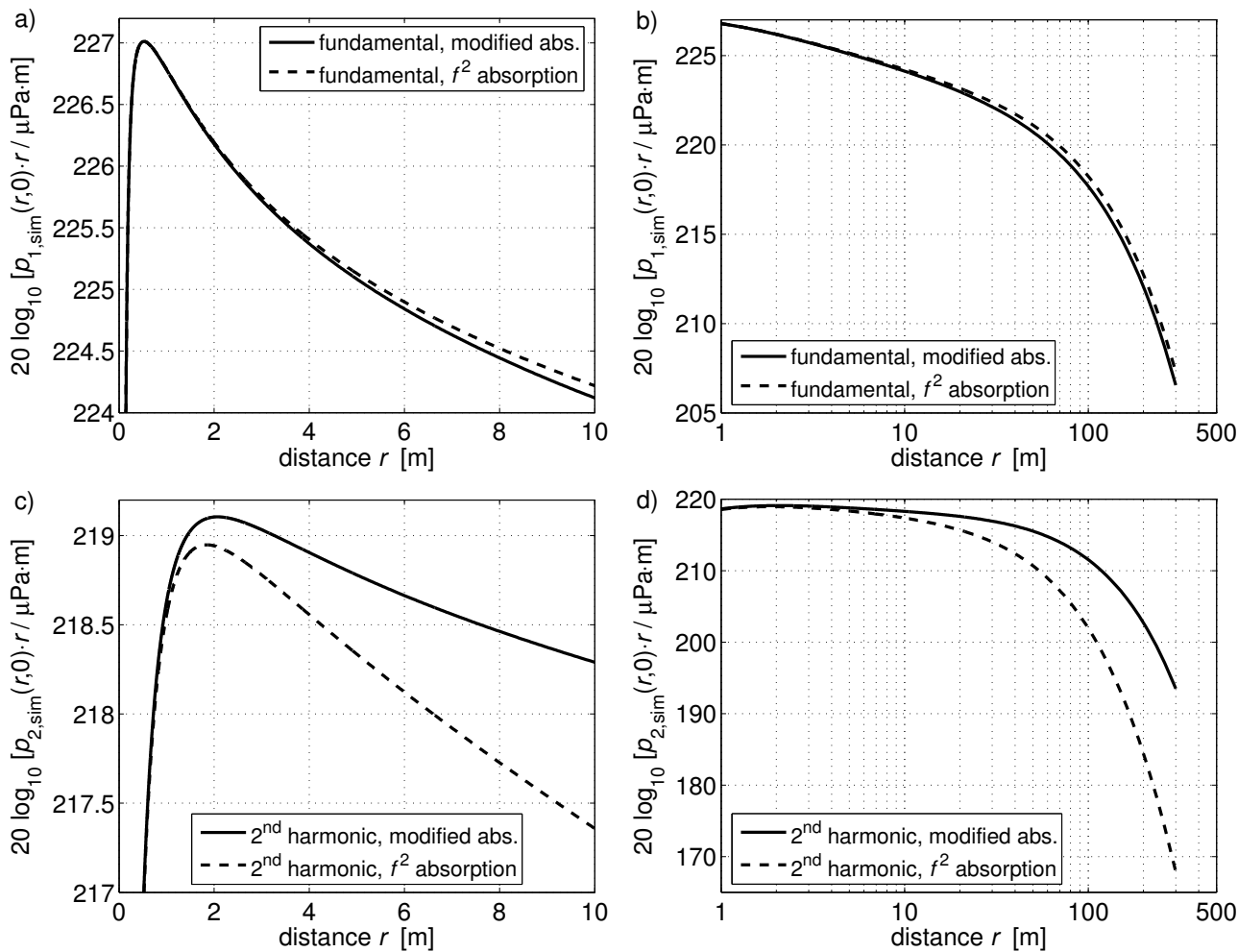


Figure 6.11. Simulated axial fields, 200 kHz (G2 parameters), 1000 W power setting. Comparison between square power law absorption and measured absorption (Francois-Garrison¹⁰⁶) inserted for the second harmonic frequency component.

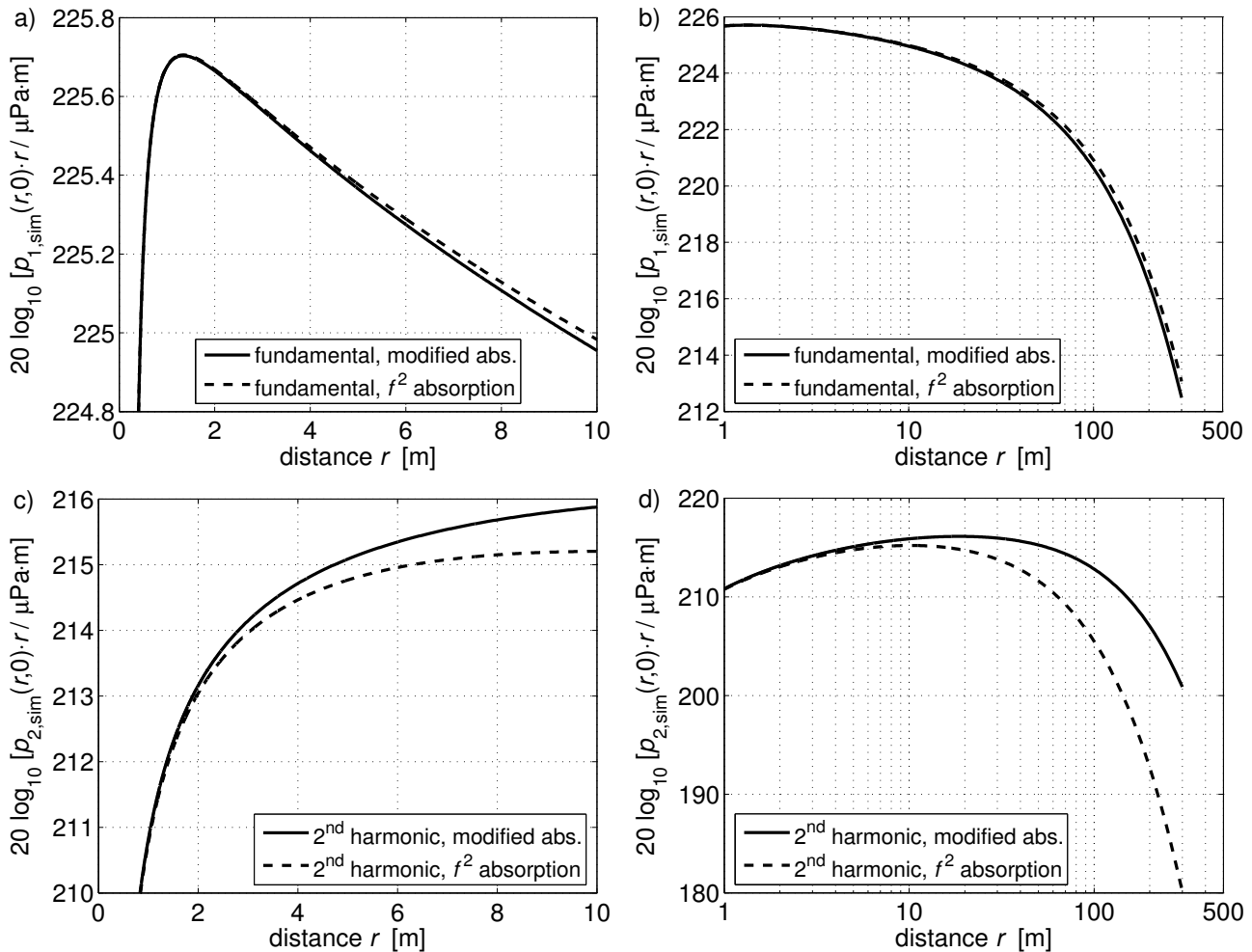


Figure 6.12. Simulated axial fields, 120 kHz (G2 parameters), 1000 W power setting. Comparison between square power law absorption and measured absorption (Francois-Garrison¹⁰⁶) inserted for the second harmonic frequency component.

6.2.3. Bubbles and inhomogeneities

Seawater contains naturally produced gas bubbles in varying concentrations.^{189,267,174} The bubble density is greatest near the sea surface, where they are generated by breaking waves and biological activity. Several factors such as water depth, bubble depth, wind speed, rainfall, cloud cover, and temperature have influence on bubble production.¹⁷⁴ Their presence can have a dramatic effect on sound attenuation and phase velocity,^{189,77,66,153,104} and the consequences of such effects for echo sounder and sonar measurements have been investigated by several researchers.^{173,82,61} Solid particles in the

water may also influence the absorption significantly through viscous effects and scattering.^{209,210}

Gas bubbles oscillate nonlinearly and influence the nonlinear distortion of sound waves.⁶² A number of investigations of nonlinear effects in bubble layers have been made,^{185,227,16,192} primarily through measurements of the sum and difference frequency sound fields generated through the interaction of two harmonic primary waves. Simulations of nonlinear sound propagation in a bubbly liquid have been carried out by e.g. Leble and Sukhov.¹⁵⁶ Some authors have explored the possibility of using the increased nonlinearity coefficient in water with high bubble contents to improve the efficiency of parametric sound sources.^{270,260} Similar use of microbubbles is found in contrast agents for medical ultrasound harmonic imaging.^{64,164}

Nonlinear sound propagation through turbulence and inhomogeneities has also been the subject of several investigations.^{136,58,205} The contribution from each field point to the cumulative process of nonlinear distortion depends on the local sound pressure amplitude, diffraction effects, and medium parameters in that point. Accounting for the depth dependence of medium parameters may therefore yield somewhat different simulation results than if mean values are used for the whole field. Also, refraction due to a depth dependent sound speed may have a small effect on the width of the beam pattern.²³⁵

Effects of bubbles and particles are disregarded in the simulations that are carried out in the present work. The propagation medium has been treated as uniform, with sound speed, density, absorption, and nonlinearity as listed in Table 6.5.

6.3. Measurement and simulation results for sound propagation in seawater

6.3.1. Results from hydrophone measurements

The measured fundamental and second harmonic sound pressure levels from measurement sets E1 and E2b are found in Figures 6.13 and 6.14, respectively (Table 6.1). Simulation results have been included with full-drawn curves. The simulations have been performed with the Francois-Garrison¹⁰⁶ absorption coefficients for the fundamental and second harmonic frequency components (Section 6.2.2). The absorption coefficients for the higher harmonics follow the square frequency power law, with the coefficient α_2 chosen such that it yields agreement at the fundamental frequency.

The plotted measurement results (marked with + and \circ) are average sound pressure amplitudes calculated from 10 recorded sound bursts. The error bars in the directivity plots (Figures 6.13 c, d, and e and Figures 6.14 c and d) indicate the standard deviation between the measured amplitudes for each point.

200 kHz operating frequency

Measurements along the sound beam axis for the 200 kHz echo sounder (Figure 6.13a and 6.13b) were made on two consecutive days (Table 6.1). An overlapping measurement point at $r = 3.6$ m indicates good agreement between the measurement sets, although the salinity near the surface changed somewhat between the two mornings (Figure 6.7). Figures 6.13a and 6.13b show results for the 100 W, 200 W, 500 W, and 1000 W transmit power settings on the EK60 echo sounder. Agreement within 0.5 dB is observed between the axial measurement and simulation results for the fundamental frequency component (Figure 6.13a).

The level of the axial second harmonic component generated through nonlinear distortion is shown relative to the fundamental in Figure 6.13b,

$$\langle \text{plotted value} \rangle = 20 \cdot \log_{10} \frac{|p_2(r, 0, 0)|}{|p_1(r, 0, 0)|}. \quad (6.1)$$

As seen for the fresh water measurements described in the previous chapter, the second harmonic frequency component grows towards -6 dB relative to the fundamental when the source level is high. Although the overall absorption is stronger and the source levels are lower than for the fresh water measurements, slightly higher relative levels are measured for the second harmonic in seawater. A possible reason is that the absorption for the second harmonic compared to the fundamental is lower in seawater than in fresh water. The agreement between measured and simulated relative levels as described by Equation (6.1) is within approximately 0.7 dB.

The shape of the main lobe for the 200 kHz echo sounder transducer is investigated at $r = 8.6$ m distance. The 100 W, 500 W, and 1000 W power settings are used (Figure 6.13, c, d, and e, respectively). Sound pressure levels for the fundamental frequency component are shown in all three plots. The second harmonic is included in the two latter, as in these cases its level is high enough that both components can be shown in the same figure. The agreement between simulations and measurements for angles up to 4° off axis seems approximately as for the axial field. Both the fundamental and second harmonic main lobes become flatter as the amplitude is increased. The -3 dB beam angle (half-beamwidth) for the simulated fundamental frequency component with 100 W power setting is 3.6° . For 1000 W nominal output power, the same angle becomes 4.3° (Figure 6.13e). One should note that the spacing between the ticks along the ordinate axis of Figure 6.13c is different from in Figures 6.13d and 6.13e.

120 kHz operating frequency

Figure 6.14 a shows measured and simulated fundamental sound pressure amplitudes along the axis of the 120 kHz sound beam. Also here results are shown for the 100 W, 200 W, 500 W, and 1000 W transmit power settings.

Good agreement between measurements and simulations is seen for the two lowest source levels. The agreement is slightly worse for the 500 W and 1000 W power settings, in which case the simulations indicate 0.5 dB higher sound pressure levels than the measurements.

The axial sound pressure level of the second harmonic frequency component is shown in Figure 6.14b for the 500 W and 1000 W power settings. As also seen in the results for fresh water (Section 5.3), the simulations indicate significantly weaker second harmonic components than the measurements. The discrepancy is here approximately 3.7 dB, and slightly worse for the 500 W power setting than for 1000 W. The comparatively better agreement between experimental and theoretical results for the fundamental frequency component suggest that the measurement accuracy for the second harmonic might not be as good as expected based on the considerations in Section 6.1.1.

Some hydrophone measurements off the sound beam axis were made at distance $r = 4.6$ m from the 120 kHz sound source. The sound pressure levels for the fundamental frequency component are shown in Figures 6.14c (100 W) and 6.14d (1000 W). Although the measured second harmonic component is – maybe inaccurately – close to 6 dB below the fundamental in the case of the 1000 W power setting (cf. Figures 6.14 a and b), the observed flattening of the fundamental main lobe is much weaker than for the 200 kHz operating frequency. The simulated -3 dB beam angle increases with less than 0.1° between the 100 W and 1000 W power settings.

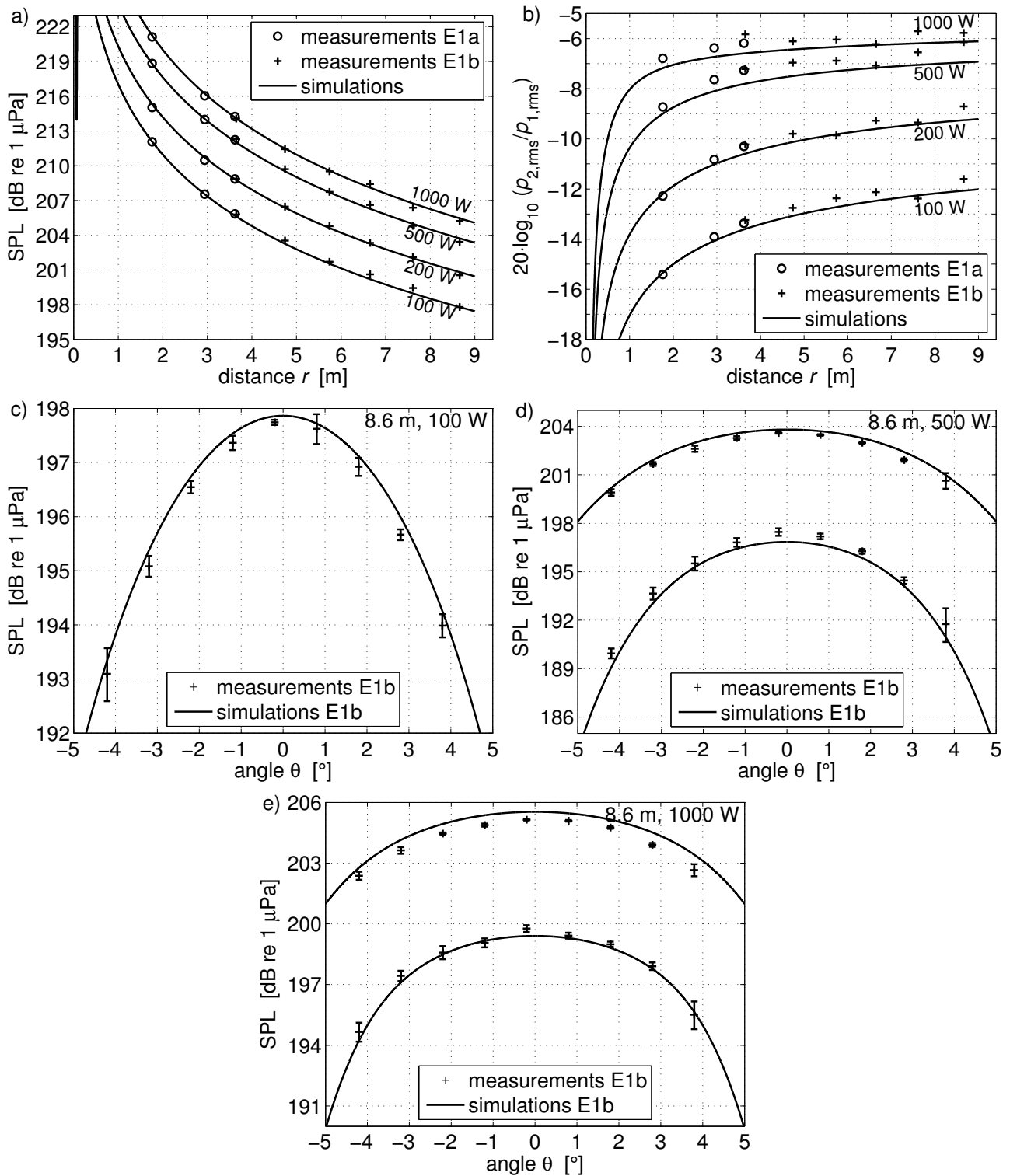


Figure 6.13. Hydrophone measurements in seawater, 200 kHz. a) Axial field, measured and simulated sound pressure level for the fundamental frequency component, b) axial field, level for the second harmonic frequency component relative to the fundamental (measured and simulated), c) sound pressure level for the fundamental frequency component at distance $r = 8.6$ m, 100 W power setting, d) 500 W, e) 1000 W. The sound pressure levels for the second harmonic frequency component is included in Figures d and e.

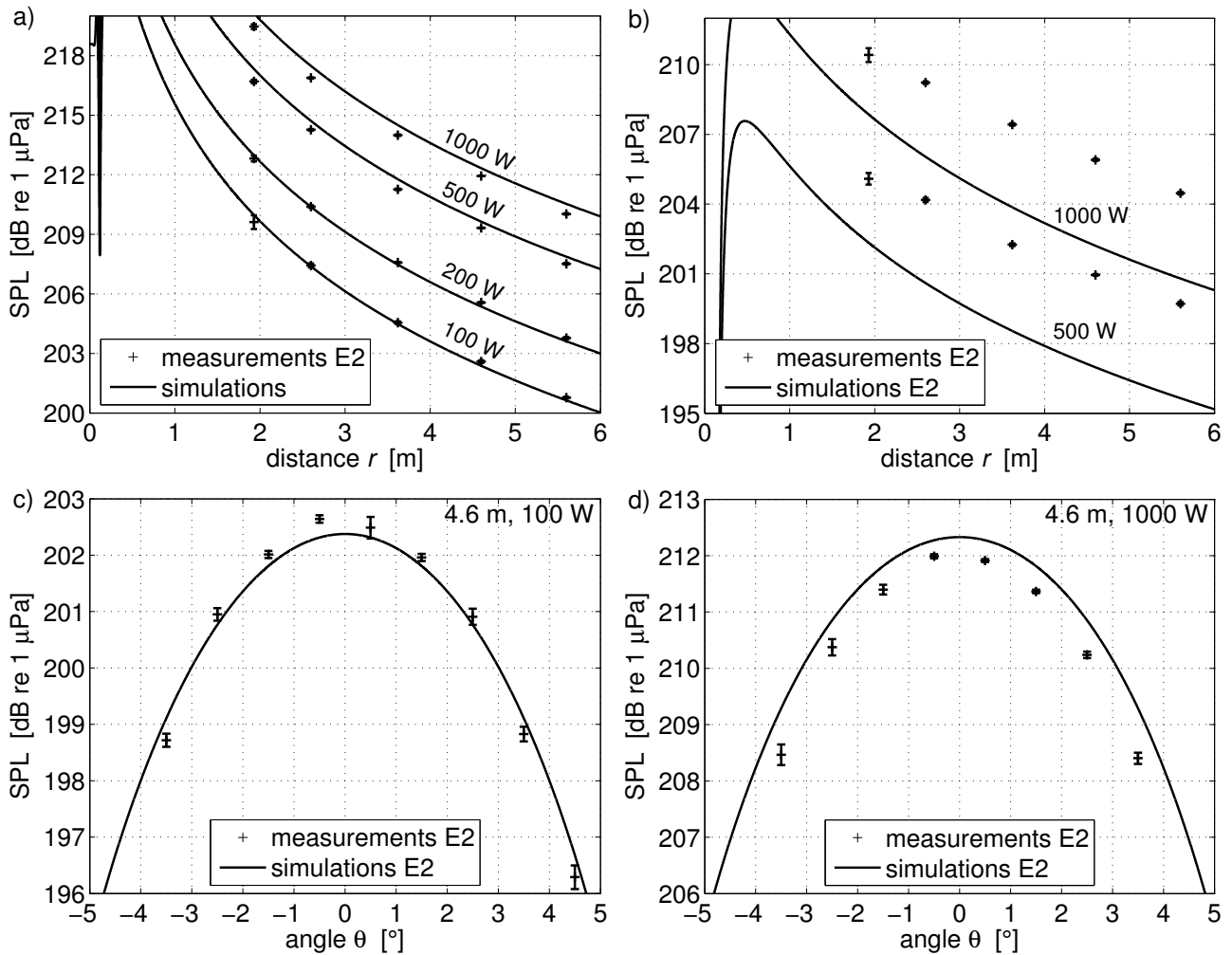


Figure 6.14. Hydrophone measurements in seawater, 120 kHz. a) Axial field, measured and simulated sound pressure level for the fundamental frequency component, b) axial field, sound pressure level for the second harmonic frequency component, c) sound pressure level for the fundamental frequency component at distance $r = 4.6$ m, 100 W power setting, d) 1000 W.

6.3.2. Results from calibration sphere measurements

The target strength measurements at Espesrend and Uggdalseid (E2a, G1 and G3, Table 6.1) were made with Simrad EK60 echo sounders by recording the backscattered signal from a 38.1-mm-diameter tungsten carbide calibration sphere with 6% cobalt binder. Distances and angles taken from the echo sounder single echo detection functionality are used for the sphere position.

An unexplained increase with distance is found in the measured target strength for low power settings. The product αr of the absorption coefficient and the

distance from the sound source has been subtracted from all the measurement results for target strength presented below. This almost removes the apparent TS distance dependence when the lowest power settings are used. No physical justification of the chosen compensation is made, but it facilitates the comparison between measurement and simulation results in Figures 6.15–6.18 considerably. As the αr compensation grows slowly with distance and is applied equally to all the measurement results, it has negligible effect on the shape of the main lobes and also on the difference in measured TS between different power settings. These are the features of greatest interest to the present investigation.

The term “apparent TS” (TS_{meas}) is used for the target strength reported by the echo sounder with αr subtracted. For the directivity measurements, the “Uncompensated TS” values from the echo sounder software are presented, to which the beam compensation function has not been applied (Section 2.1).

Simulation results for the apparent TS were prepared the same way as in Section 5.3.3 (Equation (5.13)). The values for the constant C were chosen to obtain approximate agreement with the target strengths measured with the lowest power settings. The values are shown in Table 6.8. The simulations for comparison with calibration sphere measurements are described in Section 5.2.1.

Target strength along the sound beam axis

Results for the axial fields are shown in Figures 6.15 and 6.16 for the 200 kHz and 120 kHz operating frequencies, respectively. Only detected echoes from angles less than $\theta = 0.20^\circ$ off the sound beam axis have been accepted. Simulated apparent target strengths are shown with full-drawn curves.

The measured target strength decreases with the power of the transmitted signal. The simulated difference between apparent target strengths using different power settings seems to agree reasonably well for the case of the

200 kHz echo sounder (Figure 6.15). With the calibration sphere at 40 m distance from the sound source, the simulated apparent TS is approximately 3.4 dB lower for the 1000 W power setting than for the 50 W and 100 W power settings. The difference between measurement results from using the 50 W and 100 W power settings is smaller than the variation in measurement results for each power setting. The simulations predict a difference of approximately 0.2 dB at $r = 40$ m.

Table 6.8. Values chosen for the constant C in Equation (5.13).

| Measurement set | $10 \log_{10} C$ |
|------------------------------|------------------|
| Axial field | |
| G3b (120 kHz) | -37.8 |
| G3a (200 kHz) | -33.0 |
| G1a (200 kHz) | -33.0 |
| Measurements off axis | |
| E2a (120 kHz) | -37.7 |
| G1b (120 kHz) | -37.4 |
| G3a (200 kHz) | -33.0 |
| G1a (200 kHz) | -33.0 |

The target strength measurements with the 120 kHz echo sounder are shown in Figure 6.16. The agreement between measurements and simulations is not as close as for 200 kHz. Approximately 2 dB nonlinear attenuation is measured with the target at 30 m distance from the transducer, while the simulations predict 0.9 dB. A clear difference between the TS measurements using the 100 W and 250 W power settings is not seen. The simulations indicate approximately 0.1 dB difference at 30 m distance.

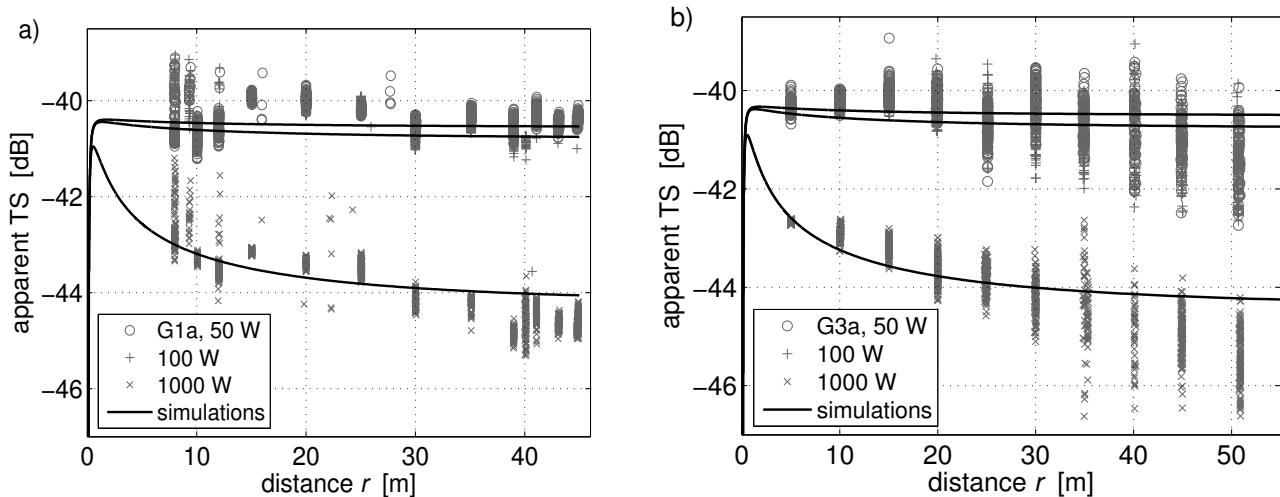


Figure 6.15. Target strength measurements with the calibration sphere on the sound beam axis of a 200 kHz echo sounder. The measurements have been made on RV G. O. Sars at two different times (G1 and G3, see Table 6.1).

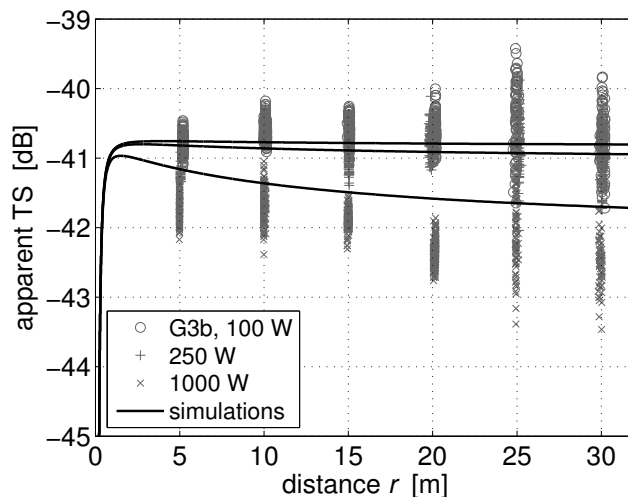


Figure 6.16. Target strength measurements with the calibration sphere on the sound beam axis of a 120 kHz echo sounder (measurement set G3b, see Table 6.1).

Target strength measurements off axis

Several directivity measurements have been made within the main lobe by means of calibration spheres. As the echo sounder beam compensation function has not been applied to the results, correct TS measurements are expected only on the sound beam axis (Section 2.1). Measurement and simulation results are found in Figures 6.17 and 6.18 as function of the off-axis angle θ , for the

200 kHz and 120 kHz operating frequency, respectively. The simulation results are shown with full-drawn curves.

Figures 6.19 and 6.20 indicate where in the sound beams the measurements have been made. The vertical axis corresponds to the alongship direction, forward angles being above the horizontal axis. The port side angles are to the left, while the starboard side is to the right.

The distance between the transducer and the calibration sphere was kept as constant as possible during each directivity measurement. The intended distances and maximum measured deviations from them are shown in Table 6.9. The echo sounder's "40 log r " time varying gain function was applied to each individual target strength measurement according to the particular measured distance.

Table 6.9. Distances to the calibration sphere and maximum deviations from them during the directivity measurements in seawater.

| measurement | figure | distance r | max. distance deviation |
|-------------|-------------|----------------|-------------------------|
| G3a | 6.17a | 5.0 m | 0.3 m |
| G3a | 6.17b | 10.0 m | 0.3 m |
| G3a | 6.17c | 20.0 m | 0.4 m |
| G3a | 6.17d | 35.0 m | 0.4 m |
| G3a | 6.17e | 50 m | 1 m |
| G1a | 6.17f | 41.0 m | 0.5 m |
| E2a | 6.18a | 10.0 m | 0.1 m |
| G3b | 6.18b–6.18d | 10.0 m, 20.0 m | 0.2 m |
| G3b | 6.18e | 45.0 m | 0.3 m |

Target strength measurement and simulation results for the 200 kHz echo sounder are shown in Figure 6.17. The distances between the echo sounder transducer and the reference target range from 5 m to 50 m. Results are shown for 50 W (all figures), 100 W (Figures e and f), 150 W (Figures a–d), and

1000 W (all figures) EK60 power settings. The simulations seem to predict the difference between measurement results obtained with different power settings to within approximately 0.5 dB in general, although the spread between target strength measurements is somewhat greater when the sphere is at the farthest positions from the transducer.

Measurement results for two 120 kHz echo sounders are shown in Figure 6.18. Figure 6.18a shows measurements made at Espegrend with the ES120-7C (s/n 230) transducer. The power settings used are 100 W and 1000 W, and the distance between the echo sounder transducer and the calibration sphere is 10 m. The rest of the plots in Figure 6.18 show results from Uggdalseid, where the EK60 echo sounder on RV G. O. Sars has been used with power settings 100 W, 250 W, and 1000 W. Measurements have been made with the calibration sphere at 10 m, 20 m, and 45 m distance from the transducer. As seen earlier, the simulations tend to underestimate the nonlinear attenuation for the 120 kHz operating frequency. A reason for this has not been found in the present work. The discrepancy between measured and simulated nonlinear attenuation is approximately 0.9 dB near the sound beam axis. Figure 6.18d is a close-up of the axial measurement results in Figure 6.18c. The difference between the measurements using 100 W and 250 W power settings is not distinguishable in the figure.

For both operating frequencies, the simulations overestimate the apparent TS somewhat at great angles off the sound beam axis (θ approximately greater than 3° , depending on distance from the transducer). The flattening of the main lobe that occurs due to nonlinear attenuation is seen well in Figures 6.17 and 6.18. The attenuation is strongest near the sound beam axis, where sound pressure levels are high, and weakens with the angle off axis.

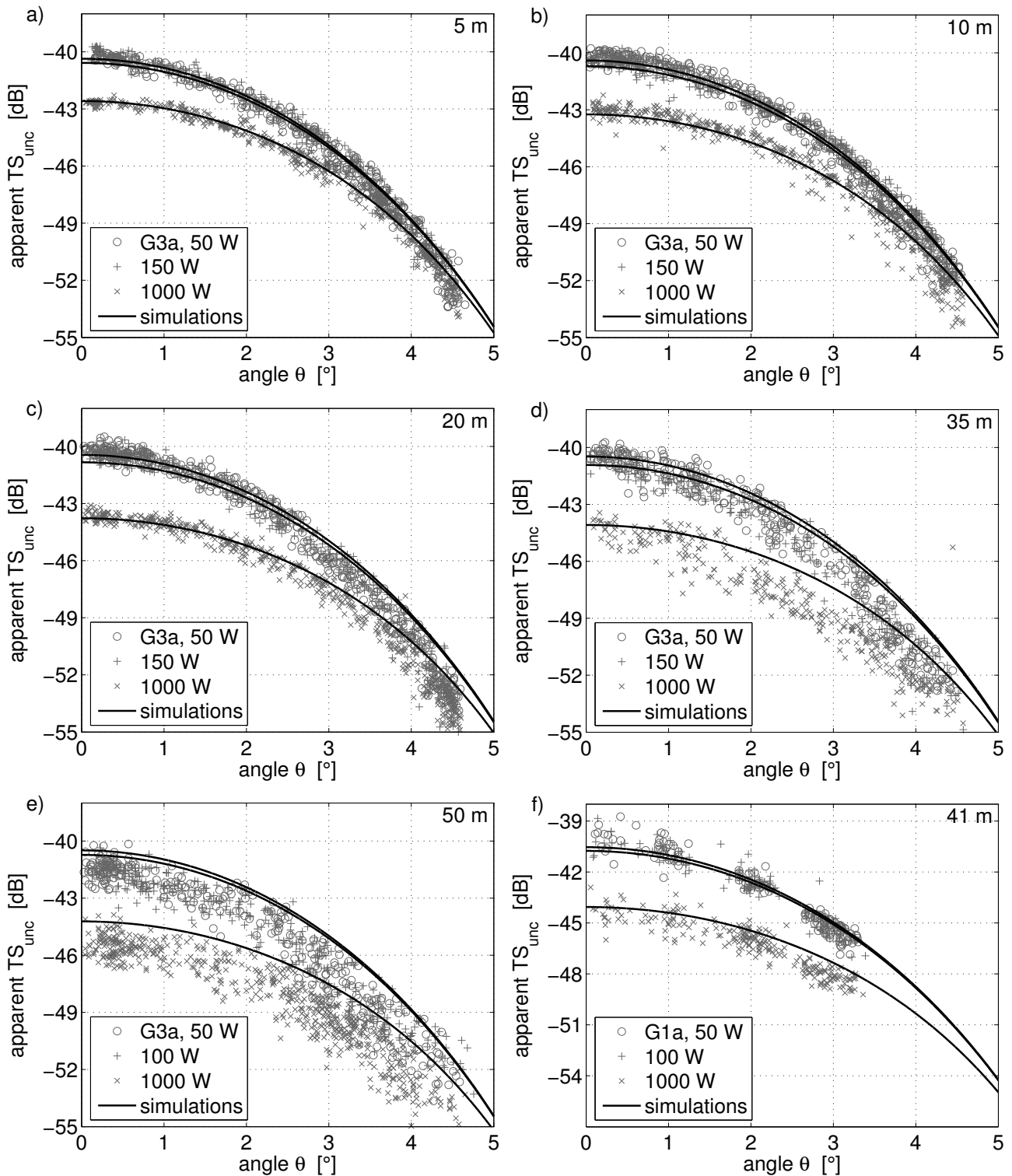


Figure 6.17. Target strength measurements for 200 kHz echo sounders using a calibration sphere.

The beam compensation function has not been applied to the results. a) Measurement set G3a, $r = 5$ m distance from the transducer, 50 W, 150 W, and 1000 W power settings. b) Same as a), $r = 10$ m, c) $r = 20$ m, d) $r = 35$ m, e) $r = 50$ m. f) Measurement set G1a, $r = 41$ m, 50 W, 100 W, and 1000 W power settings.

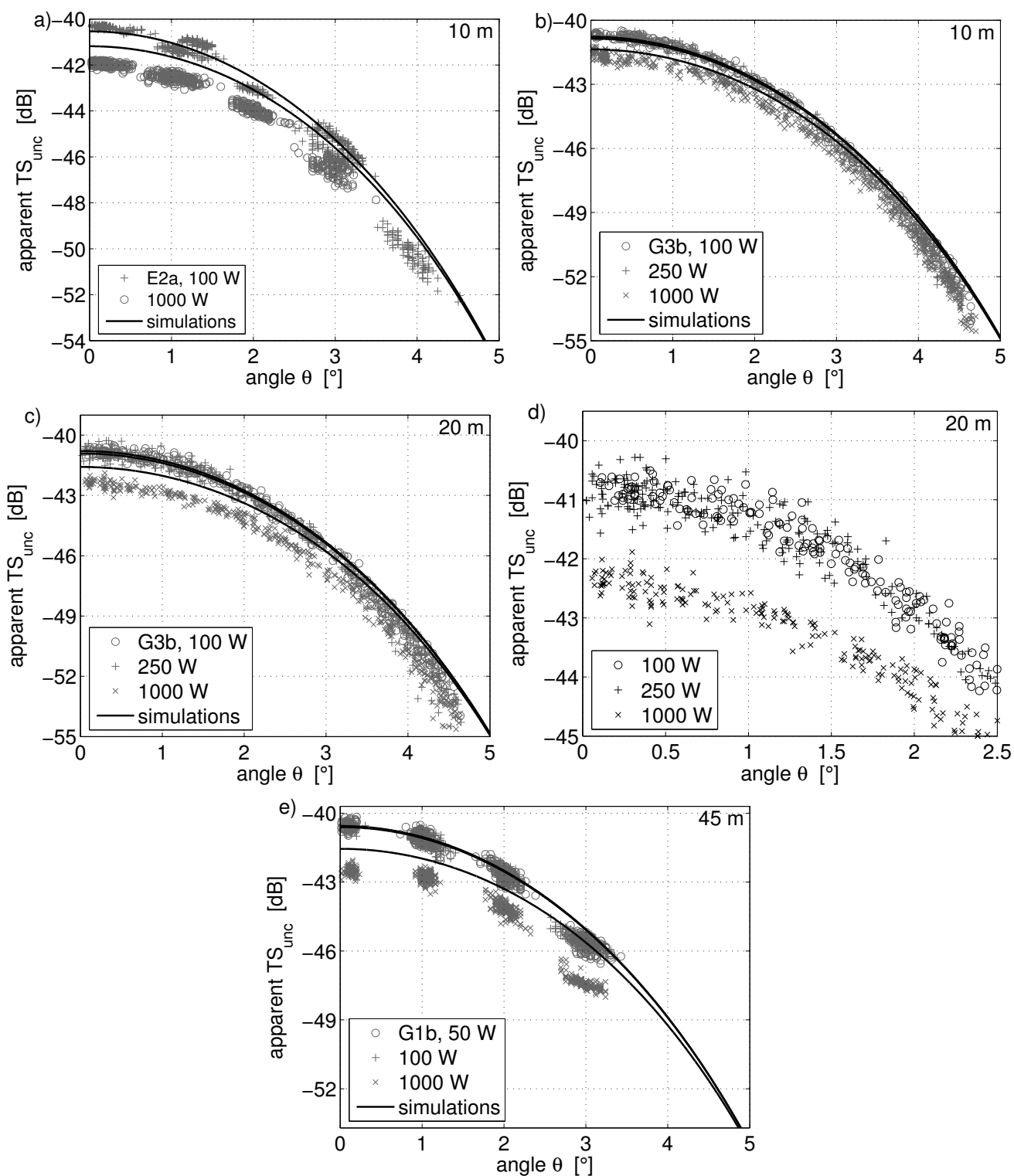


Figure 6.18. Measured and simulated uncompensated target strength for 120 kHz echo sounders using a calibration sphere. Figures a) and b) show measurements taken at distance $r = 10$ m, at Espegrend and Uggdalseid, respectively (measurement sets E2a and G3b). Results from the G3b measurement set for distances $r = 20$ m and $r = 45$ m are seen in Figures c), d) and e). Figures c) and d) are for the same measurement, Figure d) being a close-up of the measurement results near the sound beam axis.

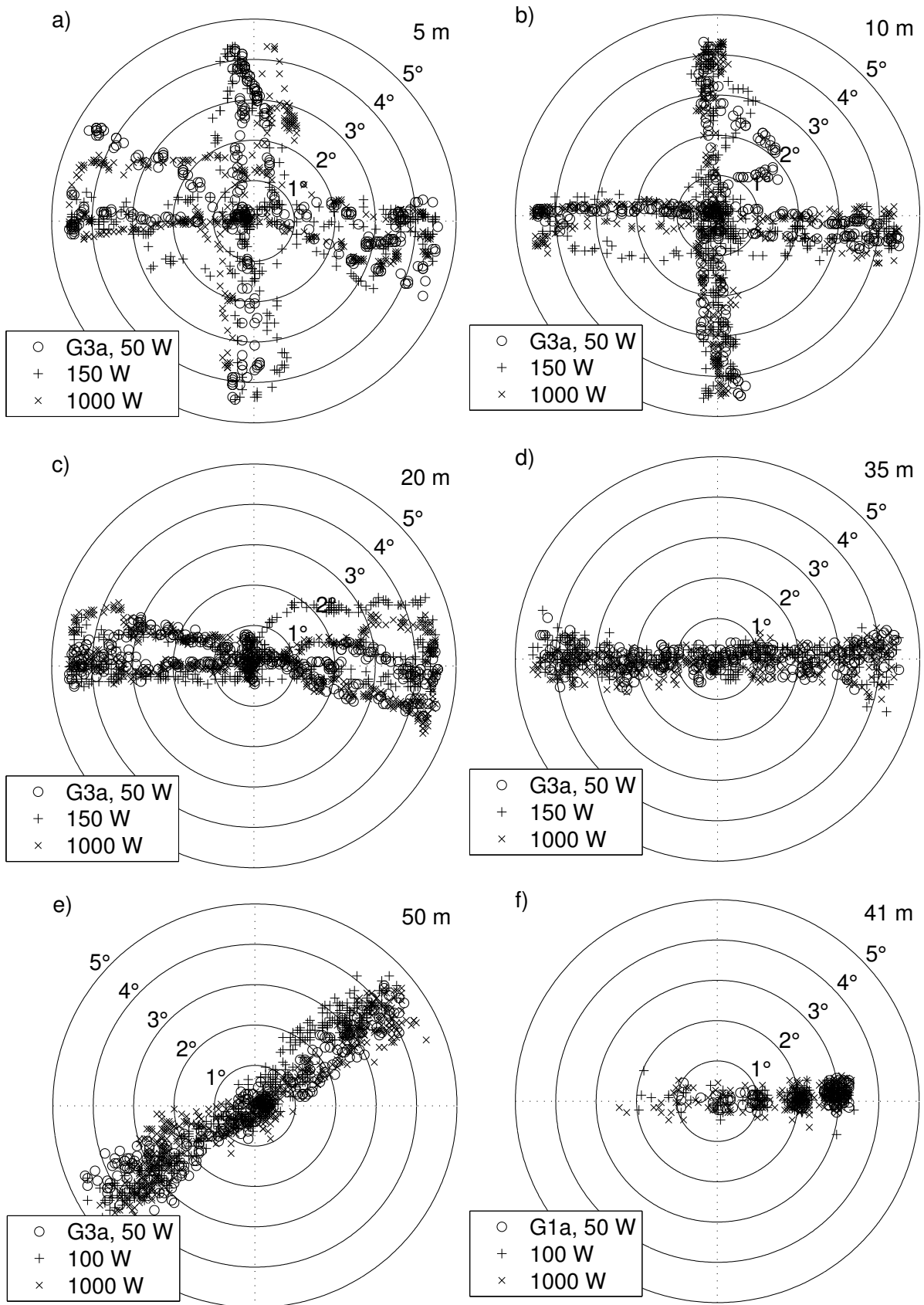


Figure 6.19. Measured positions of the calibration sphere in the sound beam for measurements with 200 kHz echo sounders. The marked points correspond to the TS measurements shown in Figure 6.17.

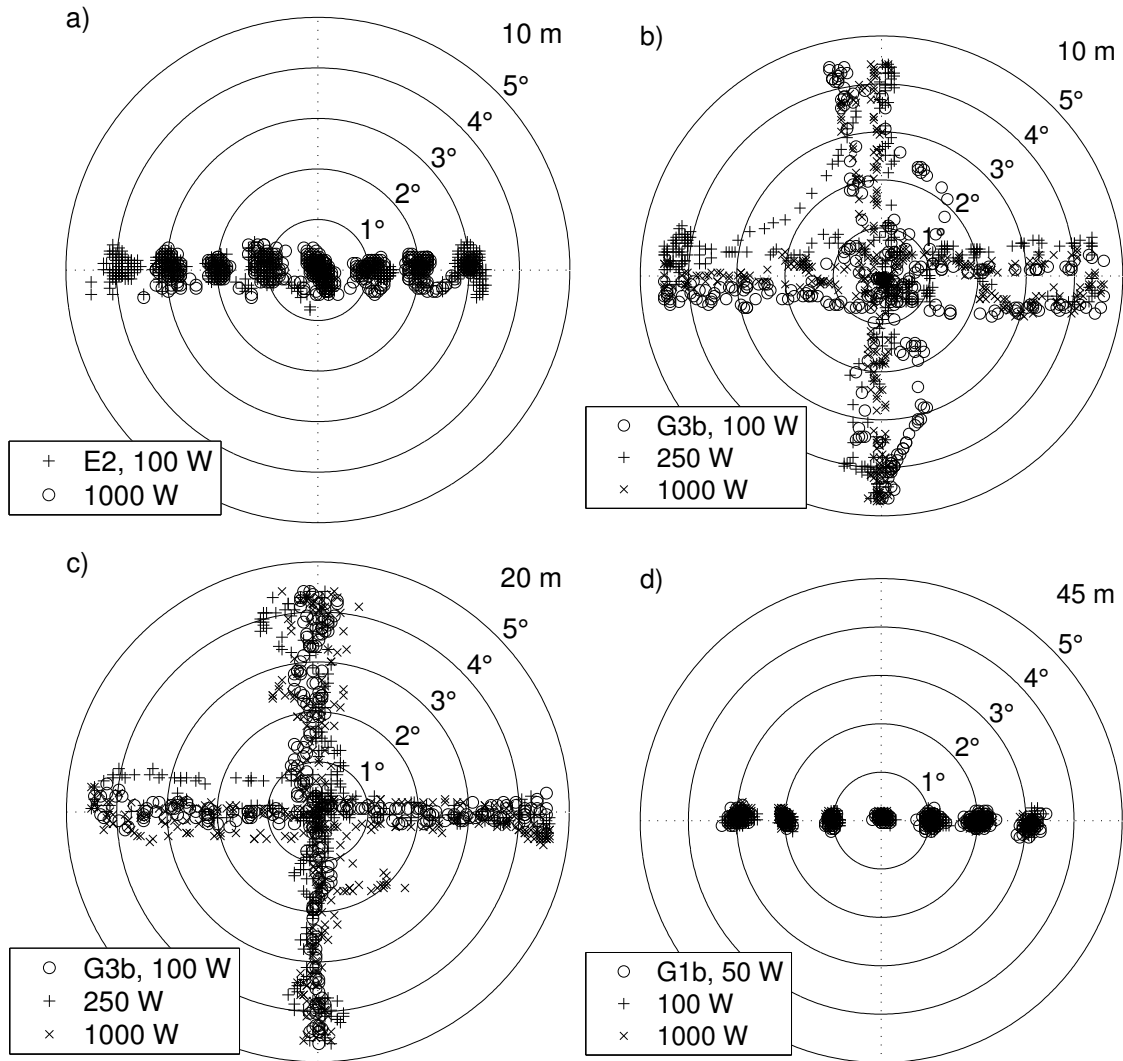


Figure 6.20. Measured positions of the calibration sphere in the sound beam for measurements with 120 kHz echo sounders. The marked points correspond to the TS measurements shown in Figure 6.18.

6.3.3. Nonlinear attenuation along the sound beam axis

By comparing cases with and without accounting for nonlinear effects, but with otherwise the same parameters, simulation results are used to isolate the excess attenuation due to nonlinear effects. Sound pressure amplitudes from the simulations presented in Sections 6.3.1 and 6.3.2 are normalized to the source condition pressure amplitudes p_0 and compared to corresponding simulation results with $p_0 = 1$ Pa (negligible nonlinear effects). The simulated nonlinear attenuation is defined as in Section 5.3.2 (Equation (5.10)). In principle, NA_{sim} could be used as an indicator of the error due to nonlinear attenuation in target

strength measurements along the sound beam axis. However, an additional compensation must be made to account for nonlinear effects during the echo sounder calibration that was made prior to the measurement in question (Chapter 7).

Results from simulations with different medium parameters for seawater (Table 6.5) are shown in Figure 6.21 for the 200 kHz operating frequency and Figure 6.22 for 120 kHz. Some values for NA_{sim} along the sound beam axis are also listed in Table 6.10. The widening of the main lobe that accompanies this axial loss is discussed in Chapter 7. Comparison with Table 5.9 shows that stronger nonlinear attenuation was experienced in the fresh water measurements than in seawater. This is attributed to the difference in absorption coefficients (Tables 5.6 and 6.5). At 9 m distance from the sound source, the simulated nonlinear attenuation is approximately 3 dB and 0.7 dB for the 200 kHz and 120 kHz operating frequencies, respectively. The simulations predict approximately 4 dB and 1.3 dB attenuations, respectively, at 300 m distance.

There is some discrepancy between measured and simulated sound pressure levels (Section 6.3.1), although the agreement is generally within 0.5 dB. This should be taken into account when reading the simulation results in Figures 6.21–6.22 and Table 6.10. Quadratic frequency power law attenuation has been used in the simulations shown in Figures 6.21 and 6.22. The α_2 absorption coefficient has been chosen such that the Francois-Garrison¹⁰⁶ absorption is obtained for the fundamental frequency component. As shown in Figures 6.11 and 6.12, modifying the absorption for the second harmonic component to match the properties of seawater¹⁰⁶ causes an increase in NA_{sim} . At $r = 10$ m with the 1000 W power setting, the differences are 0.1 dB and 0.03 dB for the 200 kHz and 120 kHz operating frequencies, respectively. The corresponding differences at 300 m distance are 0.7 dB and 0.6 dB (Section 6.2.2). With the modified absorption coefficient, the simulated nonlinear attenuation for $r = 300$ m and 1000 W power setting become close to

5 dB at 200 kHz and 2 dB for the 120 kHz operating frequency. Some results from such simulations are shown in Figure 6.23. The actual nonlinear attenuation might be even stronger.

Table 6.10. Simulated axial nonlinear attenuation (Equation (5.10)) in seawater for some distances r from the sound source.

| | $r = 5.6 \text{ m}$ | $r = 9 \text{ m}$ | $r = 50 \text{ m}$ | $r = 100 \text{ m}$ | $r = 300 \text{ m}$ |
|----------------|---------------------|-------------------|--------------------|---------------------|---------------------|
| 200 kHz | | | | | |
| 50 W | 0.1 dB | 0.1 dB | 0.2 dB | 0.3 dB | 0.3 dB |
| 100 W | 0.2 dB | 0.3 dB | 0.5 dB | 0.6 dB | 0.6 dB |
| 150 W | 0.3 dB | 0.4 dB | 0.7 dB | 0.8 dB | 0.8 dB |
| 200 W | 0.5 dB | 0.7 dB | - | - | - |
| 500 W | 1.3 dB | 1.6 dB | - | - | - |
| 1000 W (E1) | 2.5 dB | 3.0 dB | - | - | - |
| 1000 W (G) | 2.4 dB | 2.8 dB | 3.9 dB | 4.1 dB | 4.1 dB |
| 120 kHz | | | | | |
| 45 W | 0.02 dB | 0.03 dB | - | - | - |
| 100 W | 0.04 dB | 0.06 dB | 0.1 dB | 0.1 dB | 0.1 dB |
| 250 W | 0.1 dB | 0.1 dB | 0.3 dB | 0.3 dB | 0.3 dB |
| 500 W (E2) | 0.3 dB | 0.3 dB | - | - | - |
| 1000 W (E2) | 0.5 dB | 0.7 dB | - | - | - |
| 1000 W (G) | 0.5 dB | 0.6 dB | 1.1 dB | 1.2 dB | 1.3 dB |

During recent fisheries research surveys made by the Institute of Marine Research, 120 W and 250 W power settings have been used for the 200 kHz and 120 kHz echo sounders, respectively.^{143,144} Simrad recommends maximum power settings of 100 W for the 200 kHz operating frequency and 500 W for 120 kHz.¹³ According to the simulation results, the power settings used by IMR keep the nonlinear axial attenuation less than 0.5 dB for both operating frequencies (Figures 6.21 and 6.22). The Simrad recommendation yields somewhat stronger nonlinear attenuation at 120 kHz. It should be noted that higher nonlinear attenuation can occur due to air bubbles or other factors that

are not accounted for here. Also, the measurements indicate somewhat stronger nonlinear attenuation than the simulations. The power settings should thus be set at least as low as those used by IMR if nonlinear attenuation less than 0.5 dB along the sound beam axis is to be avoided. The consequences of nonlinear attenuation to measurements of the volume scattering coefficients is treated in Chapter 7.

Based on the work of Shooter *et al.*,²²¹ Simmonds and MacLennan²²³ suggest source level limits of 222 dB for the 200 kHz operating frequency and 226 dB for 120 kHz. In terms of the linear-equivalent source levels shown in Tables 6.3 and 6.2, their suggestions correspond approximately to 300 W and 1000 W EK60 power settings, respectively. Somewhat more than 1 dB nonlinear attenuation is predicted for both operating frequencies within 300 m distance (Figures 6.21 and 6.22).

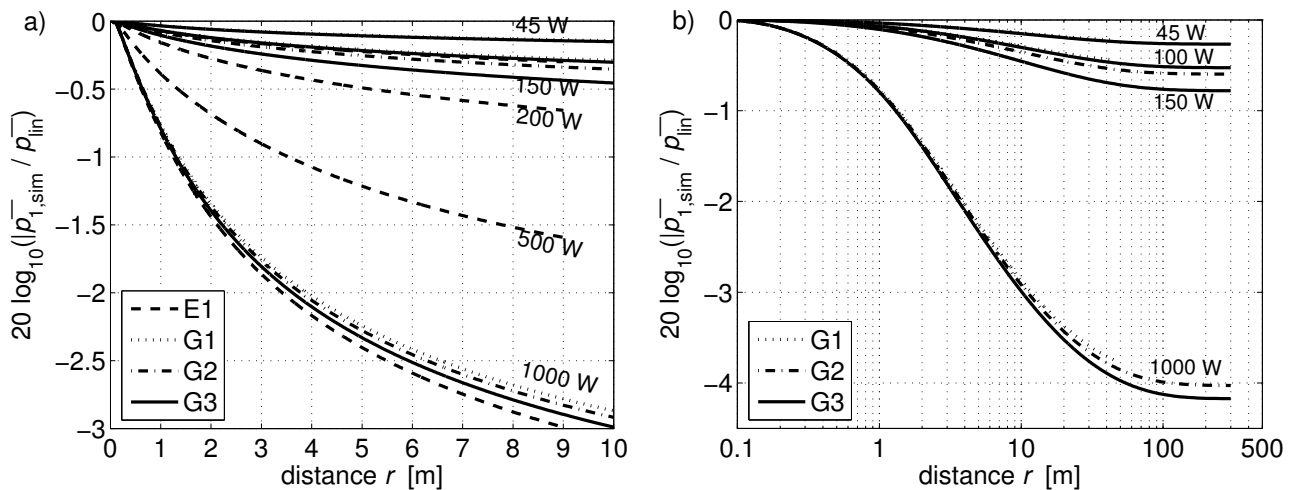


Figure 6.21. Simulated nonlinear attenuation for the 200 kHz echo sounders. a) Close-up of the distances for which hydrophone measurements have been made, b) simulation results for distances up to 300 m.

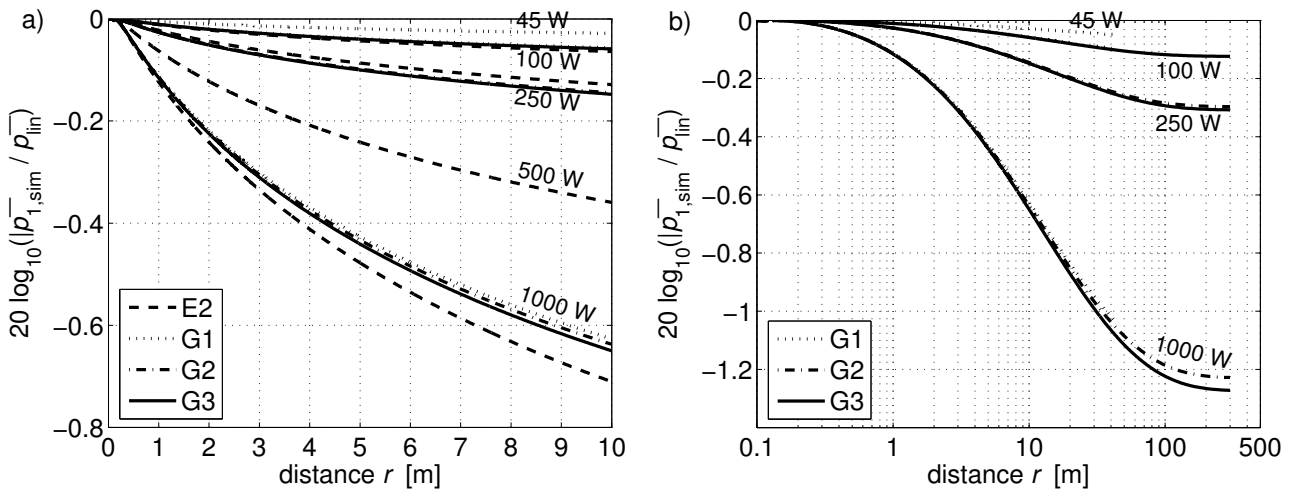


Figure 6.22. Simulated nonlinear attenuation for the 120 kHz echo sounders. a) Close-up of the distances for which hydrophone measurements have been made, b) simulation results for distances up to 300 m.

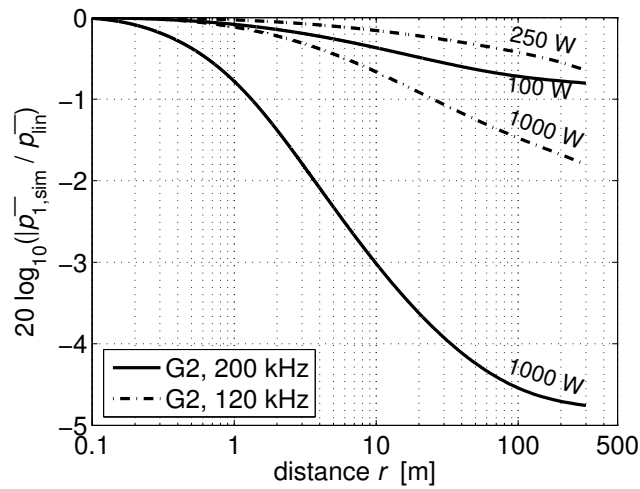


Figure 6.23. Simulated nonlinear attenuation with the absorption coefficients for the second harmonic component changed to comply with tabulated values for seawater.¹⁰⁶

Chapter 7. Volume scattering

The importance of nonlinear effects for the measurement of backscattered acoustic energy from a distribution of small targets is of special interest in connection with biomass estimation and discrimination between species of fish and plankton at sea. A method is proposed in which simulation results are used to compensate the volume backscattering coefficient for the simulated nonlinear attenuation (Section 7.1). Possible correction factors based on simulations made in the present work are calculated. The importance of the echo sounder calibration made prior to the acoustic measurements is discussed. In Section 7.2 experimental results for the area backscattering coefficient obtained by measurements on fish schools are presented. The results from measurements with different power settings are compared with the theoretical results from Section 7.1.



7.1. Compensation of volume backscattering measurements

A way to compensate volume backscattering coefficients for nonlinear attenuation is suggested in this section. Given the measured water parameters of the G1 and G2 measurement sets (Section 6.1), Bergen Code simulations are used to calculate compensation factors for three different special cases that correspond to different echo sounder calibrations.

7.1.1. Compensated volume backscattering coefficient

The volume backscattering coefficient s_v is defined as backscattering cross-section per unit volume (Section 2.1). In the following, the symbol s_v will be used for the coefficient measured by the echo sounder, i.e., calculated from the backscattered signal intensity under the assumption of linear sound propagation. By replacing G_0^2 with $G_0G'_0$, in Equation (2.35), one obtains

$$s_v = \frac{P_r 32\pi^2 \cdot r^2 10^{\frac{2\alpha}{10}r}}{G_0 G'_0 \psi P_r \lambda^2 c_0 \tau F_z} = \frac{P_r \cdot f_{TVG20} \cdot \langle \text{constant} \rangle}{G_0 G'_0 \psi}, \quad (7.1)$$

where

$$\psi = \frac{1}{G_0 G'_0} \int_{4\pi} G(\theta, \varphi) G'(\theta, \varphi) d\Omega. \quad (7.2)$$

Here the two-way transducer gain $G^2(\theta, \varphi)$ (Section 2.1) has been split into a transmit transducer gain function $G(\theta, \varphi)$ and a receive transducer gain function $G'(\theta, \varphi)$. G_0 and G'_0 are the axial transmit and receive transducer gains, respectively.

Further, it is here suggested that the reduction in acoustic intensity due to nonlinear attenuation be expressed as a correction to the transmit gain function $G(\theta, \varphi)$. As the transducer gain refers to intensity, G is proportional to the square of the transmitted sound pressure amplitude in the far field. As the nonlinear attenuation depends on propagation distance, so does the “nonlinearity compensated” transmit transducer gain $G_n(r, \theta, \varphi)$. Calculated from numerical simulation results, it becomes

$$G_n(r, \theta, \varphi) = G(\theta, \varphi) \cdot \left(\frac{\bar{p}_{1,\text{sim}}(r, \theta, \varphi)}{\bar{p}_{\text{lin}}(r, \theta, \varphi)} \right)^2. \quad (7.3)$$

$\bar{p}_{1,\text{sim}}(r, \theta, \varphi)$ is the simulated effective (rms) sound pressure for the fundamental frequency component, normalized to the source condition

amplitude $p_{0,\text{rms}} \cdot \bar{p}_{\text{lin}}(r, \theta, \varphi)$ is the corresponding simulated sound pressure calculated with $p_{0,\text{rms}} = 1 \text{ Pa} / \sqrt{2}$, i.e., with negligible nonlinear effects (Equation (5.9)). As in Sections 5.3.3 and 6.3.2, the backscattered sound wave is taken to propagate linearly. A nonlinearity compensated two-way equivalent beam angle ψ_n , which also becomes range dependent, can be defined as

$$\psi_n = \psi_n(r) = \frac{1}{G_{0,n}(r) \cdot G'_0} \int_{4\pi} G_n(r, \theta, \varphi) G'(\theta, \varphi) d\Omega, \quad (7.4)$$

where $G_{0,n}(r) = G_n(r, 0, 0)$.

It is first assumed that the echo sounder has been calibrated with sufficiently low power setting to disregard nonlinear effects. If this assumption does not hold, an additional factor should be included in Equation (7.1) (cf. Section 7.1.2). Volume backscattering coefficients measured with higher power settings can be compensated for nonlinear attenuation by replacing G_0 with $G_{0,n}$ and ψ with ψ_n in Equation (7.1),

$$s_{v,n}(r) = s_v(r) \cdot \frac{G_0 \psi}{G_{0,n}(r) \psi_n(r)} = s_v(r) \cdot \frac{\int_{4\pi} G(\theta, \varphi) G'(\theta, \varphi) d\Omega}{\int_{4\pi} G_n(r, \theta, \varphi) G'(\theta, \varphi) d\Omega}. \quad (7.5)$$

$s_{v,n}$ is the volume backscattering coefficient compensated for nonlinear attenuation.

7.1.2. Nonlinear effects in echo sounder calibration

The s_v corrections above apply when nonlinear effects during echo sounder calibration can be disregarded. This is not necessarily the case.

The two-way axial transducer gain $G_0 G'_0$ and the beam compensation function for target strength measurement (not used in volume backscattering measurements, cf. Section 2.1) are adjusted and monitored through regular echo sounder calibrations. The value of the equivalent two-way beam angle ψ is supplied individually with each transducer from the manufacturer.

Measurements of ψ can be made on hull-mounted transducers,^{191,208} but this is not part of the regular calibration routine. The two-way axial transducer gain used for s_v measurements is measured with the calibration sphere close to the sound beam axis.

Calibration measurements are performed with the reference target at an approximately fixed distance r_{cal} from the echo sounder transducer. Calibration distances of 10 m–12 m are common. Norwegian research vessels calibrating at Uggdalseid south of Bergen often use 20 m–25 m calibration distances. The simulated effective sound pressure for the fundamental frequency component (accounting for nonlinear propagation) at the position of the calibration sphere is $p_{1,\text{cal}}(r_{\text{cal}}, 0, 0)$. When nonlinear attenuation occurs during calibration, the two-way transducer gain appears lower than if the sound propagation were linear,

$$G_{0,\text{cal}}G'_0 = G_0G'_0 \cdot \left(\frac{\bar{p}_{1,\text{cal}}(r_{\text{cal}}, 0, 0)}{\bar{p}_{\text{lin},\text{cal}}(r_{\text{cal}}, 0, 0)} \right)^2. \quad (7.6)$$

$p_{\text{lin},\text{cal}}(r, \theta, \varphi)$ is the effective sound pressure simulated without accounting for nonlinear effects. As before, this has been done by setting the peak source condition amplitude equal to 1 Pa. $G_{0,\text{cal}}G'_0$ is the apparent two-way axial transducer gain. As in Equation (7.3), the bars in Equation (7.6) denote normalization to the source condition amplitude. By replacing G_0 with $G_{0,\text{cal}}$ in Equation (7.5), one obtains for the compensated $s_{v,n}$,

$$\frac{s_{v,n}(r)}{s_v(r)} = \frac{G_{0,\text{cal}}\psi}{G_{0,n}(r)\psi_n(r)} = \frac{\int_{4\pi} G(\theta, \varphi)G'(\theta, \varphi)d\Omega}{\int_{4\pi} G_n(r, \theta, \varphi)G'(\theta, \varphi)d\Omega} \cdot \left(\frac{\bar{p}_{1,\text{cal}}(r_{\text{cal}}, 0, 0)}{\bar{p}_{\text{lin},\text{cal}}(r_{\text{cal}}, 0, 0)} \right)^2. \quad (7.7)$$

Equation (7.7) is used in the following to calculate values of $s_{v,n}/s_v$ from simulation results.

7.1.3. Compensation factors from simulations

Calculations

A set of Bergen Code simulations is run to calculate the ratio of volume scattering coefficients $s_{v,n}/s_v$ (Equation (7.7)) for comparison with measurement results. Source conditions, numerical calculation parameters, and seawater parameters are chosen as for measurement set G2 in Section 6.2. 1 Pa peak source condition amplitude is used to calculate $p_{\text{lin}}(r, \theta, \varphi)$.

The linear transmit and receive transducer gain functions $G(\theta, \varphi)$ and $G'(\theta, \varphi)$ refer to intensity and are thus proportional to the square of the simulated linear beam pattern. The simulated effective sound pressures p_{lin} for linear and $p_{1,\text{sim}}$ for nonlinear sound propagation are normalized to their corresponding source condition amplitudes and combined to (Equation (7.7))

$$\begin{aligned} \frac{s_{v,n}}{s_v} &= \frac{\int_{4\pi} \bar{p}_{\text{lin}}^4(r, \theta, \varphi) d\Omega}{\int_{4\pi} \bar{p}_{\text{lin}}^4(r, \theta, \varphi) \cdot \left(\frac{\bar{p}_{1,\text{sim}}(r, \theta, \varphi)}{\bar{p}_{\text{lin}}(r, \theta, \varphi)} \right)^2 d\Omega} \cdot \frac{\bar{p}_{1,\text{cal}}^2(r_{\text{cal}}, 0, 0)}{\bar{p}_{\text{lin},\text{cal}}^2(r_{\text{cal}}, 0, 0)} \\ &= \frac{\int_{4\pi} \bar{p}_{\text{lin}}^4(r, \theta, \varphi) d\Omega}{\int_{4\pi} \bar{p}_{\text{lin}}^2(r, \theta, \varphi) \cdot \bar{p}_{1,\text{sim}}^2(r, \theta, \varphi) d\Omega} \cdot \frac{\bar{p}_{1,\text{cal}}^2(r_{\text{cal}}, 0, 0)}{\bar{p}_{\text{lin},\text{cal}}^2(r_{\text{cal}}, 0, 0)}. \end{aligned} \quad (7.8)$$

As the simulated sound field is axisymmetric, the sound pressure amplitude does not depend on the azimuth angle φ . The substitution $d\Omega = \sin \theta d\theta d\varphi$ and integration with respect to φ yields

$$\frac{s_{v,n}}{s_v} = \frac{\int_0^\pi \bar{p}_{\text{lin}}^4(r, \theta) \cdot \sin \theta d\theta}{\int_0^\pi \bar{p}_{\text{lin}}^2(r, \theta) \cdot \bar{p}_{1,\text{sim}}^2(r, \theta) \sin \theta d\theta} \cdot \frac{\bar{p}_{1,\text{cal}}^2(r_{\text{cal}}, 0)}{\bar{p}_{\text{lin},\text{cal}}^2(r_{\text{cal}}, 0)}. \quad (7.9)$$

Although side lobe levels are typically below -25 dB relative to the main lobe for the transducers in question,^{6,7} they contribute by a small amount to the equivalent two-way beam angle. As discussed in Section 3.1, the KZK equation is not valid at great angles off the sound beam axis. So far in the present work,

only simulation results within $\theta = 6^\circ$ have been used for comparison with measurements. The results show that nonlinear attenuation is strongest close to the sound beam axis and weakens rapidly with increasing θ . This gives good reason to assume that the simulation results for $\theta \leq 6^\circ$ is sufficient for determining the ratio of volume backscattering coefficients $s_{v,n}/s_v$. The simulated linear value for the equivalent beam angle when only the results within 6° are included,

$$\Psi_{\text{lin}} = 10 \cdot \log_{10} \left[\frac{1}{p_{\text{lin}}^4(r, 0)} \int_0^{6^\circ} p_{\text{lin}}^4(r, \theta) \sin \theta \, d\theta \right], \quad (7.10)$$

becomes -21.05 dB re 1 steradian (sr) for both the 120 kHz and the 200 kHz sound field. $\Psi = -21$ dB is stated as a typical equivalent beam angle in the transducer data sheets.^{6,7} During the G2 measurements, -20.5 dB and -21.0 dB were used for the 200 kHz and 120 kHz transducers, respectively. Increasing the upper integration limit from 6° to 12° in Equation (7.10) yields a 0.02 dB increase in Ψ_{lin} . The integrals of Equation (7.9) are thus truncated,

$$\frac{s_{v,n}}{s_v} \approx \frac{\int_0^{6^\circ} \bar{p}_{\text{lin}}^4(r, \theta) \cdot \sin \theta \, d\theta}{\int_0^{6^\circ} \bar{p}_{\text{lin}}^2(r, \theta) \cdot \bar{p}_{1,\text{sim}}^2(r, \theta) \sin \theta \, d\theta} \cdot \frac{\bar{p}_{1,\text{cal}}^2(r_{\text{cal}}, 0)}{\bar{p}_{\text{lin},\text{cal}}^2(r_{\text{cal}}, 0)}. \quad (7.11)$$

Simulation results are inserted for the integrands, and the integrations are performed with the trapezoidal rule.

The ratio $s_{v,n}/s_v$ is calculated for three cases (Table 7.1). In the first, the echo sounder calibration has been performed with sufficiently low source level so that nonlinear attenuation can be disregarded. $\bar{p}_{1,\text{cal}}$ and $\bar{p}_{\text{lin},\text{cal}}$ are thus equal. For the second and third case, it is assumed that calibration was performed with the 1000 W EK60 power setting and with the calibration sphere at distances $r_{\text{cal}} = 12$ m and $r_{\text{cal}} = 25$ m, respectively. The seawater parameters for the G1

measurement set (Table 6.5) are used to calculate the calibration correction factor $\bar{p}_{1,\text{cal}}^2(r_{\text{cal}}, 0) / \bar{p}_{\text{lin},\text{cal}}^2(r_{\text{cal}}, 0)$.

Table 7.1. Parameters for $s_{v,n}/s_v$ calculations based on simulations.

| | calibration | calibration | $20 \cdot \log_{10}(\bar{p}_{1,\text{cal}} / \bar{p}_{\text{lin},\text{cal}})$ | | figure number |
|--------|--------------------|---------------------------|--|---------|---------------|
| | EK60 power setting | distance r_{cal} | 200 kHz | 120 kHz | |
| Case 1 | low | - | 0 dB | 0 dB | 7.2 |
| Case 2 | 1000 W | 12 m | -3.0 dB | -0.7 dB | 7.3a |
| Case 3 | 1000 W | 25 m | -3.5 dB | -0.9 dB | 7.3b |

Simulation results

Figure 7.1 shows simulation results for the -3 dB beam angle $\theta_{-3\text{ dB}}(r)$ and the two-way equivalent beam angle. The simulated equivalent beam angle for the 1000 W power setting (Figure 7.1b) increases with approximately 1 dB due to nonlinear effects.

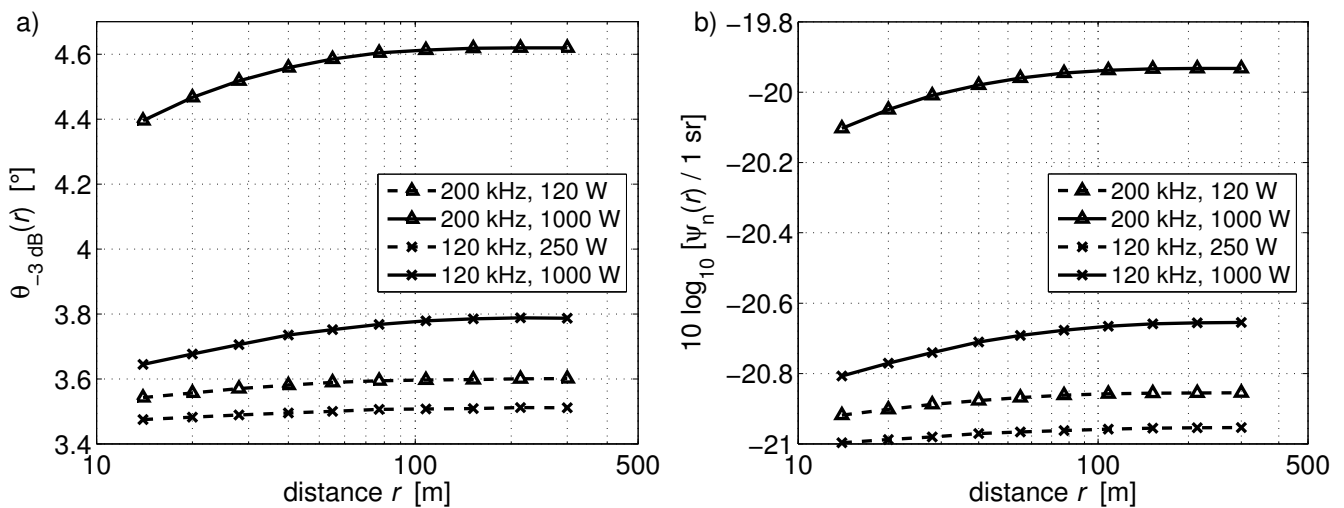


Figure 7.1. a) Simulated -3 dB beam angle as function of distance r from the sound source. b) Simulated effective two-way beam angle $\psi_n(r)$ as function of axial distance from the sound source.

The increase in ψ and the weakening of the axial sound field due to nonlinear attenuation (Figures 6.21 and 6.22) have opposite effects on s_v measurement

results. Simulation values for $s_{v,n}/s_v$ calculated without accounting for nonlinear effects during calibration (Case 1 in Table 7.1) are shown in Figure 7.2. In this case, nonlinear attenuation causes the echo sounder to underestimate s_v at all distances. For the 1000 W power setting and 200 kHz operating frequency, $10 \log_{10}(s_{v,n}/s_v)$ approaches 3 dB. In the 120 kHz case, the corresponding result is approximately equal to 0.8 dB at 300 m distance from the echo sounder transducer.

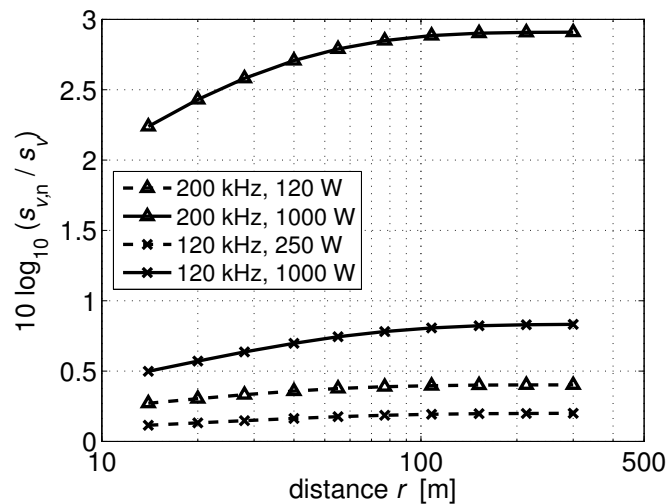


Figure 7.2. Simulated values for $s_{v,n}/s_v$ when nonlinear effects during echo sounder calibration are negligible.

The still commonly used Simrad EK500 echo sounder uses 1000 W as the standard electrical transmit power setting for transducers with 7° opening angle at both the 120 kHz and 200 kHz operating frequencies. If the echo sounder calibrations prior to the s_v measurements are performed with the 1000 W power setting for both operating frequencies, the transducer gain appears lower than in Case 1. As shown in Figure 7.3, this acts upon measurement results for s_v in the opposite direction of nonlinear attenuation during the s_v measurements themselves. Figure 7.3a shows the simulation results for $s_{v,n}/s_v$ in Case 2 (Table 7.1). Here, calibration has been performed with the 1000 W power setting and the calibration sphere at distance $r_{\text{cal}} = 12$ m from the echo sounder transducer. For the 200 kHz operating frequency, $10 \log_{10}(s_{v,n}/s_v)$ is decreased with 3 dB (Figure 7.3a). Although the resulting s_v compensation is reduced, the

change in the sampling volume ensonified by the echo sounder is the same as in Case 1 (Figure 7.1). The simulation results for Case 3 are shown in Figure 7.3b. The 1000 W calibration with $r_{\text{cal}} = 25$ m yields yet lower values for $10 \log_{10}(s_{v,n}/s_v)$. In this case, the plotted decibel value is negative for both operating frequencies and all propagation distances up to 300 m.

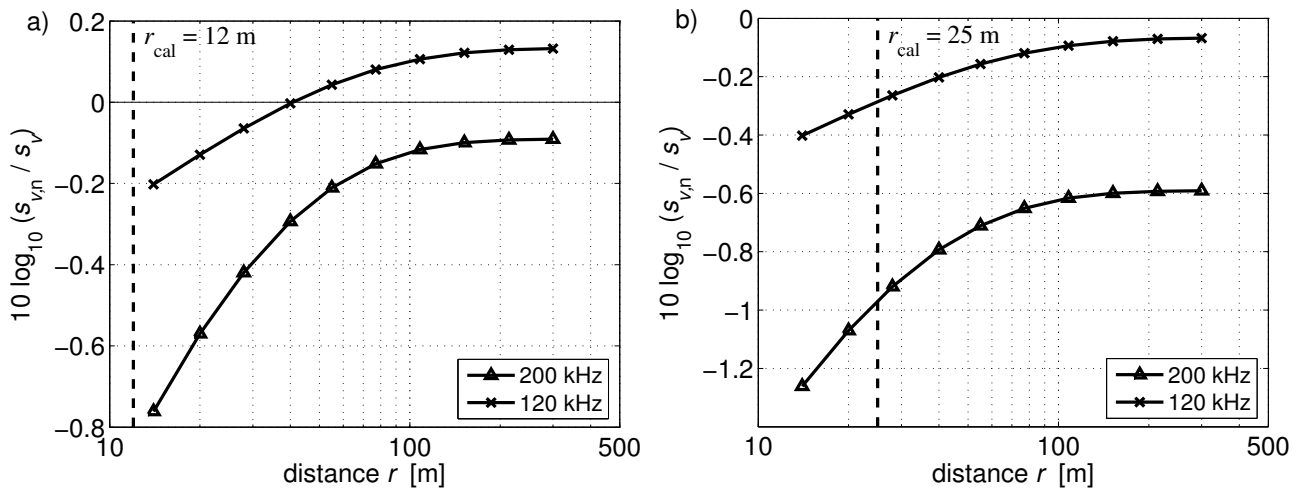


Figure 7.3. Simulated values of $s_{v,n}/s_v$ in seawater (G2) for an EK60 echo sounder with ES120-7C and ES200-7C transducers. The echo sounder has been calibrated with the 1000 W power setting and the calibration sphere at distance a) $r_{\text{cal}} = 12$ m and b) $r_{\text{cal}} = 25$ m. The power used for the s_v measurements is also 1000 W.

Figure 7.4 shows simulation results similar to those shown in Figure 7.3, but for other calibration distances r_{cal} . As for the cases listed in Table 7.1, the 1000 W power setting has been assumed used for both calibration and s_v measurements. As above, the seawater medium parameters for the G2 measurement set have been used to simulate the s_v measurements, while the corrections due to nonlinear effects during calibration have been calculated with the G1 medium parameters (Table 6.5). The simulation results shown in Figures 7.3 and 7.4 refer to the EK60 echo sounder with ES120-7C and ES200-7C transducers.

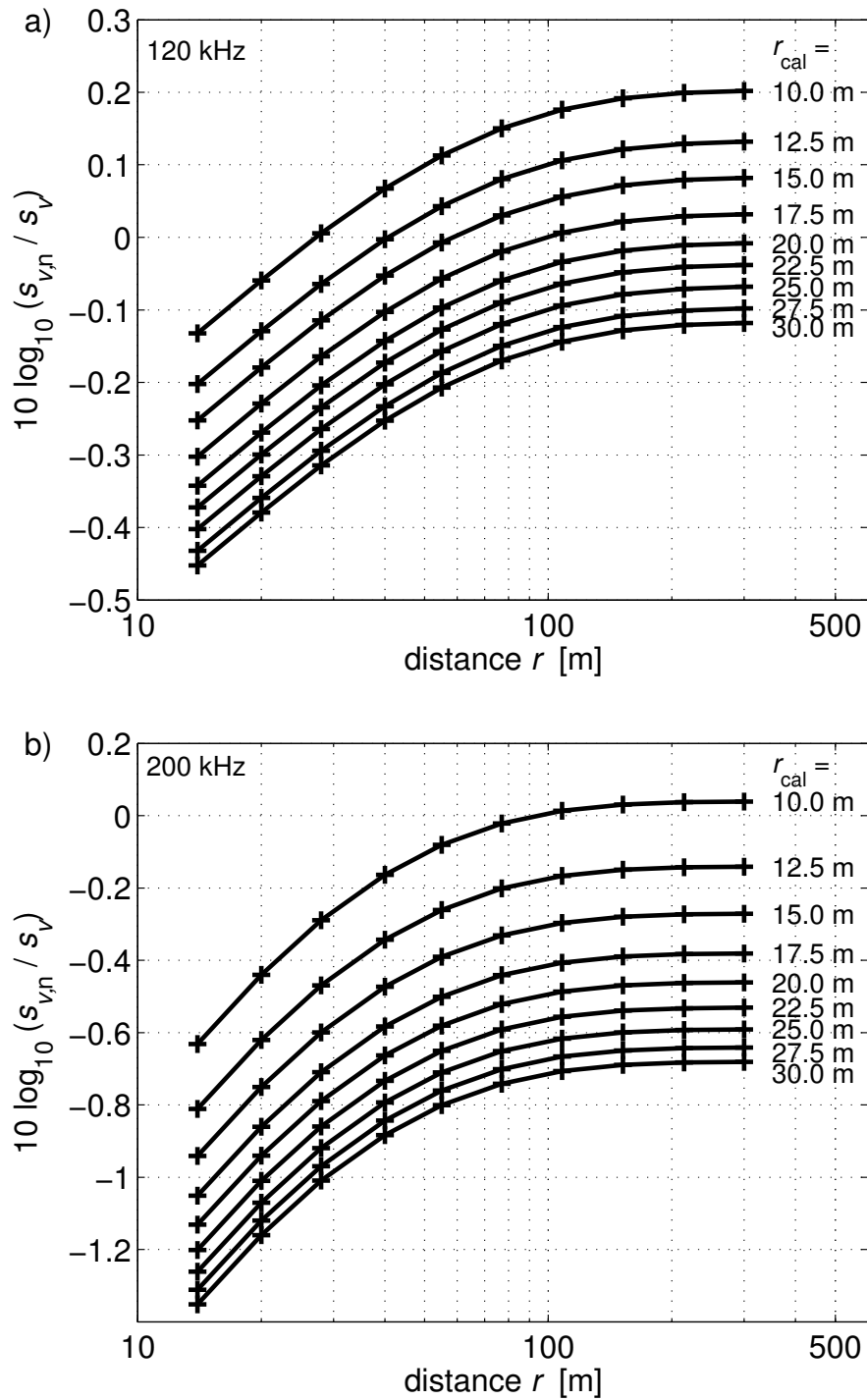


Figure 7.4. Simulated values of $s_{v,n}/s_v$ in seawater (G2) for an EK60 echo sounder set to 1000 W output power, with ES120-7C and ES200-7C transducers. The echo sounder has been calibrated with the 1000 W power setting and the calibration sphere at distances 10.0 m, 12.5 m, 15.0 m, 17.5 m, 20.0 m, 22.5 m, 25.0 m, 27.5 m, and 30.0 m. a) 120 kHz operating frequency. b) 200 kHz operating frequency.

The several assumptions and possible errors in the simulation results pointed out in Chapter 3 and Section 6.3 also apply to the results presented here. The simulations are performed without the modification to the absorption coefficient described in Section 6.2.2. The reduced absorption for the second harmonic frequency component would yield slightly increased nonlinear attenuation. Also, some discrepancy is reported between measurement and simulation results for the nonlinear attenuation (Section 6.3). It is important to note that several parameters may influence the simulated value for $s_{v,n}/s_v$, as well as the echo sounder measurement result s_v . For example, the influence of gas bubbles in the water has not been accounted for here. The results reported here apply only to the described special cases.

A measured volume scattering coefficient s_v may be compensated for nonlinear attenuation by means of a factor such as $s_{v,n}/s_v$. However, in addition to changing the value of the measured s_v , the flattening of the main also changes the sampling volume that the measurement refers to. The ensonified volume is larger than predicted by a linear sound propagation model (Figure 7.1). As for target strength measurements close to the sound beam axis, the power limits used by IMR¹⁴³ (Section 6.3) or lower are recommended for minimizing errors due to nonlinear attenuation. Even lower power settings might be necessary to keep the error in 200 kHz measurements below 0.5 dB.

7.2. Experiment

Some measurements of area backscattering coefficients of mackerel schools are presented in the following. High and low power settings are used for the 120 kHz and 200 kHz operating frequencies. The experimentally obtained backscattering coefficients are compared, and the results are held together with the theoretical results from Section 7.1.3.

7.2.1. Measurement of area backscattering coefficient

Echo sounder measurements on mackerel were performed from RV G. O. Sars during a survey in the North Sea in November 2004. A Simrad EK60 echo sounder operated simultaneously with transceivers and transducers for 18 kHz, 38 kHz, 70 kHz, 120 kHz, 200 kHz and 364 kHz frequencies. The six transducers are mounted closely together for optimal overlap between their sound beams.¹⁴¹ The vessel crossed back and forth over an area with several fish schools while the power settings for the 120 kHz and 200 kHz were alternated between low and high for each crossing. The “low” power settings are 250 W and 120 W, respectively, while the “high” setting is 1000 W for both frequencies. Measurements were made over a few hours on two consecutive days. Most of the fish schools extended from approximately 25 m to 75 m–100 m. Example echograms are shown in Figure 7.6. 39 passes over mackerel schools were recorded (Table 7.2). The measurements are referred to as measurement set G2 in Table 6.1.

The echo sounders were calibrated using the low power settings immediately before the survey cruise. This was during the same stay at Uggdalseid as when the G1 measurements were made as part of the present work (Chapter 6). CTD data for the G1 and G2 measurement sets are shown in Figure 6.8.

The nautical area scattering coefficient s_A is measured in m^2/nmi^2 (nmi is nautical mile) and defined as (2.37)

$$s_A = 4\pi(1852)^2 s_a.$$

Mean s_A for each school are calculated with the Simrad BI60 post processing software. The results are shown in Table 7.2. The values obtained at 120 kHz with the 250 W power setting, range from $450 \text{ m}^2/\text{nmi}^2$ to $10500 \text{ m}^2/\text{nmi}^2$. The average is $3235 \text{ m}^2/\text{nmi}^2$, and the standard deviation is $2900 \text{ m}^2/\text{nmi}^2$.

The relative frequency response $r(f)$ is defined as the volume backscattering coefficient measured with the operating frequency f , divided by that measured simultaneously in the same volume at 38 kHz,^{142,141}

$$r(f) \equiv \frac{s_v(f)}{s_v(38 \text{ kHz})}. \quad (7.12)$$

For the purpose of the present investigation, the relative area backscatter frequency response $r_a(f)$ is here defined correspondingly,

$$r_a(f) \equiv \frac{s_a(f)}{s_a(38 \text{ kHz})} = \frac{s_A(f)}{s_A(38 \text{ kHz})}. \quad (7.13)$$

Table 7.2 shows the measurement results for the 39 passes that were made over fish schools. The entries have been sorted after which combination of echo sounder power settings has been used. The results are plotted in terms of $R_a(f) = 10 \log_{10} r_a(f)$ in Figure 7.5. The measurement results indicate a clear difference between $R_a(f)$ measured with high and low power settings. For the 200 kHz operating frequency, increasing the power setting from 120 W to 1000 W yields an approximate decrease of 3 dB in $R_a(200 \text{ kHz})$. When the 120 kHz output power setting is switched from 250 W to 1000 W, $R_a(120 \text{ kHz})$ decreases with approximately 1 dB.

The 3 data points in each of Figures 7.5a and 7.5b that deviate the most strongly from the general trend are due to measurements 8, 26, and 38 (Table 7.2). $s_A(38 \text{ kHz})$ is less than 150 in all three measurements. Stable $r_a(f)$ measurements are not expected for such small s_A , possibly indicating that e.g. backscatter from only the periphery of a fish school has been measured.¹⁴⁵

The power dependence of the echo sounder measurement results is ascribed to nonlinear attenuation in the water. Using too high output powers can clearly yield errors in volume and area backscattering coefficients measured at 120 kHz and 200 kHz operating frequencies. The 200 kHz frequency is the most sensitive to the power setting of the two. Stronger nonlinear attenuation is

expected for higher operating frequencies such as 364 kHz and 400 kHz. Because of the integration over the sound beam, the nonlinear attenuation has somewhat less effect on volume scattering measurements than on target strength measurements along the sound beam axis.

Table 7.2. Nautical area scattering coefficients s_A obtained through post processing of the G2 measurement set, using the BI60 software. The unit for s_A is m^2/nmi^2 .

| measurement number | $s_A(38 \text{ kHz})$ (2000 W) | $s_A(120 \text{ kHz})$ 250 W | $s_A(120 \text{ kHz})$ 1000 W | $s_A(200 \text{ kHz})$ 120 W | $s_A(200 \text{ kHz})$ 1000 W |
|--------------------|-----------------------------------|---------------------------------|----------------------------------|---------------------------------|----------------------------------|
| 1 | 3616 | 6105 | - | 10082 | - |
| 2 | 2749 | 4931 | - | 7864 | - |
| 3 | 1568 | 3146 | - | 4887 | - |
| 4 | 2116 | 3636 | - | 6333 | - |
| 5 | 377 | 735 | - | 1206 | - |
| 6 | 1250 | 2374 | - | 3797 | - |
| 7 | 2194 | 3807 | - | | - |
| 8 | 105 | 518 | - | 651 | - |
| 9 | 4141 | 8318 | - | 13184 | - |
| 10 | 5707 | 10484 | - | 18865 | - |
| 11 | 4146 | 7559 | - | 12842 | - |
| 12 | 5271 | 8996 | - | 15512 | - |
| 13 | 886 | 1628 | - | 3221 | - |
| 14 | 339 | 671 | - | 1173 | - |
| 15 | 1976 | 3600 | - | 6833 | - |
| 16 | 758 | 1441 | - | 2457 | - |
| 17 | 672 | - | - | 2156 | - |
| 18 | 521 | 1104 | - | 1895 | - |
| 19 | 1093 | 1983 | - | 3621 | - |
| 20 | 808 | 1706 | - | 3620 | - |
| 21 | 1495 | 3000 | - | 5865 | - |
| 22 | 831 | 1699 | - | 2900 | - |

| | | | | | |
|----|------|------|------|------|------|
| 23 | 484 | 1040 | - | - | - |
| 24 | 229 | 449 | - | - | - |
| 25 | 659 | 1288 | - | - | 1220 |
| 26 | 134 | 664 | - | - | 525 |
| 27 | 2113 | - | 3062 | - | 2942 |
| 28 | 1075 | - | 1377 | - | 1671 |
| 29 | 1623 | - | 2183 | - | 2723 |
| 30 | 1365 | - | 1921 | - | 2275 |
| 31 | 847 | - | 1027 | - | 1252 |
| 32 | 2755 | - | 3560 | - | 4218 |
| 33 | 851 | - | 1361 | - | 1553 |
| 34 | 3841 | - | 5377 | - | 6311 |
| 35 | 5241 | - | 5879 | - | 6672 |
| 36 | 755 | - | 1201 | - | 1287 |
| 37 | 591 | - | 929 | 1709 | - |
| 38 | 132 | - | 510 | 830 | - |
| 39 | 995 | - | 1994 | 3228 | - |

7.2.2. Comparison with simulation results

Measured values for the area backscattering coefficient s_a (Equation (2.36)) can be compensated for nonlinear attenuation by replacing s_v with $s_{v,n}$,

$$s_{a,n} = \int_{z_1}^{z_2} s_{v,n} dz . \quad (7.14)$$

If uniform backscatter is assumed in the depth layer $[z_1, z_2]$, so that $s_{v,n}$ is constant within this interval, one can write

$$\frac{s_{a,n}}{s_a} = \frac{s_{v,n} \int_{z_1}^{z_2} dz}{s_{v,n} \int_{z_1}^{z_2} \frac{s_v}{s_{v,n}} dz} = \left[\frac{1}{z_2 - z_1} \int_{z_1}^{z_2} \frac{s_v}{s_{v,n}} dz \right]^{-1} . \quad (7.15)$$

$s_{a,n}/s_a$ should thus be similar to the average $s_{v,n}/s_v$ across a narrow depth layer. The integrand $s_v/s_{v,n}$ is substituted from Equation (7.5).

The differences between $R_a(f)$ values from measurements using different output powers are compared with the differences between corresponding simulation results for $10 \log_{10}(s_{v,n}/s_v)$ (Figure 7.2). The measurement results yield approximately 3 dB loss for the 200 kHz operating frequency and 1 dB for the 120 kHz operating frequency. The corresponding simulation results for $10 \log_{10}(s_{v,n}/s_v)$ at distances between 50 m and 100 m are 2.4 dB and 0.6 dB for the two operating frequencies, respectively (Figure 7.2). The discrepancies between simulation and measurement results are thus approximately 0.6 dB and 0.4 dB for the two frequencies. It is likely that more accurate simulation results can be obtained by accounting more correctly for absorption in seawater (cf. Section 6.2.2).

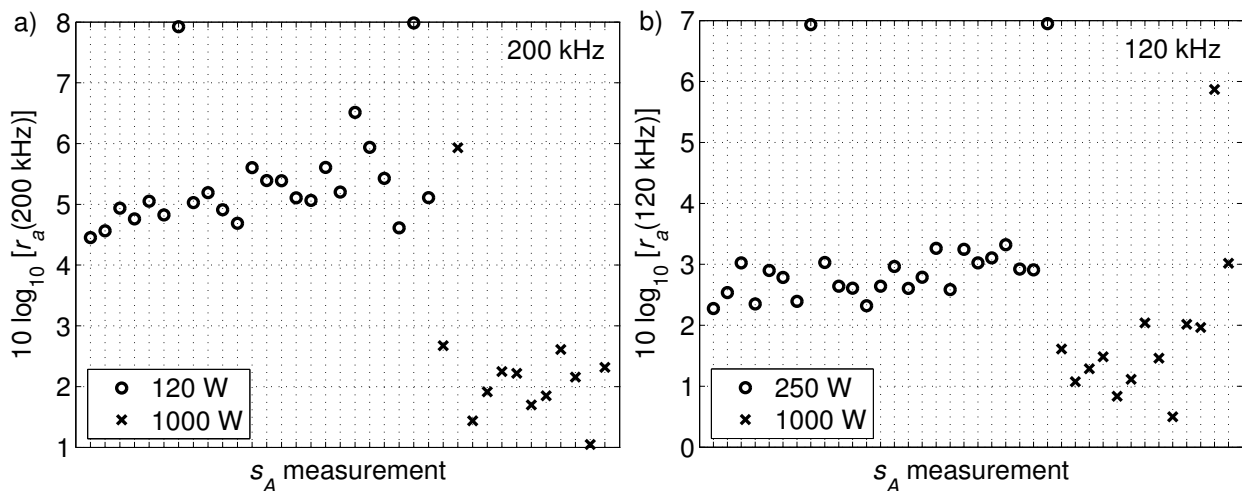


Figure 7.5. Measured area backscatter relative frequency response from measurement set G2.

- a) $r_a(200 \text{ kHz})$ from s_A measurements with 120 W and 1000 W power settings. b) $r_a(120 \text{ kHz})$ from s_A measurements with 250 W and 1000 W power settings.

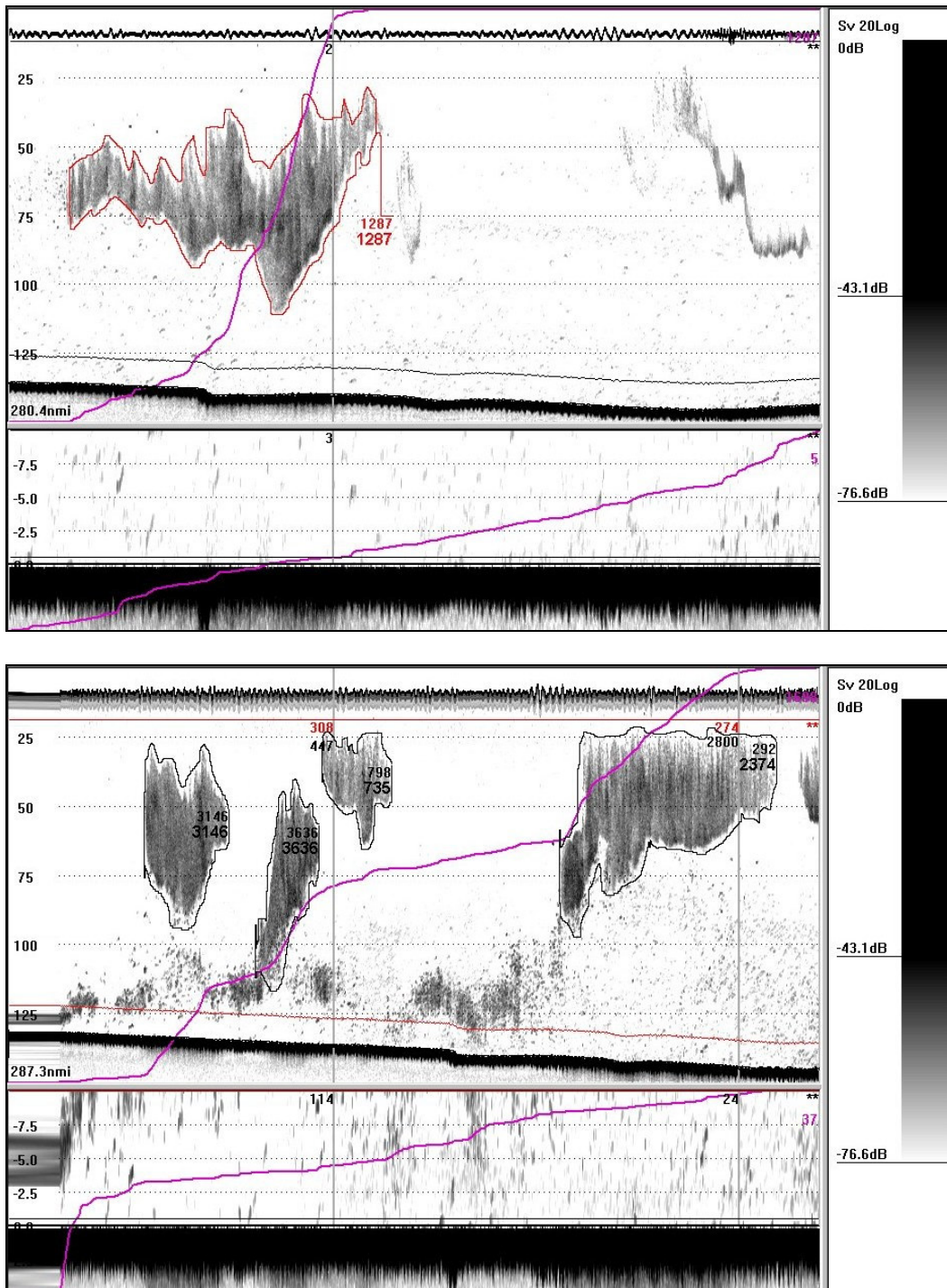


Figure 7.6. Example fish schools from the G2 measurement set. The displayed echograms are screen shots from the Simrad BI60 post processing software. The frequencies and EK60 power settings are 200 kHz, 1000 W (top) and 120 kHz, 250 W (bottom).

Chapter 8. Conclusion

A summary of the presented work and its conclusions is given in Section 8.1. In Section 8.2, suggestions are made for future investigations.

8.1. Summary

Tichy *et al.*²³⁴ presented measurement and simulation results for the axial field of a 200 kHz fisheries research echo sounder in fresh water. The results indicate a potential error in target strength measurements caused by excess attenuation due to nonlinear effects. Tichy *et al.* suggested that an adjustment should be made to measured target strengths to account for nonlinear attenuation. They also recommended that low transmitted power should be used in order to minimize the nonlinear effects.²³⁴ The results obtained by Tichy *et al.* raised questions regarding the nonlinear attenuation in sea water under the various conditions encountered in fisheries research. The nonlinear attenuation on and off the sound beam axis and at relevant distances from the sound source are of interest. In addition to the consequences for target strength measurements, it is also necessary to determine how nonlinear attenuation affects measurements of the volume backscattering coefficient.

Nonlinear sound propagation effects depend on several factors such as properties of the sound source, operating frequency, sound intensity, temperature, salinity, pressure (depth), propagation distance, absorption, and gas bubbles and other particles in the water. In the present work, measurements and simulations have been made for 120 kHz and 200 kHz echo sounders in fresh water and seawater with a few different salinities and water temperatures. The axial fields and radiation patterns have been investigated experimentally with a calibrated hydrophone, by target strength measurements using a

reference target, and by echo sounder measurements on fish schools. The measurement results have been compared with numerical simulations based on the Khokhlov-Zabolotskaya-Kuznetsov^{151,271} second order parabolic wave equation. A goal for the work has been to provide a basis for reducing or correcting for measurement errors in fisheries research due to nonlinear attenuation. Measurements of both target strength and the volume backscattering coefficient have been investigated.

A version of the Bergen Code^{44,45,254} was used for simulating nonlinear sound propagation. The relative standard uncertainty of the simulation results was estimated for some relevant special cases to ± 0.3 dB for the fundamental frequency component and ± 0.6 dB for the second harmonic. Only the radiated field 6° or less off the sound beam axis was considered. Uncertainty contributions related to the employed model (KZK equation^{151,271}), the numerical algorithm, and the input parameters were considered separately. Some important factors were not accounted for in the uncertainty estimates. In particular, the sound source was taken to be a uniformly vibrating, plane circular piston in an infinitely stiff baffle. This idealization deviates from the vibration pattern of the sound sources used in the experiments. Moreover, the absorption was assumed to increase quadratically with frequency, which can be a poor approximation for sea water within some frequency bands.¹⁰⁶ The incorrect absorption is an important contributor to the simulation error for sound propagation in seawater. The possible importance of gas bubbles in the water has not been addressed in the present work.

Near field measurements were made to characterize three echo sounder transducers as sound sources, and axisymmetric source conditions for use with the Bergen Code were obtained from the results. Simulations were carried out with the measured source conditions and with uniform piston source conditions. The results were compared with each other and with measurement results for the radiated sound field in fresh water. The source conditions based on near field measurements give improved agreement between the simulations

and some of the measurements, in particular off the sound beam axis. The uniform piston source condition was however judged the generally best suited for prediction of nonlinear attenuation and the amplitude of the generated second harmonic component. Quantitative studies for fresh water and seawater were therefore based on simulations using the uniform plane piston source conditions.

A calibrated hydrophone was used to measure the sound pressure in the radiated fields of Simrad EK60 echo sounders with 120 kHz and 200 kHz operating frequencies. In addition, experimental target strength measurements were carried out using a calibration sphere as a reference target. Different transmit power settings were used in order to investigate the influence of transmitted power on nonlinear attenuation and measured target strength. Practical considerations limited the hydrophone measurements to distances shorter than 10 metres from the sound source both in fresh water and in seawater. Target strength measurements were performed with the calibration sphere at distances up to approximately 11 metres in fresh water and 50 metres in seawater.

Simulations were compared with the measurements and used to evaluate the excess attenuation due to nonlinear effects. The strongest nonlinear effects were observed in an indoor fresh water tank. On the sound beam axis at 9 m distance from the sound source, the simulated excess attenuations were 0.8 dB and 3.3 dB for the 120 kHz and 200 kHz operating frequencies, respectively, with the 1000 W power setting. The simulations predict 2.1 dB and 5.5 dB nonlinear attenuation for the two frequencies at 100 m distance with the same water properties and power setting. The -3 dB beam angle was measured to 3.4° for both frequencies with low transmitted power. In fresh water, with the 1000 W power setting and approximately 9 m from the sound source, the measured beam angles were increased to 3.7° and 4.3°, respectively.

The results from hydrophone measurements in seawater indicate somewhat less

nonlinear attenuation than in the room-tempered fresh water. This is ascribed to the stronger absorption in seawater. The simulated nonlinear attenuation on the sound beam axis at 9 m distance from the source is 0.6 dB and 3.0 dB for the 120 kHz and 200 kHz operating frequencies, respectively, using the 1000 W power setting. At 100 m distance, the simulated nonlinear attenuation becomes 1.2 dB and 4.1 dB, respectively. Although there is some flattening of the second harmonic main lobe due to energy transfer to higher harmonics, it is narrower than the main lobe for the fundamental frequency component.

A second harmonic frequency component is generated through nonlinear distortion. For 1000 W and 1500 W power settings most of the measurement results for its axial sound pressure level approach -6 dB relative to that of the fundamental frequency component. The simulation results tend to indicate significantly weaker growth for the second harmonic component.

For distances shorter than 10 m, the agreement between simulated and measured axial sound pressure levels for the fundamental frequency component is within approximately 0.5 dB for the fundamental frequency component. The simulated difference between target strength results using high and low transmitted power seems to agree with the calibration sphere measurements to within 0.5 dB for the 200 kHz operating frequency and within 0.9 dB for the 120 kHz frequency.

The volume backscattering coefficient for a distribution of small targets is an important measurement result in fisheries acoustics. A set of experimental measurements on mackerel schools between 25 m and 100 m depths is reported. When the 120 kHz power setting was changed from 250 W to 1000 W, the measured area backscattering coefficient was reduced with approximately 1 dB. Similarly, a change from 120 W to 1000 W in the power setting for the 200 kHz operating frequency yielded an approximate 3 dB reduction in the measured area backscattering coefficient. The measurement results and predictions based on Bergen Code simulations seem to agree to

within approximately 0.6 dB for volume backscattering measurements.

The choice of transmitted power is an important factor for the degree of nonlinear distortion. It can easily be manipulated both in experiments and in practical fisheries research applications. 1000 W is a common upper limit to the allowed power settings in both 120 kHz and 200 kHz Simrad EK60 echo sounders. It is also the standard transmit power for the same operating frequencies in the commonly used echo sounder Simrad EK500. In order to avoid nonlinear attenuation, IMR have chosen to limit the power settings to 250 W for their 120 kHz echo sounders and 120 W for the 200 kHz operating frequency.¹⁴³ The current power limits recommended by Simrad^{13 2002} are 500 W and 100 W, respectively. The simulations carried out in the present work indicate less than 0.5 dB nonlinear attenuation with the power settings used by IMR for propagation distances less than 300 m. Somewhat stronger attenuation is indicated for the 120 kHz operating frequency when the Simrad recommendations are used. One should be aware that there is a certain discrepancy between measurements and simulations for the 120 kHz operating frequency. The simulated nonlinear attenuation is somewhat weaker than indicated by the measurement results. The IMR power limits seem preferable to those suggested by Simrad.^{13 2002}

The present work provides increased knowledge of the possible errors in target strength and volume backscattering measurements due to nonlinear attenuation. Measurement results have been presented both for the axial field and for the shape of the main lobe, in both fresh water and seawater. Experimental target strength measurements have been made with the target at distances up to 50 m from the echo sounder transducer, and volume backscattering measurements have been made on fish schools under relevant conditions for fisheries research. Both 120 kHz and 200 kHz echo sounders have been used. In earlier works published in connection with fisheries research, the experimental results have been limited to 200 kHz echo sounders in fresh water and 12 m maximum

propagation distance.^{233,234,193} Simulations have been made for longer distances.³⁰

The utility of the Bergen Code as a tool for predicting nonlinear attenuation within the paraxial region has been established up to a certain level, and some important uncertainty contributors have been identified. The region of validity of the KZK equation seems sufficient for the purpose of compensating for nonlinear attenuation in the cases that have been investigated. A method for compensating for nonlinear attenuation in volume backscattering measurements by means of numerical simulations has been proposed. The important contribution of nonlinear attenuation during calibration has been taken into account in the compensation.

The results reported here apply to the described special cases. Generalizations should be made with caution. The several assumptions and simplifications that have been made in the calculations must be taken into account, as well as the level of agreement between the simulation and measurement results.

8.2. Suggestions for further work

The degree of nonlinear distortion through sound propagation depends on several parameters, such as transmitted power and frequency, the vibration pattern of the sound source, propagation distance, temperature, pressure (depth), density, salinity, and bubble and particle contents of the water. The experimental basis obtained here for compensating for nonlinear effects in echo sounder measurements can be improved by collecting measurement data for a wider range of relevant salinities and temperatures. The importance of bubble layers should be investigated theoretically and experimentally. It is important to obtain knowledge of the variability of nonlinear distortion due to such factors.

Quantification of the nonlinear attenuation at higher frequencies than those

used in the present work are of interest.¹⁴⁵ In addition, one could explore the possibilities for exploiting nonlinear sound propagation effects in fisheries research. Utilizing the generated second harmonic frequency component may be one possibility; low-frequency sound generation by means of a parametric array could be another.

The sound propagation distances covered in the present work were predominantly 50 m or shorter. Measurements should also be made for longer propagation distances of relevance to fisheries acoustics. Sites for hydrophone measurements in seawater with 100 m–200 m horizontal propagation distances were sought as part of the investigation presented here. Experimental measurements were made using floating platforms in a sheltered bay in Os, Norway, but results of any value to the present work were not achieved. The most important problems were the sound speed profiles and the positioning and orientation of the transducers. Target strength measurements with calibration spheres were used as an alternative to hydrophone measurements at distances between 10 m and 50 m. Further pursuit of this approach should be the most effective for investigating the excess attenuation due to nonlinear effects.

Calibration sphere measurements are normally performed with a research vessel or other platform anchored in sheltered coastal waters. Alternatives for nonlinearity measurements at sea could be considered. Volume backscattering measurements on schools of fish have been tried in the present work. The obtained results show promising agreement with theory, and the described method can be used during normal survey cruises, i.e., under the same conditions as the measurements that are made for fish abundance estimation. A great number of repetitions are necessary to obtain sufficient accuracy in measurements on fish schools. This is time consuming and somewhat resource demanding.

The numerical algorithm used here may have a potential for predicting the far fields more accurately through optimised sound source descriptions. Improved

source characteristics can be obtained through further acoustical or optical measurements,¹²⁵ and by simulating the behaviour of the echo sounder transducers numerically. Measurements for a number of similar transducers could give useful information about the variation between vibration patterns. Generic source conditions for each transducer type or operating frequency could thus be obtained.

Further investigation of the assumptions and limitations of the theoretical model could be advantageous. In the simulations in the present work, constant values have been set for the parameters of the water. It could be useful to investigate the importance of depth dependent temperature and salinity. Bubble layers might also be included in the numerical simulations. The frequency dependence of absorption in sea water should be properly accounted for, including a correct dispersion relation.

References

- 1 *EK 500 operator manual*. (Simrad Subsea AS, Horten, Norway).
- 2 "Procedures for calibration of underwater electroacoustic transducers," American national standard. ANSI S1.20-1988, Acoustical Society of America, New York, USA, 1988.
- 3 *Guide to the expression of uncertainty in measurement*. (International Organization for Standardization, 1995).
- 4 *Product instruction MP 30 E for M-500 linear positioning stages*. (Physik Instrumente GmbH, 1996).
- 5 *Operating manual MP 33E for M-501.xx series linear positioning stages*. (Physik Instrumente GmbH, 1998).
- 6 "Simrad ES120-7C split-beam composite transducer," brochure, 855-164381 Rev. B, Simrad, 2001.
- 7 "Simrad ES200-7C split-beam composite transducer," brochure, 855-204465 Rev. B, Simrad, 2001.
- 8 *Agilent 54620 and 54640 series user's guide*. (Agilent Technologies, 2002).
- 9 *Calibration certificate for TC 4034 hydrophone, serial number 3103019*. (Reson AS, Slangerup, Denmark, 2003).
- 10 *EK60 Operator manual*. (Simrad AS, Horten, Norway, 2003).
- 11 *Certificate of calibration - Reson TC 4034 hydrophone, serial number 3103019. Reference U1954*. (National Physical Laboratory, Teddington Middlesex, UK, 2004).
- 12 *Certificate of calibration - Reson TC 4034 hydrophone, serial number 3103019. Reference U1948*. (National Physical Laboratory, Teddington Middlesex, 2004).
- 13 "Non-linear effects: Recommendation for fishery research investigations," Simrad News Bulletin, March, 2002.
- 14 J. Ablitt, National Physical Laboratory, Teddington, Middlesex, UK, personal communication, 2004.
- 15 G. B. Airy, "On a difficulty in the problem of sound," *Phil. Mag.* (series 3) **34**, 401-405 (1849).

- 16 V. A. Akulichev and V. A. Bulanov, "On a correlation between the cavitation strength, nonlinearity parameter, and bubble concentration in liquid," *Dokl. Phys.* **44** (9), 634-637 (1999).
- 17 J. J. Ambrosiano, D. R. Plante, B. E. McDonald, and W. A. Kuperman, "Nonlinear propagation in an ocean acoustic waveguide," *J. Acoust. Soc. Am.* **87** (4), 1473-1481 (1990).
- 18 L. N. Andersen, Simrad AS, Horten, Norway, personal communication, 2006.
- 19 M. A. Averkiou, Y.-S. Lee, and M. F. Hamilton, "Self-demodulation of amplitude- and frequency-modulated pulses in a thermoviscous fluid," *J. Acoust. Soc. Am.* **94** (5), 1876-2883 (1993).
- 20 M. A. Averkiou and M. F. Hamilton, "Measurements of harmonic generation in a focused finite-amplitude sound beam," *J. Acoust. Soc. Am.* **98** (6), 3439-3442 (1995).
- 21 M. A. Averkiou and M. F. Hamilton, "Nonlinear distortion of short pulses radiated by plane and focused circular pistons," *J. Acoust. Soc. Am.* **102** (5), 2539-2548 (1997).
- 22 M. A. Averkiou and R. O. Cleveland, "Modeling of an electrohydraulic lithotripter with the KZK equation," *J. Acoust. Soc. Am.* **106** (1), 102-112 (1999).
- 23 A. C. Baker, K. Anastasiadis, and V. F. Humphrey, "The nonlinear pressure field of a plane circular piston: Theory and experiment," *J. Acoust. Soc. Am.* **84** (4), 1483-1487 (1988).
- 24 A. C. Baker and V. F. Humphrey, "Nonlinear propagation of short ultrasonic pulses in focused fields," in *Frontiers of Nonlinear Acoustics: Proceedings of 12th ISNA, Austin, Texas, August 1990*, edited by M. F. Hamilton and D. T. Blackstock (Elsevier, London, 1990), pp. 185-190.
- 25 A. C. Baker, "Nonlinear pressure fields due to focused circular apertures," *J. Acoust. Soc. Am.* **91** (2), 713-717 (1992).
- 26 A. C. Baker and V. F. Humphrey, "Distortion and high-frequency generation due to nonlinear propagation of short ultrasonic pulses from a plane circular piston," *J. Acoust. Soc. Am.* **92** (3), 1699-1704 (1992).
- 27 A. C. Baker, A. M. Berg, A. Sahin, and J. Naze Tjøtta, "The nonlinear pressure field of plane, rectangular apertures: Experimental and theoretical results," *J. Acoust. Soc. Am.* **97** (6), 3510-3517 (1995).

- 28 A. C. Baker, B. Ward, and V. F. Humphrey, "The effect of receiver size in nonlinear pressure field measurements," *J. Acoust. Soc. Am.* **100** (4), 2062-2069 (1996).
- 29 A. C. Baker and P. Lunde, "Nonlinear propagation from circular echo-sounder transducers," Technical note CMR-TN01-F10010, Christian Michelsen Research AS, Bergen, Norway, 2001 (Confidential).
- 30 A. C. Baker and P. Lunde, "Nonlinear effects in sound propagation from echo sounders used in fish abundance estimation. Numerical simulation results," Technical note CMR-TN02-F10008, Christian Michelsen Research AS, Bergen, Norway, 2002 (Confidential).
- 31 N. S. Bakhvalov, Ya. M. Zhileikin, E. A. Zabolotskaya, and R. V. Khokhlov, "Nonlinear propagation of a sound beam in a nondissipative medium," *Sov. Phys. Acoust.* **22** (4), 272-274 (1976).
- 32 N. S. Bakhvalov, Ya. M. Zhileikin, E. A. Zabolotskaya, and R. V. Khokhlov, "Focused high-amplitude sound beams," *Sov. Phys. Acoust.* **24** (1), 10-15 (1978).
- 33 N. S. Bakhvalov, Ya. M. Zhileikin, E. A. Zabolotskaya, and R. V. Khokhlov, "Propagation of finite-amplitude sound beams in a dissipative medium," *Sov. Phys. Acoust.* **24** (4), 271-275 (1978).
- 34 N. S. Bakhvalov, Ya. M. Zhileikin, and E. A. Zabolotskaya, "Parametric interaction of sound beams," *Sov. Phys. Acoust.* **25** (4), 280-283 (1979).
- 35 T. Barkve and S. I. Aanonsen, "Modelligninger i ikkelineær akustikk," Cand. scient. thesis, University of Bergen, 1982.
- 36 H. E. Bass and R. Raspet, "Vibrational relaxation effects on the atmospheric attenuation and rise times of explosion waves," *J. Acoust. Soc. Am.* **64**, 1208-1210 (1978).
- 37 J. L. S. Bellin and R. T. Beyer, "Experimental investigation of an end-fire array," *J. Acoust. Soc. Am.* **34** (8), 1051-1054 (1962).
- 38 A. M. Berg and J. Naze Tjøtta, "Numerical simulation of the sound pressure field from finite amplitude, plane or focusing, rectangular apertures," in *Advances in Nonlinear Acoustics, Proceedings of the 13th International Symposium on Nonlinear Acoustics, Bergen, Norway, 28 June-2 July 1993*, edited by H. Hobæk (World Scientific, Singapore, 1993), pp. 309-314.
- 39 H. O. Berktaay, "Parametric amplification by the use of acoustic nonlinearities and some possible application," *J. Sound Vib.* **2** (4), 462-470 (1965).

- 40 H. O. Berktaay, "End-fire array of virtual acoustic sources produced by the interaction of cylindrically spreading acoustic waves," *Electron. Lett.* **1** (7), 202 (1965).
- 41 H. O. Berktaay and T. G. Muir, "Arrays of parametric receiving arrays," *J. Acoust. Soc. Am.* **53** (5), 1377-1383 (1973).
- 42 J. Berntsen, J. Naze Tjøtta, and S. Tjøtta, "Nearfield of a large acoustic transducer. Part IV: Second harmonic and sum frequency radiation," *J. Acoust. Soc. Am.* **75** (5), 1383-1391 (1984).
- 43 J. Berntsen and E. H. Vefring, "User documentation. Programs SOLTRI, SOLFIV, and SOLSEV," University of Bergen, Department of Mathematics, Bergen, Norway, 1986.
- 44 J. Berntsen and E. H. Vefring, "Numerical computation of a finite amplitude sound beam," Report no. 81, Department of Mathematics, University of Bergen, Bergen, Norway, 1986.
- 45 J. Berntsen, "On the use of the Richtmyer procedure to compute a finite amplitude sound beam from a piston source," Report no. 82, Department of Applied Mathematics, University of Bergen, Norway, 1987.
- 46 J. Berntsen, Jacqueline N. Tjøtta, and S. Tjøtta, "Interaction of sound waves. Part IV: Scattering of sound by sound," *J. Acoust. Soc. Am.* **86** (5), 1968-1983 (1989).
- 47 J. Berntsen, "Numerical calculations of finite amplitude sound beams," in *Frontiers of Nonlinear Acoustics: Proceedings of 12th ISNA, Austin, Texas, August 1990*, edited by M. F. Hamilton and D. T. Blackstock (Elsevier, Austin, Texas, 1990), pp. 191-196.
- 48 J. Berntsen, Department of Mathematics, University of Bergen, Bergen, Norway, personal communication, 2003.
- 49 R. T. Beyer, "The Parameter B/A," in *Nonlinear Acoustics*, edited by M. F. Hamilton and D. T. Blackstock (Academic Press, San Diego, CA, 1997), pp. 25-39.
- 50 N. Bilaniuk and G. S. K. Wong, "Speed of sound in pure water as a function of temperature," *J. Acoust. Soc. Am.* **93** (3), 1609-1612 (1993).
- 51 P. Biquard, "Sur l'absorption des ondes ultra-sonores par les liquides," *Ann. Physique (ser. 11)* **6**, 195-304 (1936).
- 52 L. Bjørnø, "Non-linear ultrasound - a review," in *proc. Ultrasonics International 1975 Conference*, 1975.

- 53 L. Bjørnø, "40 Years of Nonlinear Underwater Acoustics," *Acta Acustica united Acustica* **88**, 771-775 (2002).
- 54 D. T. Blackstock, "Thermoviscous Attenuation of Plane, Periodic, Finite-Amplitude Sound Waves," *J. Acoust. Soc. Am.* **36** (3), 534-542 (1964).
- 55 D. T. Blackstock, "Connection between the Fay and Fubini solutions for plane sound waves of finite amplitude," *J. Acoust. Soc. Am.* **39** (6), 1019-1026 (1966).
- 56 D. T. Blackstock, "Generalized Burgers equation for plane waves," *J. Acoust. Soc. Am.* **77** (6), 2050-2053 (1985).
- 57 D. T. Blackstock, "History of Nonlinear Acoustics: 1750s - 1930s," in *Nonlinear Acoustics*, edited by M. F. Hamilton and D. T. Blackstock (Academic Press, San Diego, CA, 1997), pp. 1-23.
- 58 P. Blanc-Benon, B. Lipkens, L. Dallois, M. F. Hamilton, and D. T. Blackstock, "Propagation of finite amplitude sound through turbulence: Modeling with geometrical acoustics and the parabolic approximation," *J. Acoust. Soc. Am.* **111** (1), 487-498 (2002).
- 59 A. Bouakaz, C. T. Lancée, P. J. A. Frinking, and N. de Jong, "Simulations and measurements of nonlinear pressure field generated by linear array transducers," in *proc. 1999 IEEE Ultrasonics symposium*, 1999.
- 60 A. Bouakaz, C. T. Lancée, and N. De Jong, "Harmonic ultrasonic field of medical phased arrays: Simulations and measurements," *IEEE Trans. Ult. Ferr. Freq. Control* **50** (6), 730-735 (2003).
- 61 D. R. O. Bruno and J. C. Novarini, "High-frequency sound attenuation caused by the wind-generated bubble layer in the open sea," *J. Acoust. Soc. Am.* **73** (3), 1064-1065 (1983).
- 62 V. A. Bulanov and I. V. Korskov, "Acoustic Nonlinearity, Attenuation and Scattering of a Sound in water with Vapor-Gas Bubbles," in *Nonlinear Acoustics at the Beginning of the 21st Century*, edited by O. V. Rudenko and O. A. Sapozhnikov (Faculty of Physics, MSU, Moscow, 2002), pp. 915-918.
- 63 J. M. Burgers, "A mathematical model illustrating the theory of turbulence," in *Advances in Applied Mechanics*, edited by Mises and Kármán (Academic Press, New York, 1948), Vol. 1, pp. 171-199.
- 64 P. N. Burns, D. H. Simpson, and M. A. Averkiou, "Nonlinear Imaging," *Ult. Med. Biol.* **26** (S1), S19-S22 (2000).

- 65 C. Campos-Pozuelo, B. Dubus, and J. A. Gallego-Juárez, "Finite-element analysis of the nonlinear propagation of high-intensity acoustic waves," *J. Acoust. Soc. Am.* **106** (1), 91-101 (1999).
- 66 E. L. Carstensen and L. L. Foldy, "Propagation of sound through a liquid containing bubbles," *J. Acoust. Soc. Am.* **19** (3), 481-501 (1947).
- 67 E. L. Carstensen, W. K. Law, N. D. McKay, and T. G. Muir, "Demonstration of nonlinear acoustical effects at biomedical frequencies and intensities," *Ult. Med. Biol.* **6**, 359-368 (1980).
- 68 K. Castor, B. E. McDonald, and W. A. Kuperman, "Equations of Nonlinear Acoustics and Weak Shock Propagation," in *Nonlinear Acoustics at the Beginning of the 21st Century*, edited by O. V. Rudenko and O. A. Sapozhnikov (Faculty of Physics, MSU, Moscow, 2002), pp. 129-133.
- 69 K. Castor, P. Gerstoft, P. Roux, W. A. Kuperman, and B. E. McDonald, "Long-range propagation of finite-amplitude acoustic waves in an ocean waveguide," *J. Acoust. Soc. Am.* **116** (4), 2004-2010 (2004).
- 70 C.-T. Chen and F. J. Millero, "Speed of sound in seawater at high pressures," *J. Acoust. Soc. Am.* **62** (5), 1129-1135 (1977).
- 71 P. T. Christopher and K. J. Parker, "New approaches to nonlinear diffractive field propagation," *J. Acoust. Soc. Am.* **90** (1), 488-499 (1991).
- 72 P. T. Christopher, "Modeling the Dornier HM3 lithotripter," *J. Acoust. Soc. Am.* **96** (5), 3088-3095 (1994).
- 73 T. Christopher, "Source prebiasing for improved second harmonic bubble-response imaging," *IEEE Trans. Ult. Ferr. Freq. Control* **46** (3), 556-563 (1999).
- 74 R. O. Cleveland, J. P. Chambers, H. E. Bass, R. Raspet, D. T. Blackstock, and M. F. Hamilton, "Comparison of computer codes for the propagation of sonic boom waveforms through isothermal atmospheres," *J. Acoust. Soc. Am.* **100** (5), 3017-3027 (1996).
- 75 R. O. Cleveland, M. F. Hamilton, and D. T. Blackstock, "Time-domain modeling of finite-amplitude sound in relaxing fluids," *J. Acoust. Soc. Am.* **99** (6), 3312-3318 (1996).
- 76 J. D. Cole, "On a quasi-linear parabolic equation occurring in aerodynamics," *Quart. Appl. Math.* **IX** (3), 225-236 (1951).

- 77 K. W. Commander and A. Prosperetti, "Linear pressure waves in bubbly liquids: Comparison between theory and experiments," *J. Acoust. Soc. Am.* **85** (2), 732-746 (1989).
- 78 B. D. Cook, *J. Acoust. Soc. Am.* **34**, 941-946 (1962).
- 79 F. D. Cotaras and C. L. Morfey, "Polynomial expressions for the coefficient of nonlinearity β and $\beta/(\rho c^5)^{1/2}$ for fresh water and seawater," *J. Acoust. Soc. Am.* **94** (1), 585-588 (1993).
- 80 J. Crank and P. Nicholson, "A practical method for numerical evaluation of solutions of partial differential equations of the heat-conducting type," *Proc. Cambridge Philos. Soc.* **43**, 50-67 (1947).
- 81 E. O. Dahl, K.-E. Frøysa, and P. Lunde, *Handbook of uncertainty calculations - fiscal orifice gas and turbine oil metering stations*. (The Norwegian Society for Oil and Gas Measurement, 2003).
- 82 J. Dalen and A. Løvik, "The influence of wind-induced bubbles on echo integration surveys," *J. Acoust. Soc. Am.* **69** (6), 1653-1659 (1981).
- 83 C. M. Darvennes, M. F. Hamilton, J. Naze Tjøtta, and S. Tjøtta, "Effects of absorption on the nonlinear interaction of sound beams," *J. Acoust. Soc. Am.* **89** **3** (1028-1036) (1991).
- 84 S. A. Divall and V. F. Humphrey, "Finite difference modelling of the temperature rise in non-linear medical ultrasound fields," *Ultrasonics* **38**, 273-277 (2000).
- 85 L. R. Dragonette, R. H. Vogt, L. Flax, and W. G. Neubauer, "Acoustic reflection from elastic spheres and rigid spheres and spheroids. II. Transient analysis," *J. Acoust. Soc. Am.* **55** (6), 1130-1137 (1974).
- 86 L. R. Dragonette, S. K. Numrich, and L. J. Frank, "Calibration technique for acoustic scattering measurements," *J. Acoust. Soc. Am.* **69** (4), 1186-1189 (1981).
- 87 G. Du and M. A. Breazeale, "Harmonic distortion of a finite amplitude Gaussian beam in a fluid," *J. Acoust. Soc. Am.* **80** (1), 212-216 (1986).
- 88 F. A. Duck, "Nonlinear Acoustics in Diagnostic Ultrasound," *Ult. Med. Biol.* **28** (1), 1-18 (2002).
- 89 S. Earnshaw, "On the mathematical theory of sound," *Phil. Trans. Roy. Soc.* **150**, 133-148 (1860).
- 90 C. Eckart, "Vortices and streams caused by sound waves," *Phys. Rev.* **73** (1), 68-76 (1948).

- 91 M. Ehrhardt, "Efficient Numerical Implementation of Discrete Transparent Boundary Conditions for Parabolic Equations in Underwater Acoustics," *Acta Acustica united Acustica* **88**, 711-713 (2002).
- 92 R. D. Fay, "Plane sound waves of finite amplitude," *J. Acoust. Soc. Am.* **3**, 222-241 (1931).
- 93 F. H. Fenlon, "A Recursive Procedure for Computing the Nonlinear Spectral Interactions of Progressive Finite-Amplitude Waves in Nondispersive Fluids," *J. Acoust. Soc. Am.* **50** (5), 1299-1312 (1971).
- 94 N. P. Fofonoff and R. C. Millard Jr., "Algorithms for computation of fundamental properties of seawater," 1983.
- 95 K. G. Foote, "Optimizing copper spheres for precision calibration of hydroacoustic equipment," *J. Acoust. Soc. Am.* **71** (3) (1982).
- 96 K. G. Foote, "Linearity of fisheries acoustics, with addition theorems," *J. Acoust. Soc. Am.* **73** (6), 1932-1940 (1983).
- 97 K. G. Foote and D. N. MacLennan, "Comparison of copper and tungsten carbide calibration spheres," *J. Acoust. Soc. Am.* **75** (2), 612-616 (1984).
- 98 K. G. Foote, H. P. Knudsen, G. Vestnes, D. N. MacLennan, and E. J. Simmonds, "Calibration of acoustic instruments for fish density estimation: A practical guide," ICES cooperative research report 144, 1987.
- 99 K. G. Foote, J. Naze Tjøtta, and S. Tjøtta, "Performance of the parametric receiving array: Effects of misalignment," *J. Acoust. Soc. Am.* **82**, 1753 (1987).
- 100 K. G. Foote, "Spheres for calibrating an eleven-frequency acoustic measurement system," *J. Cons. int. Explor. Mer* **46**, 284-286 (1990).
- 101 S. T. Forbes and O. Nakken, *Manual of methods for fisheries resource survey and appraisal*. (Food and Agriculture Organization of the United Nations, Rome, Italy, 1972).
- 102 F. E. Fox and G. D. Rock, "Ultrasonic absorption in water," *J. Acoust. Soc. Am.* **12**, 505-510 (1941).
- 103 F. E. Fox and W. A. Wallace, "Absorption of Finite Amplitude Sound Waves," *J. Acoust. Soc. Am.* **26** (6), 994-1006 (1954).

- 104 F. E. Fox, S. R. Curley, and G. S. Larson, "Phase velocity and absorption measurements in water containing air bubbles," *J. Acoust. Soc. Am.* **27** (3), 534-539 (1955).
- 105 R. E. Francois and G. R. Garrison, "Sound absorption based on ocean measurements. Part I: Pure water and magnesium sulfate contributions," *J. Acoust. Soc. Am.* **72** (3), 896-907 (1982).
- 106 R. E. Francois and G. R. Garrison, "Sound absorption based on ocean measurements. Part II: Boric acid contribution and equation for total absorption," *J. Acoust. Soc. Am.* **72** (6), 1879-1890 (1982).
- 107 K.-E. Frøysa, J. Naze Tjøtta, and J. Berntsen, "Finite amplitude effects in sound beams. Pure tone and pulsed excitation," in *Advances in Nonlinear Acoustics, Proceedings of the 13th International Symposium on Nonlinear Acoustics, Bergen, Norway, 28 June-2 July 1993*, edited by H. Hobæk (World Scientific, Singapore, 1993), pp. 233-238.
- 108 E. Fubini-Ghiron, "Anomalies in the propagation of an acoustic wave of large amplitude," *Alta Freq.* **4**, 532-581 (1935).
- 109 M. Furusawa, M. Hamada, and C. Aoyama, "Near range errors in sound scattering measurements of fish," *Fisheries Sci.* **65** (1), 109-116 (1999).
- 110 J. H. Ginsberg and M. F. Hamilton, "Computational methods," in *Nonlinear Acoustics*, edited by M. F. Hamilton and D. T. Blackstock (Academic Press, San Diego, CA, 1997).
- 111 S. Ginter, "Numerical simulation of ultrasound-thermotherapy combining nonlinear wave propagation with broadband soft-tissue absorption," *Ultrasonics* **37**, 693-696 (2000).
- 112 R. K. Gould, C. W. Smith, A. O. Williams, Jr., and R. P. Ryan, "Measured structure of harmonics self-generated in an acoustic beam," *J. Acoust. Soc. Am.* **40** (2), 421-427 (1965).
- 113 I. M. Hallaj and R. O. Cleveland, "FDTD simulation of finite-amplitude pressure and temperature fields from biological ultrasound," *Acoust. Res. Lett. Online* **1**, 7-12 (1999).
- 114 M. F. Hamilton, J. Naze Tjøtta, and S. Tjøtta, "Nonlinear effects in the farfield of a directive sound source," *J. Acoust. Soc. Am.* **78** (1), 202-216 (1985).
- 115 M. F. Hamilton and C. L. Morfey, "Model Equations," in *Nonlinear Acoustics*, edited by M. F. Hamilton and D. T. Blackstock (Academic Press, San Diego, CA, 1997), pp. 41-63.

- 116 T. B. Hansen, "Probe-corrected near-field measurements on a truncated
cylinder," *J. Acoust. Soc. Am.* **119** (2), 792-807 (2006).
- 117 M. E. Haran and B. D. Cook, "Distortion of finite amplitude ultrasound
in lossy media," *J. Acoust. Soc. Am.* **73** (3), 774-779 (1983).
- 118 T. S. Hart and M. F. Hamilton, "Nonlinear effects in focused sound
beams," *J. Acoust. Soc. Am.* **84** (4), 1488-1496 (1988).
- 119 R. Hickling, "Analysis of echoes from a solid elastic sphere in water," *J.*
Acoust. Soc. Am. **34** (10), 1582-1592 (1962).
- 120 H. Hobæk, "Experimental investigation of an acoustical end-fire array,"
J. Sound Vib. **6** (3), 460-463 (1967).
- 121 J. Hoffelner, H. Landes, M. Kaltenbacher, and R. Lerch, "Numerical
simulation of nonlinear wave propagation in thermoviscous fluids
including dissipation," in *proc. 1999 IEEE Ultrasonics Symposium*,
1999.
- 122 J. Hoffelner, H. Landes, and R. Lerch, "Calculation of Acoustic
Streaming Velocity and Radiation Force Based on Finite Element
Simulations of Nonlinear Wave Propagation," in *proc. 2000 IEEE*
Ultrasonics Symposium, 2000.
- 123 E. Hopf, "The Partial Differential Equation $ut + uux = mxx$," *Commun.*
Pure Appl. Math. **3**, 201-230 (1950).
- 124 J. Huijssen, A. Bouakaz, M. D. Verweij, and N. de Jong, "Simulations
of the nonlinear acoustic pressure field without using the parabolic
approximation," *2003 IEEE Ultrasonics Symposium*, 1851-1854 (2003).
- 125 V. F. Humphrey, S. P. Robinson, P. D. Theobald, G. Hayman, P. N.
Gélat, and A. D. Thompson, "Comparison of optical and hydrophone-
based near-field techniques for full characterisation of high frequency
sonars," in *proc. Underwater Acoustic Measurements: Technologies and*
Results, Heraklion, Greece, 28 June-1 July, 2005.
- 126 V. F. Humphrey, "Nonlinear propagation in ultrasonic fields:
measurements, modelling and harmonic imaging," *Ultrasonics* **38**, 267-
272 (2000).
- 127 T. Huttunen, J. P. Kaipio, and K. Hynynen, "Modeling of anomalies due
to hydrophones in continuous-wave ultrasound fields," *IEEE Trans. Ult.*
Ferr. Freq. Control **50** (11), 1486-1500 (2003).
- 128 U. Ingard and D. C. Pridmore-Brown, "Scattering of sound by sound," *J.*
Acoust. Soc. Am. **28** (3), 367-369 (1956).

- 129 Y. Kagawa, T. Tsuchiya, T. Yamabuchi, H. Kawabe, and T. Fujii, "Finite element simulation of non-linear sound wave propagation," *J. Sound Vib.* **154** (1), 125-145 (1992).
- 130 T. Kamakura, N. Hamada, K. Aoki, and Y. Kumamoto, "Nonlinearly generated spectral components in the nearfield of a directive sound source," *J. Acoust. Soc. Am.* **85** (6), 2331-2337 (1989).
- 131 T. Kamakura, M. Tani, Y. Kumamoto, and K. Ueda, "Harmonic generation in finite amplitude sound beams from a rectangular aperture source," *J. Acoust. Soc. Am.* **91** (6), 3144-3151 (1992).
- 132 T. Kamakura, T. Ishiwata, and K. Matsuda, "A new theoretical approach to the analysis of nonlinear sound beams using the oblate spheroidal coordinate system," *J. Acoust. Soc. Am.* **105** (6), 3083-3086 (1999).
- 133 W. Keck and R. T. Beyer, "Frequency spectrum of finite amplitude ultrasonic waves in liquids," *Phys. Fluids* **3**, 346-352 (1960).
- 134 V. A. Khokhlova and O. A. Sapozhnikov, "Modification of the Spectral Method for the Description of Shock Wave Propagation," in proc. IEEE Ultrasonics symposium, 1995.
- 135 V. A. Khokhlova, R. Souchon, J. Tavakkoli, O. A. Sapozhnikov, and D. Cathignol, "Numerical modeling of finite-amplitude sound beams: Shock formation in the near field of a cw plane piston source," *J. Acoust. Soc. Am.* **110** (1), 95-108 (2001).
- 136 V. A. Khokhlova, Ph. Blanc-Benon, M. V. Averianov, and R. O. Cleveland, "Propagation of nonlinear acoustic signals through inhomogeneous moving media," in proc. 2004 IEEE Ultrasonics Symposium, 2004.
- 137 L. V. King, "On the acoustic radiation field of the piezo-electric oscillator and the effect of viscosity on transmission," *Can. J. Res.* **11**, 135-155 (1934).
- 138 L. E. Kinsler, A. R. Frey, A. B. Coppens, and J. V. Sanders, *Fundamentals of Acoustics*, 3rd ed. (John Wiley & Sons, Inc., New York, 1982).
- 139 R. J. Korneliussen, "Multifrequency echograms," in proc. 22nd Scandinavian Symposium on Physical Acoustics, Ustaoset, Norway, 1999.
- 140 R. J. Korneliussen, "Some applications of multiple frequency echo sounder data," presented at the 24th Scandinavian Symposium on Physical Acoustics, Ustaoset, Norway, 2001.

- 141 R. J. Korneliussen, "Analysis and presentation of multi-frequency echograms," Dr. scient thesis, Department of Physics, University of Bergen, Bergen, Norway, 2002.
- 142 R. J. Korneliussen and E. Ona, "An operational system for processing and visualizing multi-frequency acoustic data," *ICES Journal of Marine Science* **59**, 293-313 (2002).
- 143 R. J. Korneliussen, N. Diner, E. Ona, and P. G. Fernandes, "Recommendations for the collection of multi-frequency acoustic data," *ICES CM2004/R:36*, 2004.
- 144 R. J. Korneliussen, Institute of Marine Research, Bergen, Norway, personal communication, 2005.
- 145 R. J. Korneliussen, Institute of Marine Research, Bergen, Norway, personal communication, 2006.
- 146 A. Korpel, "Frequency approach to nonlinear dispersive waves," *J. Acoust. Soc. Am.* **67** (6), 1954-1958 (1980).
- 147 D. Kourtiche, L. Ait Ali, L. Alliès, M. Nadi, and A. Chitnalah, "Harmonic propagation of finite-amplitude sound beams: Second harmonic imaging in ultrasonic reflection tomography," *Meas. Sci. Technol.* **15**, 21-28 (2004).
- 148 V. A. Krasil'nikov, V. V. Shklovskaya-Kordy, and L. K. Zarembo, "On the propagation of ultrasonic waves of finite amplitude in liquids," *J. Acoust. Soc. Am.* **29** (5), 642-647 (1957).
- 149 M. Kristen, A. Doehle, H. Landes, J. Hoffelner, and R. Lerch, "Ultrasonic Standing Waves in Industrial Applications," 2003 IEEE Ultrasonics Symposium, 2045-2048 (2003).
- 150 V. E. Kunitsyn and O. V. Rudenko, "Second-harmonic generation in the field of a piston radiator," *Sov. Phys. Acoust.* **24** (4), 310-313 (1978).
- 151 V. P. Kuznetsov, "Equations of nonlinear acoustics," *Sov. Phys. Acoust.* **16** (4), 467-470 (1971).
- 152 V. Labat, J. P. Remenieras, O. Bou Matar, A. Ouahabi, and F. Patat, "Harmonic propagation of finite amplitude sound beams: experimental determination of the nonlinearity parameter B/A," *Ultrasonics* **38**, 292-296 (2000).
- 153 D. T. Laird and P. M. Kendig, "Attenuation of sound in water containing air bubbles," *J. Acoust. Soc. Am.* **24** (1), 29-32 (1952).

- 154 R. W. Lardner, "Acoustic saturation and the conversion efficiency of the parametric array," *J. Sound Vib.* **82** (4), 473-487 (1982).
- 155 V. Lauvstad and S. Tjøtta, "Nonlinear interaction of two soundbeams," *J. Acoust. Soc. Am.* **34** (3), 929-930 (1962).
- 156 S. B. Leble and A. Sukhov, "On solutions of the Khokhlov-Zabolotskaya equation with KdV dispersion term," in *Nonlinear Acoustics at the Turn of the Millennium: ISNA 15*, edited by W. Lauterborn and T. Kurz (AIP CP524, 2000), pp. 497-500.
- 157 Y.-S. Lee and M. F. Hamilton, "Time-domain modeling of pulsed finite-amplitude sound beams," *J. Acoust. Soc. Am.* **97** (2), 906-917 (1995).
- 158 Y. Li and J. A. Zagzebski, "Computer Model for Harmonic Ultrasound Imaging," *IEEE Trans. Ult. Ferr. Freq. Control* **47** (5), 1259-1272 (2000).
- 159 M. Liebler, S. Ginter, T. Dreyer, and R. E. Riedlinger, "Full wave modeling of therapeutic ultrasound: Efficient time-domain implementation of the frequency power-law attenuation," *J. Acoust. Soc. Am.* **116** (5), 2742-2750 (2004).
- 160 M. J. Lighthill, "On sound generated aerodynamically I. General theory," *Proc. Roy. Soc. A* **211** (1107), 564-587 (1952).
- 161 M. J. Lighthill, "On sound generated aerodynamically II. Turbulence as a source of sound," *Proc. Roy. Soc. A* **222** (1148), 1-32 (1954).
- 162 J. C. Lockwood, "Two problems in high-intensity sound," Report number 71-26, Appl. Res. Lab., The University of Texas at Austin, Austin, Texas, 1971.
- 163 J. C. Lockwood, T. G. Muir, and D. T. Blackstock, "Directive harmonic generation in the radiation field of a circular piston," *J. Acoust. Soc. Am.* **53** (4), 1148-1153 (1973).
- 164 J. Ma, J. Yu, Z. Fan, Z. Zhu, X. Gong, and G. Du, "Acoustic nonlinearity of liquid containing encapsulated microbubbles," *J. Acoust. Soc. Am.* **116** (1), 186-193 (2004).
- 165 W. R. MacLean, "Absolute measurement of sound without a primary standard," *J. Acoust. Soc. Am.* **12**, 140-146 (1940).
- 166 D. N. MacLennan, "Time varied gain functions for pulsed sonars," *J. Sound Vib.* **110** (3), 511-522 (1986).
- 167 D. N. MacLennan, "Acoustical measurement of fish abundance," *J. Acoust. Soc. Am.* **87** (1), 1-15 (1990).

- 168 D. N. MacLennan, P. G. Fernandes, and J. Dalen, "A consistent approach to definitions and symbols in fisheries acoustics," *ICES J. Mar. Sci.* **59**, 365-369 (2002).
- 169 H. W. Marsh, "Attenuation of Explosive Sounds in Sea Water," *J. Acoust. Soc. Am.* **35**, 1837 (1963).
- 170 B. E. McDonald and W. A. Kuperman, "Time-domain solution of the parabolic equation including nonlinearity," *Comp. and Math. with Appl.* **11** (7-8), 843-851 (1985).
- 171 B. E. McDonald and W. A. Kuperman, "Time domain formulation for pulse propagation including nonlinear behavior at a caustic," *J. Acoust. Soc. Am.* **81** (5), 1406-1417 (1987).
- 172 B. E. McDonald, "Nonlinear Effects in Source Localization," in *proc. Ocean Acoustic Interference Phenomena and Signal Processing*, San Fransisco, CA, USA, 2002.
- 173 H. Medwin, "Acoustic fluctuations due to microbubbles in the near-surface ocean," *J. Acoust. Soc. Am.* **56**, 1100-1104 (1974).
- 174 H. Medwin and C. S. Clay, *Fundamentals of acoustical oceanography*. (Academic Press, San Diego, CA, 1998).
- 175 R. H. Mellen, D. G. Browning, and W. L. Konrad, "Parametric sonar transmitting array measurements," *J. Acoust. Soc. Am.* **49** (1), 90 (A) (1971).
- 176 H. M. Merklinger, "Fundamental-frequency component of a finite-amplitude plane wave," *J. Acoust. Soc. Am.* **54** (6), 1760-1761 (1973).
- 177 H. M. Merklinger, R. H. Mellen, and M. B. Moffett, "Finite-amplitude losses in spherical sound waves," *J. Acoust. Soc. Am.* **59** (4), 755-759 (1976).
- 178 O. A. Misund, "Underwater acoustics in marine fisheries and fisheries research," *Rev. Fish Biol. Fish.* **7**, 1-34 (1997).
- 179 M. B. Moffett and R. H. Mellen, "Model for parametric acoustic sources," *J. Acoust. Soc. Am.* **61** (2), 325-337 (1977).
- 180 M. B. Moffett, "Measurement of fundamental and second harmonic pressures in the field of a circular piston source," *J. Acoust. Soc. Am.* **65** (2), 318-323 (1979).
- 181 T. G. Muir and E. L. Carstensen, "Prediction of nonlinear acoustic effects at biomedical frequencies and intensities," *Ult. Med. Biol.* **6**, 345-357 (1980).

- 182 S. Nachef, D. Cathignol, J. Naze Tjøtta, A. M. Berg, and S. Tjøtta,
"Investigation of a high intensity sound beam from a plane transducer.
Experimental and theoretical results," J. Acoust. Soc. Am. **98** (4), 2303-
2323 (1995).
- 183 O. Nakken and Ø. Ulltang, "A comparison of the reliability of acoustic
estimates of fish stock abundance and estimates obtained by other
assessment methods in Northeast Atlantic," FAO Fish Rep. **300**, 249-
260 (1983).
- 184 V. Narasimhan and R. T. Beyer, "Attenuation of ultrasonic waves of
finite amplitude in liquids," J. Acoust. Soc. Am. **28** (6), 1233-1236
(1956).
- 185 K. A. Naugol'nykh and S. A. Rybak, "Wave interaction in a liquid
containing gas bubbles," Sov. Phys. Acoust. **20** (1), 102-103 (1974).
- 186 J. Naze and S. Tjøtta, "Nonlinear interaction of two sound beams," J.
Acoust. Soc. Am. **37**, 174-175 (1965).
- 187 T. H. Neighbors and L. Bjørnø, "Focused Finite-Amplitude Ultrasonic
Pulses in Liquids," in *Frontiers of nonlinear acoustics: Proceedings of
12th ISNA, Austin, Texas, August 1990*, edited by M. F. Hamilton and D.
T. Blackstock (Elsevier, 1990), pp. 209-214.
- 188 T. Nouri-Baranger, E. Closset, and D. Cathignol, "Numerical solution for
nonlinear acoustic beam radiated from non-axisymmetric plane
transducers using the operator splitting method," in proc. 2001 IEEE
Ultrasonics symposium, 2001.
- 189 J. C. Novarini and D. R. Bruno, "Effects of the sub-surface bubble layer
on sound propagation," J. Acoust. Soc. Am. **72** (2), 510-514 (1982).
- 190 B. K. Novikov, "Exact solutions of the Burgers equation," Sov. Phys.
Acoust. **24** (4), 326-328 (1978).
- 191 E. Ona and G. Vestnes, "Direct measurements of equivalent beam angle
on hull-mounted transducers," ICES CM 1985/B:43, 1985.
- 192 L. A. Ostrovsky, A. M. Sutin, I. A. Soustova, A. L. Matveyev, A. I.
Potapov, and Z. Kluzek, "Nonlinear scattering of acoustic waves by
natural and artificially generated subsurface bubble layers in sea," J.
Acoust. Soc. Am. **113** (2), 741-749 (2003).
- 193 A. Pedersen, M. Vestrheim, and P. Lunde, "Quantification of non-linear
sound propagation effects in fisheries and research echo sounders," in
proc. Underwater Acoustic Measurements: Technologies and Results,
Heraklion, Greece, 28 June-1 July, 2005.

- 194 A. Pedersen, "Nonlinear effects in fisheries and research echo sounders and sonars," presented at the 2003 seminar for PhD students under the MARE research programme. Research council of Norway, Tromsø, Norway, 28 October, 2003.
- 195 A. Pedersen, "Nonlinear effects in fisheries and research echo sounders and sonars," presented at the 2004 seminar for PhD students under the MARE research programme. Research Council of Norway, Oslo, Norway, 14-15 October, 2004.
- 196 A. Pedersen, P. Lunde, and M. Vestrheim, "Convergence and accuracy of the Bergen Code for investigating nonlinear effects in fishery echo sounders," in proc. 27th Scandinavian Symposium on Physical Acoustics, edited by U. R. Kristiansen, Ustaoset, Norway, 2004. ISBN 82-8123-000-2.
- 197 A. Pedersen, P. Lunde, and M. Vestrheim, "Nonlinear effects in fisheries and research echo sounders and sonar," presented at the final seminar for the MARE research programme, Research Council of Norway, Oslo, Norway, 12-13 October, 2005.
- 198 A. Pedersen, M. Vestrheim, and P. Lunde, "Consequences of nonlinear sound propagation for target strength measurement - preliminary studies," presented at the meeting of the ICES Working Group on Fisheries Acoustic Science and Technology, Rome, Italy, 19-22 April, 2005.
- 199 A. Pedersen, M. Vestrheim, and P. Lunde, "Ikkelineær lydforplantning ved bruk av ekkolodd i fiskeriforskning (Nonlinear sound propagation in fisheries research applications of echo sounders)," presented at the 2005 meeting of the Norwegian Physical Society, Ulvik, Norway, 11-14 August, 2005.
- 200 A. Pedersen, M. Vestrheim, and P. Lunde, "Nonlinear sound propagation effects in fisheries research echo sounders - measurements and simulations in fresh water," in proc. 28th Scandinavian Symposium on Physical Acoustics, edited by U. R. Kristiansen, Ustaoset, Norway, 23-26 January, 2005. ISBN 82-8123-000-2 (abstract).
- 201 F. M. Pestorius and D. T. Blackstock, "Propagation of finite-amplitude noise," in *Finite-Amplitude Wave Effects in Fluids, Proceedings of the 1973 symposium in Copenhagen*, edited by L. Bjørnø (IPC Science and Technology, Guilford, England, 1973), pp. 24-29.
- 202 Yu. A. Pishchal'nikov, O. A. Sapozhnikov, and V. A. Khokhlova, "A modification of the spectral description of nonlinear acoustic waves with discontinuities," *Acoust. Phys.* **42** (3), 362-367 (1996).

- 203 W. J. M. Rankine, "On the thermodynamic theory of waves of finite longitudinal disturbance," *Phil. Trans. Roy. Soc.* **160**, 277-288 (1870).
- 204 E. Reiso, "Acoustic beam propagation in inhomogeneous media," presented at the Scandinavian Cooperation Meeting in Acoustics/Hydrodynamics, Ustaoset, Norway, 28.-31. January, 1990.
- 205 E. Reiso, "Nonlinear equations of acoustics in inhomogeneous, thermoviscous fluids," Dr. Scient. thesis, University of Bergen, 1990.
- 206 J.-P. Remenieras, O. B. Matar, V. Labat, N. Felix, and F. Patat, "Time-domain nonlinear distortion of pulsed finite-amplitude sound beam: Calculation and experiments," in *proc. 1999 IEEE Ultrasonics symposium*, 1999.
- 207 J.-P. Remenieras, O. B. Matar, V. Labat, and F. Patat, "Time-domain modeling of nonlinear distortion of pulsed finite amplitude sound beams," *Ultrasonics* **38**, 305-311 (2000).
- 208 P. Reynisson, "Monitoring of equivalent beam angles of hull-mounted acoustic survey transducers in the period 1983-1995," *ICES J. Mar. Sci.* **55**, 1125-1132 (1998).
- 209 S. D. Richards, A. D. Heathershaw, and P. D. Thorne, "The effect of suspended particulate matter on sound attenuation in seawater," *J. Acoust. Soc. Am.* **100** (3), 1447-1450 (1996).
- 210 S. D. Richards, "The effect of temperature, pressure, and salinity on sound attenuation in turbid seawater," *J. Acoust. Soc. Am.* **103** (1), 205-211 (1998).
- 211 R. D. Richtmyer, *Difference methods for initial value problems*. (Interscience, New York, 1957).
- 212 M. Rielly, V. F. Humphrey, and F. A. Duck, "A Theoretical and Experimental Investigation of Nonlinear Ultrasound Propagation Through Tissue Mimicking Fluids," in *proc. 2000 IEEE Ultrasonics symposium*, 2000.
- 213 T. L. Riley, "Generation of harmonics in finite amplitude sound radiated in water by a circular piston," M. S. Thesis, The University of Texas at Austin, Austin, Texas, 1983.
- 214 S. Robinson, *Technical guidance note - electrical loading corrections*. (National Physical Laboratory, Teddington Middlesex, UK, 2004).
- 215 O. V. Rudenko, S. I. Soluyan, and R. V. Khokhlov, "Problems in the theory of nonlinear acoustics," *Sov. Phys. Acoust.* **20** (3), 271-275 (1974).

- 216 O. V. Rudenko, S. I. Soluyan, and R. V. Khokhlov, "Confinement of a
quasiplane beam of periodic perturbations in a nonlinear medium," *Sov.
Phys. Acoust.* **19** (6), 556-559 (1974).
- 217 A. Sahin and A. C. Baker, "Nonlinear propagation in the pressure fields
of plane and focused rectangular apertures," in *Advances in Nonlinear
Acoustics, Proceedings of the 13th International Symposium on
Nonlinear Acoustics, Bergen, Norway, 28 June-2 July 1993*, edited by
H. Hobæk (World Scientific, Singapore, 1993), pp. 303-308.
- 218 S. Saito, B. C. Kim, and T. G. Muir, "Second harmonic component of a
nonlinearly distorted wave in a focused sound field," *J. Acoust. Soc.
Am.* **82** (2), 621-628 (1987).
- 219 O. A. Sapozhnikov, V. A. Khokhlova, and D. Cathignol, "Nonlinear
waveform distortion and shock formation in the near field of a continuous
wave piston source," *J. Acoust. Soc. Am.* **115** (5), 1982-1987 (2004).
- 220 M. Scalerandi and V. Agostini, "Simulation of the propagation of
ultrasonic pulses in nonlinear and/or attenuative media," *J. Comp.
Acoust.* **10** (3), 275-294 (2002).
- 221 J. A. Shooter, T. G. Muir, and D. T. Blackstock, "Acoustic saturation of
spherical waves in water," *J. Acoust. Soc. Am.* **55** (1), 54-62 (1974).
- 222 E. J. Simmonds, "Very accurate calibration of a vertical echo sounder: a
five-year assessment of performance and accuracy," *Rapp. P.-v. Réun.
Cons. int. Explor. Mer.* **189**, 183-191 (1990).
- 223 J. Simmonds and D. MacLennan, *Fisheries acoustics*, 2nd ed.
(Blackwell Science Ltd, Oxford, UK, 2005).
- 224 V. W. Sparrow and R. Raspet, "A numerical method for general finite
amplitude wave propagation in two dimensions and its application to
spark pulses," *J. Acoust. Soc. Am.* **90** (5), 2683-2691 (1991).
- 225 H. Stark, F. B. Tuteur, and J. B. Anderson, *Modern electrical
communications - analog, digital, and optical systems*. (Prentice Hall,
Englewood Cliffs, USA, 1988).
- 226 M. A. Stokes, "On a difficulty in the theory of sound," *Phil. Mag. (series
3)* **33**, 349-356 (1848).
- 227 A. M. Sutin, S. W. Yoon, E. J. Kim, and I. N. Didenkulov, "Nonlinear
acoustic method for bubble density measurements," *J. Acoust. Soc. Am.*
103 (5), 2377-2384 (1998).
- 228 T. L. Szabo, "Time domain nonlinear wave equations for lossy media,"
in *Advances in Nonlinear Acoustics, Proceedings of the 13th*

International Symposium on Nonlinear Acoustics, Bergen, Norway, 28 June-2 July 1993, edited by H. Hobæk (World Scientific, Singapore, 1993), pp. 89-94.

- 229 C. Tao, J. Ma, Z. Zhu, and G. Du, "The shock formation distance in a bounded sound beam of finite amplitude," *J. Acoust. Soc. Am.* **114** (1), 114-121 (2003).
- 230 J. Tavakkoli, O. A. Sapozhnikov, R. Souchon, and D. Cathignol, "A time-domain numerical model for simulating the acoustic field of a high-amplitude focused source in biological media," in *proc. 1997 IEEE Ultrasonics Symposium*, 1997.
- 231 J. Tavakkoli, D. Cathignol, R. Souchon, and O. A. Sapozhnikov, "Modeling of pulsed finite-amplitude focused sound beams in time domain," *J. Acoust. Soc. Am.* **104** (4), 2061-2072 (1998).
- 232 A. L. Thuras, R. T. Jenkins, and H. T. O'Neil, "Extraneous frequencies generated in air carrying intense sound waves," *J. Acoust. Soc. Am.* **6**, 173-180 (1935).
- 233 F. E. Tichy, "Cavitation and nonlinear effects in echo sounder measurements," presented at the 25th Scandinavian Symposium on Physical Acoustics, Ustaoset, Norway, 2002.
- 234 F. E. Tichy, H. Solli, and H. Klaveness, "Non-linear effects in a 200-kHz sound beam and the consequences for target-strength measurement," *ICES Journal of Marine Science* **60**, 571-574 (2003).
- 235 F. E. Tichy, Kongsberg Maritime AS, Horten, Norway, personal communication, 2005.
- 236 J. Naze Tjøtta and S. Tjøtta, "An analytical model for the nearfield of a baffled piston transducer," *J. Acoust. Soc. Am.* **68** (1), 334-339 (1980).
- 237 J. Naze Tjøtta and S. Tjøtta, "Nonlinear equations of acoustics, with application to parametric acoustic arrays," *J. Acoust. Soc. Am.* **69** (6), 1644-1652 (1981).
- 238 J. Naze Tjøtta and S. Tjøtta, "Interaction of sound waves. Part I: Basic equations and plane waves," *J. Acoust. Soc. Am.* **82** (4), 1425-1428 (1987).
- 239 J. Naze Tjøtta, S. Tjøtta, and E. H. Vefring, "Propagation and interaction of two collinear finite amplitude sound beams," *J. Acoust. Soc. Am.* **88** (6), 2859-2869 (1990).

- 240 J. Naze Tjøtta, S. Tjøtta, and E. H. Vefring, "Effects of focusing on the nonlinear interaction between two collinear finite amplitude sound beams," *J. Acoust. Soc. Am.* **89** (3), 1017-1027 (1991).
- 241 J. Naze Tjøtta and S. Tjøtta, "Model equation and boundary conditions for the sound field from a high frequency, strongly curved and highly intense transducer," *Acta acustica* **1**, 69-87 (1993).
- 242 S. Tjøtta, "On some nonlinear effects in ultrasonic fields," *Ultrasonics* **38** (278-283) (2000).
- 243 S. Tjøtta, "Higher Order Model Equations in Nonlinear Acoustics," *Acta Acustica united Acustica* **87**, 316-321 (2001).
- 244 G. J. Too and J. H. Ginsberg, "Evaluation of a finite amplitude sound beam in the time domain using a modified version of the NPE computer code," in *Frontiers of Nonlinear Acoustics: Proceedings of 12th ISNA, Austin, Texas, August 1990*, edited by M. F. Hamilton and D. T. Blackstock (Elsevier, London, 1990), pp. 215-220.
- 245 G. J. Too and J. H. Ginsberg, "Cylindrical and spherical coordinate versions of NPE for transient and steady-state sound beams," *J. Vib. Acoust.* **114**, 420-424 (1992).
- 246 G. J. Too and S. T. Lee, "A numerical simulation for tone bursts of finite amplitude transient sound beams," in *Advances in Nonlinear Acoustics, Proceedings of the 13th International Symposium on Nonlinear Acoustics, Bergen, Norway, 28 June-2 July 1993*, edited by H. Hobæk (World Scientific, Singapore, 1993), pp. 245-250.
- 247 G. J. Too and S. T. Lee, "Thermoviscous effects on transient and steady-state sound beams using nonlinear progressive wave equation models," *J. Acoust. Soc. Am.* **97** (2), 867-874 (1995).
- 248 D. M. Towle and R. B. Lindsay, "Absorption and velocity of ultrasonic waves of finite amplitude in liquids," *J. Acoust. Soc. Am.* **27** (3), 530-533 (1955).
- 249 D. H. Trivett and A. L. Van Buren, "Propagation of plane, cylindrical, and spherical finite amplitude waves," *J. Acoust. Soc. Am.* **69** (4), 943-949 (1981).
- 250 R. J. Urick, *Principles of underwater sound*, 3rd ed. (McGraw-Hill, Inc., New York, 1983).
- 251 A. L. Van Buren and M. A. Breazeale, "Reflection of finite-amplitude ultrasonic waves. II. Propagation," *J. Acoust. Soc. Am.* **44** (4), 1021-1027 (1968).

- 252 C. J. Vecchio and P. A. Lewin, "Finite amplitude acoustic propagation modeling using the extended angular spectrum method," *J. Acoust. Soc. Am.* **95** (5), 2399-2408 (1994).
- 253 E. H. Vefring, "Lydfeltet fra en parametrisk antenne med høy intensitet (The sound field of a parametric array with high intensity)," Cand. Scient. thesis, Department of Mathematics, University of Bergen, 1986.
- 254 E. H. Vefring, "Nonlinear propagation and interaction of collinear sound beams," Dr. Scient. thesis, Department of Physics, University of Bergen, 1989.
- 255 E. H. Vefring, "Nonlinear propagation and interaction of collinear sound beams," Report no. 86, Department of Applied Mathematics, University of Bergen, Bergen, Norway, 1989.
- 256 E. H. Vefring, J. Naze Tjøtta, and S. Tjøtta, "Nonlinear effects in the sound field of a bifrequency source," in *Frontiers of Nonlinear Acoustics: Proceedings of 12th ISNA, Austin, Texas, August 1990*, edited by M. F. Hamilton and D. T. Blackstock (Elsevier, London, 1990), pp. 251-256.
- 257 E. M. Vorob'ev and E. A. Zabolotskaya, "Propagation of high-frequency sound beams," *Sov. Phys. Acoust.* **19** (6), 523-525 (1974).
- 258 W. Wagner and A. Pruß, "The IAPWS formulation 1995 for the thermodynamic properties of ordinary water substance for general and scientific use," *J. Phys. Chem. Ref. Data* **31** (2), 387-535 (2002).
- 259 B. Ward, A. C. Baker, and V. F. Humphrey, "Nonlinear propagation applied to the improvement of resolution in diagnostic medical ultrasound," *J. Acoust. Soc. Am.* **101** (1), 143-154 (1997).
- 260 Y. Watanabe and T. Asada, "On the possibility of shock formation in bubbly medium," in *Advances in Nonlinear Acoustics, Proceedings of the 13th International Symposium on Nonlinear Acoustics, Bergen, Norway, 28 June-2 July 1993*, edited by H. Hobæk (World Scientific, Singapore, 1993), pp. 202-207.
- 261 A. J. Watson, V. F. Humphrey, A. C. Baker, and F. A. Duck, "Nonlinear propagation of focused ultrasound in tissue-like media," in *Frontiers of Nonlinear Acoustics: Proceedings of 12th ISNA, Austin, Texas, August 1990*, edited by M. F. Hamilton and D. T. Blackstock (Elsevier, London, 1990), pp. 445-450.
- 262 P. J. Westervelt, "Scattering of Sound by Sound," *J. Acoust. Soc. Am.* **29** (8), 934-935 (1957).

- 263 P. J. Westervelt, "Scattering of Sound by Sound," *J. Acoust. Soc. Am.* **29** (2), 199-203 (1957).
- 264 P. J. Westervelt, "Parametric acoustic array," *J. Acoust. Soc. Am.* **35** (4), 535-537 (1963).
- 265 G. Wojcik, J. Mould Jr., F. Lizzi, N. Abboud, M. Ostromogilsky, and D. Vaughan, "Nonlinear modeling of therapeutic ultrasound," in *proc. 1995 IEEE Ultrasonics Symposium*, 1995.
- 266 H. C. Woodsum and P. J. Westervelt, "A general theory for the scattering of sound by sound," *J. Sound Vib.* **76** (2), 179-186 (1981).
- 267 J. Wu, "Bubble population and spectra in near-surface ocean: Summary and review of field measurements," *J. Geophys. Res.* **68**, 457-463 (1981).
- 268 X. Yang and R. O. Cleveland, "Time domain simulation of nonlinear acoustic beams generated by rectangular pistons with application to harmonic imaging," *J. Acoust. Soc. Am.* **117** (1), 113-123 (2005).
- 269 B. Ystad and J. Berntsen, "Numerical Solution of the KZK Equation for Focusing Sources," *Acta acustica* **3**, 323-330 (1995).
- 270 E. A. Zabolotskaya and S. I. Soluyan, "A possible approach to the amplification of sound waves," *Sov. Phys. Acoust.* **13** (2), 254-256 (1967).
- 271 E. A. Zabolotskaya and R. V. Khokhlov, "Quasi-plane waves in the nonlinear acoustics of confined beams," *Sov. Phys. Acoust.* **15** (1), 35-40 (1969).
- 272 E. A. Zabolotskaya and R. V. Khokhlov, "Convergent and divergent sound beams in nonlinear media," *Sov. Phys. Acoust.* **16** (1), 39-42 (1970).
- 273 Ya. M. Zhileikin, "Numerical solution of the equation for non-linear acoustics of confined beams," *U.S.S.R. Comput. Maths. Math. Phys.* **22** (5), 140-156 (1982).
- 274 V. A. Zverev and A. I. Kalachev, "Measurement of the scattering of sound by sound in the superposition of parallel beams," *Sov. Phys. Acoust.* **14** (2), 173-178 (1968).
- 275 O. Østerbø, "Om Zabolotskaya-Khokhlovs ligning med anvendelse i lineær og ikkelineær akustikk (On the Zabolotskaya-Khokhlov equation with application in linear and nonlinear acoustics)," *Cand. Real. thesis*, Department of Mathematics, University of Bergen, 1980.

- 276 S. I. Aanonsen, "Numerical computation of the nearfield of a finite amplitude sound beam," Report no. 73, University of Bergen, Department of Applied Mathematics, Bergen, Norway, 1983.
- 277 S. I. Aanonsen, T. Barkve, J. Naze Tjøtta, and S. Tjøtta, "Distortion and harmonic generation in the nearfield of a finite amplitude sound beam," J. Acoust. Soc. Am. **75** (3), 749-768 (1984).
- 278 S. I. Aanonsen, M. F. Hamilton, J. Naze Tjøtta, and S. Tjøtta, "Nonlinear effects in sound beams," presented at the 10th International Symposium on Nonlinear Acoustics, Kobe, Japan, 1984.

Appendix A: List of symbols

| | |
|----------------------|---|
| a | uniform piston source radius |
| a_f | radius of transducer face |
| b | isothermal sound speed |
| C | constant in the calculation of TS_{lin} and TS_{meas} |
| c_0 | small-signal sound speed |
| C_L | capacitance of receiver circuit |
| c_P | specific heat, constant pressure |
| c_V | specific heat, constant volume |
| $D(\theta, \varphi)$ | directivity function |
| d_{max} | distance from hydrophone to farthest point on transducer face |
| EL | echo level |
| $E(p_{\text{sim}})$ | simulation relative standard uncertainty |
| $E(q_m)$ | relative standard uncertainty in the parameter q_m |
| E_{cont} | model relative standard uncertainty contribution due to the assumption of a continuous wave |
| E_{fd} | numerical relative standard uncertainty contribution due to the |

finite differences

| | |
|---------------------|--|
| E_{geom} | relative standard uncertainty contribution due to a difference in beam pattern conventions |
| E_{grid} | numerical relative standard uncertainty contribution due to the resolution of the numerical grid |
| E_{harm} | numerical relative standard uncertainty contribution due to spectral truncation |
| E_{imp} | numerical relative standard uncertainty contribution due to the number and length of initial implicit calculation steps |
| E_{misc} | simulation relative standard uncertainty contributions due to factors that have not been identified in the present work |
| E_{model} | simulation relative standard uncertainty contribution due to the theoretical model |
| E_{np} | numerical relative standard uncertainty contributions due to the parameters that govern the calculation process |
| E_{num} | simulation relative standard uncertainty contribution due to the numerical algorithm |
| E_{order} | model relative standard uncertainty contribution due to the KZK equation being of second order |
| E_{par} | model relative standard uncertainty contribution due to the parabolic approximation inherent in the KZK equation |
| E_{param} | relative standard simulation uncertainty contribution due to uncertainties in input parameters |
| E_{rnd} | numerical relative standard uncertainty contribution due to rounding or truncation of numeric values |
| E_{s} | numerical relative standard uncertainty contribution used for the extrapolation of E_{num} from low amplitudes to high amplitudes |
| E_{source} | model relative standard uncertainty contribution due to the description of the sound source |
| E_{symm} | model relative standard uncertainty contribution due to the assumption of axisymmetry |

| | |
|-----------------------|--|
| E_{width} | numerical relative standard uncertainty contribution due to finite width of the numerical grid |
| E_{α} | model relative standard uncertainty contribution due to the assumption of a quadratic absorption power law |
| E_m | simulation relative standard uncertainty contribution due to the parameter q_m |
| f | frequency |
| $f_s(\xi)$ | source condition |
| f_{TVG20} | time varying gain function for volume backscattering measurement |
| f_{TVG40} | time varying gain function for target strength measurement |
| F_Z | impedance matching factor |
| $G(\theta, \varphi)$ | transducer gain function |
| $G'(\theta, \varphi)$ | receive transducer gain function |
| G_0 | axial transducer gain |
| G'_0 | axial receive transducer gain |
| $G_{0,\text{cal}}$ | apparent axial transmit transducer gain (calibration result) |
| g_n | Fourier coefficient for simulation result |
| h_n | Fourier coefficient for simulation result |
| $H(\theta, \varphi)$ | directional factor |
| i | electrical current amplitude (complex) |
| I_{bs} | intensity of backscattered sound at reference distance r'_0 |
| I_{ref} | reference acoustic intensity, $I_{\text{ref}} = 1 \text{ W/m}^2$ |
| I_t | intensity of transmitted sound wave |
| $I_{\text{t,sph}}$ | acoustic intensity due to point source |
| IL | intensity level |

| | |
|---|--|
| $I_{a,1}, I_{a,2},$ $I_{b,1}, I_{b,2}$ | indicator values for sensitivity analyses, fundamental frequency component |
| $I'_{a,1}, I'_{a,2},$ $I'_{b,1}, I'_{b,2}$ | indicator values for sensitivity analyses, second harmonic frequency component |
| j | imaginary unit |
| J_1 | first order Bessel function of first kind |
| J_s | spherical reciprocity parameter (complex) |
| k | wave number, $k = 2\pi f/c_0$ |
| l_D | plane wave shock formation distance |
| l_{mount} | dimension on hydrophone mounting arrangement |
| l_{imp} | length of implicit steps in simulation algorithm |
| l_σ | length of steps in simulation algorithm |
| \mathcal{L} | Lagrangian density |
| m | index |
| M | hydrophone sensitivity (complex) |
| M_L | end-of-cable loaded hydrophone sensitivity |
| n | index (harmonic number) |
| N | Fourier transform length |
| N_d | number of damped harmonics in simulation algorithm |
| N_h | number of harmonics in simulation algorithm |
| N_{imp} | number of implicit steps in simulation algorithm |
| N_u | number of numerical grid points in transverse direction |
| NA | nonlinear attenuation |
| NA_{sim} | simulated nonlinear attenuation |
| p | sound pressure amplitude (complex) |

| | |
|----------------------|--|
| p_{rms} | effective sound pressure |
| p_{ref} | reference effective sound pressure, $p_{\text{ref}} = 1 \mu\text{Pa}$ |
| p_n | sound pressure amplitude for the n th harmonic component (complex) |
| p_n'' | sound pressure amplitude for the n th harmonic component after damping to reduce spectral truncation artefacts (complex) |
| P | pressure |
| P_0 | equilibrium pressure |
| p' | sound pressure, $p' = P - P_0$ |
| p_{inc} | sound pressure amplitude of incident wave (complex) |
| p_n | near field sound pressure amplitude (complex) |
| p_s | source condition sound pressure amplitude (complex) |
| p_0 | peak sound pressure amplitude of uniform piston source condition (real) |
| $p_{0,\text{rms}}$ | effective sound pressure for uniform piston source condition |
| $p_{1,\text{rms}}$ | effective sound pressure, fundamental frequency component |
| $p_{2,\text{rms}}$ | effective sound pressure, second harmonic frequency component |
| p_{sim} | simulated effective sound pressure |
| $p_{1,\text{sim}}$ | simulated effective sound pressure, fundamental frequency component |
| $p_{2,\text{sim}}$ | simulated effective sound pressure, second harmonic frequency component |
| $p_{1,\text{cal}}$ | simulated effective sound pressure during calibration |
| p_{lin} | simulated effective sound pressure, linear sound propagation |
| $p_{\text{lin,cal}}$ | simulated effective sound pressure during calibration, linear sound propagation |
| \bar{p} | normalized sound pressure, $\bar{p} = p' / \rho_0 c_0 v_0$ |

| | |
|--------------------------|--|
| $\bar{p}_{1,\text{sim}}$ | normalized simulated sound pressure amplitude, fundamental frequency component, $\bar{p}_{1,\text{sim}} = p_{1,\text{sim}} / p_{0,\text{rms}}$ |
| $\bar{p}_{2,\text{sim}}$ | normalized simulated sound pressure amplitude, second harmonic frequency component, $\bar{p}_{2,\text{sim}} = p_{2,\text{sim}} / p_{0,\text{rms}}$ |
| \bar{p}_{lin} | normalized simulated sound pressure amplitude, linear sound propagation, $\bar{p}_{\text{lin}} = p_{\text{lin}} / p_{0,\text{rms}}$ |
| p_{lt} | sound pressure amplitude from linear theory (complex) |
| p_{par} | sound pressure amplitude from analytical solution of the linearized parabolic equation (complex) |
| P_{r0} | power frequency response of echo sounder system |
| P_{t} | electric transmit power |
| q_m | physical parameter for simulations |
| r | distance from sound source |
| r_0 | reference distance for sound source, $r_0 = 1$ m |
| r'_0 | reference distance for backscattering, $r'_0 = 1$ m |
| r_{cal} | distance to calibration sphere during echo sounder calibration (calibration distance) |
| r_n | distance from transducer symmetry axis, $r_n = (x^2 + y^2)^{1/2}$ |
| R_0 | Rayleigh distance, $R_0 = ka^2/2$ |
| $r(f)$ | relative frequency response, $r(f) = s_v(f) / s_v(38 \text{ kHz})$ |
| $r_a(f)$ | relative area backscattering frequency response, $r_a(f) = s_a(f) / s_a(38 \text{ kHz})$ |
| $R_a(f)$ | relative area backscattering frequency response in decibels, $R_a = 10 \log_{10} r_a(f)$ |
| R_L | receiver circuit resistance |
| R_T | electric transducer input resistance |
| R'_T | electric transducer output resistance |

| | |
|---------------------|---|
| S | current source sensitivity (complex) |
| S_V | voltage source sensitivity |
| s | entropy, $s = s_0 + s'$ |
| s' | entropy perturbation |
| s_0 | entropy at equilibrium |
| s_a | area backscattering coefficient [m^2/m^2] |
| s_A | nautical area scattering coefficient (NASC) [m^2/nmi^2] |
| $s_{a,n}$ | area backscattering coefficient compensated for linear attenuation |
| s_v | volume backscattering coefficient [m^2/m^3] |
| $s_{v,n}$ | volume backscattering coefficient compensated for linear attenuation |
| SL | source level |
| SPL | sound pressure level |
| $s(q_m)$ | relative sensitivity coefficient due to the parameter q_m |
| t | time |
| t' | retarded time |
| t_0 | start time for near field measurement time window |
| $t_{0,\text{axis}}$ | start time for near field measurement time window, $r_n = 0$ |
| t_{end} | end time for near field measurement time window |
| Δt | sample interval |
| T | temperature |
| T' | transformed beam equation pressure variable, $T' = (1 + \sigma)\bar{p}$ |
| TL | transmission loss |
| TS | target strength |

| | |
|--------------------------------|---|
| TS_{lin} | apparent target strength, nonlinear attenuation absent |
| TS_{meas} | apparent target strength, nonlinear attenuation present |
| TS_{unc} | uncompensated target strength (beam compensation function not applied) |
| TVR | transmit voltage response |
| U | voltage amplitude (complex) |
| U_0 | open circuit voltage amplitude (complex) |
| $U(t)$ | electric voltage |
| $\hat{U}(f)$ | Fourier transform of voltage signal |
| U_t | effective transmit voltage (rms) |
| \mathbf{u} | transformed transverse coordinate, $\mathbf{u} = \xi/(1 + \sigma)$ |
| u | transformed distance from the sound beam axis, $u = \mathbf{u} $ |
| u_{max} | width of numerical grid |
| $u(p_{\text{sim}})$ | standard uncertainty |
| V | volume |
| V_0 | volume |
| $\mathbf{v} = (v_1, v_2, v_3)$ | particle velocity |
| v | particle speed, $v = \mathbf{v} $ |
| v_0 | particle speed peak amplitude for uniform piston source condition (real) |
| W | EK60 power setting |
| (x, y, z) | Cartesian coordinates, z axis coincides with the sound beam axis |
| $\mathbf{x} = (x_1, x_2, x_3)$ | Cartesian coordinates (KZK equation), x_3 axis coincides with the sound beam axis |
| (x'_1, x'_2, x'_3) | slow scale coordinates |

| | |
|-----------------------|--|
| X_L | receiver circuit reactance |
| X_T | electric transducer input reactance |
| X'_T | electric transducer output reactance |
| Z_H | electric hydrophone output impedance |
| Z_L | receiver circuit impedance |
| Z_T | electric transducer input impedance |
| Z'_T | electric transducer output impedance |
| α | absorption coefficient [dB/m] |
| α' | absorption coefficient, $\alpha' = \alpha_2 f^2$ [Np/m] |
| α_2 | absorption coefficient [Np/m/Hz ²] |
| α'_0 | absorption coefficient [Np/m/Hz ^{γ}] |
| β | nonlinearity coefficient |
| δ | sound diffusivity |
| ε | acoustic Mach number |
| $\tilde{\varepsilon}$ | ordering parameter |
| ϕ_n | phase of p_n (near field measurements) |
| ϕ_s | phase of p_s (near field measurements) |
| φ | azimuth angle |
| γ | real exponent in absorption power law |
| η | electroacoustic efficiency (transducer description) |
| η | Stokes' number (nonlinear sound propagation) |
| κ | heat conductance |

| | |
|---------------------------|---|
| λ_σ | step length parameter |
| μ | shear viscosity |
| μ_B | bulk viscosity |
| θ | polar angle |
| θ_x | along ship angle |
| θ_y | athwart ship angle |
| $\theta_{-3\text{ dB}}$ | -3 dB beam angle |
| $\theta_{-3\text{ dB},x}$ | along ship -3 dB beam width |
| $\theta_{-3\text{ dB},y}$ | athwart ship -3 dB beam width |
| $\Delta\theta_x$ | along ship angle offset |
| $\Delta\theta_y$ | athwart ship angle offset |
| ρ | density, $\rho = \rho_0 + \rho'$ [kg/m ³] |
| ρ' | density perturbation |
| ρ_0 | equilibrium density |
| σ_{bs} | backscattering cross-section |
| $\sigma_{\text{bs,eff}}$ | effective backscattering cross-section |
| σ_{sp} | spherical scattering cross-section |
| τ | sound burst duration |
| τ' | dimensionless retarded time |
| τ_p | transformed retarded time |
| Ω | solid angle |
| ω | angular frequency, $\omega = 2\pi f$ |

| | |
|--------------------------|---|
| (ξ_1, ξ_2, σ) | dimensionless coordinates, $(\xi_1, \xi_2, \sigma) = (x_1/a, x_2/a, x_3/R_0)$ |
| ξ | dimensionless transverse coordinates, $\xi = \xi_1 \mathbf{e}_1 + \xi_2 \mathbf{e}_2$ |
| ξ | dimensionless distance from the sound beam axis, $\xi = \xi $ |
| $\xi_{\max}(\sigma)$ | dimensionless width of the numerical grid |
| $\Delta \xi$ | dimensionless distance between numerical grid points in the transverse direction |
| ψ | two-way effective beam angle |
| Ψ | two-way effective beam angle, $\Psi = 10 \cdot \log_{10}(\psi / 1 \text{ steradian})$ |
| ψ_n | compensated two-way effective beam angle |
| Ψ_{lin} | simulated two-way effective beam angle, linear propagation |
| ∇_{\perp}^2 | transverse Laplacian operator |
| $\bar{\nabla}_{\perp}^2$ | dimensionless transverse Laplacian operator |
| $\nabla_{\mathbf{u}}^2$ | transformed dimensionless transverse Laplacian operator |

Appendix B: Bergen Code program listing

```

PROGRAM BEAM
IMPLICIT NONE
INTEGER IXMAX, NHARM, NUMBE, NH, NCOEFFWRI, DMPWIDTH, DMPSWITCH, I, IMPSTP
INTEGER HARM_DMPWIDTH, HARM_DMPSWITCH
PARAMETER (IXMAX=16000, NHARM=50, NUMBE=6, NCOEFFWRI=2)
DOUBLE PRECISION OMEGA(0:IXMAX, NHARM, 2), WINDWX, START, STOP,
+           WBEAM(NUMBE), COEFFWRI_POS(NCOEFFWRI),
+           COLD(NHARM), CNEW(NHARM)
DOUBLE PRECISION KHALF(NHARM), NONLI(0:IXMAX, NHARM, 2),
+           A(2, 2, -1:1, 0:IXMAX), W(2, 0:IXMAX),
+           F(2, 0:IXMAX), WORK(12*IXMAX+12), IMP_STL
DOUBLE PRECISION FREQ, RADIUS, SSPEED, ALPHA2, BETA, MACH, PI,
+           R0, RD, K, RHO, P0, SOURCE_TP, SOURCE_TA,
+           COEFFPOS(NCOEFFWRI), UPPER_ENERGY, OUTER_ENERGY
DOUBLE PRECISION PABSOR, PNONLI, ISSTEP
INTEGER SCOUNT, ECOUNT
REAL TIME, DTIME, TARRAY(2)
REAL DWAX, DWTR

```

```

EXTERNAL COEFF, NONLIN, STEPP, BEWRI, BEWRI2, COEFFWRI
COMMON /PARAM/PABSOR, PNONLI
COMMON /AXSTEP/ISSTEP
COMMON /OUTPUT/RADIUS, R0, DWTR, NH
COMMON /BRD_DMP/DMPWIDTH, DMPSWITCH
COMMON /HARM_DMP/HARM_DMPWIDTH
COMMON /WARNINGS/UPPER_ENERGY, OUTER_ENERGY, SCOUNT, ECOUNT

OPEN (UNIT=10, FILE='tr_amp.bc', STATUS='unknown')
OPEN (UNIT=11, FILE='ax_amp.bc', STATUS='unknown')
OPEN (UNIT=12, FILE='waveform.bc', STATUS='unknown')
OPEN (UNIT=13, FILE='tr_phase.bc', STATUS='unknown')
OPEN (UNIT=14, FILE='ax_phase.bc', STATUS='unknown')
OPEN (UNIT=15, FILE='settings.log', STATUS='unknown')

PI = 4*ATAN(1.0D0)

C
C
C PHYSICAL PARAMETERS
C Frequency [Hz]
FREQ = 121.212D3
C Amplitude at the sound source [Pa]
P0 = 396.D3
C Source radius [m] (X = x/RADIUS)
RADIUS = 52.8D-3
C
C Sound speed [m/s]
SSPEED = 1462.D0
C Convergence tests: 1500 m/s
C
C Absorption constant [Np/m/Hz^2]
ALPHA2 = 2.25D-13
C Coefficient of nonlinearity
BETA = 3.48
C
C Density [kg/m^3]
RHO = 1025.1D0
C
C Wave number
K = 2*PI*FREQ/SSPEED
C Rayleigh distance [m] (sigma = z/r0)
R0 = RADIUS**2*K/2
C Shock distance [m]
mach = p/rho/sspeed**2
C rd = 1/(beta*mach*k)
RD = RHO*SSPEED**2/BETA/K/P0

PABSOR = ALPHA2*FREQ**2*R0
PNONLI = R0/RD

C
C CALCULATION GRID
C Number of fully implicit steps
IMPSTP = 10
C Step length when the fully implicit method is used
IMP_STL = 5.5D-3
C Factor for calculating the step sizes when using the
C Richtmeyer procedure (see STEPP)
ISSTEP = 2.D-4
C Width of the calculation area (source radii at z=0)
WINDWX = 10.
C

```

```

C      DAMPING AT THE BORDER OF THE CALCULATION AREA
C      Number of points submitted to damping
      DMPWIDTH = 2000
C      Choice of damping method at the border of the calculation area;
C      0:No damping, 1:Linear damping, 2:Sine curve damping,
C      3:Newtonian friction flow relaxation scheme (Ystad, Berntsen)
      DMPSWITCH = 0
C
C      DAMPING OF THE HIGHEST HARMONIC COMPONENTS
C      Number of harmonics to be affected by the damping scheme
      HARM_DMPWIDTH = 20
C      Turn damping of the highest harmonic components on or off
C      0:No damping, 1:Parabolic damping (analog to the FRS above)
      HARM_DMPSWITCH = 0
C
C      TAPERING OF THE SOURCE
C      Radius for the inner area of the source with amplitude 1
C      [Outer source radii (RADIUS)]
      SOURCE_TP = 1.D0
C      Amplitude of the outer ring,
C      "SOURCE_TA = 1." means no tapering.
      SOURCE_TA = 1.D0
C
C      Initialise warning parameters
      UPPER_ENERGY = 0.D0
      OUTER_ENERGY = 0.D0
      SCOUNT = 0.D0
      ECOUNT = 0.D0
C
C      OUTPUT
C      Number of harmonics written to file.
C      (It may be necessary to edit the FORMAT statements in bewri.f
C      when this parameter is changed.)
      NH = 5
C      Distance between written data points along the beam axis
      DWAX = 1.D-2/R0
      DWAX = 0.
C      Distance between written data points in the transverse direction
      DWTR = 0.
C
C      Positions on the z-axis for recording the solution in the
C      transverse direction. Also determines z_max (STOP).
      WBEAM(1) = 5.0D0/R0
      WBEAM(2) = 10.0D0/R0
      WBEAM(3) = 20.0D0/R0
      WBEAM(4) = 35.0D0/R0
      WBEAM(5) = 50.0D0/R0
      WBEAM(6) = 100.0D0/R0
C      Positions on the z-axis for recording all the coefficients
      COEFFWRI_POS(1) = 10.D0/R0
      COEFFWRI_POS(2) = 50.D0/R0
C
C      Write settings to log file
C
      WRITE(15,*) '*** Log file ***'
      WRITE(15,*)
      WRITE(15,*)
      WRITE(15,*) '--- Input parameters ---'
      WRITE(15,*)
      WRITE(15,*) 'FREQ:      ',SNGL(FREQ)
      WRITE(15,*) 'P0:        ',SNGL(P0)

```

```

WRITE(15,*) 'RADIUS: ',SNGL(RADIUS)
WRITE(15,*) 'SSPEED: ',SNGL(SSPEED)
WRITE(15,*) 'ALPHA2: ',SNGL(ALPHA2)
WRITE(15,*) 'BETA: ',SNGL(BETA)
WRITE(15,*) 'RHO: ',SNGL(RHO)
WRITE(15,*)
WRITE(15,*)
WRITE(15,*) 'IXMAX: ',IXMAX
WRITE(15,*) 'NHARM: ',NHARM
WRITE(15,*) 'IMPSTP: ',IMPSTP
WRITE(15,*) 'IMP_STL: ',SNGL(IMP_STL)
WRITE(15,*) 'ISSTEP: ',SNGL(ISSTEP)
WRITE(15,*) 'WINDWX: ',SNGL(WINDWX)
WRITE(15,*)
WRITE(15,*) 'Damping of the solution near the outer border'
WRITE(15,*) 'of the calculation region'
WRITE(15,*) 'DMPSWITCH: ',DMPSWITCH
WRITE(15,*) 'DMPWIDTH: ',DMPWIDTH
WRITE(15,*)
WRITE(15,*) 'Damping of the upper harmonics'
WRITE(15,*) 'HARM_DMPSWITCH: ',HARM_DMPSWITCH
WRITE(15,*) 'HARM_DMPWIDTH: ',HARM_DMPWIDTH
WRITE(15,*)
WRITE(15,*) 'Tapering of the sound source'
WRITE(15,*) 'SOURCE_TP: ',SNGL(SOURCE_TP)
WRITE(15,*) 'SOURCE_TA: ',SNGL(SOURCE_TA)
WRITE(15,*)
WRITE(15,*) '---- Calculated parameters ----'
WRITE(15,*)
WRITE(15,*) 'k: ',SNGL(K)
WRITE(15,*) 'ka: ',SNGL(K*RADIUS)
WRITE(15,*) 'r0: ',SNGL(R0)
WRITE(15,*) 'rd: ',SNGL(RD)
WRITE(15,*)
WRITE(15,*) 'PABSOR: ',SNGL(PABSOR)
WRITE(15,*) 'PNONLI: ',SNGL(PNONLI)
WRITE(15,*)
WRITE(15,*) '--- Output ---'
WRITE(15,*) 'NH: ',NH
WRITE(15,*) 'DWAX: ',SNGL(DWAX)
WRITE(15,*) 'DWTR: ',SNGL(DWTR)
WRITE(15,*) 'NUMBE: ',NUMBE
WRITE(15,*) 'WBEAM: ',(SNGL(WBEAM(I)),I=1,NUMBE)
WRITE(15,*) 'NCOEFFWRI: ',NCOEFFWRI
WRITE(15,*) 'COEFFWRI_POS: ',(SNGL(COEFFWRI_POS(I)),I=1,NCOEFFWRI)
C
C Write headers in data output files
C
WRITE(10,20) IXMAX,NH,NUMBE
WRITE(13,20) IXMAX,NH,NUMBE
WRITE(12,25) NHARM,NCOEFFWRI,FREQ,P0
20 FORMAT(i5,1x,i5,1x,i5)
25 FORMAT(i5,1x,i5,1x,e16.10,1x,e16.10)
C
C
C Initialise the Fourier coefficients
C
C Uniform piston or simple amplitude shading
CALL INIT(WINDWX,OMEGA,IXMAX,NHARM,SOURCE_TP,SOURCE_TA)
C
cC Read source condition from file

```



```

c      CALL INIT2 (WINDWX, OMEGA, IXMAX, NHARM)
C
C
C      Integrate the differential equations.
C
      START = 0.
      STOP = MAX (WBEAM (NUMBE) , COEFFWRI_POS (NCOEFFWRI) )
      TIME = DTIME (TARRAY)
      CALL KZKCYL (OMEGA, IXMAX, NHARM, WINDWX, START, STOP, WBEAM, NUMBE,
+               COEFFWRI_POS, NCOEFFWRI,
+               IMPSTP, COEFF, NONLIN, STEPP, BEWRI, COLD, CNEW, KHALF, NONLI,
+               A, W, F, WORK, DWAX, IMP_STL, HARM_DMPSWITCH)
      TIME = DTIME (TARRAY)
      WRITE (15, *)
      WRITE (15, *) '--- Performance ---'
      WRITE (15, *)
      WRITE (15, *) 'Time: ', TIME
      WRITE (15, *)
      WRITE (15, *) '--- Warnings ---'
      WRITE (15, *)
      WRITE (15, *) 'Square sums of the omega values close to'
      WRITE (15, *) 'the boundaries of the calculation region'
      WRITE (15, *)
      WRITE (15, *) 'UPPER_ENERGY: ', SNGL (UPPER_ENERGY)
      WRITE (15, *) 'OUTER_ENERGY: ', SNGL (OUTER_ENERGY)
      WRITE (15, *)
      WRITE (15, *) 'Step count: ', SCOUNT
      WRITE (15, *) 'Wrong ratios: ', ECOUNT
      CLOSE (10)
      CLOSE (11)
      CLOSE (12)
      CLOSE (13)
      CLOSE (14)
      CLOSE (15)
      STOP
      END

```

```

      SUBROUTINE KZKCYL (OMEGA, IXMAX, NHARM, WINDWX, START, STOP, WBEAM, NUMBE,
+                      COEFFWRI_POS, NCOEFFWRI,
+                      IMPSTP, COEFF, NONLIN, STEPP, BEWRI, COLD, CNEW, KHALF,
+                      NONLI, A, W, F, WORK, DWAX, IMP_STL, HARM_DMPSWITCH)

```

```

C
C***BEGIN PROLOGUE KZKCYL
C***AUTHOR Jarle Berntsen, University of Bergen,
C          EDB-senteret, Herman Fossgt 6, 5007 Bergen, NORWAY.
C***PURPOSE KZKCYL computes approximations to the Khokhlov-
C          Zabolotzkaya-Kuznetsov equation, see [1,2].
C          After a Fourier-series expansion of the pressure,
C          we may compute approximations to the KZK equation by
C          solving a system of nonlinear parabolic equations of
C          the form:
C
C           $dg(n)/d\sigma = -c(n, \sigma)g(n) + k(n, \sigma)\text{Laplacian}(h(n)) +$ 
C              $il1(n, \sigma, g, h)$ 
C
C           $dh(n)/d\sigma = -c(n, \sigma)h(n) - k(n, \sigma)\text{Laplacian}(g(n)) +$ 
C              $il2(n, \sigma, g, h)$ 
C

```

```

C
C           g(n) and h(n) are interchanged with respect to
C           Aanonsen et al. (1984)
C
C           The terms on the right hand side of the equality sign are
C           due to (from left to right) absorbtion, diffraction and
C           nonlinearity.
C           In KZKCYL the Laplacian is cylindrical coordinates.
C
C***DESCRIPTION Two numerical techniques are applied in KZKCYL in order
C           to compute approximations to the system of equations
C           given above.
C           For uniform sources which are of particular interest,
C           Gibbs oscillations appear in the numerical solution.
C           In order to damp these we first take a few steps with
C           a fully implicit method.
C           In order to control the damping
C           the S first harmonics of the Fourier expansion
C           of the initial values are kept to 99.9 per cent of
C           their full strength.
C           S is set as a parameter in KZKCYL.
C
C           After having removed the Gibbs oscillations we continue
C           with the Trapezoidal rule (or Crank-Nicolson method or
C           on this particular problem, Richtmyers procedure)
C           which has 2'nd order accuracy and is unconditionally
C           stable.
C
C           The linear systems of equations that have to be solved
C           in each step are solved with the routine TRIDIA.
C
C ON ENTRY
C
C OMEGA Real array of dimension (0:IXMAX,NHARM,2).
C           Contains in each step approximative values to g(n) and
C           h(n).
C           The first index defines the values of x for which g(n)
C           and h(n) are approximated.
C           The second index defines the harmonic number.
C           If the last index is 1, approximations to g(n) are given.
C           If the last index is 2, approximations to h(n) are given.
C           On entry OMEGA must specify the initial values of g(n)
C           and h(n).
C
C IXMAX Integer.
C           Defines the number of interior grid points.
C
C NHARM Integer.
C           Defines the number of harmonics retained in the numerical
C           solution.
C
C WINDWX Real.
C           WINDWX is the upper limit of x.
C
C START Real.
C           The starting value of sigma.
C
C STOP Real.
C           The final value of sigma.
C
C WBEAM Real array of dimension NUMBE.

```

```

C           Specifies the values of sigma where we want print out
C           of OMEGA.
C
C NUMBE  Integer.
C           The length of the array WBEAM.
C
C COEFF  Subroutine, supplied by the user.
C           COEFF must be declared as external in the calling program.
C           COEFF is called by KZKCYL to compute the coefficients
C           c(n,sigma) and k(n,sigma).
C
C           Its specification is:
C           SUBROUTINE COEFF(SIGC,SIGK,C,K,NHARM)
C           INTEGER NHARM
C           DOUBLE PRECISION SIGC,SIGK,C(NHARM),K(NHARM)
C
C           SIGC defines on entry the value of sigma for which
C           you want to compute the coefficients c(n,sigma).
C
C           SIGK defines on entry the value of sigma for which
C           you want to compute the coefficients k(n,sigma).
C
C           C contains on exit the
C           values of c(n,SIGC), n=1,...,NHARM.
C
C           K contains on exit the
C           values of k(n,SIGK), n=1,...,NHARM.
C
C NONLIN Subroutine, supplied by the user.
C           NONLIN must be declared as external in the calling program.
C           NONLIN is called by KZKCYL to compute the nonlinear terms
C           il1(n,sigma,g,h) and il2(n,sigma,g,h).
C
C           Its specification is:
C           SUBROUTINE NONLIN(SIGMA,OMEGA,IXMAX,NHARM,NONLI)
C           INTEGER IXMAX,NHARM
C           DOUBLE PRECISION SIGMA
C           DOUBLE PRECISION OMEGA(0:IXMAX,NHARM,2)
C           DOUBLE PRECISION NONLI(0:IXMAX,NHARM,2)
C
C           SIGMA defines on entry the value of sigma for which
C           you want to compute the nonlinear terms.
C
C           OMEGA defines on entry the computed approximations to
C           g(n) and h(n).
C
C           NONLI must on exit contain the nonlinear terms.
C           If the last index is 1, approx. to il1 is indicated.
C           If the last index is 2, approx. to il2 is indicated.
C
C STEPP  Real function, supplied by the user.
C           STEPP must be declared as external in the calling program.
C           STEPP defines the step size in sigma direction.
C
C           Its specification is:
C           DOUBLE PRECISION FUNCTION STEPP(SIGMA)
C           DOUBLE PRECISION SIGMA
C
C BEWRI  Subroutine, supplied by the user.
C           BEWRI must be declared as external in the calling program.

```

```

C          BEWRI is called by KZKCYL to write information in OMEGA to
C          file(s).
C
C          Its specification is:
C          SUBROUTINE BEWRI(WINDWX,SIGMA,OMEGA,IXMAX,NHARM)
C          INTEGER IXMAX,NHARM
C          DOUBLE PRECISION WINDWX,SIGMA
C          DOUBLE PRECISION OMEGA(0:IXMAX,NHARM,2)
C
C ON RETURN
C
C          OMEGA contains the approximations to g(n) and h(n) at sigma=STOP.
C
C          COLD Real work array of dimension NHARM.
C
C          CNEW Real work array of dimension NHARM.
C
C          KHALF Real work array of dimension NHARM.
C
C          NONLI Real work array of dimension (0:IXMAX,NHARM,2).
C
C          A Real work array of dimension (2,2,-1:1,0:IXMAX).
C
C          W Real work array of dimension (2,0:IXMAX).
C
C          F Real work array of dimension (2,0:IXMAX).
C
C          WORK Real work array of dimension (12*IXMAX+12).
C
C***REFERENCES
C [1]Zabolotskaya,E.A. and Khokhlov,V.Pa,
C Quasi-plane waves in the nonlinear acoustics of confined beams,
C Sov.Phys.Acoust.,15,1969,pp.35-40.
C [2]Kuznetsov,V.P.,Equations of nonlinear acoustics,
C Sov.Phys.Acoust.,16,1971,pp.467-470.
C [3]Hamilton,M.F. and Naze Tjotta,J. and Tjotta.S,
C Nonlinear effects in the farfield of a directive sound source,
C J.Acoust.Soc.Am.,78,1985,pp.202-216.
C [4]Berntsen,J.,The numerical calculation of the Khokhlov-
C Zabolotskaya-Kuznetsov equation for piston sources,
C Unpublished paper,1988.
C***ROUTINES CALLED COEFF,NONLIN,STEPP,BEWRI,TRIDIA
C***END PROLOGUE KZKCYL
C
C Global variables.
C
C IMPLICIT NONE
C INTEGER IXMAX,NHARM,NUMBE,NCOEFFWRI,IMPSTP,HARM_DMPSWITCH
C DOUBLE PRECISION OMEGA(0:IXMAX,NHARM,2),WINDWX,START,STOP,
C + WBEAM(NUMBE),STEPP,COLD(NHARM),CNEW(NHARM),
C + KHALF(NHARM),NONLI(0:IXMAX,NHARM,2),IMP_STL,
C + A(2,2,-1:1,0:IXMAX),W(2,0:IXMAX),F(2,0:IXMAX),
C + WORK(12*IXMAX+12),COEFFWRI_POS(NCOEFFWRI)
C DOUBLE PRECISION UPPER_ENERGY,OUTER_ENERGY
C INTEGER ECOUNT,SCOUNT
C DOUBLE PRECISION PREVHARM,THISHARM
C REAL DWAX
C EXTERNAL COEFF,NONLIN,STEPP,BEWRI,BEWRI2,COEFFWRI
C COMMON /WARNINGS/UPPER_ENERGY,OUTER_ENERGY,SCOUNT,ECOUNT
C
C Local variables.

```

```

C
  INTEGER L, I, BCOUNT, CCOUNT, S, IS, I1, I2, STEPS, WARNING_FLAG
  DOUBLE PRECISION STEP, SIG, OLDSIG, SIGMA, R, DIAG, OFFDIA, PI, XSTEP
  DOUBLE PRECISION SIGC, SIGK, FAKT1, FAKT2
  REAL WAX

C
C  IMPSTP is the number of initial fully implicit steps.
C  The strength of the S first harmonics in the Fourier expansion of
C  the initial values must not be damped more than 0.1 percent when
C  taking the IMPSTP initial steps.
C
  PARAMETER (S=20)
C
C***FIRST EXECUTABLE STATEMENT KZKCYL
C
C  Calculation of the number of steps that is needed,
C  in order to make an estimate of the progress.
C
  STEPS = IMPSTP - 1
  SIGMA = START
5  CONTINUE
  SIGMA = SIGMA + STEPP(SIGMA)
  STEPS = STEPS + 1
  IF(SIGMA.LT.STOP) THEN
    GO TO 5
  END IF
C
C  Start of the calculation
C
  WRITE(*,*) 'Starting the calculations.'
  PI = 4*ATAN(1.D0)
  BCOUNT = 1
  CCOUNT = 1
  SIGMA = START
  WAX = START
  WARNING_FLAG = 0
C
C  By setting START = STOP, we may print out the initial values.
C
  IF (START.EQ.STOP) THEN
    CALL BEWRI(WINDWX, SIGMA, OMEGA, IXMAX, NHARM)
    GO TO 999
  END IF
  XSTEP = ABS(WINDWX)/DBLE(IXMAX+1)
  SIGC = SIGMA
  SIGK = SIGMA
  CALL COEFF(SIGC, SIGK, COLD, KHALF, NHARM)
C
C  Go IMPSTP steps with the fully implicit method.
C
  DO 100 IS = 1, IMPSTP
C
C  Choose the step size such that the S first eigenvectors are
C  kept to 99.9 per cent of their initial strength after IMPSTP
C  steps.
C
  STEP = SQRT(2./ (50000.*IMPSTP))* (2*WINDWX)**2/
C  +
  (ABS(KHALF(1))*S**2*PI**2)
  STEP = IMP_STL
  SIG = SIGMA + STEP
  OLDSIG = SIGMA
  IF (BCOUNT.LE.NUMBE) THEN

```

```

        SIGMA = MIN(SIG,WBEAM(BCOUNT),STOP)
    ELSE
        SIGMA = STOP
    END IF
    STEP = SIGMA - OLDSIG
C
C   Compute the coefficients and the nonlinear
C   contributions.
C
    SIGC = SIGMA
    SIGK = SIGMA
    CALL COEFF(SIGC,SIGK,CNEW,KHALF,NHARM)
    CALL NONLIN(SIGMA,OMEGA,IXMAX,NHARM,NONLI)
    R = STEP/XSTEP**2
C
C   Loop for each harmonic L.
C
    DO 50 L = 1,NHARM
C
C   Set up the appropriate systems of equations in the
C   way required for TRIDIA.
C
        DIAG = 1 + STEP*CNEW(L)
        OFFDIA = 2*R*KHALF(L)
C
C   First the diagonal 2*2 sub-matrices.
C
        A(1,1,0,0) = DIAG
        A(1,2,0,0) = 2*OFFDIA
        A(2,1,0,0) = - A(1,2,0,0)
        A(2,2,0,0) = DIAG
        DO 10 I = 1,IXMAX
            A(1,1,0,I) = DIAG
            A(1,2,0,I) = OFFDIA
            A(2,1,0,I) = - OFFDIA
            A(2,2,0,I) = DIAG
10        CONTINUE
C
C   Then the sub-matrices above the diagonal.
C
        A(1,2,1,0) = - 2*OFFDIA
        A(2,1,1,0) = - A(1,2,1,0)
        DO 20 I = 1,IXMAX - 1
            A(1,2,1,I) = - OFFDIA* (1+1/DBLE(2*I))/2
            A(2,1,1,I) = - A(1,2,1,I)
20        CONTINUE
C
C   and the sub-matrices below the diagonal.
C
        DO 30 I = 1,IXMAX
            A(1,2,-1,I) = - OFFDIA* (1-1/DBLE(2*I))/2
            A(2,1,-1,I) = - A(1,2,-1,I)
30        CONTINUE
C
C   Define the right hand side.
C
        DO 40 I = 0,IXMAX
            F(1,I) = OMEGA(I,L,1) + STEP*NONLI(I,L,1)
            F(2,I) = OMEGA(I,L,2) + STEP*NONLI(I,L,2)
40        CONTINUE
C

```

```

C   Solve the system of equations.
C
      I1 = 1
      I2 = I1 + 8*IXMAX + 8
      CALL TRIDIA(A, IXMAX+1, W, F, WORK(I1), WORK(I2))
C
C   Insert the solution in OMEGA.
C
      DO 45 I = 0, IXMAX
          OMEGA(I, L, 1) = W(1, I)
          OMEGA(I, L, 2) = W(2, I)
45      CONTINUE
C
C   Add square sums to the warning variables
C
      DO 47 I = IXMAX-2, IXMAX
          OUTER_ENERGY = OUTER_ENERGY
+          + W(1, I)**2 + W(2, I)**2
47      CONTINUE
          IF (L.GE.(NHARM-2)) THEN
              DO 48 I = 0, IXMAX
                  UPPER_ENERGY = UPPER_ENERGY
+                  + W(1, I)**2 + W(2, I)**2
48      CONTINUE
          ENDIF
C
C   Count how many times the Lth harmonic has higher
C   amplitude than the (L-1)th
C
      THISHARM = W(1, 0)**2 + W(2, 0)**2
      IF (L.GT.1) THEN
          IF (PREVHARM.LT.THISHARM) THEN
              ECOUNT = ECOUNT + 1.D0
              WARNING_FLAG = 1
          ENDIF
      ENDIF
      PREVHARM = THISHARM
C
C   End loop for each harmonic.
C
      COLD(L) = CNEW(L)
50      CONTINUE
C
C   Stepcount/warning
C
      SCOUNT = SCOUNT + 1.D0
      IF (WARNING_FLAG.EQ.1) THEN
          WRITE(6, *) 'Warning: Harmonic higher than its parent'
          WARNING_FLAG = 0
      ENDIF
C
C   Perform damping of the solution near the border of the calculation area
C
      CALL BRDDMP(OMEGA, IXMAX, NHARM)
C
C   Perform damping of the solution's IMP_DMPWIDTH highest harmonic components
C
      IF (HARM_DMPSWITCH.EQ.1) THEN
          CALL HARMDMP(OMEGA, IXMAX, NHARM)
      END IF

```

```

C
C   Save results
C
      IF (SIGMA.GE.WAX) THEN
          CALL BEWRI2 (SIGMA,OMEGA,IXMAX,NHARM)
          WAX = WAX + DWAX
C
C       Show progress on screen
      WRITE (6,60) REAL(SCOUNT)/REAL(STEPS)*100
60  END IF
      FORMAT('Progress: ',F5.1,' %')

      IF (BCOUNT.LE.NUMBE) THEN
          IF (WBEAM(BCOUNT).LE.SIGMA) THEN
              CALL BEWRI (WINDWX,SIGMA,OMEGA,IXMAX,NHARM)
              BCOUNT = BCOUNT + 1
          END IF
      END IF
      IF (CCOUNT.LE.NCOEFFWRI) THEN
          IF (COEFFWRI_POS(CCOUNT).LE.SIGMA) THEN
              CALL COEFFWRI (SIGMA,OMEGA,IXMAX,NHARM)
              CCOUNT = CCOUNT + 1
          END IF
      END IF

      IF (SIGMA.GE.STOP) THEN
          GO TO 999
      END IF

C
C   End fully implicit loop.
C
100  CONTINUE
      WRITE(*,*) 'Implicit steps complete.'
C
C   Continue with the Richtmyer procedure
C
105  CONTINUE
      STEP = STEPP(SIGMA)
      SIG = SIGMA + STEP
      OLDSIG = SIGMA
      IF (BCOUNT.LE.NUMBE) THEN
          SIGMA = MIN(SIG,WBEAM(BCOUNT),STOP)
      ELSE
          SIGMA = STOP
      END IF
      STEP = SIGMA - OLDSIG

C
C   Compute the coefficients and the nonlinear
C   contributions.
C
      SIGC = SIGMA
      SIGK = OLDSIG + STEP/2
      CALL COEFF (SIGC,SIGK,CNEW,KHALF,NHARM)
      CALL NONLIN (SIGMA,OMEGA,IXMAX,NHARM,NONLI)
      R = STEP/XSTEP**2

C
C   Loop for each harmonic L.
C
      DO 150 L = 1,NHARM
C
C   Set up the appropriate systems of equations in the

```



```

C   way required for TRIDIA.
C
      DIAG = 1 + STEP*CNEW(L)/2
      OFFDIA = R*KHALF(L)
C
C   First the diagonal 2*2 sub-matrices.
C
      A(1,1,0,0) = DIAG
      A(1,2,0,0) = 2*OFFDIA
      A(2,1,0,0) = - A(1,2,0,0)
      A(2,2,0,0) = DIAG
      DO 110 I = 1, IXMAX
          A(1,1,0,I) = DIAG
          A(1,2,0,I) = OFFDIA
          A(2,1,0,I) = - OFFDIA
          A(2,2,0,I) = DIAG
110     CONTINUE
C
C   Then the sub-matrices above the diagonal.
C
      A(1,2,1,0) = - 2*OFFDIA
      A(2,1,1,0) = - A(1,2,1,0)
      DO 120 I = 1, IXMAX - 1
          A(1,2,1,I) = - OFFDIA* (1+1/DBLE(2*I))/2
          A(2,1,1,I) = - A(1,2,1,I)
120     CONTINUE
C
C   and the sub-matrices below the diagonal.
C
      DO 130 I = 1, IXMAX
          A(1,2, - 1,I) = - OFFDIA* (1-1/DBLE(2*I))/2
          A(2,1, - 1,I) = - A(1,2, - 1,I)
130     CONTINUE
C
C   Set up the right hand side.
C
      DIAG = 1 - STEP*COLD(L)/2
      OFFDIA = R*KHALF(L)
      F(1,0) = DIAG*OMEGA(0,L,1) + 2*OFFDIA*
+           (OMEGA(1,L,2)-OMEGA(0,L,2)) + STEP*NONLI(0,L,1)
      F(2,0) = DIAG*OMEGA(0,L,2) - 2*OFFDIA*
+           (OMEGA(1,L,1)-OMEGA(0,L,1)) + STEP*NONLI(0,L,2)
      DO 140 I = 1, IXMAX - 1
          FAKT1 = 1 + 1/DBLE(2*I)
          FAKT2 = 1 - 1/DBLE(2*I)
          F(1,I) = DIAG*OMEGA(I,L,1) +
+           OFFDIA* (FAKT1*OMEGA(I+1,L,2)-2*OMEGA(I,L,2)+
+           FAKT2*OMEGA(I-1,L,2))/2 + STEP*NONLI(I,L,1)
          F(2,I) = DIAG*OMEGA(I,L,2) -
+           OFFDIA* (FAKT1*OMEGA(I+1,L,1)-2*OMEGA(I,L,1)+
+           FAKT2*OMEGA(I-1,L,1))/2 + STEP*NONLI(I,L,2)
140     CONTINUE
          FAKT2 = 1 - 1/DBLE(2*IXMAX)
          F(1,IXMAX) = DIAG*OMEGA(IXMAX,L,1) +
+           OFFDIA* (FAKT2*OMEGA(IXMAX-1,L,2)-
+           2*OMEGA(IXMAX,L,2))/2 + STEP*NONLI(IXMAX,L,1)
          F(2,IXMAX) = DIAG*OMEGA(IXMAX,L,2) -
+           OFFDIA* (FAKT2*OMEGA(IXMAX-1,L,1)-
+           2*OMEGA(IXMAX,L,1))/2 + STEP*NONLI(IXMAX,L,2)
C
C   Solve the system of equations.

```

```

C
      I1 = 1
      I2 = I1 + 8*IXMAX + 8
      CALL TRIDIA(A, IXMAX+1, W, F, WORK(I1), WORK(I2))
C
C   Insert the solution in OMEGA.
C
      DO 145 I = 0, IXMAX
          OMEGA(I, L, 1) = W(1, I)
          OMEGA(I, L, 2) = W(2, I)
145    CONTINUE
C
C   Add square sums to the warning parameters
C
      DO 147 I = IXMAX-2, IXMAX
          OUTER_ENERGY = OUTER_ENERGY
+
          + W(1, I)**2 + W(2, I)**2
147    CONTINUE
          IF (L.GE.(NHARM-2)) THEN
              DO 148 I = 0, IXMAX
                  UPPER_ENERGY = UPPER_ENERGY
+
                  + W(1, I)**2 + W(2, I)**2
148    CONTINUE
              ENDIF
C
C   Count how many times the Lth harmonic has higher
C   amplitude than the (L-1)th
C
          THISHARM = W(1, 0)**2 + W(2, 0)**2
          IF (L.GT.1) THEN
              IF (PREVHARM.LT.THISHARM) THEN
                  ECOUNT = ECOUNT + 1.D0
                  WARNING_FLAG = 1
              ENDIF
          ENDIF
          PREVHARM = THISHARM
C
C   End loop for each harmonic.
C
          COLD(L) = CNEW(L)
150    CONTINUE
C
C   Step count/warning
C
          SCOUNT = SCOUNT + 1.D0
          IF (WARNING_FLAG.EQ.1) THEN
              WRITE(6, *) 'Warning: Harmonic higher than its parent'
              WARNING_FLAG = 0
          ENDIF
C
C   Perform damping of the solution near the border of the calculation area
C
          CALL BRDDMP(OMEGA, IXMAX, NHARM)
C
C   Perform damping of the solution's IMP_DMPWIDTH highest harmonic components
C
          IF (HARM_DMPSWITCH.EQ.1) THEN
              CALL HARMDMP(OMEGA, IXMAX, NHARM)
          END IF
C
C   Save results

```

```

C
      IF (SIGMA.GE.WAX) THEN
        CALL BEWRI2 (SIGMA, OMEGA, IXMAX, NHARM)
        WAX = WAX + DWAX
C
C      Show progress on screen
        WRITE (6, 60) REAL(SCOUNT)/REAL(STEPS)*100
      END IF
      IF (BCOUNT.LE.NUMBE) THEN
        IF (WBEAM(BCOUNT).LE.SIGMA) THEN
          CALL BEWRI (WINDWX, SIGMA, OMEGA, IXMAX, NHARM)
          BCOUNT = BCOUNT + 1
        END IF
      END IF
      IF (CCOUNT.LE.NCOEFFWRI) THEN
        IF (COEFFWRI_POS(CCOUNT).LE.SIGMA) THEN
          CALL COEFFWRI (SIGMA, OMEGA, IXMAX, NHARM)
          CCOUNT = CCOUNT + 1
        END IF
      END IF
      IF (SIGMA.GE.STOP) THEN
        GO TO 999
      END IF
C
C      End Richtmyer loop.
C
      GO TO 105
C
C***END KZKCYL
C
999   RETURN
      END

      SUBROUTINE TRIDIA(A, IXMAX, W, F, L, U)
C
C***BEGIN PROLOGUE TRIDIA
C***AUTHOR Jarle Berntsen, University of Bergen,
C      EDB-senteret, Herman Fossgt 6, 5007 Bergen, NORWAY.
C***DATE WRITTEN 880810
C***PURPOSE
C      BLOTRI SOLVES A BLOCK-THREE DIAGONAL SYSTEM OF EQUATIONS BY
C      BLOCK GAUSSIAN ELIMINATION.
C      40*IXMAX OPERATIONS ARE NEEDED.
C
C      THE BLOCKS ARE 2*2.
C      THE 2*2 SUB-MATRICES BELOW AND ABOVE THE MAIN DIAGONAL OF A MUST
C      HAVE ZEROS ON THEIR DIAGONALS.
C
C***DESCRIPTION
C
C      ON ENTRY
C          A          DOUBLE PRECISION(2,2,-1:1,IXMAX). DEFINES THE
C                    THREE-DIAGONAL MATRIX.
C                    THE FIRST TWO INDEXES DEFINES THE POSITION OF
C                    AN ELEMENT WITHIN A 2*2 SUB-MATRIX.
C                    THE THIRD INDEX DEFINES THE DISTANCE OF THE
C                    SUB-MATRIX FROM THE DIAGONAL.
C                    THE LAST INDEX DEFINES THE ROW NUMBER OF THE
C                    SUB-MATRIX.

```

```

C          THIS INDEX CONVENTION IS ALSO USED FOR L
C          AND U. UNCHANGED ON EXIT.
C
C          IXMAX      INTEGER. THE NUMBER OF DIAGONAL SUB-MATRICES.
C
C          F          DOUBLE PRECISION(2,IXMAX). DEFINES THE
C          RIGHT-HAND SIDE. MODIFIED ON EXIT.
C
C          L          DOUBLE PRECISION(2,2,-1:0,IXMAX).
C          WORKING SPACE
C          USED FOR THE SUBMATRICES ON AND BELOW THE
C          DIAGONAL
C          OF THE L-MATRIX OF THE LU-DECOMPOSITION.
C
C          U          DOUBLE PRECISION(2,2,1:1,IXMAX). WORKING SPACE
C          USED FOR THE SUBMATRICES ABOVE THE DIAGONAL OF
C          THE U MATRIX OF THE LU-DECOMP.
C          THE DIAGONAL SUBMATRICES OF U ARE UNIT 2*2.
C
C          ON RETURN
C
C          W          DOUBLE PRECISION(2,IXMAX).
C          CONTAINS THE SOLUTION.
C
C***ROUTINES CALLED NONE
C***END PROLOGUE TRIDIA
C
C  Global variables.
C
C  IMPLICIT NONE
C  INTEGER IXMAX
C  DOUBLE PRECISION A(2,2, - 1:1,IXMAX)
C  DOUBLE PRECISION W(2,IXMAX),F(2,IXMAX),L(2,2, - 1:0,IXMAX)
C  DOUBLE PRECISION U(2,2,1:1,IXMAX)
C
C  Local variables.
C
C  INTEGER I,J
C  DOUBLE PRECISION F1,F2,L21,U22
C
C  LU-DECOMPOSE.
C
C  FIRST STEP. (FIRST ROW)
C
C  L(0,1)=A(0,1)
C
C***FIRST EXECUTABLE STATEMENT TRIDIA
C
C  DO 1 I = 1,2
C    DO 1 J = 1,2
1  L(I,J,0,1) = A(I,J,0,1)
C
C  THE 2*2 SYSTEMS ARE SOLVED AS FOLLOWS: (AX=F)
C  L21=A21/A11
C  U22=A22-L21*A12
C  F2=F2-L21*F1
C  X2=F2/U22
C  X1=(F1-A12*X2)/A11
C
C  L(0,1)*U(1,1)=A(1,1)
C

```

```

L21 = L(2,1,0,1)/L(1,1,0,1)
U22 = L(2,2,0,1) - L21*L(1,2,0,1)
C   F2=A(2,1,1,1)-L21*A(1,1,1,1) (WE EXPLOIT ALL ZEROS)
F2 = A(2,1,1,1)
U(2,1,1,1) = F2/U22
C   U(1,1,1,1)=(A(1,1,1,1)-L(1,2,0,1)*U(2,1,1,1))/L(1,1,0,1)
U(1,1,1,1) = - L(1,2,0,1)*U(2,1,1,1)/L(1,1,0,1)
C
F1 = A(1,2,1,1)
F2 = - L21*F1
U(2,2,1,1) = F2/U22
U(1,2,1,1) = (F1-L(1,2,0,1)*U(2,2,1,1))/L(1,1,0,1)
C
C   SECOND AND GENERAL STEP.
C
DO 10 I = 2,IXMAX - 1
C
C   L(-1,I)=A(-1,I)
C
C   L(1,1,-1,I)=0
C   L(2,2,-1,I)=0
C   L(1,2, - 1,I) = A(1,2, - 1,I)
C   L(2,1, - 1,I) = A(2,1, - 1,I)
C
C   L(0,I)=A(0,I)-L(-1,I)*U(1,I-1)
C
C   L(1,1,0,I) = A(1,1,0,I) - L(1,2, - 1,I)*U(2,1,1,I-1)
C   L(1,2,0,I) = A(1,2,0,I) - L(1,2, - 1,I)*U(2,2,1,I-1)
C   L(2,1,0,I) = A(2,1,0,I) - L(2,1, - 1,I)*U(1,1,1,I-1)
C   L(2,2,0,I) = A(2,2,0,I) - L(2,1, - 1,I)*U(1,2,1,I-1)
C
C   L(0,I)*U(1,I)=A(1,I)
C
C   L21 = L(2,1,0,I)/L(1,1,0,I)
C   U22 = L(2,2,0,I) - L21*L(1,2,0,I)
C   F2 = A(2,1,1,I)
C   U(2,1,1,I) = F2/U22
C   U(1,1,1,I) = - L(1,2,0,I)*U(2,1,1,I)/L(1,1,0,I)
C   F1 = A(1,2,1,I)
C   F2 = - L21*F1
C   U(2,2,1,I) = F2/U22
C   U(1,2,1,I) = (F1-L(1,2,0,I)*U(2,2,1,I))/L(1,1,0,I)
10 CONTINUE
C
C   END MAIN LOOP IN LU-DECOMP.
C
C   THIRD AND LAST STEP. (LAST ROW)
C
C   L(-1,IXMAX)=A(-1,IXMAX)
C
C   L(1,1,-1,IXMAX)=0
C   L(2,2,-1,IXMAX)=0
C   L(1,2, - 1,IXMAX) = A(1,2, - 1,IXMAX)
C   L(2,1, - 1,IXMAX) = A(2,1, - 1,IXMAX)
C
C   L(0,IXMAX)=A(0,IXMAX)-L(-1,IXMAX)*U(1,IXMAX-1)
C
C   L(1,1,0,IXMAX) = A(1,1,0,IXMAX) -
+   L(1,2, - 1,IXMAX)*U(2,1,1,IXMAX-1)
C   L(1,2,0,IXMAX) = A(1,2,0,IXMAX) -
+   L(1,2, - 1,IXMAX)*U(2,2,1,IXMAX-1)

```

```

L(2,1,0,IXMAX) = A(2,1,0,IXMAX) -
+
L(2,1,-1,IXMAX)*U(1,1,1,IXMAX-1)
L(2,2,0,IXMAX) = A(2,2,0,IXMAX) -
+
L(2,1,-1,IXMAX)*U(1,2,1,IXMAX-1)
C
C   END LU FACTORISATION.
C
C   FORWARD SUBSTITUTION.
C
C   FIRST STEP.
C
L21 = L(2,1,0,1)/L(1,1,0,1)
U22 = L(2,2,0,1) - L21*L(1,2,0,1)
F(2,1) = F(2,1) - L21*F(1,1)
F(2,1) = F(2,1)/U22
F(1,1) = (F(1,1)-L(1,2,0,1)*F(2,1))/L(1,1,0,1)
C
C   SECOND AND GENERAL STEP.
C
DO 20 I = 2,IXMAX
  L21 = L(2,1,0,I)/L(1,1,0,I)
  U22 = L(2,2,0,I) - L21*L(1,2,0,I)
  F1 = F(1,I) - L(1,2,-1,I)*F(2,I-1)
  F2 = F(2,I) - L(2,1,-1,I)*F(1,I-1)
  F2 = F2 - L21*F1
  F(2,I) = F2/U22
  F(1,I) = (F1-L(1,2,0,I)*F(2,I))/L(1,1,0,I)
20 CONTINUE
C
C   END FORWARD SUBSTITUTION.
C
C   BACK SUBSTITUTION.
C
C   FIRST STEP.
C
W(1,IXMAX) = F(1,IXMAX)
W(2,IXMAX) = F(2,IXMAX)
C
C   SECOND AND GENERAL STEP.
C
DO 30 I = IXMAX - 1,1,-1
  W(1,I) = F(1,I) - U(1,1,1,I)*W(1,I+1) - U(1,2,1,I)*W(2,I+1)
  W(2,I) = F(2,I) - U(2,1,1,I)*W(1,I+1) - U(2,2,1,I)*W(2,I+1)
30 CONTINUE
C
C   END BACK SUBSTITUTION.
C
C***END TRIDIA
C
RETURN
END

SUBROUTINE COEFF(SIGC,SIGK,C,K,NHARM)
IMPLICIT NONE
INTEGER NHARM,J
DOUBLE PRECISION SIGC,SIGK,C(NHARM),K(NHARM)
DOUBLE PRECISION PABSOR,PNONLI,SC,SK
COMMON /PARAM/PABSOR,PNONLI
SC = (1+SIGC)
SK = (1+SIGK)

```

```

DO 10 J = 1,NHARM
  C(J) = PABSOR* (J**2)
  K(J) = - 1.0/ (4*J* (SK**2))
10 CONTINUE
RETURN
END
DOUBLE PRECISION FUNCTION STEPP(SIGMA)
IMPLICIT NONE
DOUBLE PRECISION SIGMA, ISSTEP
COMMON /AXSTEP/ISSTEP
STEPP = ISSTEP*(1 + SIGMA)**2
RETURN
END

SUBROUTINE NONLIN(SIGMA, OMEGA, IXMAX, NHARM, NONLI)
IMPLICIT NONE
INTEGER NHARM, IXMAX, I, J, N
DOUBLE PRECISION OMEGA(0:IXMAX, NHARM, 2)
DOUBLE PRECISION NONLI(0:IXMAX, NHARM, 2)
DOUBLE PRECISION SIGMA, FAKT, S, PABSOR, PNONLI
COMMON /PARAM/PABSOR, PNONLI
S = 1.D0 + SIGMA
DO 100 N = 1, NHARM
  DO 29 I = 0, IXMAX
    NONLI(I, N, 1) = 0
    NONLI(I, N, 2) = 0
29 CONTINUE
  DO 50 I = 0, IXMAX
    DO 30 J = 1, N - 1
C      NB! Changed from the original file!
      NONLI(I, N, 1) = NONLI(I, N, 1) +
+          OMEGA(I, J, 1)*OMEGA(I, N-J, 2) +
+          OMEGA(I, J, 2)*OMEGA(I, N-J, 1)
      NONLI(I, N, 2) = NONLI(I, N, 2) +
+          OMEGA(I, J, 2)*OMEGA(I, N-J, 2) -
+          OMEGA(I, J, 1)*OMEGA(I, N-J, 1)
30 CONTINUE
      NONLI(I, N, 1) = 0.5*NONLI(I, N, 1)
      NONLI(I, N, 2) = 0.5*NONLI(I, N, 2)
      DO 40 J = N + 1, NHARM
+          NONLI(I, N, 1) = NONLI(I, N, 1) +
+          OMEGA(I, J-N, 1)*OMEGA(I, J, 2) -
+          OMEGA(I, J-N, 2)*OMEGA(I, J, 1)
      NONLI(I, N, 2) = NONLI(I, N, 2) -
+          OMEGA(I, J-N, 1)*OMEGA(I, J, 1) -
+          OMEGA(I, J-N, 2)*OMEGA(I, J, 2)
40 CONTINUE
50 CONTINUE
      FAKT = PNONLI*N/ (2*S)
      DO 60 I = 0, IXMAX
        NONLI(I, N, 1) = FAKT*NONLI(I, N, 1)
        NONLI(I, N, 2) = FAKT*NONLI(I, N, 2)
60 CONTINUE
100 CONTINUE
RETURN
END

```

```

SUBROUTINE INIT(WINDWX,OMEGA,IXMAX,NHARM,TP,TA)
IMPLICIT NONE
INTEGER I,J,IXMAX,NHARM
DOUBLE PRECISION OMEGA(0:IXMAX,NHARM,2),WINDWX,TP,TA
DOUBLE PRECISION USTEP,TSTEP,FA,X
OPEN (UNIT=17,FILE='omega.cnd',STATUS='new')
DO 20 I = 0,IXMAX
  IF (NHARM.GT.1) THEN
    DO 10 J = 2,NHARM
      OMEGA(I,J,1) = 0
      OMEGA(I,J,2) = 0
10    CONTINUE
  END IF
  X = I*WINDWX/DBLE (IXMAX)
  OMEGA(I,1,1) = TSTEP(X,TP,TA)*SIN(FA(X)) !h
  OMEGA(I,1,2) = TSTEP(X,TP,TA)*COS(FA(X)) !g
  WRITE(17,30) OMEGA(I,1,1),OMEGA(I,1,2)
20 CONTINUE
30 FORMAT(E16.10, 1X, E16.10)
CLOSE(17)
RETURN
END

```

```

SUBROUTINE INIT2(WINDWX,OMEGA,IXMAX,NHARM)
IMPLICIT NONE
INTEGER I,J,IXMAX,NHARM
DOUBLE PRECISION X,OMEGA(0:IXMAX,NHARM,2),WINDWX,FA
DOUBLE PRECISION A(0:IXMAX),B(0:IXMAX)
OPEN (UNIT=16,FILE='source.cnd',STATUS='old')
OPEN (UNIT=17,FILE='omega.cnd',STATUS='new')
DO 20 I = 0,IXMAX
  IF (NHARM.GT.1) THEN
    DO 10 J = 2,NHARM
      OMEGA(I,J,1) = 0
      OMEGA(I,J,2) = 0
10    CONTINUE
  END IF
  X = I*WINDWX/DBLE (IXMAX)
  READ(16,30) A(I),B(I)
  OMEGA(I,1,1) = A(I)
  OMEGA(I,1,2) = B(I)
  WRITE(17,30) OMEGA(I,1,1),OMEGA(I,1,2)
20 CONTINUE
30 FORMAT(E16.9, 1X, E16.9)
CLOSE(16)
CLOSE(17)
RETURN
END

```

```

DOUBLE PRECISION FUNCTION FA(U)
DOUBLE PRECISION U
FA = (ABS(U))**2
RETURN
END

```

```

DOUBLE PRECISION FUNCTION TSTEP(U,TP,TA)
DOUBLE PRECISION U,TP,TA
IF (ABS(U).LE.(1.D0)) THEN
  IF (ABS(U).LE.TP) THEN

```



```

        TSTEP = 1
    ELSE
        TSTEP = TA
    END IF
ELSE
    TSTEP = 0
END IF
RETURN
END

SUBROUTINE BRDDMP(OMEGA, IXMAX, NHARM)

C   Routine for damping of the solution when close to the
C   border of the calculation area.
C   This must sometimes be done to prevent the simulation
C   from breaking down due to reflections for the border.
C
C   *** Global variables
    IMPLICIT NONE
    INTEGER IXMAX, NHARM, DMPWIDTH, DMPSWITCH
    DOUBLE PRECISION OMEGA(0:IXMAX, NHARM, 2)

    COMMON /BRD_DMP/DMPWIDTH, DMPSWITCH
C
C   *** Local variables
    INTEGER I, J, K
    DOUBLE PRECISION ANGLE, FACTOR(DMPWIDTH), PI
C
C   *** Executable statements
C
C   Newtonian frictional force FRS
C   (see Ystad and Berntsen 1995)
    IF (DMPSWITCH.EQ.3) THEN
        DO 5 I=1, DMPWIDTH
            FACTOR(I) = 1.D0 - (DBLE(I)/DBLE(DMPWIDTH))**2
5           CONTINUE
C
C   Sine curve damping factors
    ELSE IF (DMPSWITCH.EQ.2) THEN
        PI = 4*ATAN(1.D0)
        DO 10 I=1, DMPWIDTH
            ANGLE = PI/2 - DBLE(I)*PI/DBLE(DMPWIDTH)
            FACTOR(I) = 0.5D0 + 0.5D0*SIN(ANGLE)
10           CONTINUE
C
C   Linear damping factors
    ELSE IF (DMPSWITCH.EQ.1) THEN
        DO 15 I=1, DMPWIDTH
            FACTOR(I) = 1.D0 - DBLE(I)/DBLE(DMPWIDTH)
15           CONTINUE
C
C   No damping
    ELSE
        DO 20 I=1, DMPWIDTH
            FACTOR(I) = 1
c20           CONTINUE
        END IF
C
C   Perform damping of the solution
C

```

```

IF (DMPSWITCH.GT.0) THEN
  DO 60 K=1,2
    DO 50 J=1,NHARM
      DO 40 I=1,DMPWIDTH
        OMEGA (IXMAX-I+1, J, K) = OMEGA (IXMAX-I+1, J, K)
+
40          CONTINUE
50          CONTINUE
60          CONTINUE
      END IF

      RETURN
    END

    SUBROUTINE HARMDMP (OMEGA, IXMAX, NHARM)
C   *** Global variables
      IMPLICIT NONE
      INTEGER IXMAX, NHARM, HARM_DMPWIDTH
      DOUBLE PRECISION OMEGA (0:IXMAX, NHARM, 2)
      COMMON /HARM_DMP/HARM_DMPWIDTH
C
C   *** Local variables
      INTEGER I, J, K
      DOUBLE PRECISION FACTOR (HARM_DMPWIDTH)
C
C   *** Executable statements
C
C   Newtonian frictional force FRS
C   (see Ystad and Berntsen 1995)
      DO 5 I=1, HARM_DMPWIDTH
        FACTOR (I) = 1.D0 - (DBLE (I) / DBLE (HARM_DMPWIDTH)) ** 2
5      CONTINUE
      DO 60 K=1, 2
        DO 50 J=1, HARM_DMPWIDTH
          DO 40 I=1, IXMAX
            OMEGA (I, NHARM-J+1, K) = OMEGA (I, NHARM-J+1, K)
+
40          CONTINUE
50          CONTINUE
60          CONTINUE

          RETURN
        END

C
C   Save transverse data
C
      SUBROUTINE BEWRI (WINDWX, SIGMA, OMEGA, IXMAX, NHARM)
      IMPLICIT NONE
      INTEGER NHARM, IXMAX, J, I, NH
      DOUBLE PRECISION SIGMA, OMEGA (0:IXMAX, NHARM, 2), WINDWX
      DOUBLE PRECISION S, X, XI, AMP (NH), PH (NH), AMPL, PHASE, DB, RADIUS, R0
      REAL DWTR, WTR
      COMMON /OUTPUT/RADIUS, R0, DWTR, NH
      S = 1.D0 + SIGMA
c      wtr = 0
      WRITE (10, *) SNGL (SIGMA*R0)
      WRITE (13, *) SNGL (SIGMA*R0)
      DO 20 I = 0, IXMAX

```

```

        XI = I*WINDWX/DBLE (IXMAX) *S
        X = XI*RADIUS
c      if (X.ge.wtr) then
        DO 10 J = 1,NH
            AMP(J) = AMPL(OMEGA(I,J,1),OMEGA(I,J,2),S)
            PH(J) = PHASE(OMEGA(I,J,1),OMEGA(I,J,2),S,XI)
10     CONTINUE
        WRITE (10,28) SNGL(X), (SNGL(AMP(J)),J=1,NH)
        WRITE (13,28) SNGL(X), (SNGL(PH(J)),J=1,NH)
c      end if
20     CONTINUE
28     FORMAT(6(E16.10,1X)) ! Must be set according to the value of NH
RETURN
END

C
C
C   On the axis
C
SUBROUTINE BEWRI2(SIGMA,OMEGA,IXMAX,NHARM)
IMPLICIT NONE
INTEGER NHARM,IXMAX,NH,I
DOUBLE PRECISION SIGMA,OMEGA(0:IXMAX,NHARM,2),AMP(NH),
+
REAL DWTR
COMMON /OUTPUT/RADIUS,R0,DWTR,NH
S = 1.D0 + SIGMA
Z = SIGMA*R0
DO 25 I=1,NH
    AMP(I) = AMPL(OMEGA(0,I,1),OMEGA(0,I,2),S)
    PH(I) = PHASE(OMEGA(0,I,1),OMEGA(0,I,2),S,0)
25 CONTINUE
WRITE(11,28) SNGL(Z), (SNGL(AMP(I)), I=1,NH)
WRITE(14,28) SNGL(Z), (SNGL(PH(I)), I=1,NH)
28 FORMAT(6(E16.10,1X)) ! Must be set according to the value of NH
RETURN
END

C
C   Write all the coefficients (on axis)
C
SUBROUTINE COEFFWRI(SIGMA,OMEGA,IXMAX,NHARM)
IMPLICIT NONE
INTEGER NHARM,IXMAX,NH,I
DOUBLE PRECISION RADIUS,R0,SIGMA,OMEGA(0:IXMAX,NHARM,2),S,Z
REAL DWTR
COMMON /OUTPUT/RADIUS,R0,DWTR,NH
S = 1.D0 + SIGMA
Z = SIGMA*R0
WRITE(12,5) SNGL(Z)
DO 2 I=1,NHARM
2   WRITE(12,10) SNGL(OMEGA(0,I,1)/S), SNGL(OMEGA(0,I,2)/S)
5   FORMAT(E16.10)
10  FORMAT(E16.10,1X,E16.10)
RETURN
END

DOUBLE PRECISION FUNCTION AMPL(FA,FB,S)
C
C   Function that calculates amplitude
C
IMPLICIT NONE

```

```

DOUBLE PRECISION FA,FB,S,SD
SD = FA**2 + FB**2
IF (S.NE.0) THEN
    AMPL = DSQRT(SD)/S
ELSE
    AMPL = DSQRT(SD)
END IF
END

DOUBLE PRECISION FUNCTION PHASE(FA,FB,S,XI)
C
C Function that calculates (slow) phase
C
IMPLICIT NONE
DOUBLE PRECISION FA,FB,S,XI

IF (AND((FA.NE.0),(S.NE.0))) THEN
    PHASE = ATAN(FB/FA) + XI**2/S
ELSE
    PHASE = 0.D0
END IF
END

```

Appendix C: Hydrophone calibration data

Calibration data for the Reson TC4034 hydrophone used in the current work are reproduced below.

C.1 Reson – Calibration sheet supplied with the hydrophone
(10 pages)

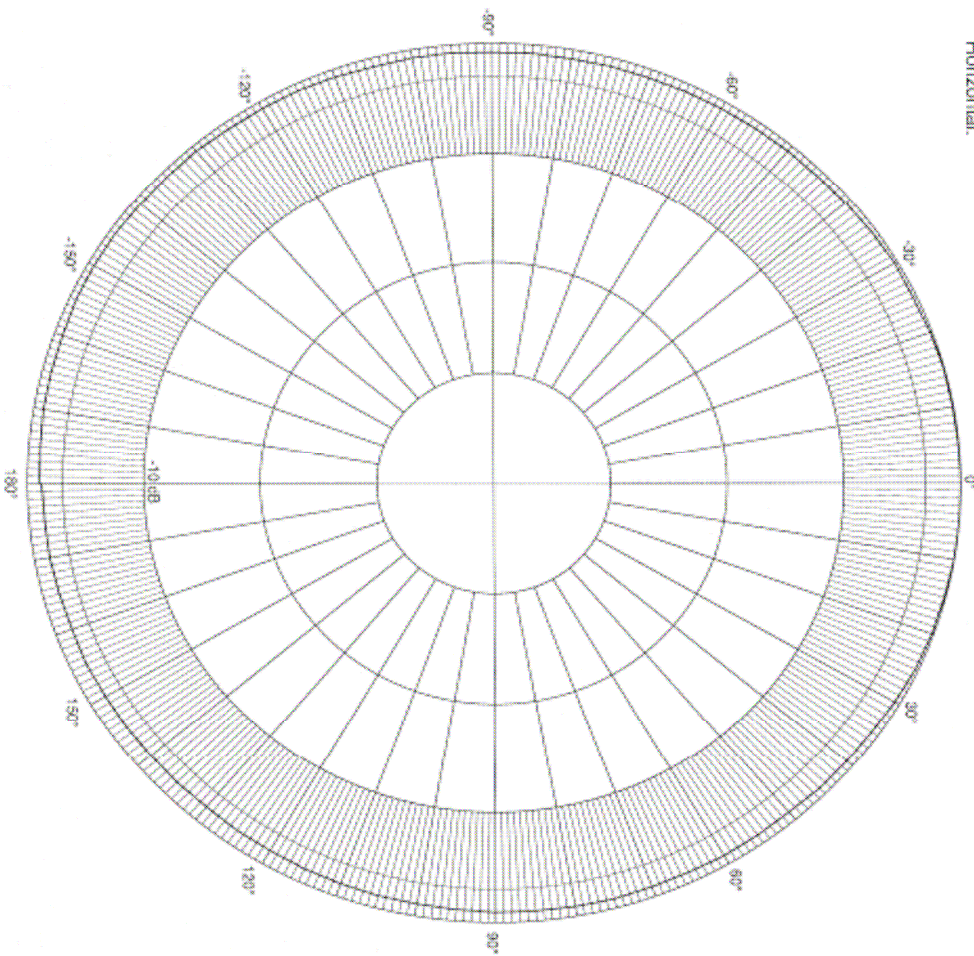


Under Test: TC4034
 S/N: 3103019
 Reference: TC4033/4034
 Date: 13 Oct 2003
 Session, Run: 3155, 1
 Max RS: -217.5 dB re 1V/μPa
 Comment: Horizontal.

HYDROPHONE DIRECTIVITY

Amplitude: 10.00 Vrms
 Pulse Width: 300.00 μs
 Angle: -180.0° to 180.0°
 Frequency: 100.00 kHz

Temperature: 20.2°C
 Depth: 1.30 m
 Distance: 0.50 m
 Tested by: HHP





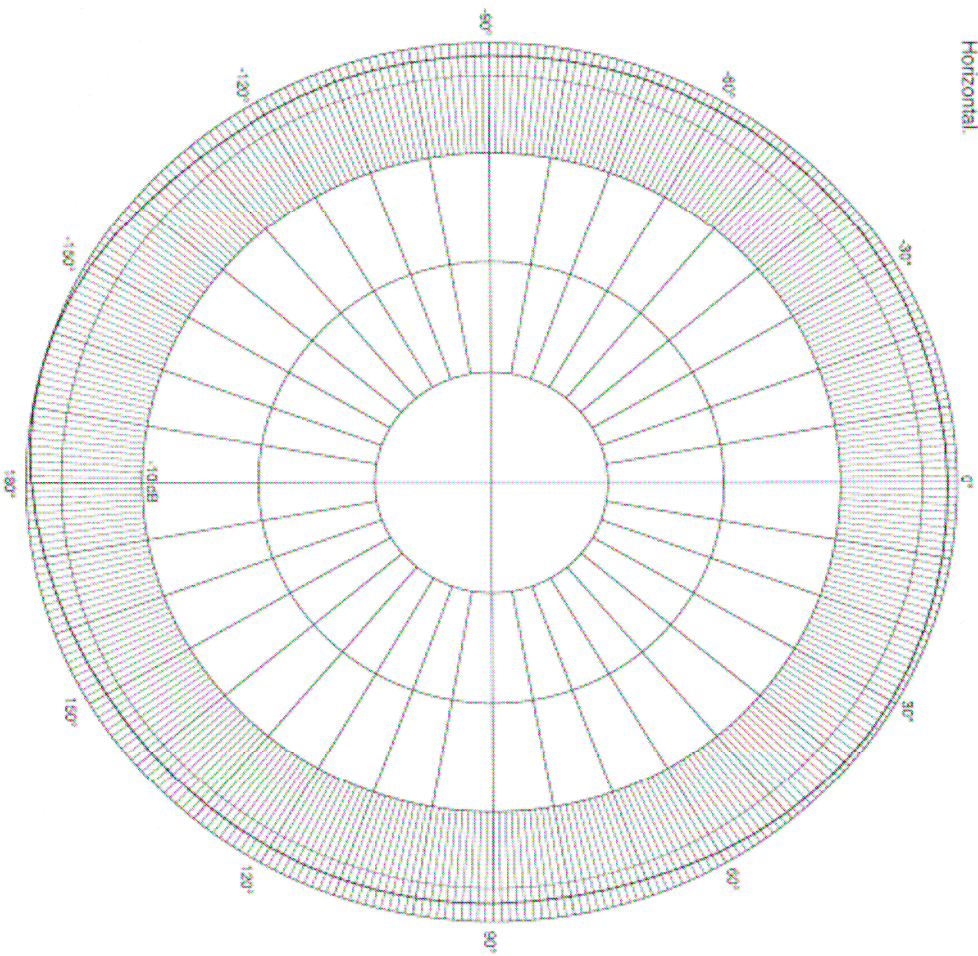
Under Test: TC4034
S/N: 3103019
Reference: TC4033/4034
Date: 13 Oct 2003
Session, Run: 3155_2
Max RS: -215.7 dB re 1V/μPa
Comment: Horizontal

HYDROPHONE DIRECTIVITY

Amplitude: 10.00 Vrms
Pulse Width: 170.00 μs
Angle: -180.0° to 180.0°
Frequency: 200.00 KHz

Temperature: 20.1 °C
Depth: 1.30 m
Distance: 0.50 m
Tested by: HHP

2003-10-16





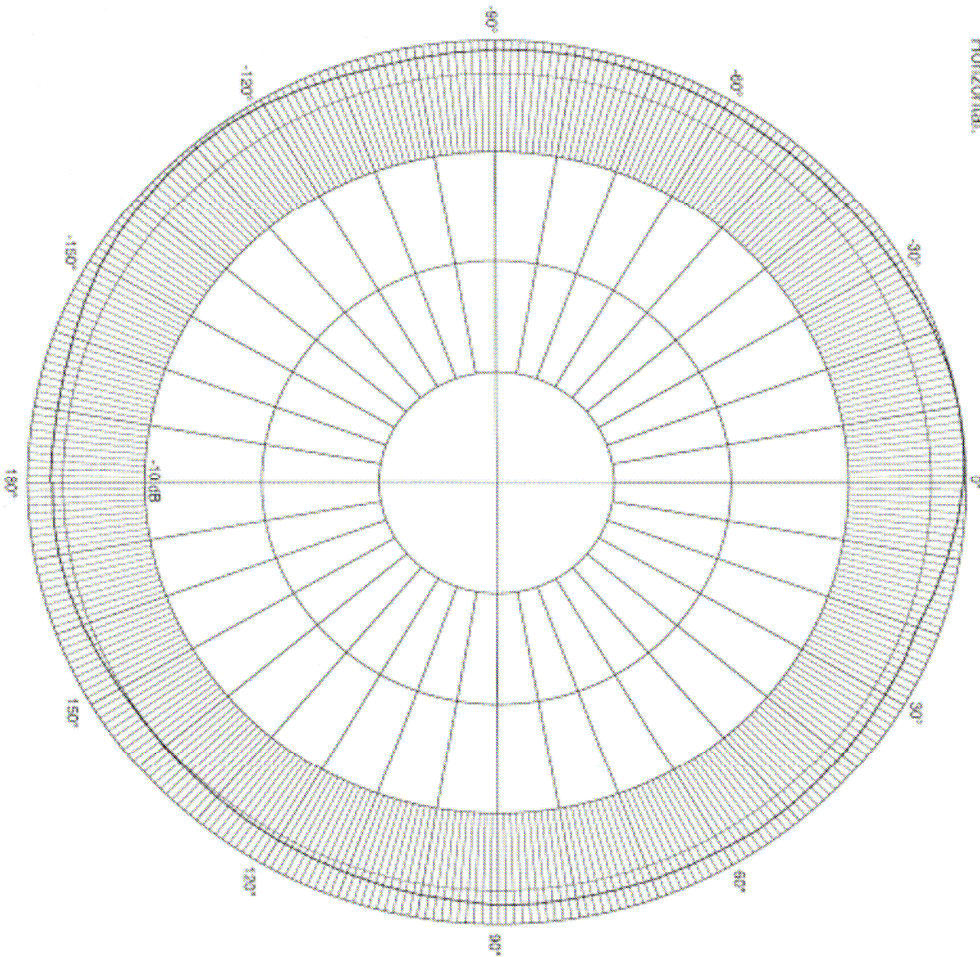
Under Test: TC4034
S/N: 3103019
Reference: TC4033/4034
Date: 13 Oct 2003
Session, Run: 3155, 3
Max RS: -213.2 dB re 1V/ μ Pa
Comment: Horizontal

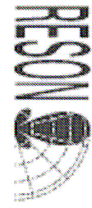
HYDROPHONE DIRECTIVITY

Amplitude: 10.00 Vrms
Pulse Width: 100.00 μ s
Angle: -180.0° to 180.0°
Frequency: 300.00 kHz

Temperature: 20.1°C
Depth: 1.30 m
Distance: 0.50 m
Tested by: HHP

2003-10-16



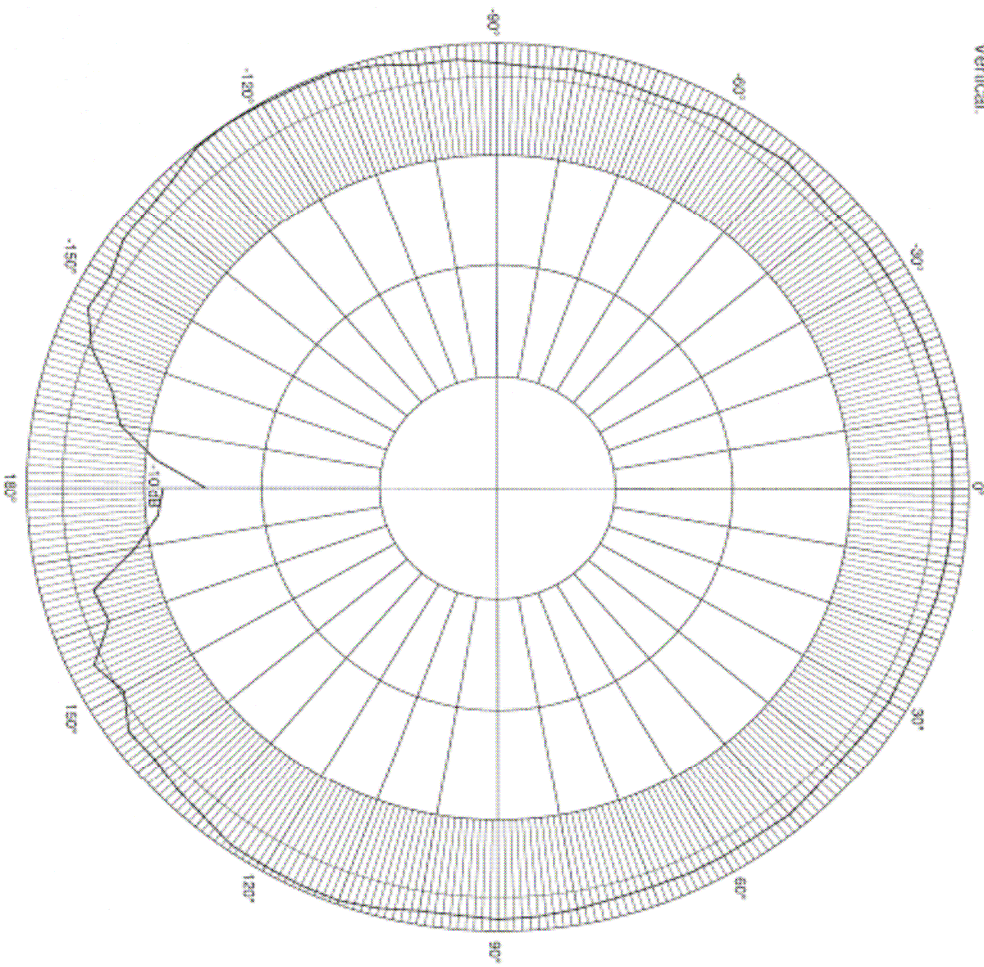
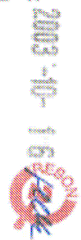


Under Test: TC4034
S/N: 3103019
Reference: TC4033/4034
Date: 13 Oct 2003
Session, Run: 3152, 6
Max RS: -216.5 dB re 1V/ μ Pa
Comment: Vertical

HYDROPHONE DIRECTIVITY

Amplitude: 10.00 Vrms
Pulse Width: 300.00 μ s
Angle: -180.0° to 180.0°
Frequency: 100.00 KHz

Temperature: 20.1°C
Depth: 1.30 m
Distance: 0.50 m
Tested by: HHP



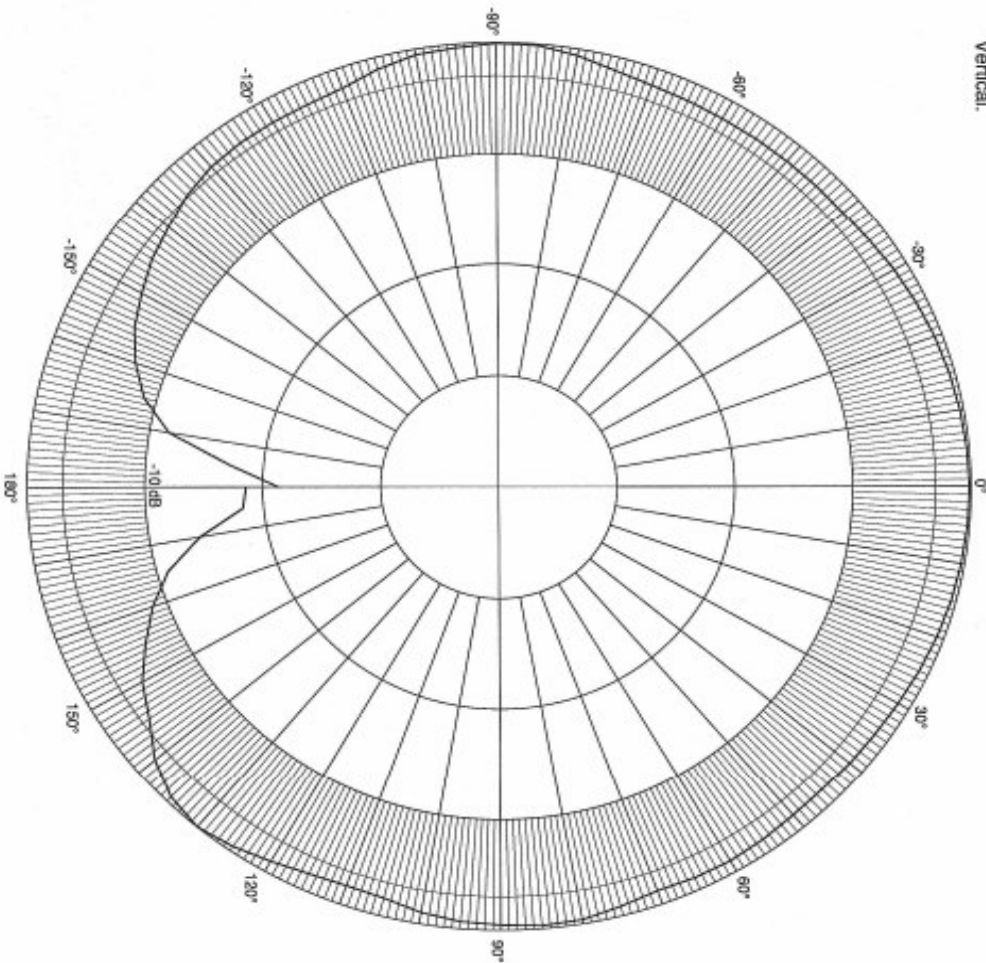


Under Test: TC4034
S/N: 3103019
Reference: TC4033/4034
Date: 13 Oct 2003
Session, Run: 3152, 5
Max RS: -216.2 dB re 1 V/ μ Pa
Comment: Vertical.

HYDROPHONE DIRECTIVITY

Amplitude: 10.00 Vrms
Pulse Width: 170.00 μ s
Angle: -180.0° to 180.0°
Frequency: 200.00 kHz

Temperature: 20.1°C
Depth: 1.30 m
Distance: 0.50 m
Tested by: HHP



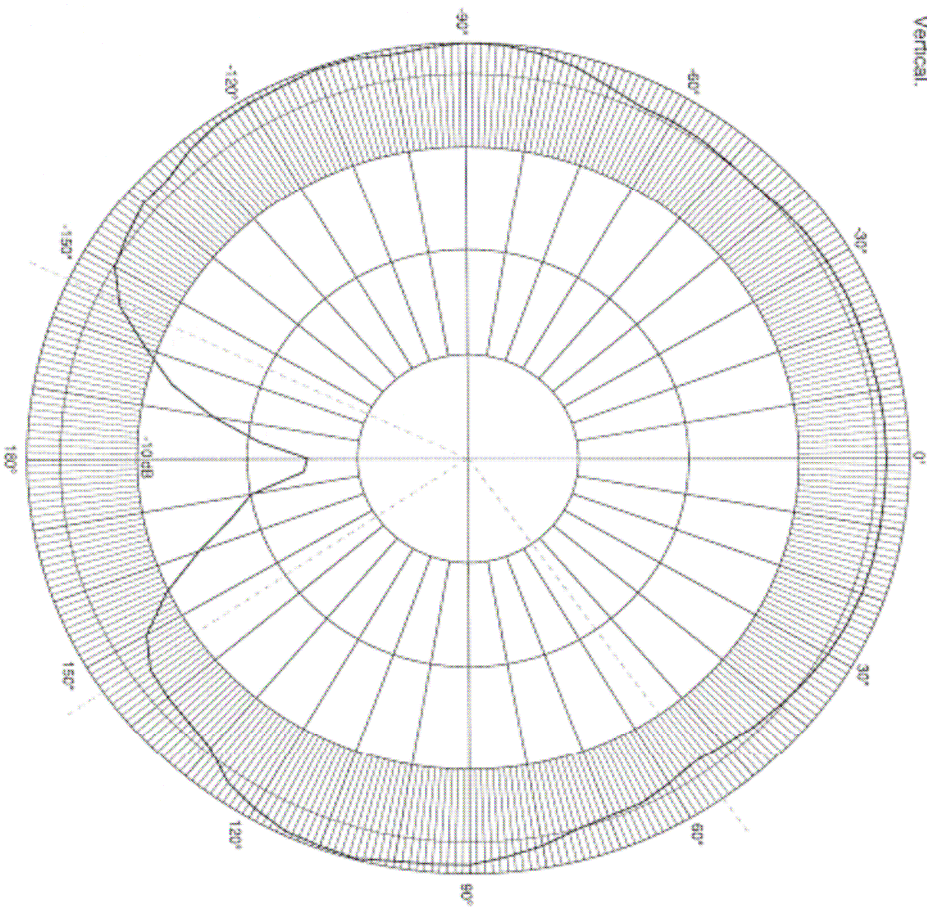


Under Test: TC4034
S/N: 3103019
Reference: TC4033/4034
Date: 13 Oct 2003
Session, Run: 3152, 4
Max RS: -213.4 dB re 1V/μPa
W: 300.5°
SL Left: 55.0°, -4.3 dB re 1V/μPa
Comment: Vertical

HYDROPHONE DIRECTIVITY

Amplitude: 10.00 Vrms
Pulse Width: 100.00 μs
Angle: -180.0° to 180.0°
Frequency: 300.00 kHz

Temperature: 20.1°C
Depth: 1.30 m
Distance: 0.50 m
Tested by: HHP





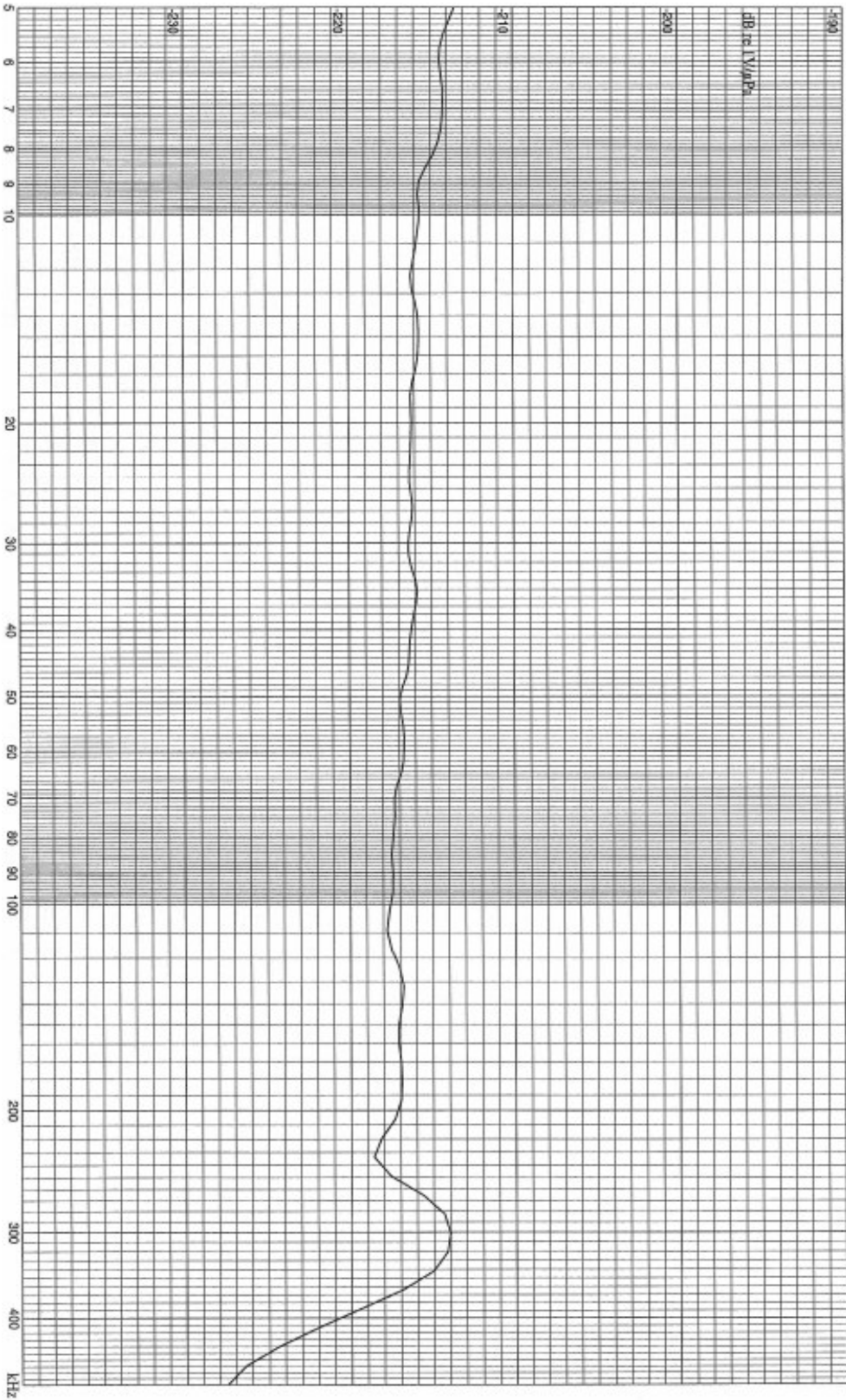
Under Test: TC4034
S/N: 3103019
Reference: TC4033/4034
Date: 13 Oct 2003
Session, Run: 3155, 7
Comment: PHO @ 250Hz: -217.0dB.

Amplitude: 29.95 Vrms
Pulse Width: 1.40 ms
Rep Rate: 100.0 ms
Averages: 8

Temperature: 20.1°C
Depth: 1.30 m
Distance: 0.50 m
Tested by: HHP



HYDROPHONE SENSITIVITY





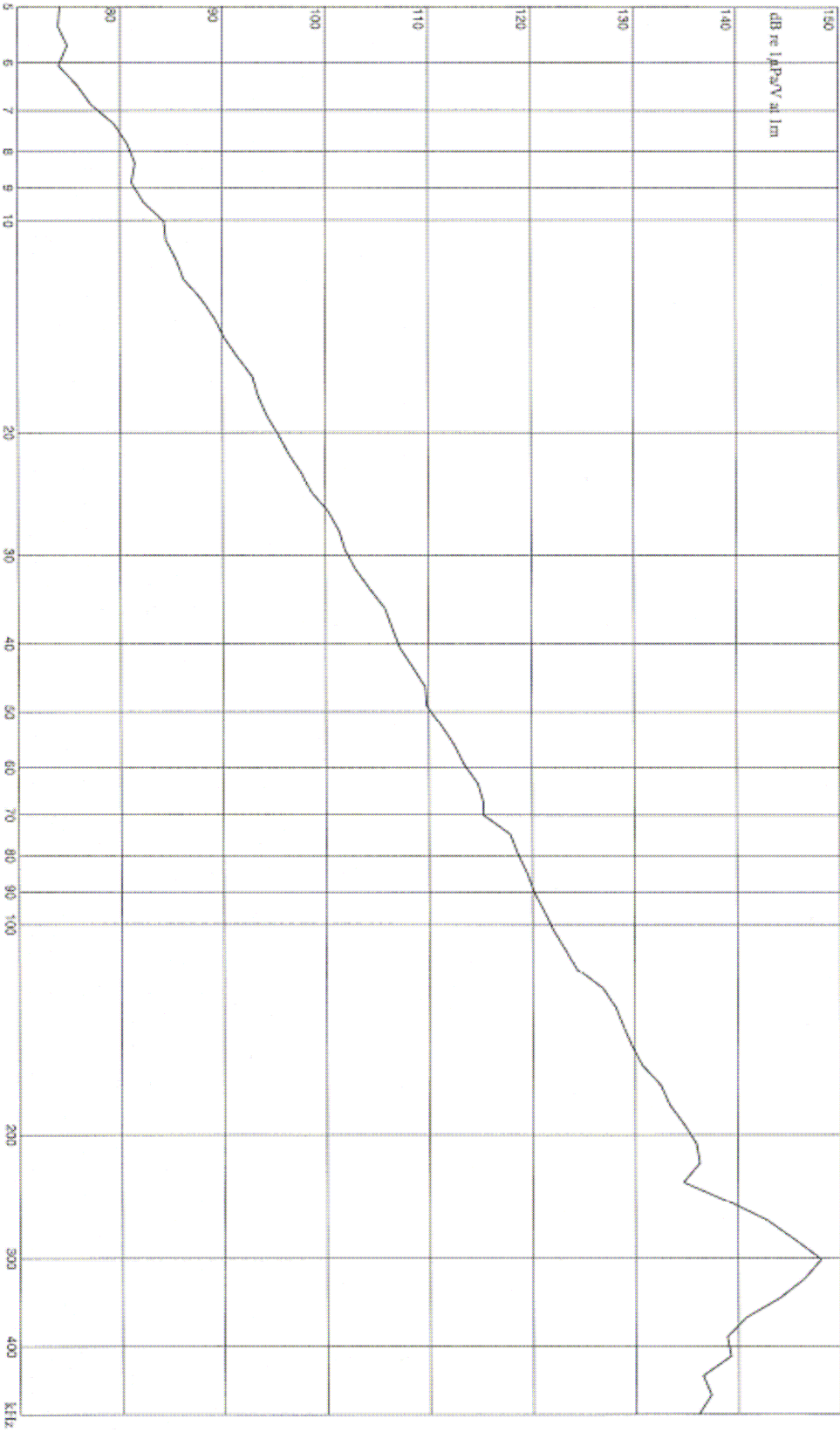
PROJECTOR SENSITIVITY

Under Test: TC4034
S/N: 3103019
Reference: TC4033/4034
Date: 13 Oct 2003
Session, Run: 3155, 8
100.00 kHz: 121.77 dB re 1/μPa/V at 1m
Comment: None

Amplitude: 30.00 Vrms
Pulse Width: 1.40 ms
Rep Rate: 66.6 ms
Averages: 8

Temperature: 20.1°C
Depth: 1.30 m
Distance: 0.50 m
Tested by: HHP

2003-10-16





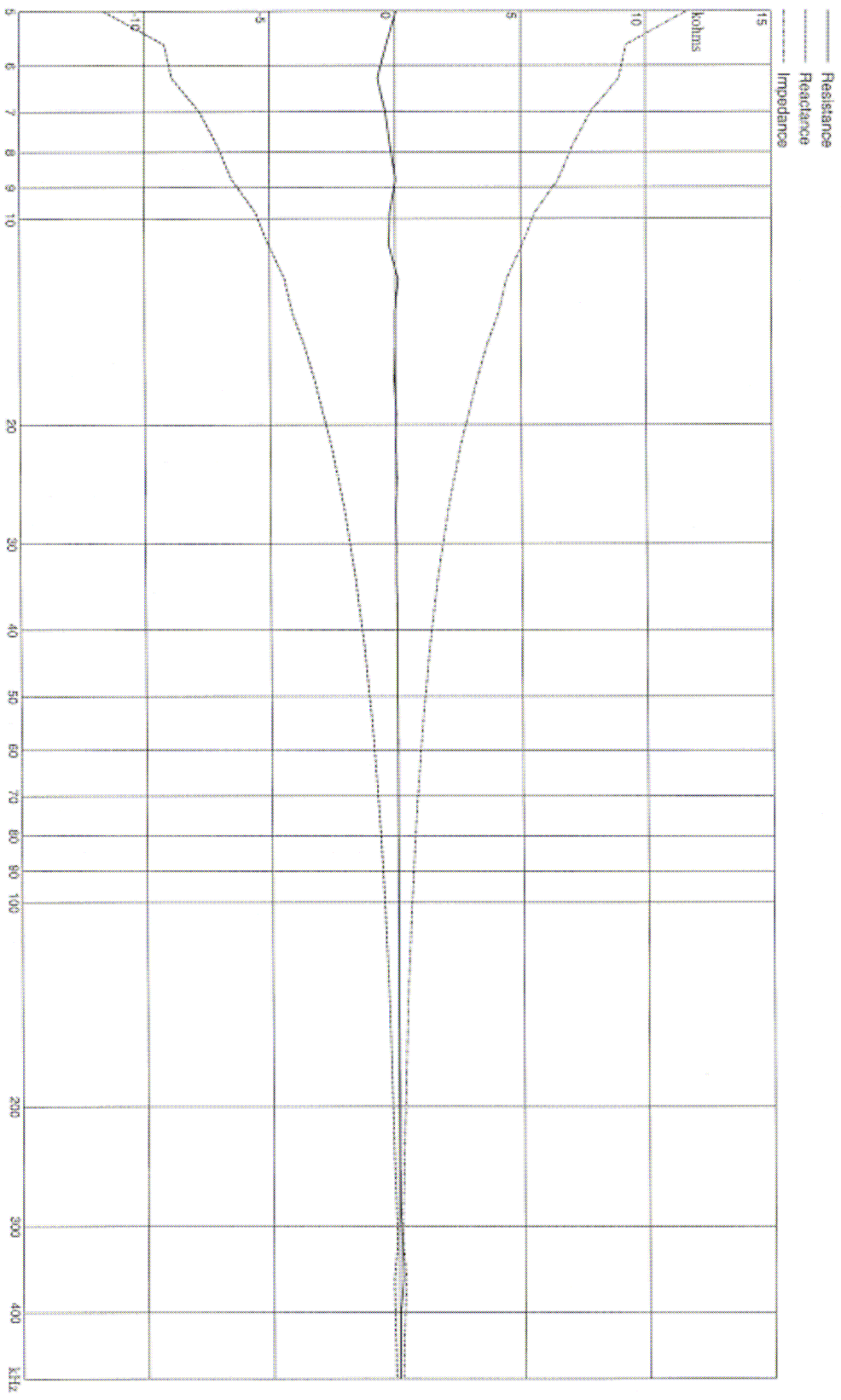
Under Test: TC4034
S/N: 3103019
Reference: TC4033/4034
Date: 13 Oct 2003
Session, Run: 2154, 31
Comment: None

Amplitude: 10.00 Vrms
Pulse Width: 6.00 ms
Rep Rate: 66.6 ms
Averages: 4

Temperature: 20.0°C
Depth: 1.00 m
Cal Resistor: 50.00 ohms
Tested by: HHP

IMPEDANCE SUMMARY

2003-10-16



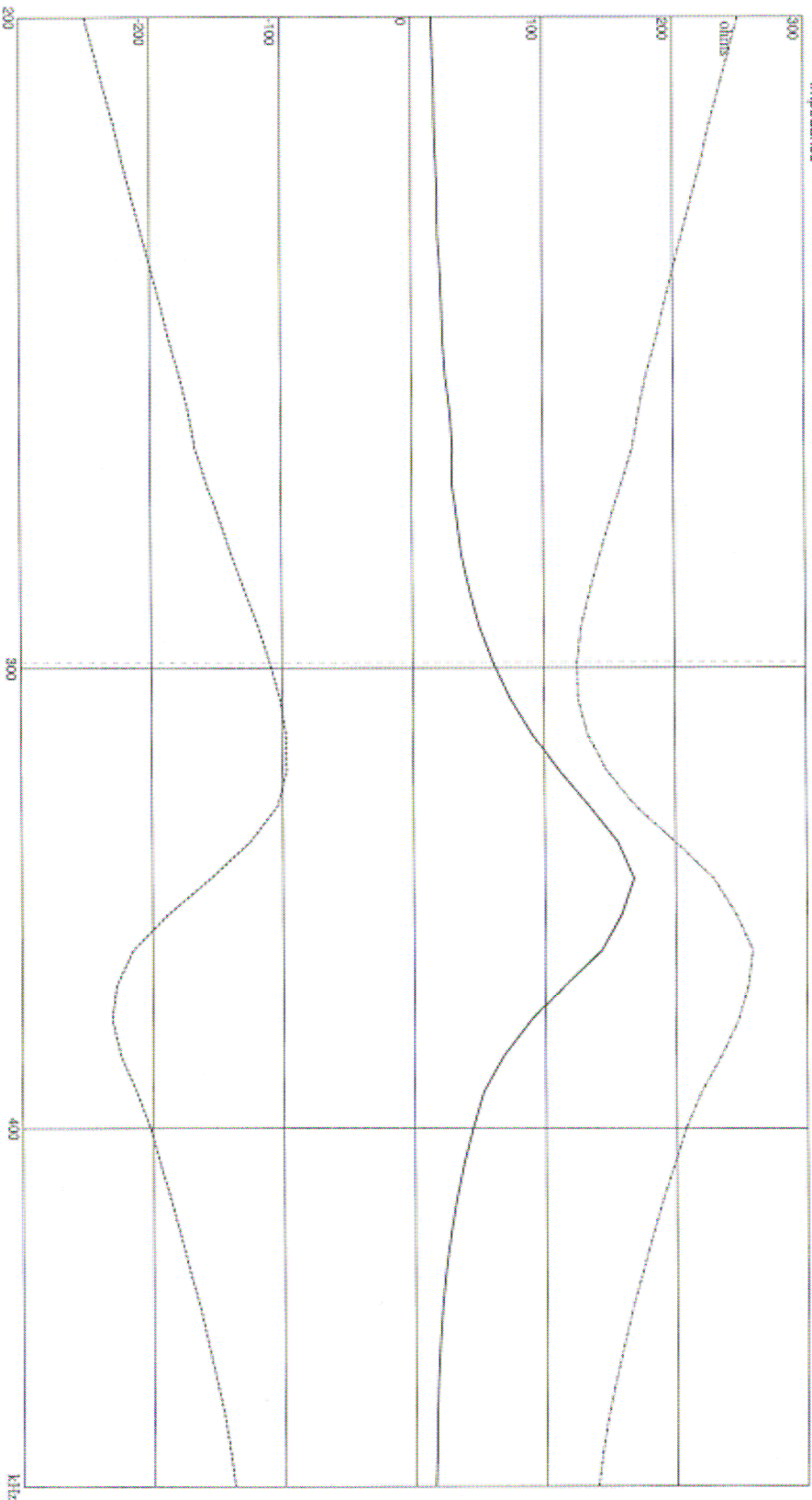


IMPEDANCE SUMMARY

Under Test: TC4034
S/N: 3103019
Reference: TC4033/4034
Date: 13 Oct 2003
Session, Run: 2154, 35
298.99 kHz: R:61.0 ohm, X:-109.4 ohm, Z:125.2 ohm, Phase:-60.9°
Comment: None

Amplitude: 10.00 Vrms
Pulse Width: 170.00 μ s
Rep Rate: 66.6 ms
Averages: 4

Temperature: 20.1°C 2003-10-16
Depth: 1.00 m
Cal Resistor: 50.00 ohms
Tested by: HHP



C.2 National Physical Laboratory – Hydrophone sensitivity
(4 pages)

NATIONAL PHYSICAL LABORATORY
Teddington Middlesex UK TW11 0LW Switchboard 020 8977 3222



Certificate of Calibration



RESON HYDROPHONE TYPE TC 4034
SERIAL NUMBER 3103019

FOR: CHRISTIAN MICHELSEN RESEARCH AS
Industrial Instrumentation
PO Box 6031 Postterminalen
N-5892 Bergen
Norway

For the attention of Mr Audun Pedersen

DESCRIPTION: Reson type TC4034 hydrophone supplied
with 10 metres of integral cable

IDENTIFICATION: Reson type TC4034, serial number 3103019


DATES OF
CALIBRATION: 26 – 27 January 2004

Reference: U1948

Page 1 of 4

Date of issue: 04 February 2004

Signed:  (Authorised Signatory)

Checked by: 

Name: S.P. Dowson for Managing Director

This certificate is issued in accordance with the laboratory accreditation requirements of the United Kingdom Accreditation Service. It provides traceability of measurement to recognised national standards, and to the units of measurement realised at the NPL or other recognised national standards laboratories. This certificate may not be reproduced other than in full, unless permission for the publication of an approved extract has been obtained in writing from the Managing Director. It does not of itself impute to the subject of the calibration any attributes beyond those shown by the data contained herein.

NATIONAL PHYSICAL LABORATORY
Continuation Sheet

MEASUREMENTS

The end-of-cable open-circuit free-field sensitivity of the hydrophone was determined by the method of three-transducer spherical-wave reciprocity in conformance with IEC 565: 1977 (BS 5652). The procedure requires that three hydrophones be operated in pairs, with one transmitting and one receiving. Of the three hydrophones used in the calibration, at least one is maintained by NPL as a reference standard.

Measurements were made on the steady-state portion of a tone-burst signal, with the hydrophone connected to a high impedance amplifier. Electrical loading corrections were applied to the results to give the end-of-cable open-circuit sensitivity of the hydrophone. When the hydrophone is connected to an electrical load, it will be necessary to take into account the effect of this loading on the sensitivity.

During the calibration, all hydrophones were positioned at a depth of 0.75 metres in a laboratory tank filled with fresh-water. During measurements, the separation distance between devices varied in the range 1.0 to 0.85 metres, the results being calculated assuming a spherical-wave field.

The hydrophone was mounted coaxially at the end of a vertical carbon fibre tube, the cable being routed along the length of the tube. A diagram of the mounting configuration used is available upon request. It should be noted that the use of a significantly different method of mounting the hydrophone may affect the measured sensitivity.

The hydrophone was orientated so that its alignment mark was facing directly towards the transmitting device with the incoming acoustic wave incident in a direction normal to the mark. The tolerance on the orientation of the hydrophone relative to the direction of propagation of the incoming wave was $\pm 3^\circ$ in the horizontal plane and $\pm 3^\circ$ in the vertical plane. Before measurements were started, all devices were cleaned, wetted and then soaked overnight in the water tank.

NATIONAL PHYSICAL LABORATORY

Continuation Sheet

RESULTS

| Frequency | End-of-cable open-circuit Sensitivity level |
|-----------|--|
| kHz | dB re 1 V/ μ Pa |
| 100.000 | -218.5 \pm 0.5 |
| 110.000 | -218.7 \pm 0.5 |
| 120.000 | -218.5 \pm 0.5 |
| 120.212 | -218.5 \pm 0.5 |
| 121.212 | -218.4 \pm 0.5 |
| 122.212 | -218.3 \pm 0.5 |
| 130.000 | -217.7 \pm 0.5 |
| 140.000 | -218.1 \pm 0.5 |
| 150.000 | -218.6 \pm 0.5 |
| 160.000 | -218.5 \pm 0.5 |
| 170.000 | -217.8 \pm 0.5 |
| 180.000 | -217.8 \pm 0.5 |
| 190.000 | -217.7 \pm 0.5 |
| 199.000 | -217.8 \pm 0.5 |
| 200.000 | -217.8 \pm 0.5 |
| 201.000 | -217.7 \pm 0.5 |
| 210.000 | -217.7 \pm 0.5 |
| 220.000 | -217.9 \pm 0.5 |
| 230.000 | -219.0 \pm 0.5 |
| 240.000 | -219.4 \pm 0.5 |
| 241.424 | -219.2 \pm 0.5 |
| 242.424 | -219.1 \pm 0.5 |
| 243.242 | -219.0 \pm 0.5 |
| 250.000 | -217.8 \pm 0.5 |
| 260.000 | -216.0 \pm 0.8 |
| 270.000 | -216.0 \pm 0.5 |
| 280.000 | -215.9 \pm 0.5 |
| 290.000 | -215.3 \pm 0.5 |
| 300.000 | -215.0 \pm 0.5 |
| 310.000 | -214.4 \pm 0.5 |
| 320.000 | -214.8 \pm 0.5 |
| 330.000 | -213.8 \pm 0.5 |
| 340.000 | -213.9 \pm 0.5 |
| 350.000 | -214.1 \pm 0.5 |
| 360.000 | -215.3 \pm 0.5 |
| 362.636 | -215.8 \pm 0.5 |
| 363.636 | -216.0 \pm 0.5 |
| 364.636 | -216.3 \pm 0.5 |
| 370.000 | -217.3 \pm 0.5 |
| 380.000 | -219.7 \pm 0.5 |
| 390.000 | -221.0 \pm 0.5 |
| 399.000 | -222.3 \pm 0.5 |

Reference: U1948

Checked by: AS JA.

Page 3 of 4

NPL-A01-99/1

NATIONAL PHYSICAL LABORATORY

Continuation Sheet

| | |
|---------|--------------|
| 400.000 | -222.3 ± 0.5 |
| 401.000 | -222.2 ± 0.5 |
| 410.000 | -220.3 ± 0.5 |
| 420.000 | -221.0 ± 0.5 |
| 430.000 | -221.8 ± 0.5 |
| 440.000 | -223.0 ± 0.8 |
| 450.000 | -226.3 ± 0.7 |
| 460.000 | -226.2 ± 0.5 |
| 470.000 | -226.9 ± 0.7 |
| 480.000 | -228.1 ± 0.9 |
| 490.000 | -229.1 ± 0.7 |
| 500.000 | -229.6 ± 0.6 |

During the measurements the temperature of the water was in the range 18.0 to 18.4 °C. The uncertainty on this temperature is ± 0.4 °C.

The reported expanded uncertainty is based on a standard uncertainty multiplied by a coverage factor, $k=2$, providing a level of confidence of approximately 95%.

The uncertainty evaluation has been carried out according to UKAS requirements.

C.3 National Physical Laboratory – Directivity at 400 kHz
(5 pages)

NATIONAL PHYSICAL LABORATORY
Teddington Middlesex UK TW11 0LW Switchboard 020 8977 3222



Certificate of Calibration



RESON HYDROPHONE TYPE TC 4034
SERIAL NUMBER 3103019

FOR: CHRISTIAN MICHELSEN RESEARCH AS
Industrial Instrumentation
PO Box 6031 Postterminalen
N-5892 Bergen
Norway

For the attention of Mr Audun Pedersen

DESCRIPTION: Reson type TC4034 hydrophone supplied
with 10 metres of integral cable

IDENTIFICATION: Reson type TC4034, serial number 3103019

DATES OF
CALIBRATION: 30 January 2004

Reference: U1954

Page 1 of 5

Date of issue: 04 February 2004

Signed: *S.P. Dowson* (Authorised Signatory)

Checked by: *ADT JA*

Name: S.P. Dowson for Managing Director

This certificate is issued in accordance with the laboratory accreditation requirements of the United Kingdom Accreditation Service. It provides traceability of measurement to recognised national standards, and to the units of measurement realised at the NPL or other recognised national standards laboratories. This certificate may not be reproduced other than in full, unless permission for the publication of an approved extract has been obtained in writing from the Managing Director. It does not of itself impute to the subject of the calibration any attributes beyond those shown by the data contained herein.

NATIONAL PHYSICAL LABORATORY

Continuation Sheet

MEASUREMENTS

The directional response of the hydrophone was determined by positioning the hydrophone in the field of an acoustic source and rotating the hydrophone about an axis that passes through its acoustic centre. The orientation of the hydrophone axis relative to the axis of rotation is specified with the results using the co-ordinate system specified in IEC 565:1977, *The calibration of hydrophones*. All results are presented with the data normalised to the maximum response.

Measurements were made on the steady-state portion of a tone-burst signal. During the calibration, both the hydrophone and projector were positioned at a depth of 0.8 metres in a laboratory tank filled with fresh-water. During measurements, the separation distance between the devices was 1.0 metre.

For the XY orientation the hydrophone was mounted coaxially at the end of a vertical carbon fibre tube, the cable being routed along the length of the tube. The hydrophone was orientated so that its alignment mark was facing directly towards the transmitting device with the incoming acoustic wave incident in a direction normal to the mark. This direction is taken to be the on-axis 0° reference point.

For the XZ orientation the hydrophone was mounted horizontally and rotated about its acoustic centre. The hydrophone was orientated so that its tip was facing directly towards the transmitting device with the incoming acoustic wave incident in a direction normal to the tip. This direction is taken to be the on-axis 0° reference point. The X-axis alignment mark was in the horizontal plane, facing to the left as viewed from the rear of the device.

For both XY and XZ configurations the tolerance on the orientation of the hydrophone (the 0° direction) relative to the direction of propagation of the incoming wave was $\pm 3^\circ$ in the horizontal plane and $\pm 3^\circ$ in the vertical plane. It should be noted that the use of a significantly different method of mounting the hydrophone may affect the measured directional response.

Before measurements were started, all devices were cleaned, wetted and then soaked overnight in the water tank.

Reference: U1954

Page 2 of 5

Checked by: ADT 

NPL-A01-94/1

NATIONAL PHYSICAL LABORATORY

Continuation Sheet

RESULTS

The directivity patterns have been presented in decibels, with all data normalised to the maximum response.

The table below gives the uncertainty based on the relative level with reference to the maximum response.

| Relative level dB | Uncertainty dB |
|-------------------|----------------|
| From 0 to -20 | 0.3 |
| From < -20 to -30 | 0.4 |
| From < -30 to -40 | 0.6 |

During the measurement the temperature of the water was 19.0 °C. The uncertainty on this temperature is ± 0.4 °C.

The reported expanded uncertainty is based on a standard uncertainty multiplied by a coverage factor, $k=2$, providing a level of confidence of approximately 95%.

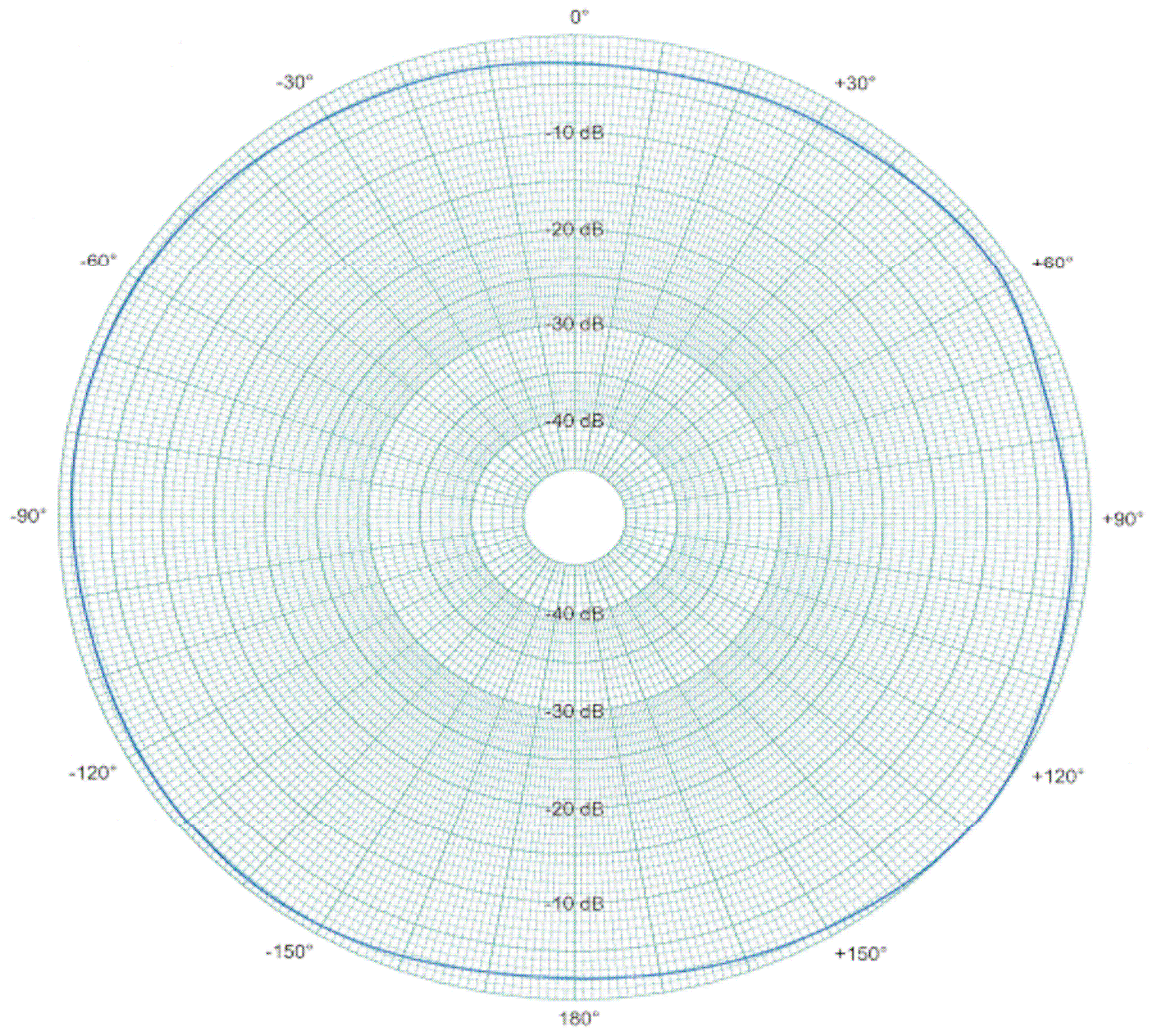
The uncertainty evaluation has been carried out according to UKAS requirements.

NATIONAL PHYSICAL LABORATORY
Continuation Sheet

RESON_TC4034 S/N: 3103019

Date: 30 Jan 2004

Frequency: 400 kHz



Remarks: XY PLANE

Reference: U1954

Checked by: *ADT*

NPL-A01-94/1

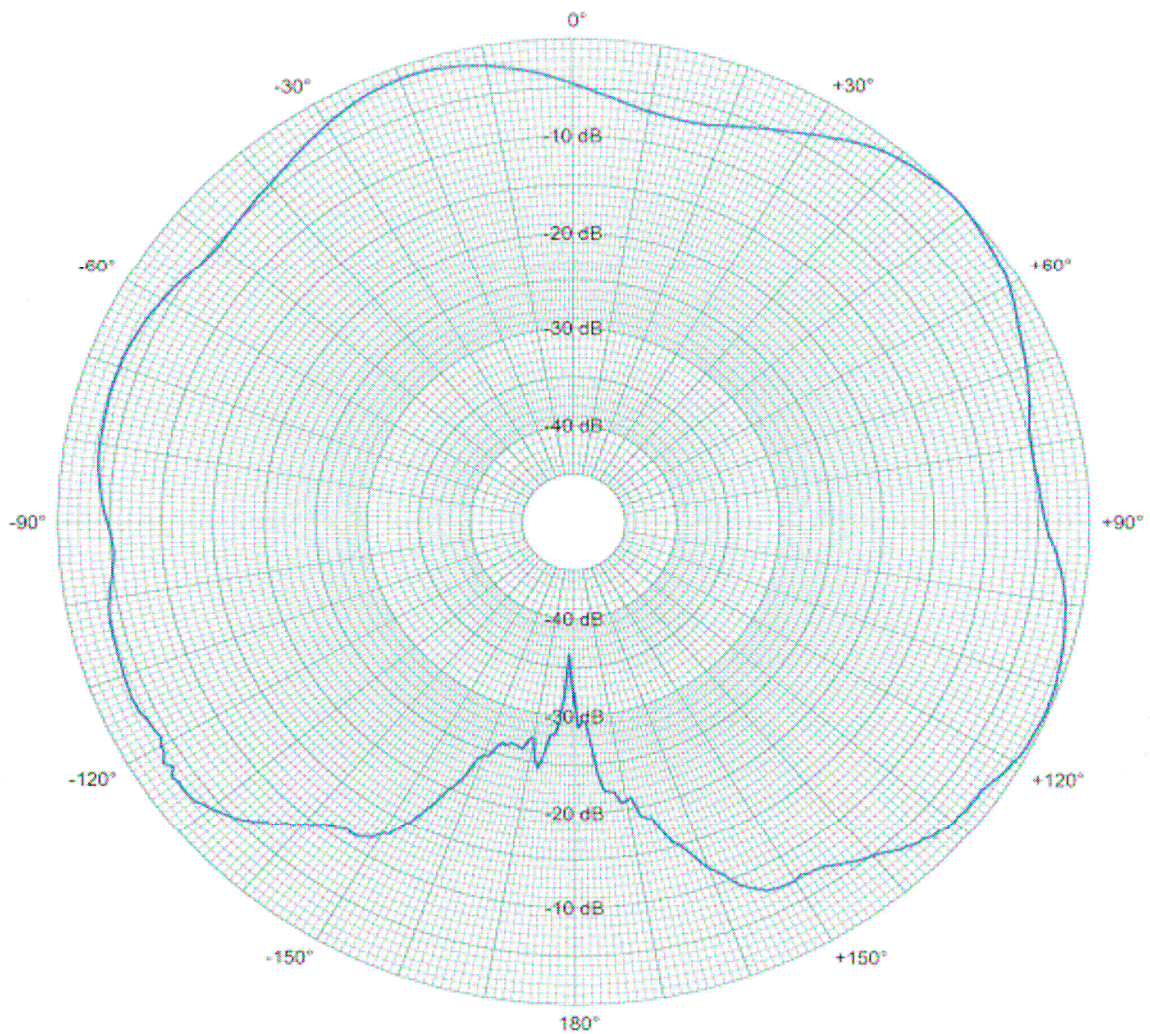
Page 4 of 5

NATIONAL PHYSICAL LABORATORY
Continuation Sheet

RESON_TC4034 S/N: 3103019

Date: 30 Jan 2004

Frequency: 400 kHz



Remarks: XZ PLANE

Reference: U1954

Checked by: AOT *at*

NPL-AQI-98/7

Page 5 of 5

